The Pennsylvania State University

The Graduate School

Aerospace Engineering Department

On the Characterization of Noise Sources in Supersonic Shock Containing Jets

A Dissertation in

Aerospace Engineering

by

Jérémy Veltin

Submitted in Partial Fulfillment
of the Requirements
for the Degree of

Doctor of Philosophy

December 2008

The dissertation of Jérémy Veltin was reviewed and approved* by the following:

Dennis K. McLaughlin
Professor of Aerospace Engineering
Dissertation Advisor
Co-chair of Committee

Philip J. Morris
Boeing / A.D. Welliver Professor of Aerospace Engineering
Co-chair of Committee

Cengiz Camci
Professor of Aerospace Engineering

Kenneth S. Brentner
Professor of Aerospace Engineering

Anthony A. Atchley
Professor of Acoustics

George A. Lesieutre
Professor of Aerospace Engineering
Head of the Department of Aerospace Engineering

*Signatures are on file in the Graduate School

ABSTRACT

Research on the noise produced by military aircraft has seen a renewed interest due to the increasing concerns of communities around airbases and airports. Radiated noise associated with high-speed military style engines is the main contributor of the overall noise produced by modern aircraft, especially in military applications where the jets typically are at very high velocity and temperature, and have low bypass ratios. The acoustic and aerodynamic properties of high-speed jets are investigated experimentally in this thesis. Measurements are conducted in the Penn State high speed jet noise facility, after the validation of the newly upgraded rig. Axisymmetric Nozzles are investigated as well as nozzles with a military style shape.

The database of flow measurements in supersonic shock containing jets is very scarce. This research focuses on performing flow measurements in shock containing jets in an effort to obtain valuable parameters for the modeling of the noise propagated by such flows. Mean flow measurements of the jets are performed with pitot probes traversing the flow. These measurements are used as a qualification tool for a CFD simulation of the flow field with good overall agreement. Measurements in supersonic rectangular jets also uncover the presence of axes switching in fully, over- and under-expanded cases, with the location of this axes switch being further downstream in the fully expanded case. Acoustic data are gathered in shock containing screeching jets. Different techniques are investigated in order to provide some reduction of the screech tones. Optical Deflectometry measurements are performed in shock containing jets and show that the screech tones have no effect on the properties of the convecting structures. On the other hand, the strength of the shock present in the flow seems to have an effect on the convection velocity. Finally, the simultaneous correlation between the flow field fluctuations and the acoustic far field is measured. This suggests that the OD sensors can be used for localizing the noise generation in the jet. Preliminary results of this kind show that the highest frequencies are generated close to the exit plane of the nozzle.

TABLE OF CONTENTS

LIST OF FIGURES

LIST OF TABLES

NOMENCLATURE

a_∞	ambient speed of sound
a_j	speed of sound at nozzle exit
D	diameter of nozzle exit
D_j	average diameter of the jet plume
D_p	diameter of static pressure probe
f	frequency
f_c	characteristic frequency
$\mathcal{F}$	Fourier transform
$G_{ii}(f)$	single sided power spectral density of signal i
$G_{ij}(f)$	single sided cross spectral density of signals i and j
h	height of the rectangular nozzle
h_j	average height of a rectangular jet plume
L_1	Shock cell length
L_{x1}	length scale of the convecting turbulent structures
L_τ	time scale of the convecting turbulent structures
M_1	local Mach number
M_a	acoustic Mach number
M_d	design Mach number of nozzle
M_j	jet Mach number
NPR	nozzle pressure ratio
$p(t)$	analogous time signal (in volts)
$p(t_k)$	sampled time signal (in volts)
P_∞	atmospheric pressure
P_1	local static pressure
P_p	local Pitot pressure
P_{to}	total pressure in the plenum
P_{t1}	local total pressure
P_{t2}	local total pressure behind a normal shock

$R_{ii}(\tau)$	autocorrelation function of signal i
$R_{ij}(\tau)$	cross-correlation function of signals i and j
$S_{ii}(f)$	double sided power spectral density of signal i
$S_{ij}(f)$	double sided cross spectral density of signals i and j
SPL	Sound Pressure Level
St	Strouhal number
sk_i	skewness of signal i
t	time
t_k	sampled time vector
T_∞	atmospheric temperature
T_0	jet stagnation temperature
T_j	jet static temperature
TTR	total temperature ratio T_0 / T_∞
U_c	convection velocity
U_j	mean exhaust velocity
U_{je}	centerline exit velocity
x_1	axial location
x_2	radial location
$x_{2(0.5)}$	half velocity point
x_h	location of static pressure ports
w	width of the rectangular nozzle

Greek:

β	nozzle off-design parameter
δ_ω	vorticity thickness
Δx_1	axial displacement
Δx_2	radial displacement
$\Phi_{Sij}(f)$	phase of the cross spectra
γ	ratio of specific heats

$\gamma_{ij}^2(f)$	coherence function between signals i and j
η	normalized radial distance
ρ	local density
$\rho_{ij}(\tau)$	cross correlation coefficient function
τ	retarded time
σ_i	variance of signal i
μ	Mach wave radiation angle
μ_i	mean of signal i

ACKNOWLEDGEMENTS

I would like to express my gratitude to my thesis advisor Prof. Dennis McLaughlin for offering me the opportunity to be his student and to learn from his experience. I am truly thankful for his patience and the fairness with which he always treated me.

I am also thankful to Prof. Philip Morris for the many valuable comments and discussions that undoubtedly benefitted my studies and my knowledge of jet noise. I would also like to thank the other members of my committee, Prof. Kenneth Brentner, Prof. Cengiz Camci and Prof Anthony Atchley for their insights on my work and their comments.

I am grateful to NASA for sponsorship of this work under the NASA Cooperative Agreement NNX07AC88A entitled, "A Comprehensive Model for the Prediction of Supersonic Jet Noise," monitored by Dr. Milo Dahl.

Acknowledgement also goes to my wife, Bilim Atli Veltin without whom I would never have begun the exhausting but rewarding experience of being a Ph. D. candidate.

Additional thanks go to Richard Auhl for his insights and technical help and to Mark Catalano and Kirk Heller for facility support. Dr. Benoit Petitjean and fellow graduate students Steve Miller, Ching-Wen Kuo, Benjamin Day, Jaehyung Lee and Ujas Patel are also acknowledged for the help they provided. Undergraduate students who contributed to the numerous facility upgrades are also thanked.

Finally, I would like to thank my family and my friends back home for their support and for cheering me up.

Chapter 1

Introduction

1.1 Motivation

Since the 1930's, the jet propulsion industry has seen a tremendous growth both in the civilian and military sectors. Prediction of air traffic for the coming decades is certainly difficult but most experts agree that a continuation of this growth is most likely, inducing an increased impact on the communities as well. Moreover, the development of military jets with enhanced capabilities (such as increased speed and maneuverability or vertical take-off) will also keep adding to the impact on the population.

The major annoyance of air traffic on communities is due to the noise exposure. Aircraft noise can be divided into three major components: turbomachinery noise, jet noise and airframe noise. In the case of civil aircraft with large bypass ratio engines, jet noise is not the dominant source of noise, because of the jet's lower velocity and due to the shielding effect of the bypassed air. In such aircraft, the turbomachinery noise (coming from the inlet fan and the aft fan) dominates, together with the airframe noise (due mainly to landing gears and flaps). On the other hand, military aircraft as well as some civil aircraft (predominantly business jets) with very low by-pass ratio have higher levels of jet noise, making it the predominant source of noise. Figure **1-1** taken from reference [**1**] illustrates these trends. This is especially true during take-off when the jet engines are used to the maximum of their capabilities.

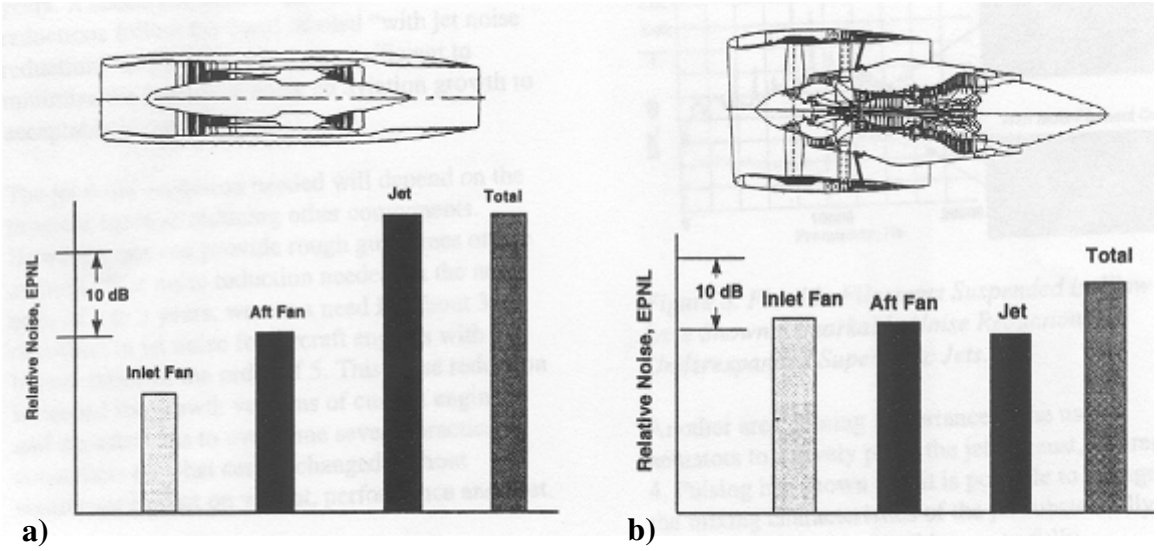

Figure **1-1**: Aircraft noise for a) low bypass ratio turbofan, b) high bypass ratio turbofan. From reference **[1]**.

As communities around military airbases get increasingly concerned by noise exposure caused by aircraft, empirical models for prediction of jet noise are being extensively used for surveys and noise reduction programs. However, these models, usually based on comprehensive experimental investigations, are still incomplete, do not account for a number of parameters, and often use many simplifying assumptions. Hence, there is an increasing need for more reliable prediction models and experimental data to help develop and validate them.

The prediction of jet noise is not a simple task and there are a number of parameters affecting the noise spectrum of a jet. Such parameters are for example the acoustic Mach number, the temperature of the jet and the polar and azimuthal angles and distance of the observer. In order to properly estimate the noise radiated, a solid understanding of the mechanisms behind the noise generation needs to be acquired.

This chapter will attempt to summarize the progress that has been made to date in understanding and reducing jet noise. A brief explanation of the physical phenomena responsible for the noise generation will be given, as well as the most recent theories. The objectives of the present work are then described in detail.

1.2 Theory of Aerodynamic noise

A brief summary of the current knowledge of jet noise is given in this section. While no attempt is made to provide a complete summary of the past works made by numerous researchers over the last 60 years, a number of references are provided that should point to the key developments in the field. A number of key parameters and definitions are introduced first, in order to familiarize the reader with the notation used thereafter.

1.2.1 Important parameters

Before going into more details on the nature of jet noise production, a number of quantities need to be defined. The jets considered are exhaust jets representative of military style engines, and exhaust from nozzles of diameter denoted by D. The nozzles are designed for a specific Mach number M_d, which corresponds to the exit Mach number of the nozzle, operating without the production of any shock waves. The flow is then called fully expanded. The Mach number of the jet itself is denoted as M_j and is calculated from the "fully expanded" jet velocity U_j and the jet acoustic velocity a_j as follows:

$$M_j = U_j / a_j \qquad \textbf{1.1}$$

When M_j is greater than M_d, the jet is called under-expanded, and when M_j is smaller than M_d, it is called over-expanded. A schlieren image for each type of running condition is presented in Figure **1-2.**

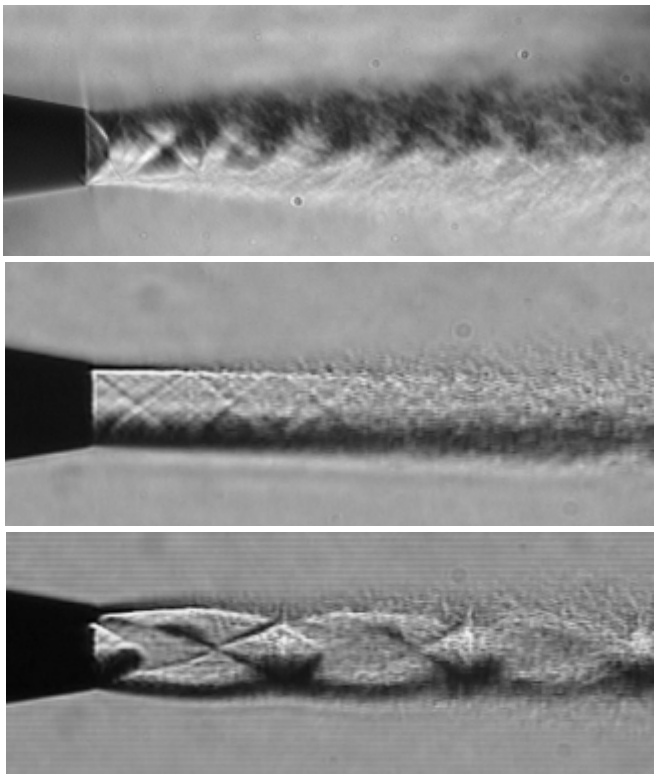

Figure **1-2**: Schlieren image of a $M_d = 1.5$ nozzle producing a jet a) over-expanded, b) fully expanded, c) under-expanded.

In under and over-expanded cases, shocks are present in the flow and the spatially averaged diameter of the plume D_j differs from the diameter of the nozzle exit. It can be calculated from the following formula, derived from isentropic relations:

$$\frac{D_j}{D} = \left[\frac{1+\frac{\gamma-1}{2}M_j^{\,2}}{1+\frac{\gamma-1}{2}M_d^{\,2}}\right]^{\frac{\gamma+1}{4(\gamma-1)}} \left(\frac{M_d}{M_j}\right)^{1/2} \qquad \textbf{1.2}$$

This average diameter D_j is estimated for the first several diameters of the jet plume, not further downstream where there is a strong divergent growth of the jet. In this formula, γ represents the ratio of specific heats of the gas considered ($\gamma = 1.4$ for air).

The parameter that controls the exit condition of the jet is the pressure ratio (*NPR*) between the air upstream and downstream of the nozzle and the temperature of the air in the upstream plenum. Since cross scale comparisons of the noise measurements are of

the utmost importance, non-dimensionalization of the frequencies is usually made. For this purpose, the Strouhal Number is used. It consists of a frequency non-dimensionalized by the flow's characteristic frequency computed from the jet velocity (U_j) and jet plume diameter (D_j) as follows:

$$St = \frac{f}{f_c} \text{ , with } f_c = U_j / D_j \qquad \textbf{1.3}$$

Noise production in high speed jets is also strongly dependent on the temperature of the flow considered. Rather than using the static jet temperature T_j when trying to match the temperature, usage is made of the total temperature ratio (*TTR*), which is the ratio of the total jet temperature T_0 with the ambient temperature T_∞ as shown in Eq. **1.4**

$$TTR = T_0 / T_\infty = T_j / T_\infty \left(1 + \frac{\gamma - 1}{2} M_j^2\right) \qquad \textbf{1.4}$$

Similarly, rather than matching the exit Mach number, for example when examining aeroacoustic properties, the acoustic Mach number M_a is most relevant. M_a is defined as the ratio of the jet velocity to the atmospheric speed of sound a_∞:

$$M_a = U_j \ / \ a_\infty \qquad \textbf{1.5}$$

Some other parameters are used throughout this work and will be introduced when first used. A brief summary of the current understanding of jet noise production is given in the following section, and the chapter concludes with a statement of the scope and goals of the research.

1.2.2 Jet noise components

It is widely accepted that sound production in a high speed jet can be divided into two main generating processes, mixing noise and shock associated noise. Mixing noise is an ever-present component of the noise generated by jets, while shock associated noise is restricted to shock containing supersonic jets.

1.2.2.1 Turbulent mixing noise

Turbulent mixing noise is a component of the noise, with a very broad frequency content, whose peak frequency varies with polar angle θ. It is the dominant noise component in the rear arc of the jet ($\theta < 90°$, where the jet downstream axis is the origin for θ), where other components have a diminished impact. It is also the only noise source for subsonic jets or fully expanded jets, where there is no shock associated noise. Since Lighthill's theory of aerodynamic noise [**2**], turbulent mixing noise has been argued to be produced by a distribution of equivalent quadrupoles. However, implementations of Lighthill's theory have repeatedly been unable [**3**], [**4**] to accurately predict the noise spectra, and it was shown [**3**] that turbulent mixing noise should rather be broken down into two components, one generated by the large scale structures, and another generated by the fine scale structures.

When large scale turbulent structures propagate supersonically, they radiate Mach waves. This Mach wave radiation has a very well defined propagation angle μ defined in Equation **1.6** and results in a strong directivity of the radiated noise.

$$\mu = \sin^{-1}(1 / M_a) \qquad \textbf{1.6}$$

This phenomenon is described by a wavy wall analogy and very well understood. However, this process also occurs in flows for which the convection speed is subsonic. This is due to the fact that turbulence is made up of different frequency components, each with different phase velocities. Thus, even though the whole turbulent structure is moving at subsonic velocity, some wavenumbers do travel supersonically, and this results in Mach wave radiation. A very good review of Mach wave radiation can be found in Krothapalli *et al.* **[5]**.

While large scale turbulence noise generation is a physical process well understood for supersonic flows, the details of fine scale turbulence noise generation remains unknown. There is not much doubt that small scale turbulence produces unsteadiness which then generates sound, but the details of the mechanism have not yet been observed and understood. However, experiments [**3**], [**6**] have shown that sound

refraction inside the jet creates the so-called cone of silence, where the intensity of the sound generated by fine turbulent structures is greatly decreased.

To illustrate turbulent mixing noise, Figure **1-3** , taken from Tam *et al.* [**3**], shows measurements made of both large and fine scale turbulence noise for different jet conditions. They are compared with the so-called similarity spectra, which are defined in [**3**] as a numerical representation of those two components of the noise, based on extensive experimental data.

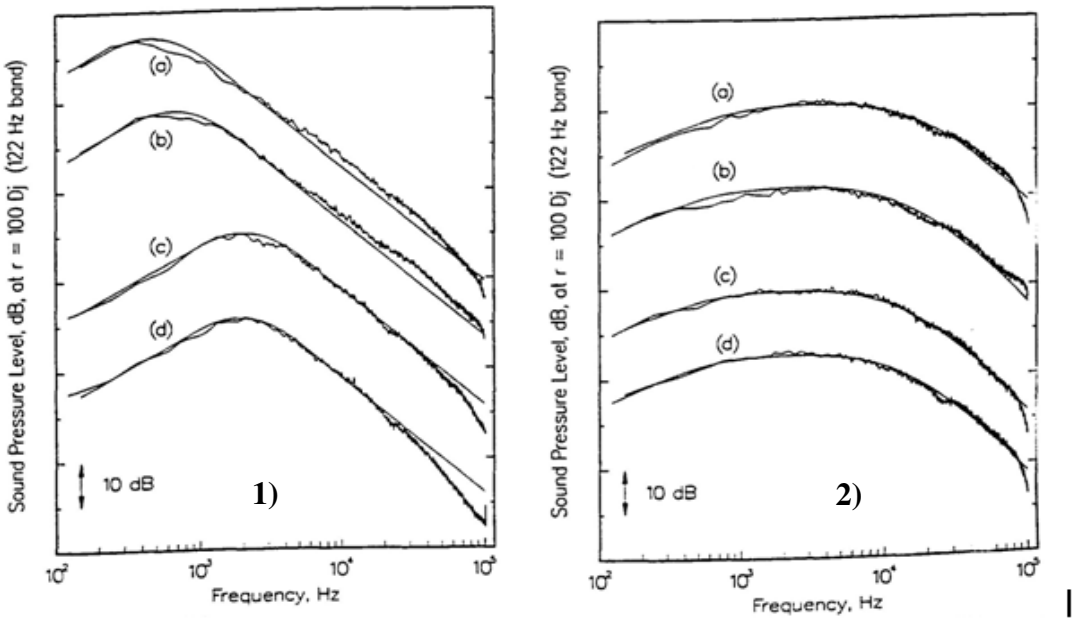

1) (a): M_j = 2.0, *TTR* = 8.8, θ = 19.9°, SPL_{max}=124.7 dB
1) (b): M_j = 2.0, *TTR* = 2.0, θ = 19.9°, SPL_{max}=121.6 dB
1) (c): M_j = 1.96, *TTR* = 3.1, θ = 41.4°, SPL_{max}=121.0 dB
1) (d): M_j = 1.49, *TTR* = 1.6, θ = 41.4°, SPL_{max}=106.5 dB
2) (a): M_j = 1.49, *TTR* = 3.4, θ = 87.1°, SPL_{max}=96 dB
2) (b): M_j = 2.0, *TTR* = 8.8, θ = 96.2°, SPL_{max}=107 dB
2) (c): M_j = 1.96, *TTR* = 1.75, θ = 96.7°, SPL_{max}=95 dB
2) (d): M_j = 1.96, *TTR* = 1.7, θ = 59.8°, SPL_{max}=100 dB

Figure **1-3**: Comparison of 1) large scale 2) fine scale turbulence mixing noise with similarity spectra for different polar angle and jet conditions. From Reference **[3]**.

The measurements for the noise from large scale turbulence have been made at small polar angle θ, in order to be in the cone of silence and hence reduce the influence of fine scale noise on the sound pressure level. Fine scale measurements were made at high polar angles where the strongly directional Mach wave radiation doesn't have a significant effect. Figure **1-4** , taken from [**3**], shows a superposition of both of those noise components in order to better visualize the differences in the spectra of noise generated by both large and fine scale turbulences.

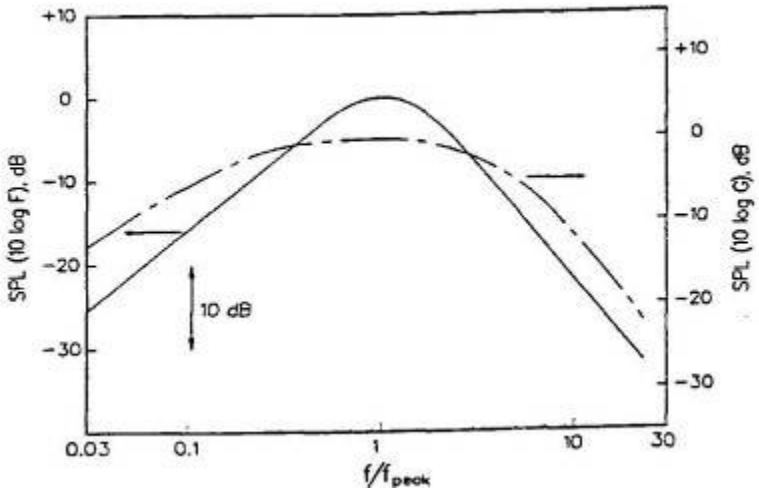

Figure **1-4**: Similarity spectra for large scale turbulence mixing noise (solid line) and fine scale turbulent mixing noise (dashed line). From Reference **[3]**.

1.2.2.2 Shock associated noise

When a jet becomes supersonic while the nozzle is designed for sonic condition (converging nozzle, M_d = 1), or when a supersonic converging-diverging jet nozzle is running at an off-design condition, whether it is under-expanded or over-expanded, shock waves appear in the flow, as can be seen in Figure **1-2**.

The interaction of these shock structures with the flow produces noise, and it was observed [**7**] that it can be divided into two components: broadband shock associated noise (BBSAN) and screech. The effect of those two components on the noise spectra is illustrated in Figure **1-5**, taken from Tanna [**7**], where the arrows show the frequency at which screech appears, and the main bump in the spectrum around 4 kHz is due to broadband shock associated noise.

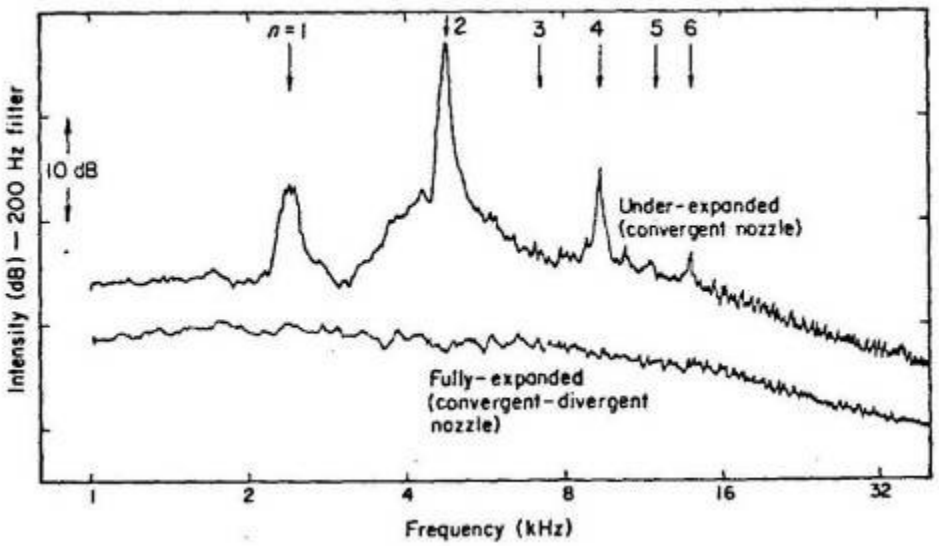

Figure **1-5**: Comparison of noise spectra from fully expanded and under-expanded jets with $M_j = 1.37$.

When shocks are present in the flow, interaction between the broadband turbulent structures and the shocks produces noise over a large frequency range, commonly known as broadband shock associated noise. The peak of this sound depends on the pressure ratio of the jet, since this is the parameter which determines the geometry of the shock cells. The intensity of noise generated was also shown by Tanna [**7**] to increase with both the pressure and temperature ratios of the jet. It was also shown by Harper-Bourne and Fisher [**8**] that the shock associated noise intensity is directly proportional to the pressure ratio through the shock waves, which is a function of the jet pressure ratio.

When a periodic shock cell structure is present in the flow, there is also the appearance of a discrete frequency phenomenon known as “screech”, as previously

shown in figure **1-5**. It is well known that this process occurs whenever a phase locked loop is initiated between the shock noise and the exit plane of the nozzle. Its frequency f_s can be predicted from the following formula:

$$f_S = \frac{U_C}{2.L_1} \cdot \frac{1}{1+M_C} \qquad \textbf{1.7}$$

L_1 is the length of the shock cell, M_c the convective Mach number and U_c the convective velocity of the turbulence passing through the shocks. The presence of screech can be visually observed when taking a schlieren photograph of a screeching jet, as shown in Figure **1-6**.

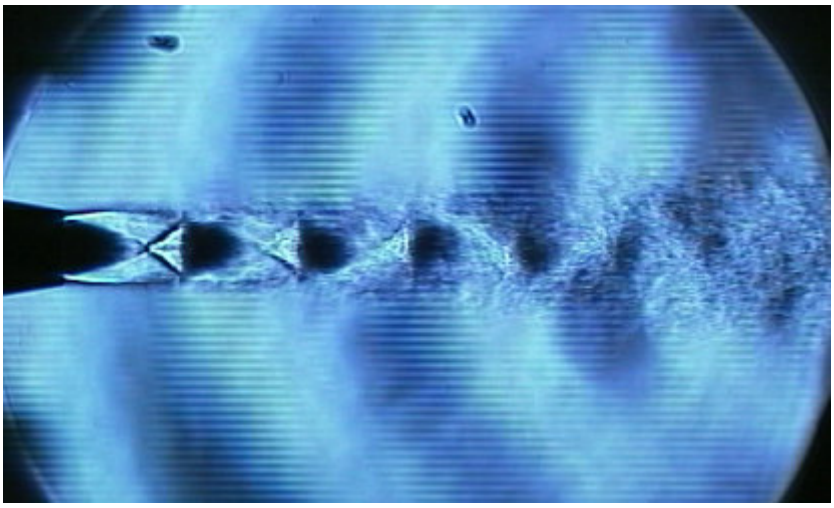

Figure **1-6**: Schlieren image of a screeching M_d = 1.0, M_j = 1.5 jet (taken at The Pennsylvania State University).

Similar visualizations taken with a spark schlieren setup can be found in Seiner [**9**]. Whereas the frequency prediction matches very well with the experimental data, there is currently no way to accurately predict the screech amplitude. Some work was carried on by Shen and Tam [**10**] and Panda [**11**] in order to predict the amplitude of the first screech tone, but the high number of parameters to consider makes it difficult to predict and only the amplitude of the first screech tone has been successfully predicted so far. More discussions on screech can be found in Seiner [**9**]. Screech suppression techniques are also discussed by Norum [**12**] and by Raman [**13**].

1.2.3 Progresses in modeling of the BBSAN

Early work on modeling the BBSAN was conducted by Harper-Bourne and Fisher [**8**] with a proposed model for prediction of the frequency of the noise as a function of a measure of the pressure imbalance, β and the polar angle θ. They made the assumption that each interaction between a shock and the mixing layer could be regarded as a separate source and managed to predict the frequency peak of the BBSAN. Correlations of the shear layer turbulence between shocks provided the data on which to base their prediction scheme. The shock noise intensity, given by Harper-Bourne and Fisher, scales with β^4 where β is the off-design parameter defined for a converging nozzle operating fully or under-expanded by the equation below:

$$\beta = \sqrt{M_j^{\,2} - 1} \qquad \textbf{1.8}$$

Advances were later made by Tam [**14**] who developed a stochastic model for BBSAN based on the interaction between the large scale structures in the jet shear layer and the jet's shock cell structure. The model of the turbulence in the jet is a random superposition of instability waves. The noise is calculated by a sum of contributions from modes generated by the interaction of the large scale turbulent structures, modeled as traveling waves, with the quasi-periodic shock cell structure, modeled using a Fourier series expansion. The turbulence model produces a prediction for the turbulent Reynolds stresses and the turbulent velocity components. Summation of these modes was proposed to produce a prediction of the BBSAN generated. However, the prediction scheme itself is based on an empirical correlation for the spectral shapes rather than first-principle predictions. So in order to improve the accuracy of the model, the database of measurements should be extended to different geometries and conditions.

More recently, Morris *et al.* [**15**] described the importance of the cross-correlations of turbulent fluctuations in producing an accurate model for prediction of jet noise. A simulation generated turbulence database was produced in order to predict the far field noise that produced relatively good agreement with experiment, but could not achieve the same resolution for high speed flows. The mean flow in noise generating jets

has also been investigated by many researchers. Work from Troutt and McLaughlin [**16**] provided some mean flow velocity and pressure measurements in jets of different conditions, and predictions were produced by Morris and Bhat [**17**]. Additionally, some mean flow pressure measurements were also made by Kinzie and McLaughlin [**18**] and by Doty and McLaughlin [**19**] with reasonable success in both cold and heat simulated cases. The present work is building on these developments at The Pennsylvania State University in order to bring some contribution to the BBSAN modeling process. However, measurements in shock containing jets have been limited and therefore the database needs to be extended.

In order to further contribute to the research in this area, a variety of experimental techniques has been used in order to produce correlations within the jet. Laser Velocimetry correlation measurements have been used by Lau [**20**] and showed very good results across a range of Mach numbers and temperature ratios. The convection velocity and decay rates were observed to depend on the jet conditions. PIV systems are also being extensively used by Bridges [**21**], and are able to provide spatial correlations of jets of different temperatures and velocities. These techniques require seeding of the flow, and a significant development to produce the high quality results that NASA has achieved. Two point correlation measurements in the shear layer of a jet were first conducted at The Pennsylvania State University using optical deflectometry by Doty and McLaughlin [**22**]. The focus was primarily on fully expanded cold jets and showed good correlations with hot-wire measurements made at lower speeds by Davies *et al.* [**23**].

1.2.4 Scaled measurements

While some of the tools were introduced in section **1.2.1** in order to allow for comparison of sound spectra across scales, the relevance of such comparison has not yet been discussed. Jet noise studies such as the one from Norum *et al.* [**24**] have been made where fly-over aircraft are used. However, this is generally impractical and costly and thus inexpensive smaller scale measurements are sought. Many researchers have therefore conducted measurements of the noise radiated from jets of smaller scales and a

good review of these findings can be found in Viswanathan [**25**]. In this review, the effect of Reynolds numbers on the measured acoustic spectra is assessed and leads to the conclusion that accurate prediction of the noise produced by a full size jet engine can be achieved with a small scale jet of Reynolds number around 500,000. This number is of the same order as the ones obtain in the measurements produced at The Pennsylvania State University small scale jet noise facility. As discussed further in section **2.1.2**, helium-air mixtures are used to simulate hot air. Details of the method for calculation of the Reynolds number in helium-air mixtures can be found in Doty [**26**].

1.3 Scope of thesis

1.3.1 Research objectives

The main goal of this study was to obtain an increased understanding of the mechanisms responsible for the noise generation process in supersonic and shock containing jets. The experiments were designed to explore three major aspects of these jets that can be used in a complementary analytical and computational modeling effort being conducted by Prof. P.J. Morris and his research assistants. These are: 1) The turbulence quantities in the jets that can be relatively easily measured and quantified. Attention is also focused on how these properties are affected by the mean flow shock cells in the case of imperfectly expanded supersonic jets; 2) The time mean flow properties, including the shock-expansion wave patterns and how well they can be predicted in the modeling effort; 3) The major features of the acoustic fields that are produced by the jet flows being studied in parts 1) and 2).

The experiments were conducted in jet flows and acoustic fields produced by both purely converging and converging-diverging (CD) nozzles with both round and rectangular cross-sections. The jets were both unheated and simulated hot using mixtures of helium and air.

The specific experiments included:

- An extensive database of schlieren flow visualization, with various operating conditions. It established independent information on the shock-expansion wave geometry in the jets as well as the spreading of the shear layers (or annulus).
- Pitot probe measurements in both under- and over-expanded jets, leading to mean flow properties of pressure, velocity, Mach number, etc. Comparisons with Computational Fluid Dynamic (CFD) simulations were made for evaluation purpose.
- Flow field turbulence measurements with the Penn State optical deflectometer system, which is directly sensitive to vertical density gradient fluctuations (these, in turn, are strongly related to vertical velocity fluctuations). Using this instrument, two point correlation measurements were made in the shock containing jets. Such correlations are used to determine the convection velocity of the turbulent structures in the mixing layer of the jets as well as their correlation length and time scales. In the acquisition of these data, screech tones appeared both in the acoustic spectra and the optical signals, introducing a significant complication in the data assembly process.
- Additional assessment of the physical properties of the turbulence in the mixing layer was made by performing different radial correlations measurements across the mixing layer. Information relative to the speed and shape of the turbulent structures was gathered.
- Correlations of the optical signals inside and just outside of the jets were also made with far field microphone signals in an attempt to relate the turbulent fluctuations to the different components of the radiated noise.
- An investigation of the reduction of the shock screech was carried out. A reduction of its influence on the correlation data was sought. This can be obtained by physically suppressing the screech with small disturbances in the nozzle or by suppressing it electronically (or computationally) with an appropriate processing method. The purpose was to produce a flow, and experimental data, that was more representative of full scale military style engine exhaust jets, which do not typically screech.

1.3.2 Thesis synopsis

The remainder of this work presents the experiments conducted in order to investigate the noise production mechanisms of different shock containing jets. Chapter 2 provides a description of the Penn State jet noise facility primarily used for the experiments. Special attention is paid to describing the modifications that were made to the laboratory in order to increase its capabilities and the quality of the measurements made. Chapter 3 offers detailed descriptions of the set-ups used for the measurements, including the acoustic set-up, the flow visualization technique used (schlieren photograph and optical deflectometry) and the pitot probe set-up for flow measurements.

The results are presented in the remaining chapters, starting with Chapter 4 that presents preliminary measurements, including acoustic validation of the newly redesigned jet noise rig, an investigation of the effectiveness of different screech suppression techniques on a supersonic under-expanded jet, and qualification measurements of the optical deflectometer. The flow field measurements obtained via the pitot probes are then summarized in Chapter 5, with qualification comparison with computational results and schlieren images. Chapter 6 presents some of the results obtained with the use of the optical deflectometer. Convection speed measurements are primarily presented, as well as radial and axial correlations in the jet shear layer and correlation with far field microphones. Some measurements made at the University of California Irvine are also shown and prove the repeatability of the measurements made. Discussions of all these results are made in Chapter 7 in an attempt to extract from these many measurements the physical mechanisms that generate the noise. Conclusions are then drawn in Chapter 8, together with recommendations for future work.

Additional information is given in the Appendices, including pictures and drawings of the facility and its components, and copies of the main codes used for the data processing.

Chapter 2

Experimental facility

2.1 Facility description

The experiments presented in this thesis were conducted in the High-Speed Jet Noise Facility at the Penn State University. Figure **2-1** below shows a schematic of the facility as of 2006. Continuous evolutions throughout the current study were made in order to increase the capabilities of the facility as well as the quality of the measurements.

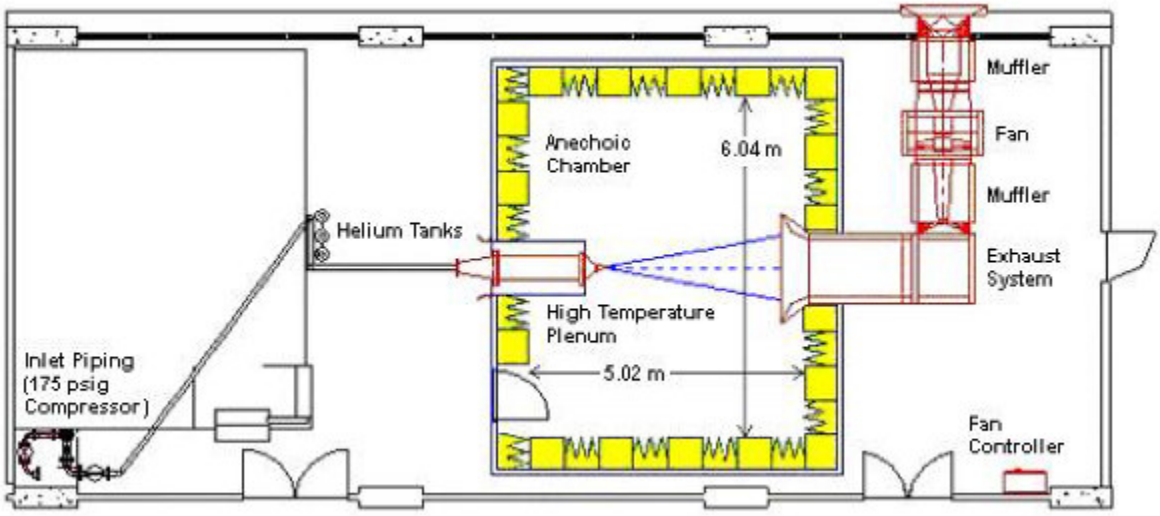

Figure **2-1**: Schematic of the Jet Noise Facility as of 2006.

2.1.1 Overview

This facility uses a *Kaeser* air compressor to pressurize two 18.9 m^3 tanks to a pressure of 1.34 MPa (195 psig). This compressed air passes through a dryer and is then piped to a plenum before exhausting through a model nozzle in the facility's anechoic chamber, as shown on the above schematic. Nozzle diameters up to 25.4 mm are typically used. Inside the anechoic chamber, fiberglass wedges are attached to each wall, resulting in chamber wedge-to-wedge dimensions of 5.02 x 6.04 x 2.79 m (16.5 x 19.82 x 9.15 ft) and a cutoff frequency of 250 Hz. An exhaust system, beginning on the wall opposing the plenum, ingests the flow in order to maintain approximately constant ambient conditions inside the chamber. The overall installation was made starting in 1999 in different stages. More details on the origin and specifications of each components of the facility can be found in Doty [**26**]. The facility was originally assembled with the intention of making heated jet measurements. Helium-air mixture is used instead.

2.1.2 Heated jet simulation

In order to make acoustic measurements that can be directly compared to aircraft engine measurements, the temperature of the jet is an important parameter that needs to be replicated. A hotter jet results in different acoustical characteristics, due to the increase in jet exit velocity and decrease in jet density. Actually heating the air that exhausts through the nozzles is done in facilities such as the one used at the NASA Glenn Research Center [**27**]. However, it requires an excessive amount of power and infrastructure, raising the overall operating costs of the facility.

The quantities that need to be matched when doing acoustic measurements in hot jets are the acoustic velocity a_j and the jet density ρ_j. A mixture of air with a different gas can be used as a mean to reach the desired values of density and Mach number. Helium was chosen for its low density and high acoustic velocity. However, it is not possible to match both a_j and ρ_j to the hot jet values, as is shown in details in Doty [**26**]. This prior experimental work, conducted in the same facility, investigated the different methods to

successfully simulate hot jet with the addition of helium. Only very small variations in the acoustic spectra were observed when comparing a_j and ρ_j matching, and it was concluded that these were smaller than the experimental uncertainties in the measurements. Therefore, matching of the acoustic velocity is made in order to simulate the heated jet with the addition of helium. A similar methodology is being used by Papamoschou [**28**] at the University of California Irvine. More details on the effectiveness of helium in simulating hot jets, as well as the implications associated with this methodology are discussed in Doty and McLaughlin [**19**] and Papamoschou [**28**]. These references also underline the safety and economic benefits of helium-air mixture over actually heated air for the experiments conducted in this facility.

Canisters pressurized at 15.9 MPa (2300 psig) are used for helium injection at a sufficient distance upstream of the plenum in order to allow for thorough mixing with the air. The partial pressure of air is measured using a pitot probe located in the settling chamber section upstream of the nozzle. When doing helium-air mixture runs, the total pressure of the mixture is measured the same way. A pressure transducer interfaces the measured pressures to the data acquisition system. Any target Mach number and simulated temperature ratio at the exit plane of the nozzle can thus easily be achieved. Details of the procedure followed for ensuring the correct composition of the mixture are discussed in section **2.4.2**.

2.1.3 Facility limitations

The facility, and more specifically its plenum, was initially dimensioned to make heated jet acoustic measurements. However, due to the very good success of the heat simulation with helium addition, the actual heating of the air was never made operational. Further explanations on the simulation of heat via helium-air mixtures are given in section **2.4.2**.

It was also previously envisioned to use co-flows in order to simulate dual stream jets. The plenum used had the ability to accommodate tri-axial flows that could achieve that purpose. However, in order to implement a forward flight capability, the outer

diameter of the plenum needed to be reduced. Therefore, the large diameter, high temperature plenum constituted a limitation and the decision was made to replace it.

Previous measurements made in the current facility were predominantly conducted with 12.7 mm (0.5") diameter jets, with a limited number of experiments made with 25.4 mm diameter jets. In order to make comparisons across different scales and to fulfill requirements for a number of contracted experiments, high speed flow needs to be attainable with such high diameter jets. Since the maximum reachable Mach number for that kind of nozzle could never exceed 1.3, a complete re-examination of the upstream piping needs to be made. This will allow an increase in the Reynolds number of the jets examined to numbers around 10^6 and therefore increase the quality of the comparisons with full scale measurements, as shown by Viswanathan [**25**].

Finally, the mixture of helium and air being done so far relied heavily on the skills of the operator, and typically consumed a considerable amount of helium. Since the accuracy of the heat simulation via helium-air mixture is now well established and will be more intensively used in the future, an upgrade of the whole mixing process needed to be undertaken. Computer interaction as well as easy-to-use control valves were implemented to improve the stability and repeatability of the jet conditions during the measurements.

2.2 Upgrades to the jet noise rig

Following specific needs of the jet noise industry and in order to remain competitive and improve the quality and relevance of the experiments made, there was a strong need for providing upgrades to the current facility. In order to extend the range of velocity that can be produced through the nozzles and to reduce the operating cost, improvements have been made to the control of the helium-air mixing. For the same purposes, the plenum was redesigned and replaced by a newly built one. The overall quality of the data obtained has also been enhanced by introducing improved control and more rigorous processing methods. Qualification experiments of the newly redesigned facility were conducted and are presented in section **4.1**.

2.2.1 Plenum

The plenum used until now in the facility was installed in 2000 and was a large diameter, stainless steel high temperature plenum with Kaowool insulation, capable of withstanding temperatures as high as 1370 K. However, since the simulation of heat was successfully demonstrated by adding helium to the air, the heated jet capability remained unused. Moreover, the large contraction ratio of 50:1 of this plenum implied that an excessively large volume needed to be filled when doing helium-air experiments before reaching stable outflow conditions. In an effort to reduce the amount of helium used, plans were made to switch to a slimmer plenum, made out of a 11.4 cm (4.5") inner diameter aluminum pipe, 1.83 m (6') long. When running 2.5 cm (1") diameter jets, this new dimensioning still gives an area ratio over 16:1. Drawings of the new plenum, together with the manifolds that were designed to be able to accommodate the old nozzles can be found in Appendix **A.1**.

A pitot probe is mounted 61 cm (2 feet) from the end of the plenum for total pressure measurement, and a temperature probe 30.5 (1 foot) upstream of it. In order to decrease the turbulence level of the flow and enhance the mixing of the helium-air mixture, a turbulence management system was designed. It consists of a conical perforated plate followed by 7.5 cm (3") of honeycomb. Both were built and attached to a sleeve that fits tightly inside the plenum and can slide in and out from the rear end. The supports for the new plenum were also completely redesigned and made much slimmer. The reduced diameter of the plenum, allows the addition of a large surrounding duct to provide a surrounding flow in order to simulate the forward flight speed of a flying aircraft. Detail drawings of most components as well as pictures can be found in Appendix **A.1**.

2.2.2 Helium-air mixture piping arrangement

In an effort to reduce the operating cost and increase the capability of the facility, a complete re-design of the whole air and helium delivery piping was undertaken.

The main flow control is achieved through a pneumatic valve located by the entrance to the control room and showed in the picture of Figure 2.2. Regulation of the flow through that valve is achieved through the use of shop air supply and air control valves. Detail on the operation of this pneumatic valve can be found in Petitjean [**29**]. A pressure relief valve was located downstream of the pneumatic valve, relieving pressures exceeding 120 psig in order to protect the downstream pipes that were not designed for higher pressure. In order to increase the maximum velocity that could be reached through a given nozzle and fully use the highest pressure available from the reservoirs, this safety valve was removed and the downstream piping changed to withstand pressures as high as 300 psi. The pneumatic valve, having a diameter of 2.54 cm (1"), still represents a choke point in the overall piping arrangement, and if higher flow rates are required in the future, it can be exchanged with the unused larger pneumatic valve (PV2, 6.35 cm diameter) with a limited amount of effort.

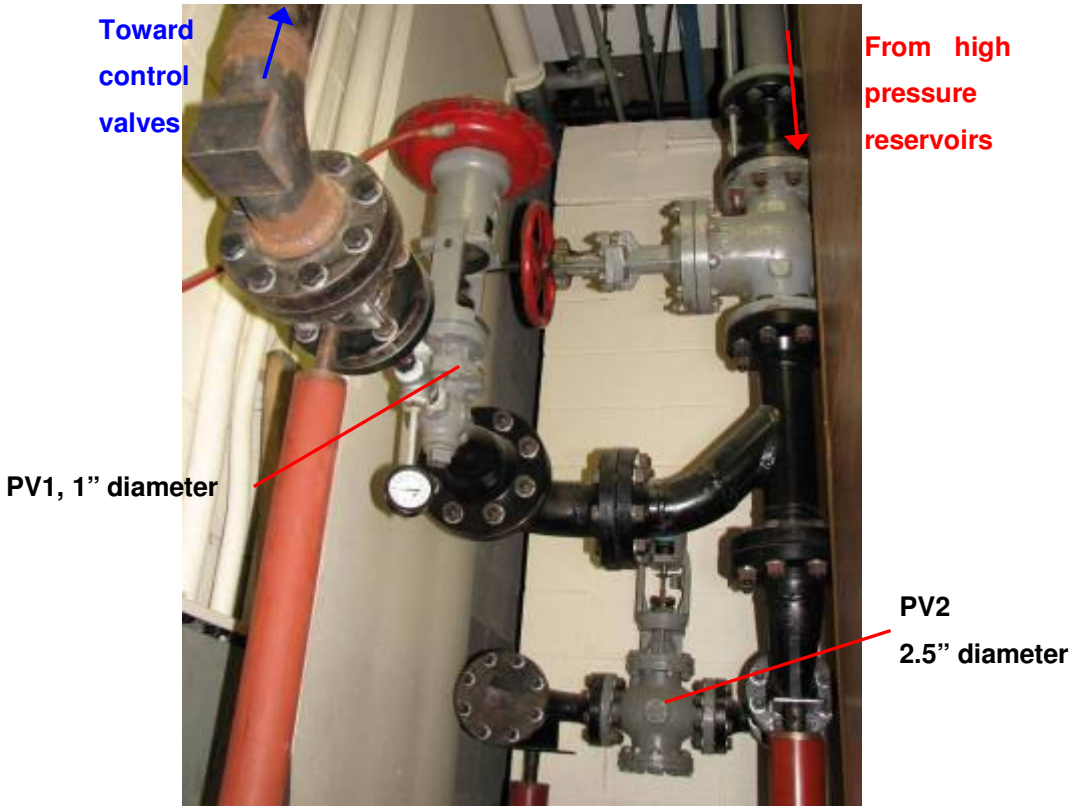

Figure **2-2:** Pneumatic valves.

Downstream of this pneumatic valve is the helium-air mixing arrangement. It was investigated in detail, with attention paid to the pressure lost in each portion of the piping. Figure 2.3 shows a picture of the piping as it was prior to any modification.

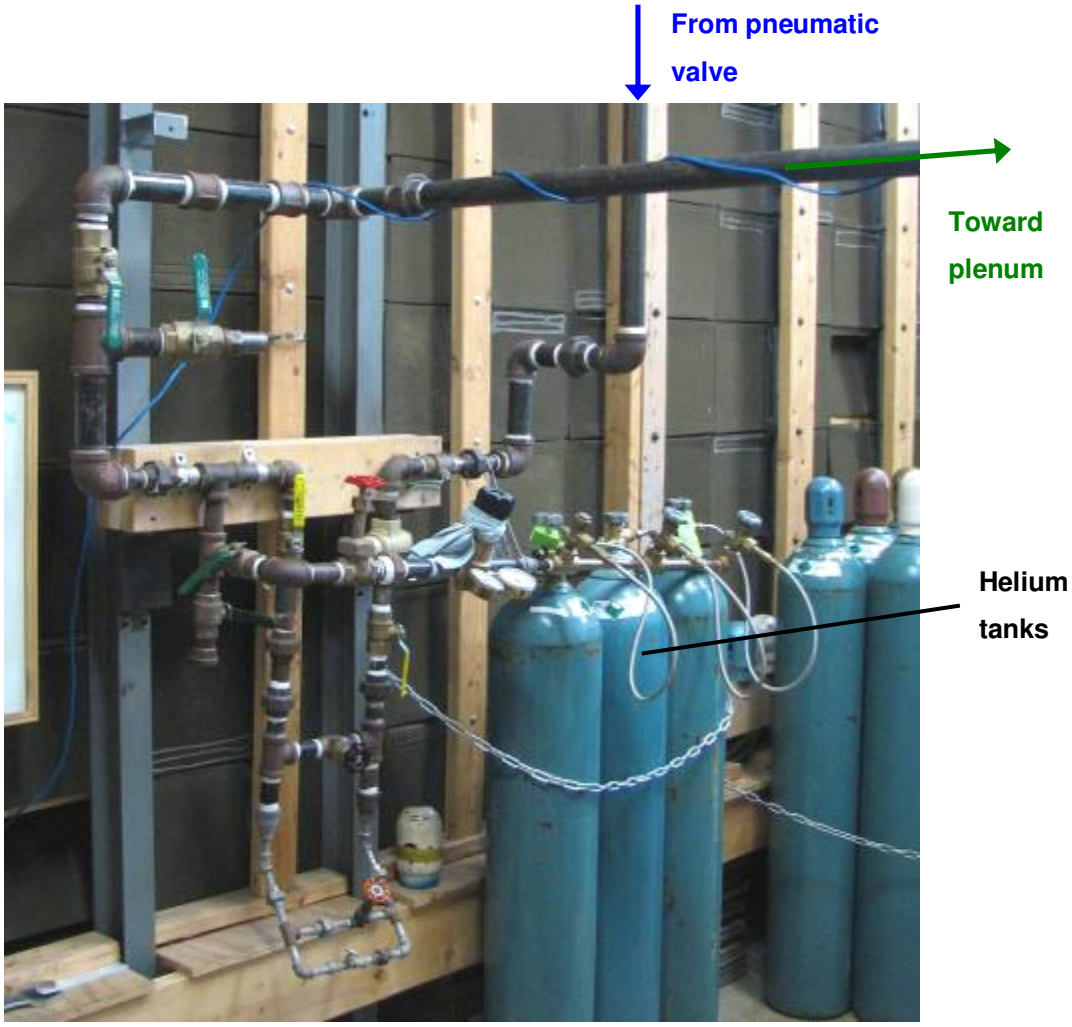

Figure **2-3**: Former helium-air mixing pipes arrangement.

Calculations and measurements showed the main regions where the head losses could be avoided and a new design was hence produced. From basic hydraulic equations in pipes, the pressure losses through elbows being non negligible, their number was reduced to a minimum, and the valves were kept a sufficient distance away from the plenum to avoid noise contamination. Effort was also made to keep large diameter pipes

wherever possible, in order to maintain a low flow speed, and hence reduce the pressure losses.

For easy regulation of the air and helium flows, a control panel was designed, and a set of gate valves, ball valves and pressure regulators was integrated for easy control of the flow. Used in conjunction with the pressure measurement in the plenum, it allows for precise control of the flow conditions. In addition, solenoid valves were introduced in the piping design in order to allow for quick computerized shut-off of the flow, hence reducing the amount of helium used as well as allowing for emergency shut-down if ever the outflow reaches unexpected values. The diagram in Figure 2.4 shows the piping arrangement. More drawings and some pictures can be found in Appendix **A.1**.

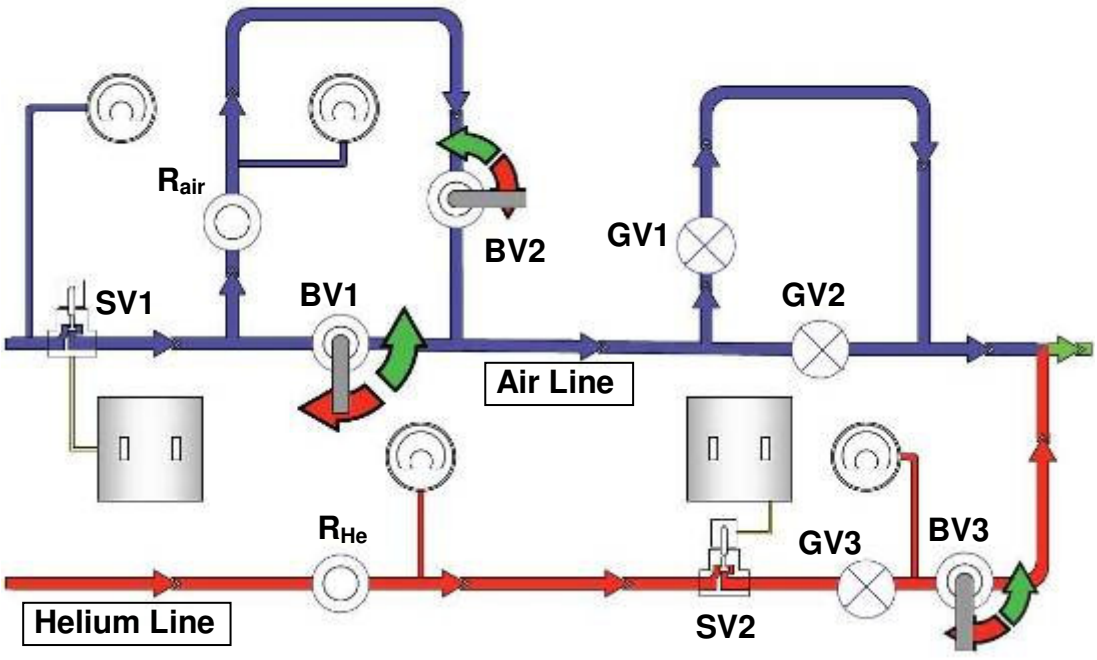

Nomenclature:

SV: Solenoid valves BV: Ball valves GV: Gate valves

R_{air} and R_{He}: Pressure regulators

Figure **2-4**: Diagram of the redesigned helium-air mixture piping.

Special attention was paid to the procedure that needs to be followed when making helium-air measurements. As described by Kinzie and McLaughlin [**30**], a choked point is required in both the helium and the air piping in order for the mass flow rates not to vary when both streams are flowing. These choked flows are obtained by making sure that the individual pressure of each gas of the mixture is sufficiently higher than the expected mixture pressure. The choke points are typically obtained at gate valves GV1 and GV2 in the air line, and at SV2 or GV3 in the helium line, as shown in the diagram of Figure 2.4.

The partial pressures are first computed from simple thermodynamic equations that can be found in textbooks such as Reynolds and Perkins [**31**]. These calculations are described in detail in Doty [**26**], as well as a Fortran code *Helium.f90* that was developed to compute the results. The air flow is then directed through pressure regulator R_{air} by closing ball valve BV1 and opening BV2. The air partial pressure is then set to the required partial pressure using gate valves GV1 and GV2, while making sure that the pressure downstream of R_{air} is above the mixture choking pressure. Then, pressure regulator R_{He} can be adjusted to the position that will produce the required helium partial pressure, with GV3 and SV2 opened and BV3 closed. BV3 is then opened, allowing for the mixture of both gases. The plenum pressure measurement triggers the acquisition of the data, and when complete, solenoid valve SV2 is automatically shut down. Extensive calibration is required in order to be able to obtain accurate positioning for R_{He}. In order to be able to run jet conditions with a large percentage of helium (simulation of a very hot jet) with large diameter nozzles, the number of helium tanks that can be used at once was also increased from 3 to 6. The whole piping arrangement was designed to fit in a wheeled cart that can me moved around the laboratory, providing the inlet and outlet quick release pipe fixtures are disconnected.

2.3 Future evolutions

In order to better measure and predict the noise created by aircraft engine exhaust jets, it becomes important to simulate the forward flight of the aircraft and measure the

way it affects the sound generation and propagation. Therefore, it was envisioned to bring a major upgrade to the facility in order to gain that capability and hence to make Penn State one of the few universities with the ability to produce that kind of experimental data. A forward flight capability is thus being developed with the target of producing a Mach 0.2 uniform flow in a 38 x 38 cm square section surrounding the high speed jet.

Most of the additional ductwork has been completed and installed. Pictures of some of the components are shown in Appendix **A.2**, as well as some more details of the design. A general diagram of the facility after completion of the forward flight installation is shown in Figure **2-5**.

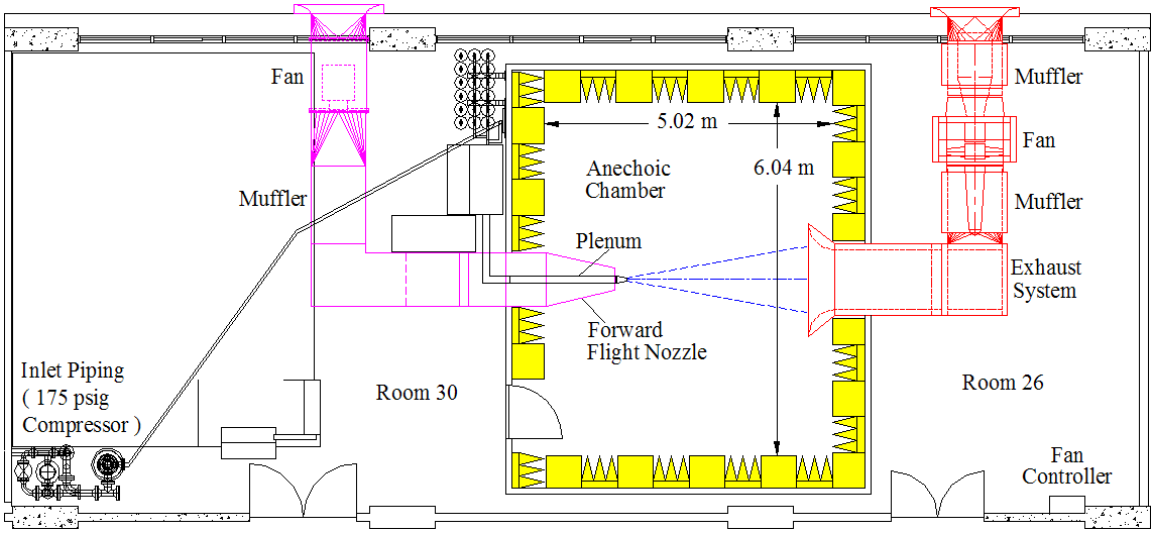

Figure **2-5**: Schematic of the Jet Noise Facility after upgrades.

As can be seen, the general layout of the facility has been changed in order to accommodate this major modification. The control cart where the helium-air mixture is made was moved across the room close to the plenum location and next to the desk where the acquisition computer is located.

Testing of the whole upgraded facility will take place during the spring semester 2009 and lead to some qualification experiments.

Chapter 3

Experimental Procedures

3.1 Data acquisition system

Once the facility is running, data acquisition is obtained via an analog to digital converter connected to a computer. In order to have sufficient acquisition rate, resolution and an increased number of channels, a new acquisition card was acquired. The board used is a 16 bit PCI-6123 *National Instrument* multiple channel DAQ. The maximum sampling rate of this A/D card is 500 kHz/second/channel and simultaneous sampling can be obtain on up to 8 channels. This allows for an increase of the number of microphones used, as well as the possibility of performing simultaneously optical deflectometry and acoustic measurements. Figure **3-1** represents a flowchart of the data acquisition process.

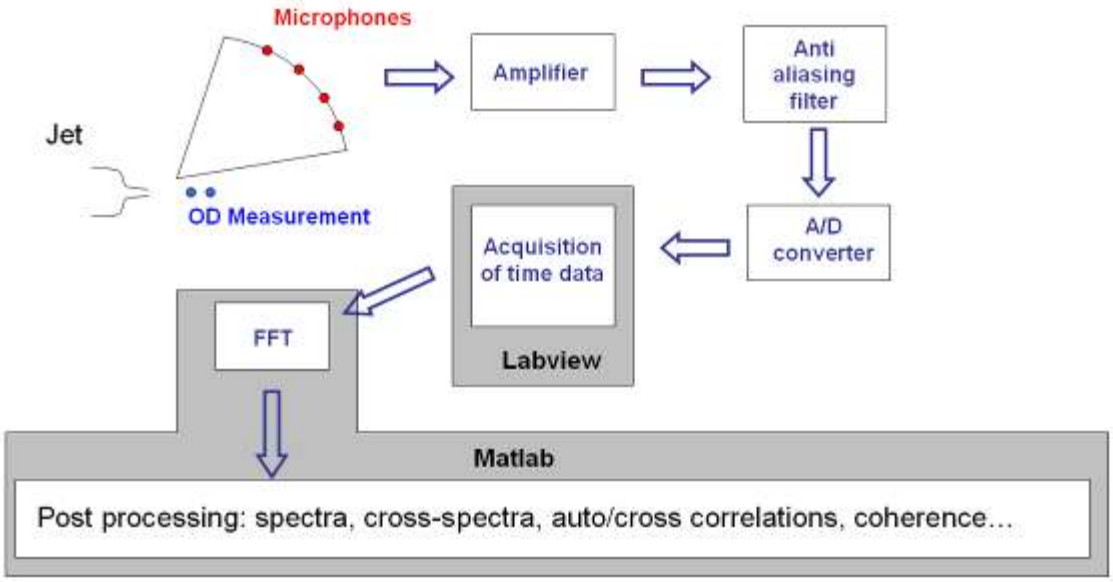

Figure **3-1**: Flowchart of data acquisition process.

The LabVIEW code for acquisition, *acquire_DAQmx_V002.vi*, is derived from the acquisition code *acquire.vi* described by Doty [**26**] with very slight modifications made in order to accommodate the new acquisition card.

3.2 Acoustic measurements

3.2.1 Acoustic setup

In order to acquire frequencies as high as 120 kHz, 3.2 mm (1/8 inch) diameter microphones are used. Most of the microphones used are pressure field microphones, type 4138 from *Brüel & Kjaer* (*B&K*). However, the number of microphones used was increased from 4 to 6. Therefore, 2 additional microphones were purchased. *GRAS* microphones model 40DP were chosen due to their ability to perform with a slightly better signal to noise ratio than the older microphones. Typically, measurements are made at different polar angles (θ) from the jet centerline between 30 and 130 degrees at a specified non-dimensional distance *R/D*, where *R* is the physical distance of the microphone from the nozzle exit plane, and *D* is the exit diameter of the nozzle, or the diameter of an effective circular area equivalent to that of exit area of the nozzle if the latter is not circular.

Depending on the required experiments, different types of supports were used in previous studies for the microphones: circular booms, linear arrays, or simply tripods. For the experiments presented in this study, and once again in order to increase the accuracy and quality of the data, a rotating array has been developed. The array rotation center can be moved downstream of the jet to the desired location and stays permanently in the facility from one experiment to another. During typical acoustic measurements, the distance and polar angle for each microphone are measured from a point located 5 diameters downstream of the nozzle exit plane, on the axis of the jet. A photograph of this rotating boom can be seen in Figure **3-2**. The microphones have also been used in previous studies in both grazing and normal incidences and it was shown [**32**] that the

grazing incidence could be preferable for a wide bandwidth, even though this orientation decreases the microphones dynamic range. Therefore, the microphones are positioned at grazing incidence, and their locations are referenced from the estimated location of the noise source.

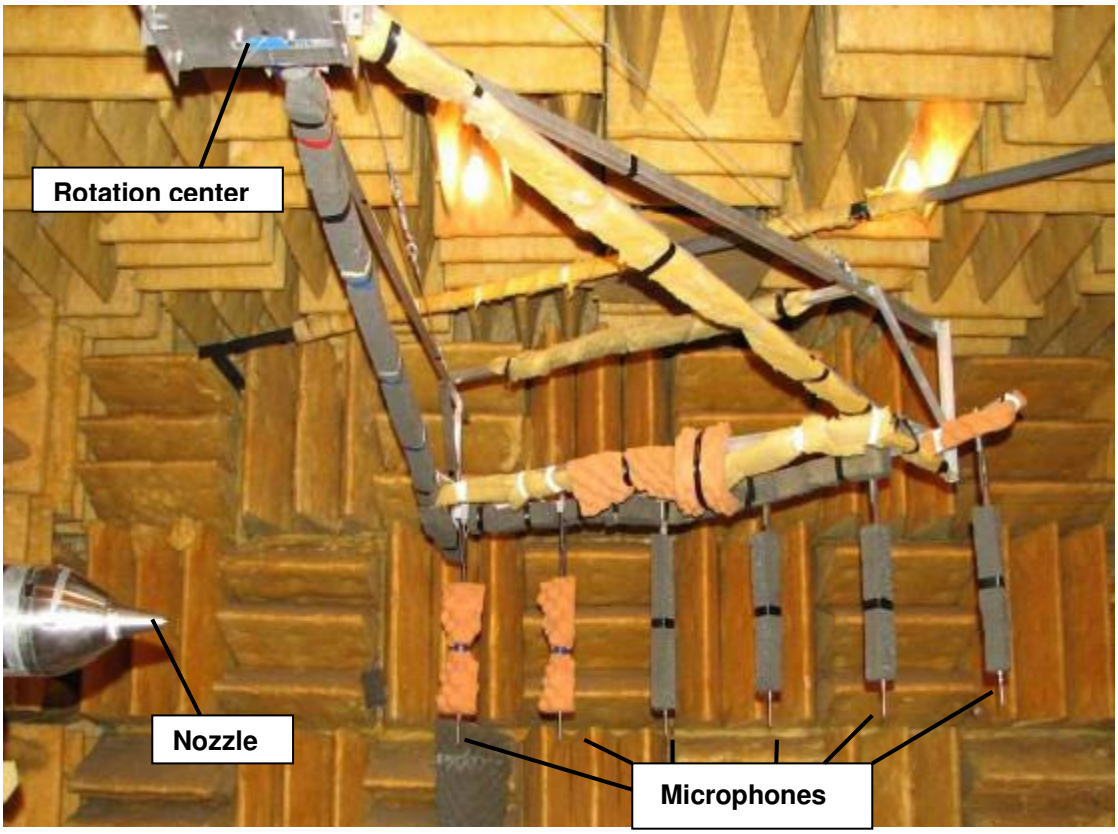

Figure **3-2**: Microphone rotating array.

Each B&K microphone is connected to an amplifier. 2 of them are powered by a B&K model 5935 power supply and the remaining two are powered by a model 2690 *NEXUS* power supply. The *GRAS* microphones are powered by a model 12AN power module which has the advantage over the *B&K* and *NEXUS* power supplies of having a cutoff frequency at 200 kHz rather than 100 kHz. This power module can support 4 channels, therefore two *B&K* microphones can also be connected to it in order to improve the high frequency content of those measured signals. The gain for each microphone signal varies between 0 and 40 dB depending on the experiments run. The signals finally

go through a model 3384 *Krohn-Hite* filter where they are high-pass filtered at 500 Hz and low-pass filtered at 120 kHz for anti-aliasing purposes before going to the DAQ board that acquires the time domain data. Since the microphones are only reliable for frequencies lower than 150 kHz, the sampling rate is set at 300 kHz and a collection of N = 409,600 data points is typically acquired with LabVIEW and stored in binary files with units of volts. During helium-air measurements, only 204,800 points are acquired in order to reduce the acquisition time (T = 0.6 s instead of 1.2 s).

To ensure that data passed to the analysis stage is free from contamination such as noise reflections and electronic noise, a first-look at the acquired noise spectrum is performed using LabVIEW immediately following the experiment. Any major error in the spectra such as large amplitude oscillations indicating the presence of reflections can often be identified before extensive processing. Based on this, measures can be taken to remove the error through correction of the set-up. Apart from this quick-view processing, all data are saved as binary files and processed using a Matlab code evolved from that described by Petitjean [**29**] and further modified by the author and by fellow PhD candidate Ching-Wen Kuo [**33**]. A copy of this processing code *JNA_CPSD_Vb.m* can be found in Appendix B.

At this point, the microphone calibration constants, previously made using a model 4231 *B&K* acoustic calibrator, are input in order to change the voltages into pressures. These calibration constants are logged into a tracking sheet to make sure they do not vary too much from one experiment day to another. The time data are split into 4096 point windows (rather than 1024 as was previously used [**29**]) in order to obtain a finer resolution in frequency. A Hanning window function is applied and 50% overlap is used between each window, resulting in 199 windows. When doing helium-air mixture measurements, only 99 windows are averaged due to the smaller number of data points used as a measure to limit helium usage. The Fast Fourier Transform (FFT) is calculated on each window of data and then averaged, yielding the power spectral density (*PSD*) for each of the individual microphones. Further manipulation converts the *PSD* to a decibel (dB) scale, referenced to 20 micro-Pascals, to yield the raw sound pressure level (*SPL*) for each acquired signal. The necessary microphone and atmospheric attenuation

corrections are then applied to the spectra in order to produce spectral outputs in *SPL* per resolution bandwidth. The following equation summarizes the corrections made to the raw SPL data:

$$SPL(f)\big/_{\text{bandwidth}} = SPL_{raw}(f) - \underbrace{\Delta C_{act}(f) - \Delta C_{ff}(f)}_{\text{Microphone Corrections}} - \underbrace{\Delta C_{atm}(f)}_{\substack{\text{Atmospheric}\\ \text{Correction}}} \qquad \textbf{3.1}$$

The atmospheric correction accounts for sound absorption in the atmosphere and is a function of the ambient conditions (temperature, pressure and humidity). Further details on the microphone corrections and processing are discussed in Petitjean [**29**].

3.2.2 Methodology for acoustic comparisons

Usually, computing the Sound Pressure Level (*SPL*) per unit Strouhal number makes comparison easier between different scale experiments. It is calculated from the *SPL* per resolution bandwidth as follow:

$$SPL(f)\big/_{\text{unit } St} = \overbrace{SPL(f)\big/_{bandwidth} - \underbrace{10\times\log_{10}\Delta f}_{\substack{\text{Scaling to 1 Hz}\\ \text{bandwidth}}}}^{SPL(f)\big/_{Hz}} + \underbrace{10\times\log_{10} f_c}_{\substack{\text{Strouhal Number}\\ \text{Scaling}}} \qquad \textbf{3.2}$$

Some data in the literature are only available in 1/3 octave band. Therefore, in order to make comparisons with these, the *SPL* per resolution bandwidth needs to be converted into *SPL* per 1/3 octave band by summing the *SPL* in all the bands comprised in every 1/3 octave band, as shown below:

$$SPL(f)\big/_{1/3 octave\ band} = 10\times\log_{10}\left(\sum_{f_{low}}^{f_{up}}\exp\left[\frac{SPL(f)\big/_{bandwidth}}{10}\right]\right) \qquad \textbf{3.3}$$

Linear interpolation is used at the edges of the bands in order to obtain an accurate SPL value for the 1/3 octave bands. Comparisons can be made with data from the literature with different nozzle dimensions and *R*/*D* locations of the microphones, but similar jet conditions. In order to properly compare the spectra, these spectra have been

put into the same format. For example, in order to compare spectra from two different nozzle diameters D_1 and D_2, the following correction is made:

$$SPL_{D_1}(f) = SPL_{D_2}(f \times D_1 / D_2) \qquad \textbf{3.4}$$

Obviously, as mentioned in section **1.2.1**, when a jet is designed for a Mach number M_d and run at a different Mach number M_j, one should use the diameter of the fully expanded jet, defined from isentropic relations in Eq. **1.2**.

Similarly, the data should be at the same nondimensional distance relative to the nozzle exit. It has been shown [**34**] that nonlinearities occur when very high amplitude sound propagates. However, the linear propagation approximation holds whenever the propagation distance is reasonably small. Hence, for spectra measured from nozzles of the same diameter at two different distances R_1 and R_2, the following correction is applied, assuming spherical spreading and linear propagation of the sound:

$$SPL_{R_2}(f) = SPL_{R_1}(f) + 20 \times \log_{10}\left(R_1 / R_2 \right) \qquad \textbf{3.5}$$

Some spectra comparisons produced using this methodology are presented in section **4.1**.

3.3 Optical measurements

As a complement to acoustic measurements, optical diagnostic of the flow was designed to provide information on the flow characteristics that produce the propagated sound. Two kinds of measurements were made: qualitative observation of the flow using a schlieren setup, and quantitative measurements of the turbulence properties contained in the jets with Optical Deflectometry.

3.3.1 Schlieren setup

3.3.1.1 Setup overview

An advantage of a schlieren setup, when compared to other optical methods like PIV or LDV, is that no seeding of the flow is required. Hence, measurements can be made for flows such as the studied jets, where the seeding can be problematic, or when collection of the flow markers downstream of the test section is a problem. Furthermore, this technique provides a time history, which is ideal for capturing turbulence.

The setup used is a conventional Z-type schlieren system, shown schematically in Figure **3-3.** A parabolic mirror 15.2 cm (6") in diameter is used to produce a parallel beam of light that illuminates the jet. The light source used is a short duration spark light (*Spectrum Dynamics Spectralite* Model 900 xenon lamp) and is transformed into a very small dimension source after passing through a focusing lens and a slit. The actual size of this source is a function of the size of the arc produced by the spark light, the distance to the lens and the size of the slit. It typically consists of a rectangle of dimensions 2 mm by 0.5 mm. The slit is positioned at the focal length of the first parabolic mirror - 1.22 m (4ft) focal length – to produce a parallel light beam. A second identical parabolic mirror receives this light after it passes through the jet, and focuses it onto the edge of a knife so that part of the light is stopped. Any small deflection of the light (at any point of the "object" plane) due to a variation of density gradient will result in more or less light being cut by the knife edge, and hence be visualized as darker or brighter areas at a corresponding location on the image recorded by the camera.

Ideally, with no flow on, the image is uniformly gray. However, due to slight imperfections in the mirrors, lenses and the fact that the source is not a perfect point, a perfectly uniform shade is only approximately obtained.

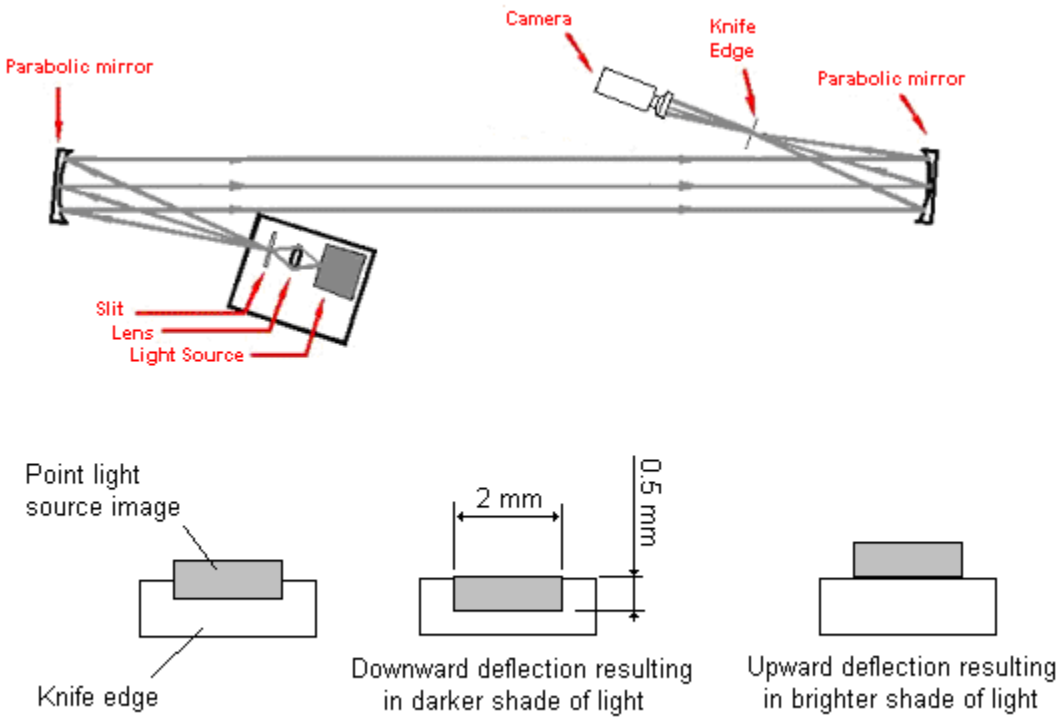

Figure **3-3**: Schematic of Z-type schlieren setup.

3.3.1.2 Image acquisition and stroboscopic light frequency

The image acquisition is obtained through the use of *Safety & Security* model 109B Black and White CCD camera with a *Minolta* 50 mm lens. The image rate of the camera is 50Hz and cannot be changed, limiting the time resolution of the schlieren imaging. However, the stroboscopic light is externally controlled by a *B&K Precision* model 4084 signal generator which gives full control of the frequency of the light pulses. Therefore, the number of flashes per image captured can be easily controlled. As an example, using a 100 Hz stroboscopic rate and a 50 Hz camera rate usually results in the averaging of two frames in the camera output. Depending on the flow characteristics that need to be visualized, different settings are used on the stroboscopic light. A very small number of averages is necessary in order to be able to visualize structures such as Mach

wave radiation or in order to obtain a sharp picture of the turbulent structures. On the other hand, if shock cells need to be visualized, it is more appropriate to average a large number of light flashes onto one picture in order to obtain a clear image of the shock position. Figure **3-4** shows an example of schlieren images obtained with different stroboscopic light settings. The shocks are more clearly visible in the high frequency case, thanks to the averaging (10 flashes per image acquired by the video camera), while the turbulence is more sharply defined with the low frequency flashes (2 flashes per image acquired by the video camera).

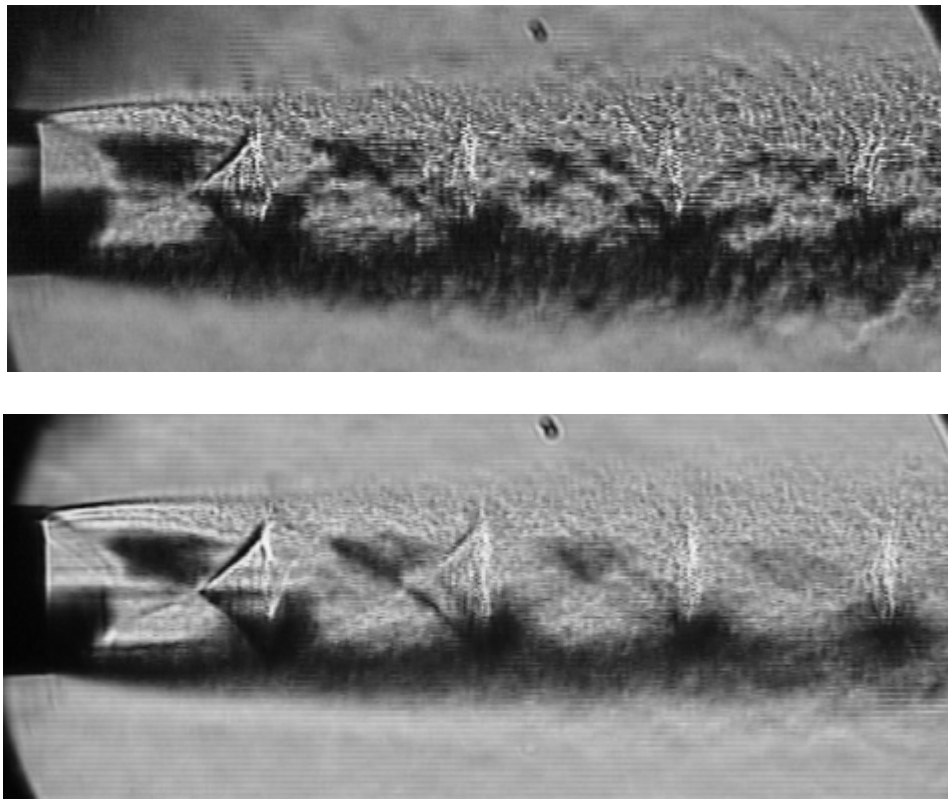

a)

b)

Figure **3-4**: Schlieren image of a M_d = 1.0, M_j = 1.5, 2.54 cm (1") diameter jet with the stroboscopic light set at a) 100 Hz, b) 500 Hz.

3.3.1.3 Knife edge settings

Different knife edge orientations were used in order to visualize different flow characteristics. A vertical knife edge is preferable in order to obtain a clear picture of the vertical shock waves or the Mach waves radiated. A horizontal knife edge is used when making measurements of vertical density gradients and thus provides more clearly information on the turbulence in the shear layer. Incidentally, the light intensity between one side of the jet and the other is inverted, as the density gradients have opposite directions, resulting in a dark and a light shear layer. This can be seen in Figure **3-5**. Obviously, a 90° rotation of the knife edge must also be accompanied by a similar rotation of the light source and its slit in order to keep a good contrast on the image.

a)

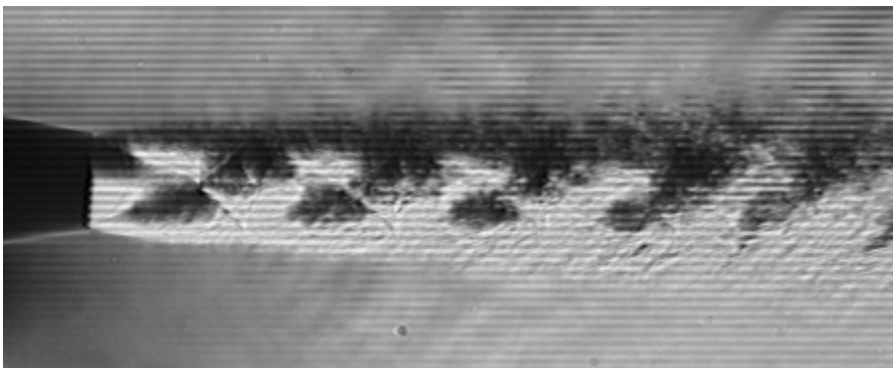

b)

Figure **3-5**: Schlieren image of a $M_d = 1.0$, $M_j = 1.5$, 1.27cm diameter (0.5") jet with a) vertical knife edge, b) horizontal knife edge.

The amount of light blocked by the knife edge affects more than just the level of contrast of the image. When the whole image is blocked by the knife edge (100% knife edge) only large deflections of the light are visible on the image. Therefore, only large structures are visible, such as large scale turbulent structures or strong temperature gradients. When there is no light blocked by the knife edge, any small gradient (in one direction only) will produce a deflection that will block the light, therefore, very small scale structures appear on the image, despite the fact that the image is very bright overall. Samples of different light settings are shown in Figure **3-6.** Similar observations were made and reported by McIntyre [**35**].

a)

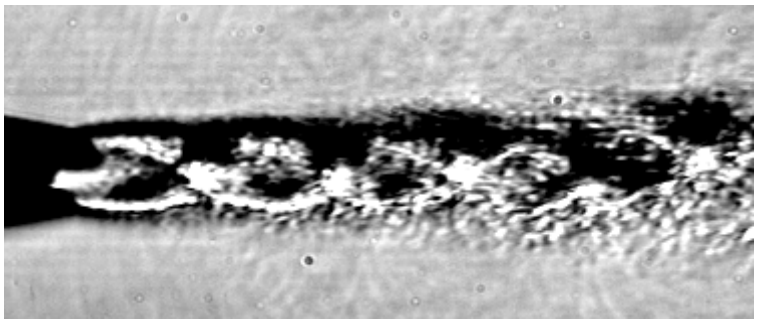

b)

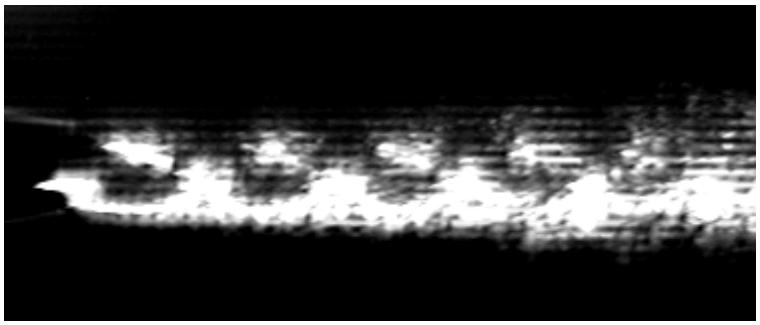

Figure **3-6**: Schlieren image of a $M_d = 1.0$, $M_j = 1.5$ jet with a) 0% knife edge, b) 100% knife edge.

Finally, it should be noted that some post processing techniques can be used in order to enhance the quality of the images. One such technique is described in Papamoschou [**36**] and is designed to enhance the Mach waves in the picture. Calibration is also possible in order to extract from the light shade some values of density gradients. These techniques are not used in this thesis but are tools that should be kept in mind for improving the quality of the measurements made.

3.3.2 Optical Deflectometry setup

3.3.2.1 Setup overview

Optical Deflectometry (OD) is based on the schlieren principle. However, instead of visualizing shades of light on a screen (or using a camera), the light beam after the knife edge is separated into two images of equal intensity using a semi-reflecting mirror, or beam splitter. A photomultiplier (PMT) is then placed in the middle of each image. These devices are probes designed to measure the light intensity through a small aperture located at their center. A mask is put in front, with a pin hole at the center in order to further reduce the size of the aperture. One of the photomultipliers is mounted on manual slides and the other one moved around using motorized traverses piloted by a stepper motor controller for high precision. Figure **3-7** offers a representation of the setup as it is used at The Pennsylvania State University. The acquisition system follows the flowchart shown in Figure **3-1**, going through an amplifier and filters before being acquired via an acquisition card into the computer.

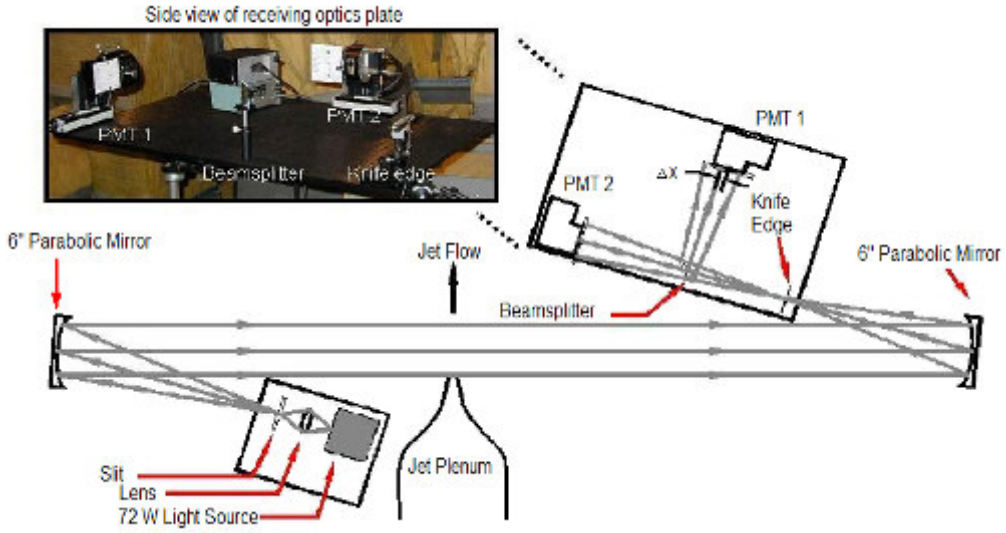

Figure **3-7**: Schematic of optical deflectometry setup.

This setup provides "instantaneous" time records of a small region of a schlieren image and therefore enables quantitative measurements of the flow properties. When analyzing a turbulent flow such as a high speed jet, the big structures of a compressible flow result in a change of density gradient that produces fluctuations of light intensity, which means a change of voltage output in the photomultipliers.

3.3.2.2 Correlation measurements: methodology

The main type of measurement made with the optical deflectometer consists of correlation measurements. Assuming a turbulent structure convects in the jet mixing layer, if the photomultipliers are located some distance apart, the same structure will pass in front of the photomultipliers with a time delay. The recorded voltages should therefore look somewhat similar with a shift in time depending on the speed of propagation of these vortices and the change in the structure made during the time interval. Cross correlation of the signal will hence give a measurement of the convection speed of the turbulence structures.

The cross correlation method was applied to high speed jets by Doty and McLaughlin [**37**] and more recently by Petitjean *et al.* [**38**]. Typically, the OD setup is used to collect information on the decay rate and the convection speed of the turbulence in the shear layer. During this kind of measurement, both photomultipliers are initially put at the same location by making sure that the coherence of their signals is as close to 1 as possible, using a *Hewlett-Packard* model 35670A digital signal analyzer. Then the first photomultiplier (PMT1) is kept fixed while the second one (PMT2) is moved downstream a distance $\Delta x_1 / D$, where D is the diameter of the nozzle and Δx_1 the displacement in the axial direction. Special care has to be taken to move the photomultiplier not only along the axis of the jet, but also radially (Δx_2) in order to follow the shear layer. For each location, the cross-correlation of the acquired signals is calculated as described in the following section. Figure **3-8** shows as an example the cross correlation functions at different separation distances for a Mach 0.9 jet. Validation of this kind of measurements was made by Doty [**22**] by comparing with hot-wire

measurements made by Davies *et al*. [**23**]. The results presented in this study were also checked for consistency with these earlier measurements.

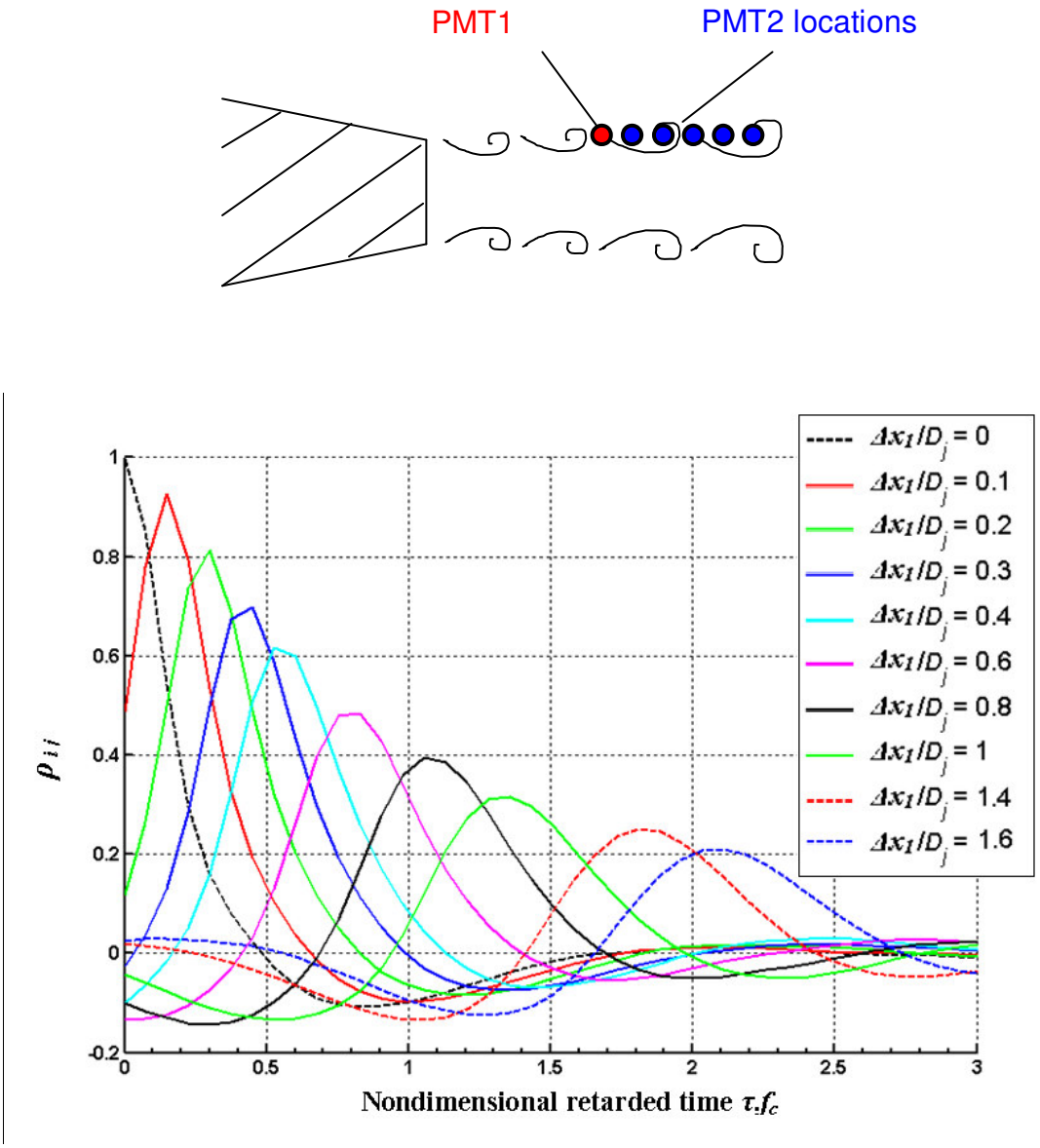

Figure **3-8**: Cross-correlation functions for a $M_j = 0.9$ jet at $x_1 / D_j = 4.0$.

3.3.2.3 Correlation measurements: acquisition and processing

Once the time data are acquired with LabVIEW, the binary files are read with Matlab and used for the processing. An acquisition frequency of 300 kHz is enough to capture all the spectral content of the flow. However, in order to obtain a finer resolution in retarded time when doing cross-correlations, the frequency is sometimes increased to 500 kHz for high speed flows.

Direct use of the time signals $p_i(t)$ and $p_j(t)$ from each individual photo detector can be made. Statistical quantities can be examined such as the mean μ_i, the variance σ_i and the skewness sk_i defined in Eqs. **3.6** to **3.8**:

$$\mu_i = \frac{1}{N}\sum_{k=1}^{N} p_i(t_k) \qquad \textbf{3.6}$$

$$\sigma_i^2 = \frac{1}{N}\sum_{k=1}^{N}\left[p_i(t_k) - \mu_x\right]^2 \qquad \textbf{3.7}$$

$$sk_i = \frac{1}{\sigma_i^3}\left[\frac{1}{N}\sum_{k=1}^{N}\left[p_i(t_k) - \mu_i\right]^3\right] \qquad \textbf{3.8}$$

Then, post-processing similar to that used for acoustic measurements can be made, where the time data are typically split into 4096 point windows in order to obtain a fine resolution in frequency. A Hanning window function is applied and 50% overlap is used between each window, resulting in a total of 199 windows. The Fast Fourier Transform (FFT) is calculated on each window and then averaged, yielding the double sided power spectral densities $S_{ii}(f)$ and $S_{jj}(f)$ and the cross spectral density $S_{ij}(f)$. From these, the single sided power spectral densities $G_{ii}(f)$ and $G_{jj}(f)$, and the cross spectral density $G_{ij}(f)$ can easily be computed. The auto and cross-correlation functions for the static and the moving photo detector signals, respectively $R_{ii}(\tau)$, $R_{jj}(\tau)$ and $R_{ij}(\tau)$, can then be calculated by taking the inverse Fourier transform of the spectral densities, as shown in Eq. **3.9**:

$$R_{ij}(\tau) = \mathfrak{F}^{-1}[S_{ij}(f)] \qquad \textbf{3.9}$$

Incidentally, the auto and cross correlation functions also relate to the time signal by a convolution, as shown in Eq. **3.10**:

$$R_{ij}(\tau) = \frac{1}{T}\int_0^T p_i(t)\ p_j(\tau + t)\ dt \qquad \textbf{3.10}$$

In this formula, T represents the time of a sample window and τ is the time delay. Typically, the time delay is non-dimensionalized by multiplying it by the characteristic frequency f_c.

Additionally the cross correlation coefficient function is calculated for different separation distances between the two PMTs, and consists of a normalization of the cross correlation function as defined in Eq. **3.11**:

$$\rho_{ij}(\tau) = \frac{R_{ij}(\tau)}{\left(R_{ij}(0)\ .\ R_{ij}(0)\right)^{1/2}} \qquad \textbf{3.11}$$

Finally, the coherence $\gamma_{ij}{}^2$ between the two signals is computed from S_{ii}, S_{jj} and S_{ij} following the formula in Eq. **3.12**:

$$\gamma_{ij}{}^2(f) = \frac{\left|S_{ij}(f)\right|^2}{S_{ij}(f)\ .\ S_{ij}(f)} \qquad \textbf{3.12}$$

The flowchart in Figure **3-9** summarizes the different steps in the processing. A copy of the processing Matlab code *OD_process_JV_V10.m* can be found in Appendix B.

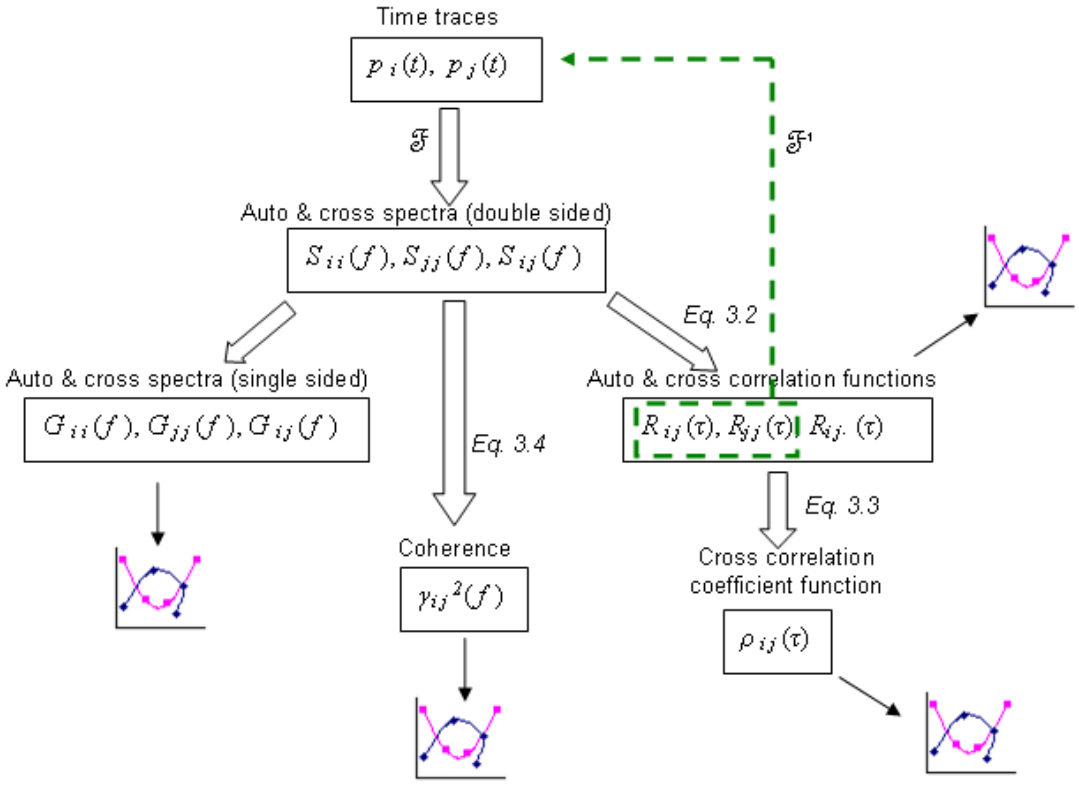

Figure **3-9**: Processing flow chart for OD measurements.

3.3.2.4 New OD setup for UCI

In order to fulfill the requirements for an ongoing NASA NRA contract, a new Optical Deflectometry instrument was designed, fabricated and then sent to the University of California, Irvine for operation. Details on the design and testing stages of the whole system can be found in Appendix **A.3**.

The basic design of this new system is in many ways very similar to the one previously developed at Penn State. Building on past experience, attention was paid to refining the design, such as maximizing the amount of light captured from the light source to produce the parallel beam. The whole system was dimensioned to fit in the UCI small scale jet noise laboratory and to be easily shipped there. A description of the small

scale jet noise facility of the University of California, Irvine can be found in Papamoschou [**28**].

However, during the design process, two major differences were incorporated between this new design and the one predominantly used in this thesis. Modification was first sought in the nature of the probe that is used to measure the light intensity fluctuations. While the Penn State setup uses photomultiplier tubes, the UCI one was designed with Avalanche Photodiodes (APD). Photodiodes are small sensors that also respond to light intensity fluctuation, producing a voltage output change. The photodiodes chosen for this application are *Hamamatsu* APD modules model C5460-01 and are referred to as APDs. These APDs were first compared to the PMTs by making some typical correlation measurements and proved to work identically well in every condition tested. Their sensitivity to low light is even higher than the PMTs. The second major deviation from the Penn State design was in the incorporation of 4 sensors, rather than 2. The reduced size and cost of the APDs compared to photomultipliers allowed for the usage of two sensors on each image. One of the pair was designed to be mounted on manual traverses (pair A) while the second pair (pair B) was fitted onto motorized traverses and piloted through a controller by the computer. This unlocked the capability of making measurements faster and to have two fixed reference points when doing cross-correlations. In order to place both APDs of the same pair close enough to each others, a system of prisms was designed that diffracts the light, as shown in the diagram of Figure **3-10**.

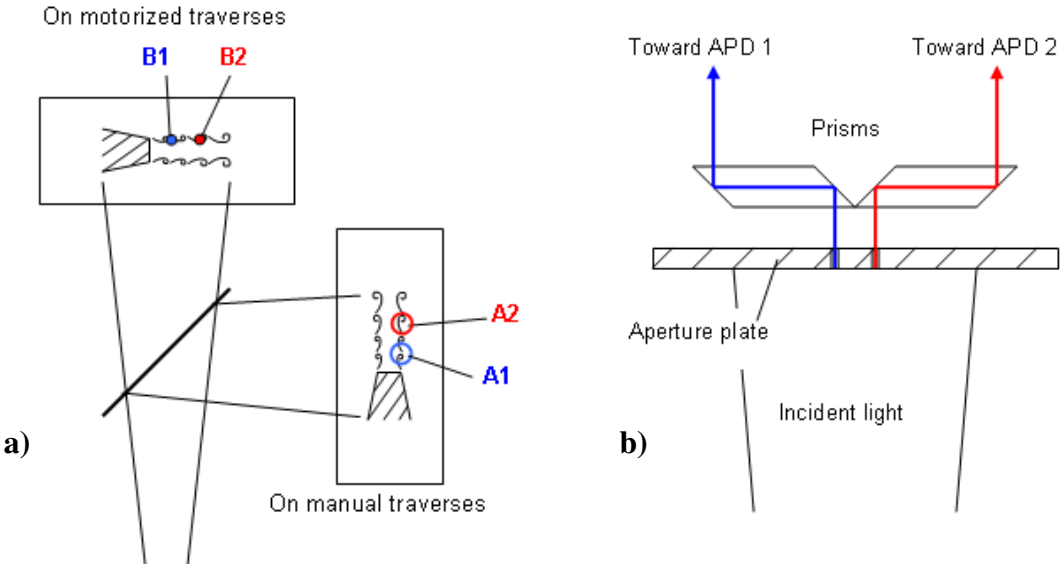

Figure **3-10**: Schematic of OD setup for UCI: a) general receiving optic setup, b) prism system.

Prior to shipping the apparatus to UCI, calibration and validation runs were performed at Penn State. A number of measurements were also made with this setup, both at Penn State and at the UCI small scale jet noise facility after its installation there during the month of August 2008. Some of these measurements are presented with the other OD results in Chapter **6**.

Additional drawings of this new OD setup can be found in Appendix **A**, together with pictures of the UCI facility and some qualification measurements performed with this new setup.

3.4 Pitot probe measurements

While optical deflectometry can give valuable measurements of turbulence convection speed, it can not easily be used for direct velocity measurements in the flow. Indeed, the photomultipliers measure fluctuation of light intensity, which itself is a measurement of the density gradient. It thus becomes complicated to link these

measurements back to a velocity, and would involve proper calibration as well as careful consideration of the integration effect involved by the fact that the light traverses the whole jet. Mean flow velocity measurements will hence be made using pitot probes that will be moved inside the jets and connected to pressure transducers, in a fashion similar to that described by McLaughlin *et al.* [**39**].

3.4.1 Supersonic pitot measurement fundamentals

Static and pitot pressure measurements were made in the jet flow. The schematics presented in Figure **3-11** show the nomenclature used for the pressures measured by the probes.

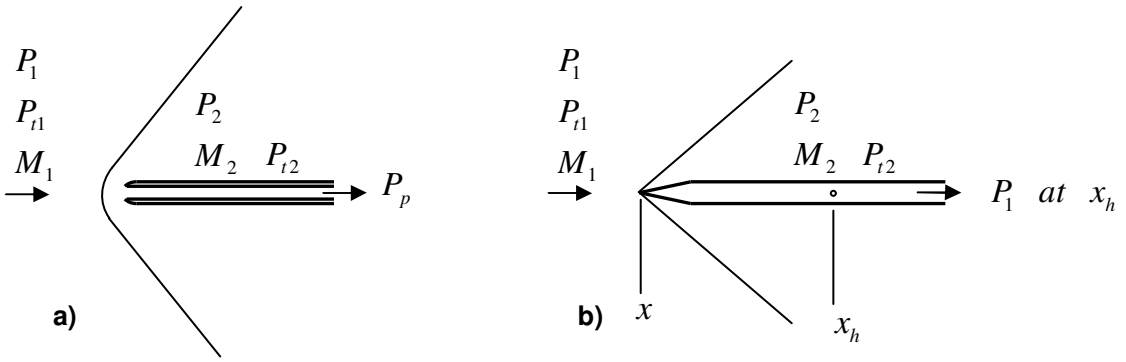

Figure **3-11**: Schematic diagrams of pressure probes in a free stream flow: a) pitot pressure probe, b) static pressure probe.

When a flow is supersonic, the pitot pressure (P_p) is equal to the total pressure after the shock (P_{t2}). P_p and the static pressure P_1 are related to the Mach number in the flow by the Rayleigh pitot formula,

$$\frac{P_p}{P_1} = \left(\frac{(\gamma+1)\, M_1^{\,2}}{2} \right)^{\gamma/(\gamma-1)} \left(\frac{\gamma+1}{2\gamma\, M_1^{\,2} - (\gamma-1)} \right)^{1/(\gamma-1)} \qquad \textbf{3.13}$$

In the mixing layer, where the Mach number falls below unity, the local isentropic flow formula is appropriate,

$$\frac{P_p}{P_1} = \left(1 + \frac{(\gamma - 1)}{2} M_1^{\,2}\right)^{\gamma/\gamma - 1} \qquad \textbf{3.14}$$

In order to obtain a good representation of the value of the static pressure in the flow without the presence of the static probe, it has been shown [**40**] that the distance between the holes and the tip of the probe, x_h - x, should be at least 10 times the diameter D_p of the static probe. Then, the static pressure P_1 measured by the probe is a good representation of the static pressure in the flow at location x_h in the absence of any probe (provided the probe is aligned with the local oncoming flow). The use of any smaller value of x_h - x leads to a measured static pressure lower than the actual value. In the present experiments, x_h - x is 12.7 mm and D_p is 1 mm.

Knowledge of three appropriate gas dynamic properties in a compressible flow is sufficient to uniquely specify all properties of the flow. In an adiabatic flow of this type the isoenergetic approximation of constant jet stagnation temperature, T_o, is very accurate. There are two viable options for the two remaining required quantities that can be measured or estimated. First, the static pressure can be combined with the pitot pressure to compute the local Mach number using Eq. **3.13** and Eq. **3.14** leading to the local Mach number. An alternative method can be used in the isentropic flow region within the shear layer and upstream of the first oblique shock waves. In this region the normal shock relation for P_{t2} / P_{t1} is,

$$\frac{P_{t2}}{P_{t1}} = \left(\frac{(\gamma+1)\ M_1^{\,2}}{(\gamma-1)\ M_1^{\,2} + 2}\right)^{\gamma/\gamma-1} \left(\frac{\gamma+1}{2\gamma\ M_1^{\,2} - (\gamma-1)}\right)^{1/\gamma-1} \qquad \textbf{3.15}$$

In this equation, $P_p = P_{t2}$ and P_{t1} is assumed equal to the jet upstream stagnation pressure P_{t0}. This formula may be used (implicitly) to compute the Mach number. This method is used in regions where the static pressure probe measurements have inaccuracies due to important (although small) inclination angles to the probe. This

method is used on some of the data presented in this paper, and will be discussed further as the processed data are presented.

3.4.2 Instrumentation

Three different probes were used for the pressure survey of the jets. A single pitot was first used in an axisymmetric jet, providing a quick setup for the first measurements of the pitot pressure. Then, a static probe was used in the same kind of jet in order to validate the assumptions made on the static pressure in the jets. Finally, in order to make refined measurements in both axisymmetric and asymmetric jets, as well as making heat simulated jet pressure measurements, a 5 pitot rake was set up. Pictures of these three probes are shown in Figure **3-12**.

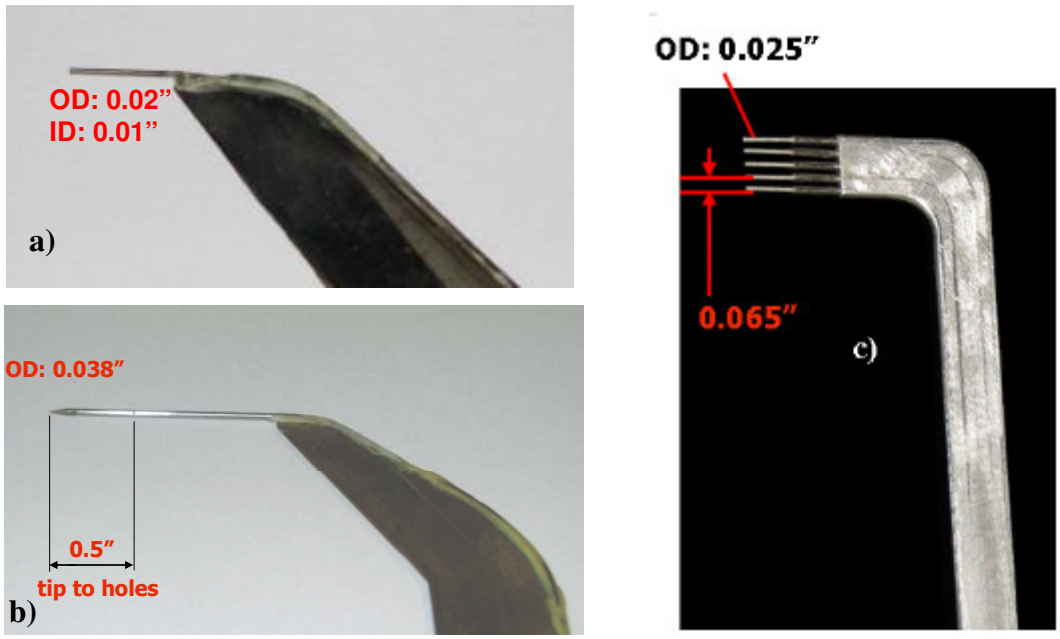

Figure **3-12**: Pressure probes pictures: a) pitot probe, b) static probe, c) pitot rake.

As can be seen on the picture, all probes were mounted on aerodynamic fins for minimum flow disturbance. Attention was paid to make sure the probes did not deflect or vibrate when exposed to a supersonic flow.

3.4.2.1 Single probe system

A first system of traverses has been designed and assembled with the help of fellow student U. Patel who reported the first pressure measurements in his thesis [**41**]. The system consists of two linear traverse stages (shown in Figure **3-13**), allowing for both radial and axial displacement of the probes. The horizontal traverse stage used is a *Velmex* motorized model MB6000. It has a minimum step of 51 μm (0.002") and a maximum travel length of travel of 15.25 cm (6"). The vertical displacement was obtained through a Superior Electrics motorized traverse, mounted on the former traverse via a 90 degree mounting plate. It has a similar minimum step value but a range of travel of only 10.2 cm (4"). Both motors were piloted via a *Velmex* VXM motion controller which was connected to the computer through the serial port. A LabView code "Probe_acquisition_v6.vi" was developed in order to control both traverses as well as automate the data acquisition of the probe at different locations in the jet. Detailed explanations of this acquisition code can be found in Patel [**41**].

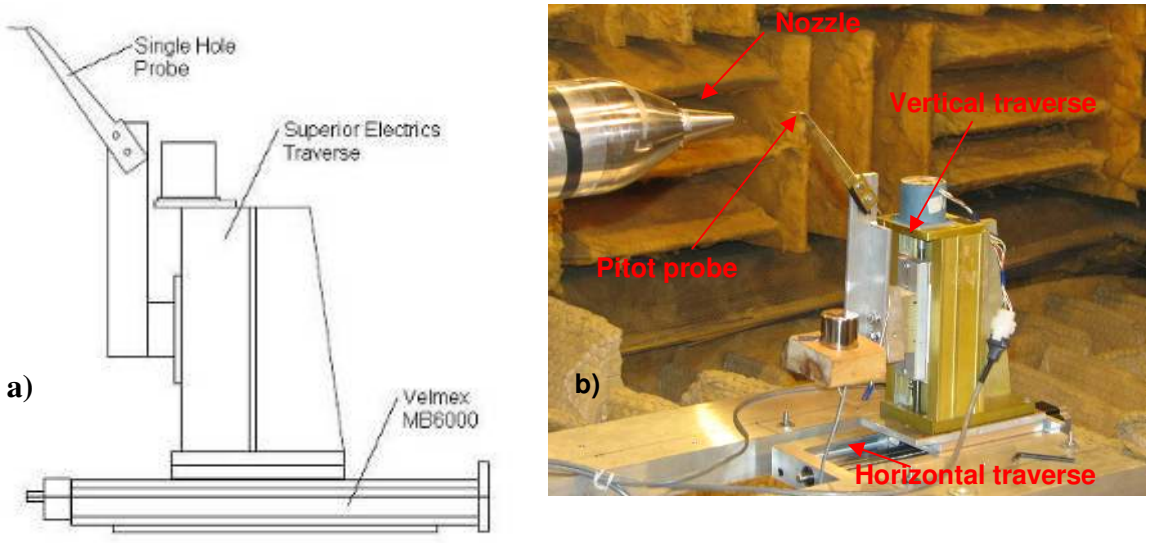

Figure **3-13**: Single probe drive traverses a) schematic, b) picture with pitot probe mounted.

3.4.2.2 Pitot rake system

In order to better map the flow and to reduce the amount of helium used during heat-simulated measurements, a 5 pitot rake has also been used. Due to the very different geometrical shape of the probe, some re-design was made on the probe holder. The rake can be mounted either horizontally or vertically, as can be seen in Figure **3-14**.

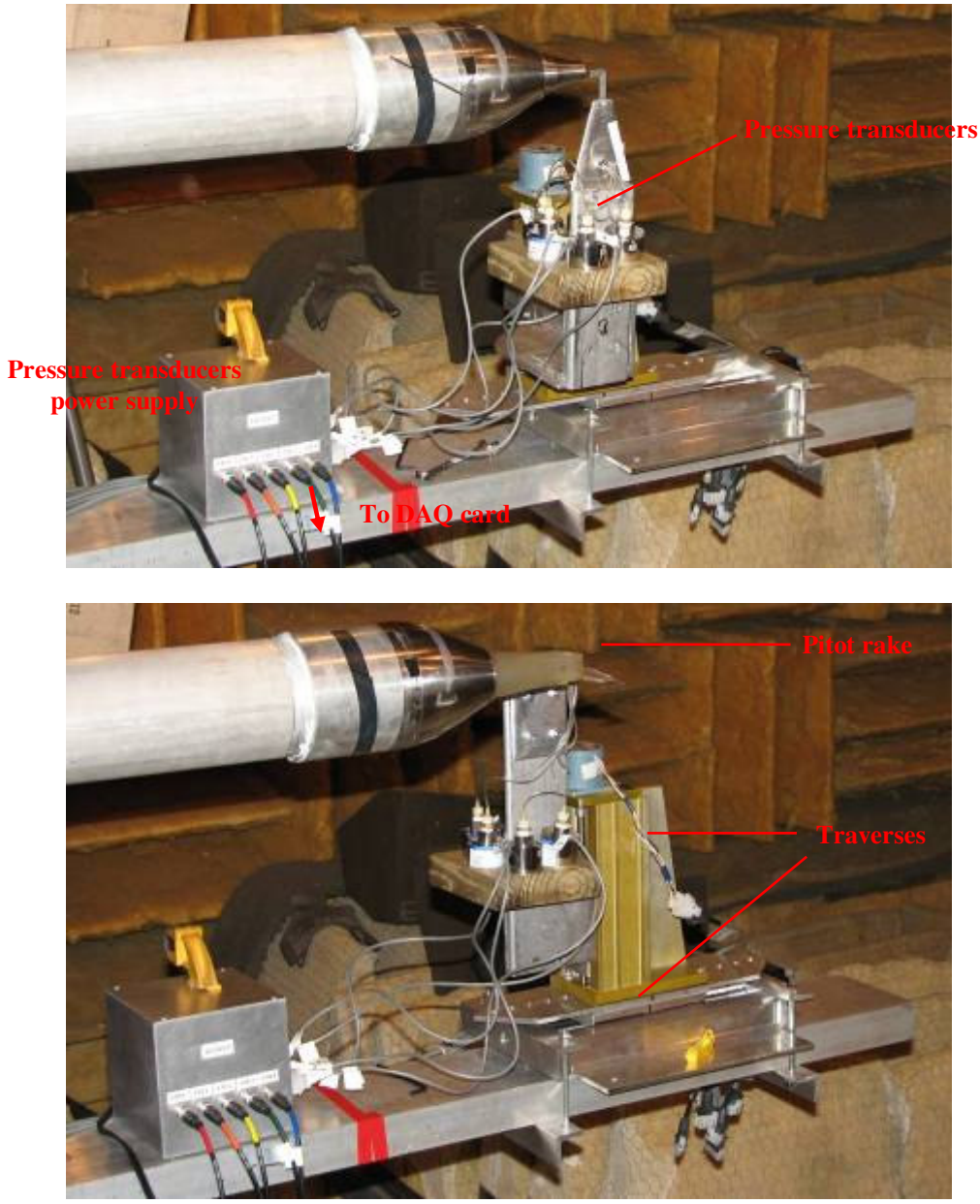

Figure **3-14**: Pitot rake set up for experiment a) horizontally, b) vertically.

When oriented horizontally, the use of the pitot rake enables 5 traverses of the jet to be performed simultaneously at different x_3 locations, as illustrated in Figure **3-15** for a rectangular jet.

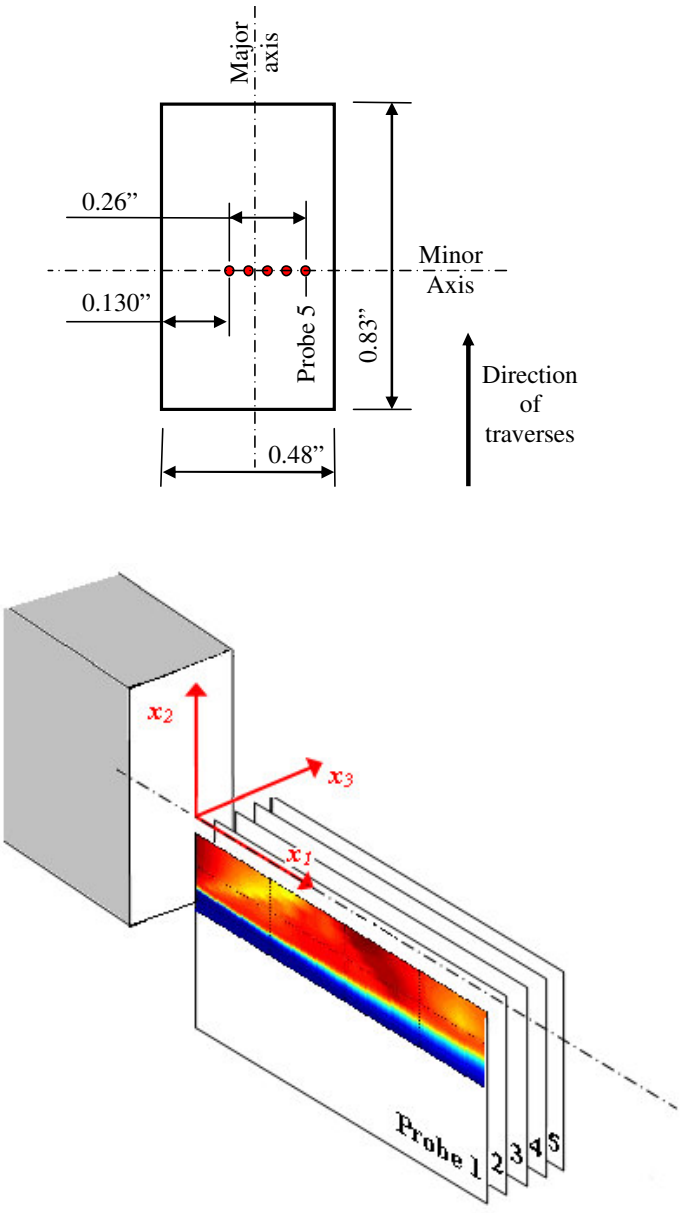

Figure **3-15**: Schematic of traverses obtained with the horizontal pitot rake.

With the rake oriented vertically, the 5 probes record the same pressure at different points of the traverse, providing an overlap that helps validating the quality of the measurements, as shown later in section **4.4.1**. It also facilitates the capability of doing time effective dynamic measurements where the rake does not need to cross the

whole jet, but rather the distance that separates two probes of the rake. This is explained in more details in Chapter **4**.

Finally, it should be noted that due to the interference of the probe and its support with the flow and the acoustic field, no meaningful acoustic measurement can be performed during these experiments. However, the schlieren setup is typically used simultaneously, offering a qualitative observation of the probe interference with the flow.

3.4.3 Pressure measurements methodology

When performing any kind of pressure measurement, the starting point is the center of the jet, at the exit plane. The probe is carefully aligned at this location, using the lip of the nozzle as reference. Since the horizontal stage has a travel of 6", it allows for downstream measurements up till 12 D in a 12.7 mm jet. If further downstream locations are required, the mounting support for the vertical stage can be moved by increments of 25.4 mm (1"), hence moving the starting location of the probe as well as the maximum reachable downstream location.

Static measurements of the pressure are usually made, where the probe is moved at one location, the pressure is measured and then the probe is moved to the next location. Figure **3-16** shows an example of the pitot probe location during pressure survey of a jet. Typical traverse measurements are made by performing radial displacement of the probe in the flow. Measured pressures are recorded every small incremental step Δx_1 in the downstream direction, usually on only half of the jet starting outside and going to the centerline, before moving to the next downstream location by a step Δx_2 , typically an order of magnitude larger than Δx_1. The exact values of Δx_1 and Δx_2 between the measured points depends on the jet conditions and the presence of shocks in the flow and will be specified for each measurement presented in Chapter **5**. The data can be mirrored along the centerline to give a full picture of the jet. Two full traverses of the jet are usually acquired at different downstream locations in order to ensure that the displacement of the probe in the x_1 direction follows the jet centerline.

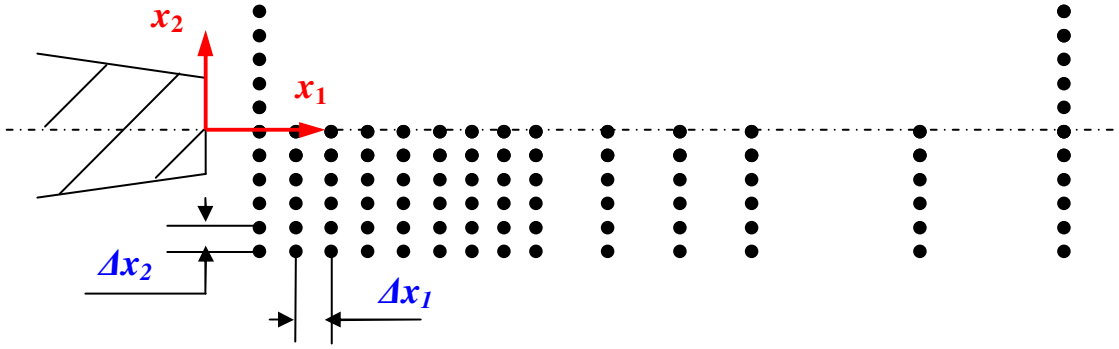

Figure **3-16**: Typical probe locations for pressure measurements.

Some refined centerline measurements can also be made, where the probe starting point is the centerline and is moved downstream with small incremental steps Δx_2. This enables a very fine survey of the centerline variations of the pressure.

Finally, in order to make helium-air mixture measurements in a time efficient manner, dynamic acquisition of the pressure is preferable. When doing such an experiment, the vertical axis (x_2) traverse is constantly moving while the voltages from the pressure transducers are being continuously recorded. Obviously, the pitot pressure measurements having a very limited frequency response, caution has to be taken in not moving faster than the time response of the pressure measurements allow. The resulting calibration experiments are presented in chapter **4**.

Chapter 4

Preliminary measurements

4.1 Acoustic validation of the newly redesigned jet noise rig

In order to validate the newly redesigned jet noise rig, qualification measurements were scheduled prior to conducting any experimental investigation. Different methodologies for jet noise rig qualifications are described in detail by Ahuja [**42**]. The method used for validation of the Penn State facility consists of comparisons between measurements made at Penn State and published data. Since the data are available for different jet diameters and at different microphone distances, scaling is applied as described in section **3.2.2**.

The first method that was used for qualification is a simple spectral comparison of the measured noise. Data from the old facility configuration were first compared with some published data as shown in Figure **4-1** Comparisons were made in 1/3 octave bands, with nozzles running at a Mach number approximately M_j = 0.9 and a total temperature ratio of approximately TTR = 2.5. The first set of data used is from the well known database from Tanna *et al*. [**43**]. The second set of data consists of noise predictions computed using a prediction method developed by the Society of Automotive Engineering and presented in the SAE ARP 876 document [**44**]. This prediction scheme was used by the author in reference [**45**] and is described in more details by Paliath [**46**]. As can be seen in Figure **4-1**, the spectra compare very well across a wide range of polar angles.

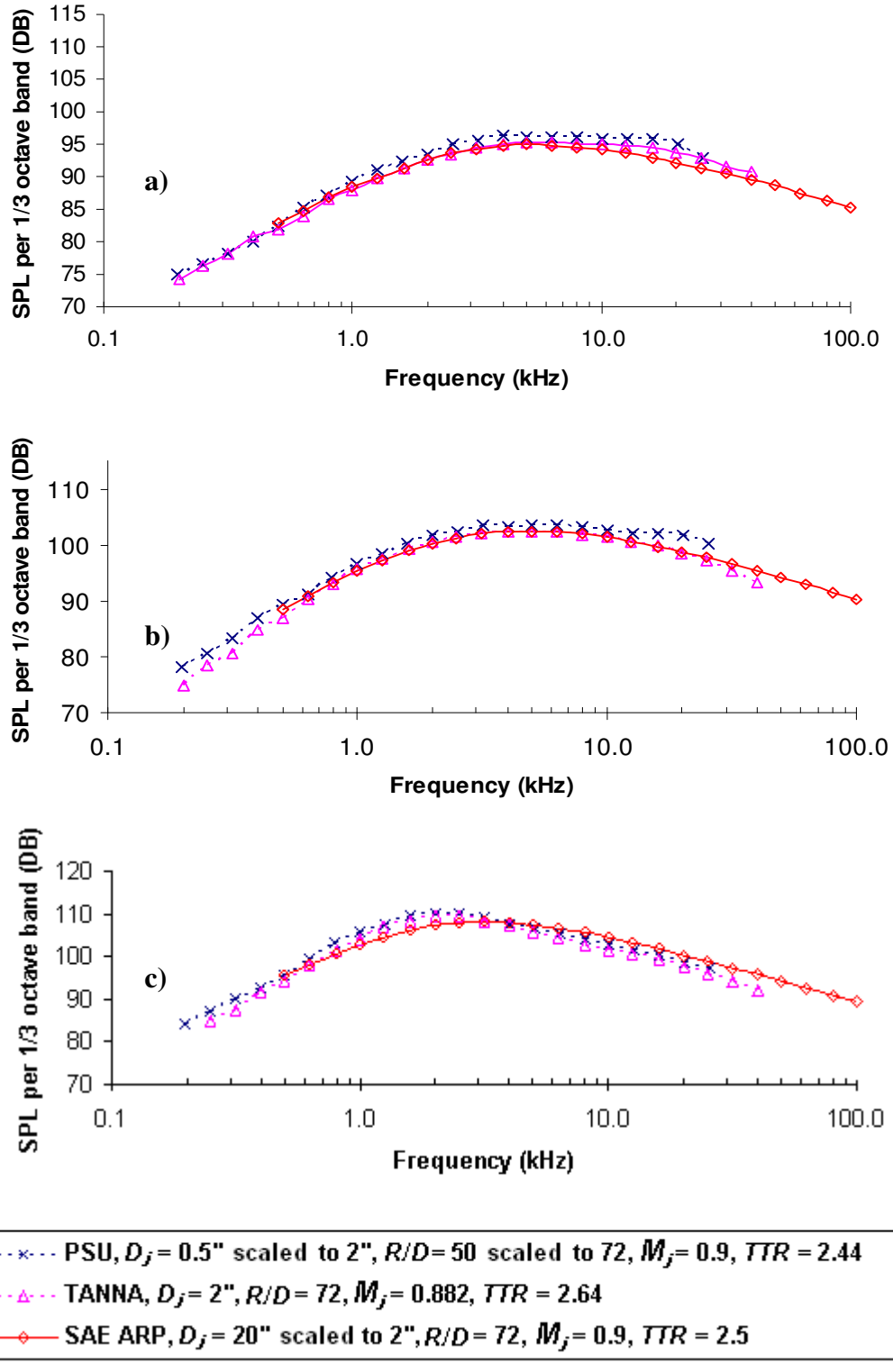

Figure **4-1**: SPL per 1/3 octave band of fully expanded $M_j \approx 0.9$ heated jets at a) $\theta = 90°$, b) $\theta = 60°$ and c) $\theta = 45°$.

Then, noise measurements were performed after the installation of the new jet noise rig, with a smaller diameter plenum and redesigned upstream piping. Information on these modifications can be found in section **2.3** and drawings can be found in Appendix **A.1**. Direct comparison is made between spectra measured before and after the upgrade and is shown in Figure **4-2**. Despite differences in the diameters of the nozzles used, and different non-dimensional distances of the microphones to the jet, the experiments show very good repeatability.

Moreover, a direct comparison can be made between measurements made in the new configuration of the facility with some data acquired at the NASA Glenn Research Center facility, described in reference [**27**]. The spectral data used for comparison were taken with a military style nozzle based on inner contours provided by GE and described in more details in section **5.4**. The NASA data were acquired with a nozzle of similar geometry but 7 times larger and were provided by Dr. James Bridges [**47**]. Figure **4-3** shows that the spectra agree reasonably well despite the differences in jet diameters. The spectral shapes are in very good agreement, as well as the amplitude of the SPL, except for polar angles 60 and 110 were there is a small 2 dB discrepancy over the whole frequency range. Incidentally, these spectra also show the shift of the BBSAN to lower frequency with increasing polar angle.

Overall, the comparisons are very good and validate the quality of the refurbished facility. Acoustic and flow measurements can thus be conducted without contamination by rig noise.

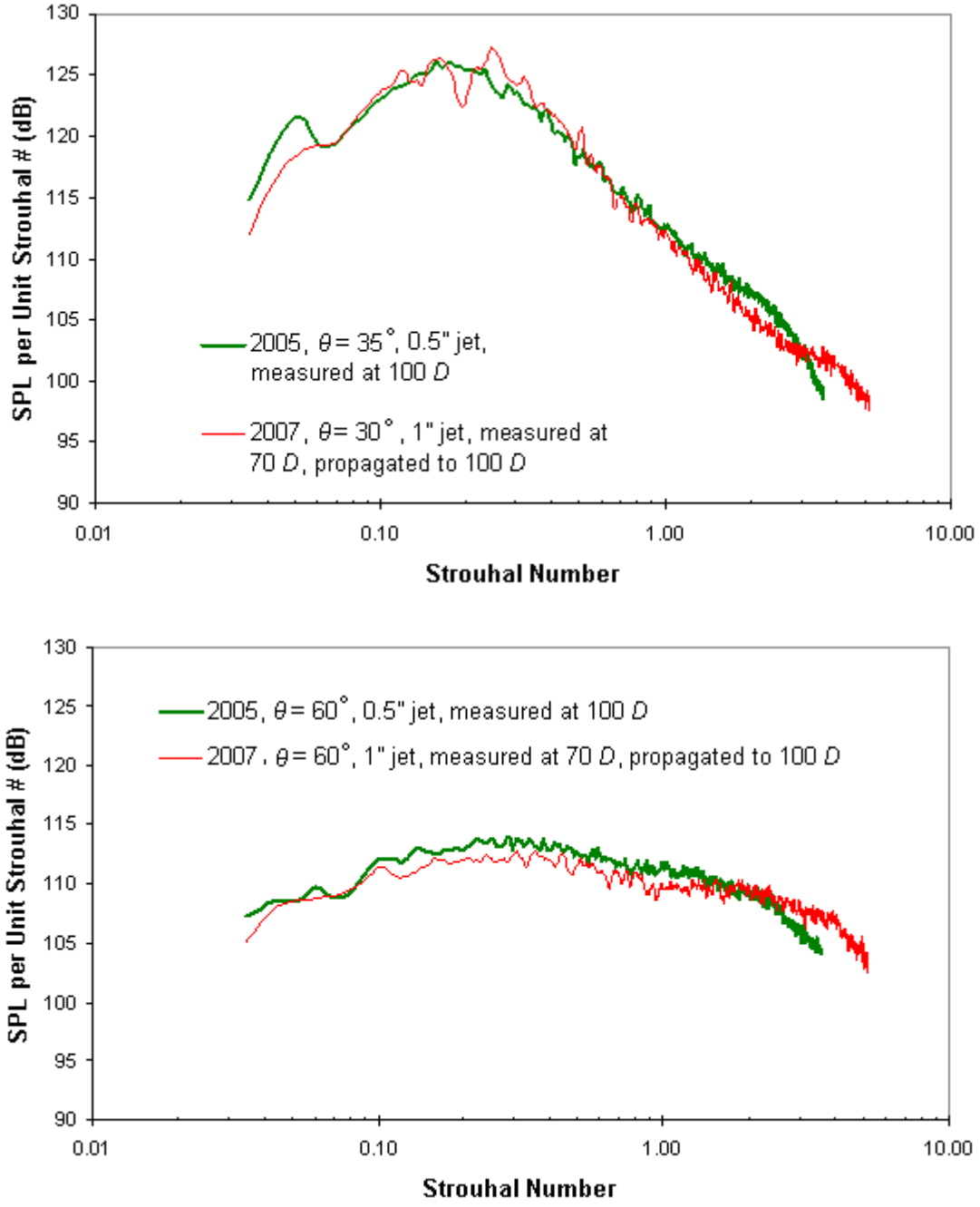

Figure **4-2**: Spectra comparison for a $M_d = M_j = 1.5$ cold jet before and after the facility upgrades for two different polar angle values.

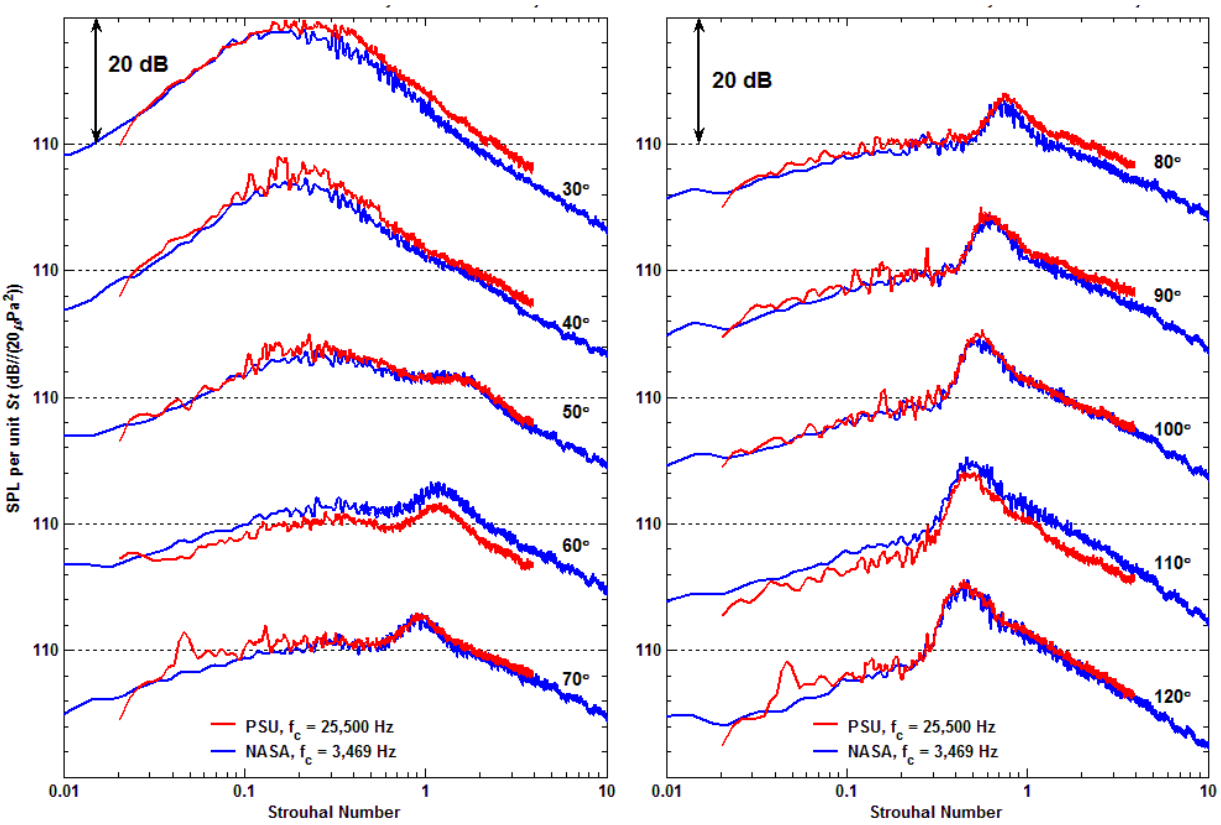

Figure **4-3**: Comparison between PSU and NASA acoustic measurements from a cold jet with a GE nozzle, $M_d = 1.5$ and $M_j = 1.64$ propagated to a distance $R/D_j = 100$. a) θ from 30° to 70°. b) θ from 80° to 130°.

4.2 Investigation of screech suppression mechanisms

4.2.1 Motivation

One of the major goals of this study was to obtain two point correlation measurements of the turbulence in shock containing supersonic jets. From such correlations, the convection velocity of the turbulent structures in the mixing layer of the jets (as well as their correlation length and time scales) can be determined. A typical cross-correlation plot, commonly called a correllelogram can be seen in Figure **4-4** for a jet operating on design at M_j = 1.5. These data were measured with an optical

deflectometer (OD) of the kind used by Doty and McLaughlin [**22**] and described in detail in section **3.3.2**. A further goal was to quantify efforts to reduce the influence of the shock screech on the data. This can be obtained by physically suppressing the screech with small disturbances in the nozzle or by suppressing it electronically (or computationally) with an appropriate processing method. The purpose is to produce a flow, and experimental data, that will be more representative of full scale military style engine exhaust jets that do not produce screech tones.

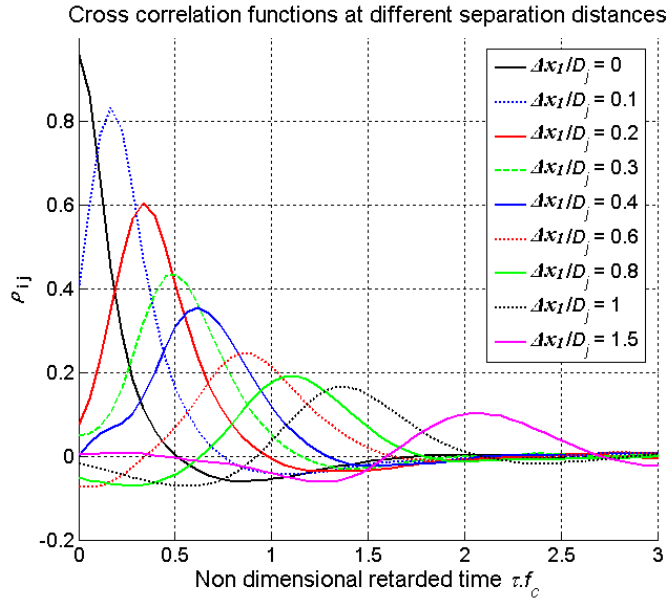

Figure **4-4**: M_d = 1.5 and M_j = 1.5 cold jet correllelogram at various probe separation distances.

When making cross correlation measurements in (laboratory) shock containing jets, the spectra are clearly dominated by (screech) tones. Such a phenomenon was already observed and reported by Kerhervé *et al.* [**49**] while making laser Doppler Velocimetry measurements in a Mach 1.2 screeching jet. However, in their measurements the screech tone was of less amplitude and therefore less influence on the data. The correllelograms obtained in a strongly screeching jet show a strong oscillation, as can be seen in Figure **4-5**. For the jet condition considered (M_d = 1.0 and M_j = 1.5), this organized feature appears to have a period of about 4 in nondimensional delay time ($\tau.f_c$) and relates to a tone seen as a line in the spectral domain. Despite its low frequency, it

still has an influence on the data that are interpreted from the small delay time portions of the plot. Thus, the estimates of the correlation times and lengths are affected by this phenomenon.

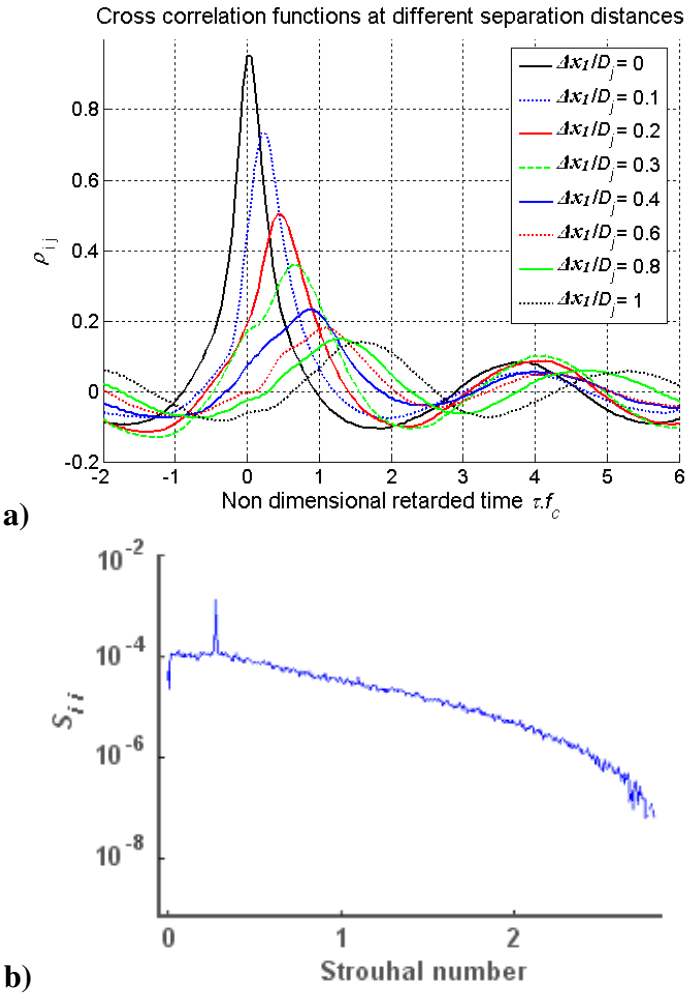

Figure **4-5**: M_d = 1.0 and M_j = 1.5 cold jet a) cross-correlation measurements at different probe separations. b) Spectrum at zero separation distance.

The screech frequency can be predicted in term of the jet conditions and the shock cell spacing, as was presented in Eq. **1.7** . However, in order to express this frequency purely in term of the jet operating conditions, it was shown by Tam *et al.* [**50**] that the following formula can be used:

$$\frac{f_s \cdot D_j}{U_j} \approx 0.67\left(M_j^{\,2}-1\right)^{-1/2}\left[1+0.7M_j\left(1+\frac{\gamma-1}{2}M_j^{\,2}\right)^{-1/2}\left(\frac{T_\infty}{T_0}\right)^{-1/2}\right]^{-1} \qquad \textbf{4.1}$$

Comparisons are made in Table **4-1** between the spectral peaks measured during a series of OD measurements and this formula, showing that the tones observed correspond to screech. Agreement is found between the prediction, the OD correlations and the acoustic measurements made at Penn State (within the accuracy of the measurements and prediction formula). Since most actual aircraft engines operating in off-design condition do not produce screech tones, suppression of the screech that occurs in typical lab experiments is closely examined in an attempt to reduce, if not remove, the effect of the tones. As mentioned above, two different approaches were considered: a physical suppression of the screech using tabs and roughness inside the nozzle lip, and post processing of the signals in order to electronically remove the unwanted tone before correlating the OD signals. The advantages and shortcomings of both methods are discussed before presenting the final results of the correlation measurements in shock containing jets.

Table **4-1**: Measured Screech Frequencies

		Fundamental screech frequency (Hz)		
M_d	M_j	Tam *et al*. [**50**]	OD	Acoustic
1.0	1.5	9,950	9,770	9,610
1.5	1.76	7,990	8,060	-

4.2.2 Acoustic assessment of screech suppression techniques

Acoustic measurements were made to show the connection to the turbulence measurements and to investigate the different screech suppression techniques. The nozzle chosen for this part of the work is a purely converging contoured nozzle (M_d = 1.0), operating off-design at M_j = 1.5. The nozzle was first run clean, without any screech suppression device in order to establish the baseline condition in the facility. Comparison of the results of these small scale experiments has been made with experiments previously performed at NASA with medium scale jets, as shown previously

in Figure **4-3**. The screech tones are clearly visible and their amplitudes are often of higher amplitude compared with other portions of the spectra, although they contain considerably less energy because of their narrow breadth.

In order to remove or reduce the screech amplitude, different concepts are investigated. Previous measurements were conducted at Penn State with nozzles with chevrons and non-axisymmetric geometries [**51**], but the focus of this study remained on devices that could be added and removed easily from the existing nozzle. Most of the concepts investigated were inspired from previous studies such as work from Norum [**12**] and from Raman [**13**]. Predominantly, tabs of various sizes and penetration angles were used, alone or in pairs, and the noise was measured at different azimuthal angles relative to the position of the tabs. Experiments were also performed with the addition of roughness inside the nozzle lip in an attempt to disrupt the feed-back loop that generates the screech tones. The effect on the sound spectra was recorded for all these different configurations, for polar angles ranging from θ = 30 to θ = 130 deg from the jet axis. Results from only two of these configurations are shown in this chapter, as representative samples of the experimental matrix. Some more tab sizes and configurations are shown in Appendix **C**, together with the resulting noise spectra.

Figure **4-6** gives the dimensions of the tab (Tab2) that produced the best screech suppression. Different configurations of the tab are also shown, including a clocking of the tab relative to the microphones and OD measurement locations. A picture of the roughness added to the lip of the nozzle is also included. Very good screech suppression was obtained with the tab, as can be seen in Figure **4-7**. A fall-off of the SPL appears at high frequencies due to a combination of microphone and amplifier response correction in the Penn State data. These issues have been recently investigated and will be reported in an upcoming AIAA paper by Kuo *et al.* [**48**]. Most of the screech disappears from the spectra with the addition of the tab; the tab also has a relatively small effect on the location of the frequency maxima of the broad band shock associated noise. Though they are not shown here (see Appendix **C**), the spectra are also moderately affected by the azimuthal location (the clocking) of the tab.

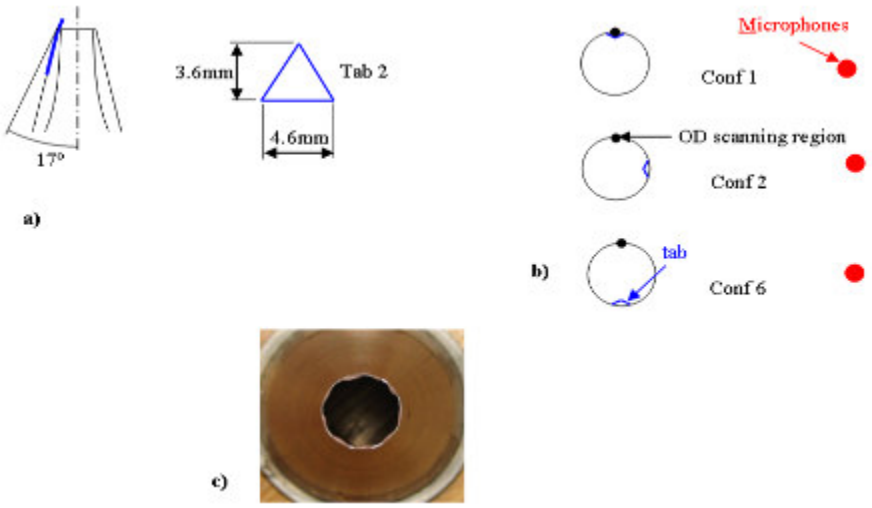

Figure **4-6**: a) Drawing of Tab2, used for screech suppression. b) Definition of the tab location with respect to the microphones and the OD scanning region. c) Picture of a nozzle with added roughness.

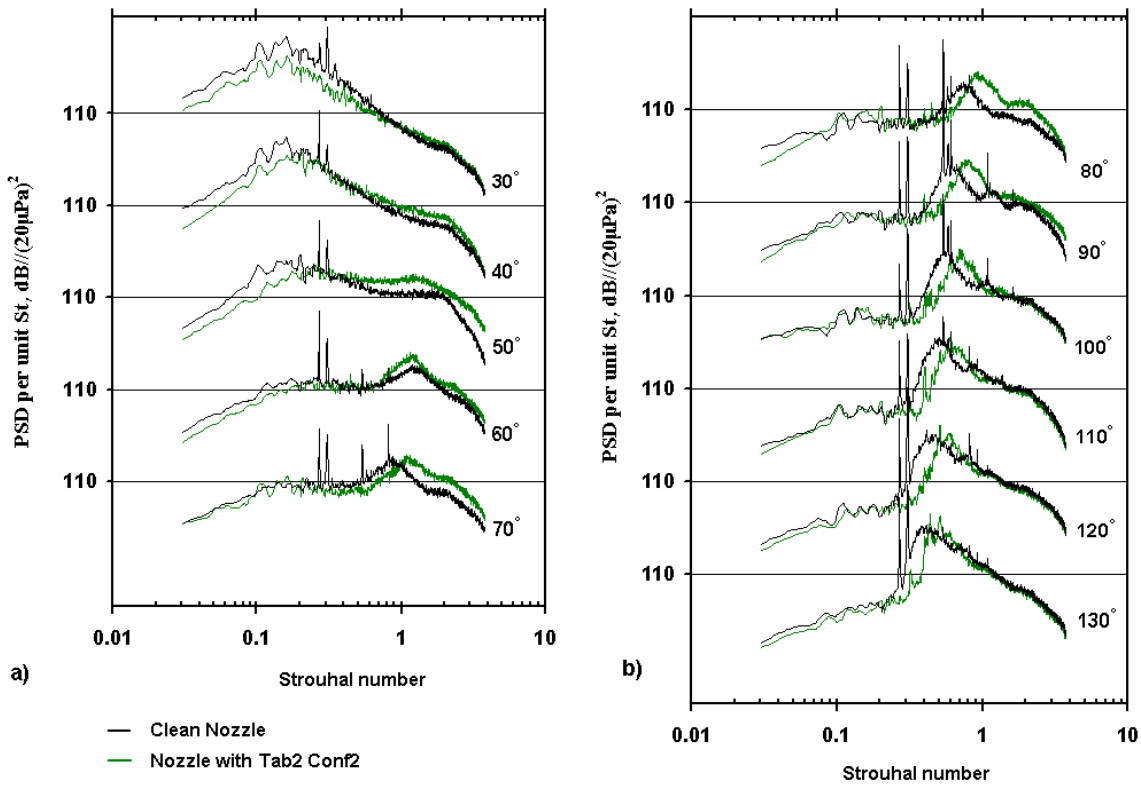

Figure **4-7**: Comparison between a clean nozzle and one with Tab2 in Configuration 2 for a cold jet, $M_d = 1.0$ and $M_j = 1.5$. a) θ from 30° to 70° . b) θ from 80° to 130°.

It is important to note that the penetration of the point of the tab extends 1.05 mm into the lip-line of the jet flow, which corresponds to 8 % of the diameter of the jet. Smaller tabs show a smaller effect on the BBSAN but do not achieve as much screech suppression, and as expected, larger tabs perform better in term of screech suppression, with less penetration angle, but affect the BBSAN much more.

Some screech suppression was also achieved by using roughness elements added to the inside of the nozzle lip. The spectra presented in Figure **4-8** show that a substantial portion of the screech amplitude is suppressed, and the effect of the roughness on the BBSAN is much less than with the addition of a tab in the flow.

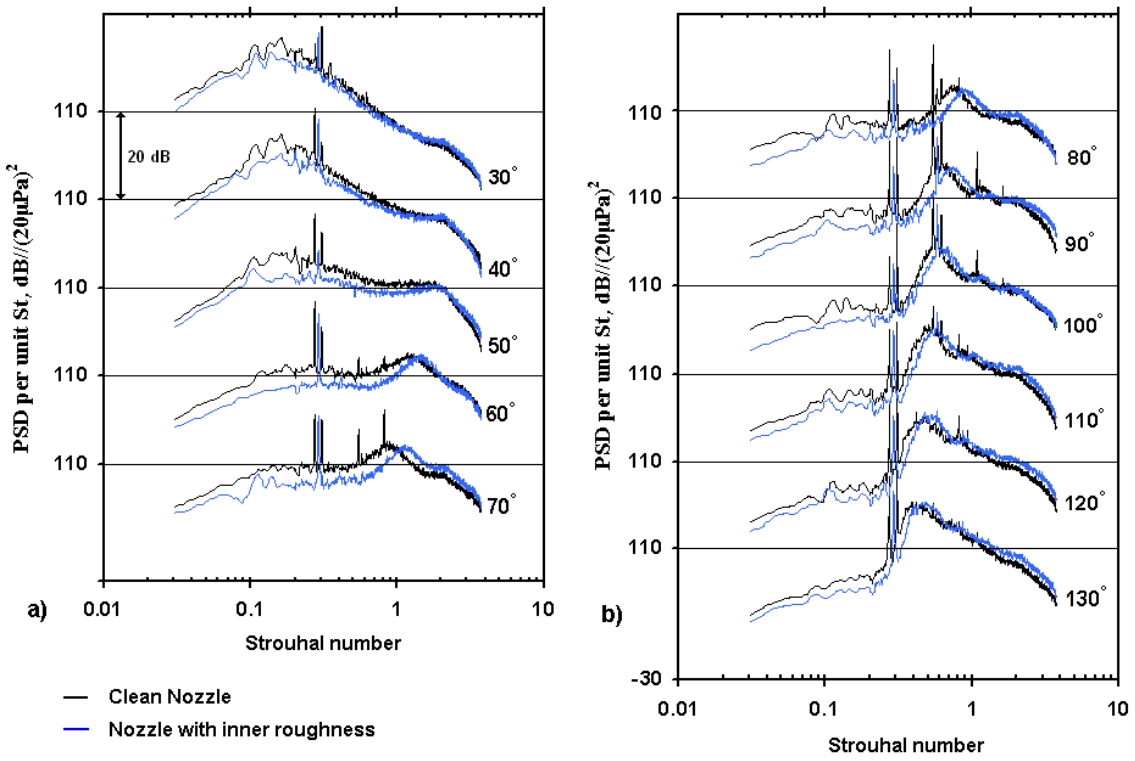

Figure **4-8**: Comparison between a clean nozzle and one with added roughness at the lip for a cold jet, $M_d = 1.0$ and $M_j = 1.5$. a) θ from 30° to 70° . b) θ from 80° to 130°.

In order to better understand the impact of these modifications on the flow, schlieren flow visualization of these different concepts have been performed and presented in Figure **4-9**. From this qualitative observation, it seems the sole effect of the roughness on the flow is an increase of the mixing layer thickness and a modest decrease

of the shock strength. However, the tab does have a much bigger impact. It significantly alters the shock cell symmetry and creates on one side of the jet a region with little visible shocks. When in configuration 2, the effect on the shock is much less visible and the mixing layer grows faster, creating a jet with an ovoid cross-section.

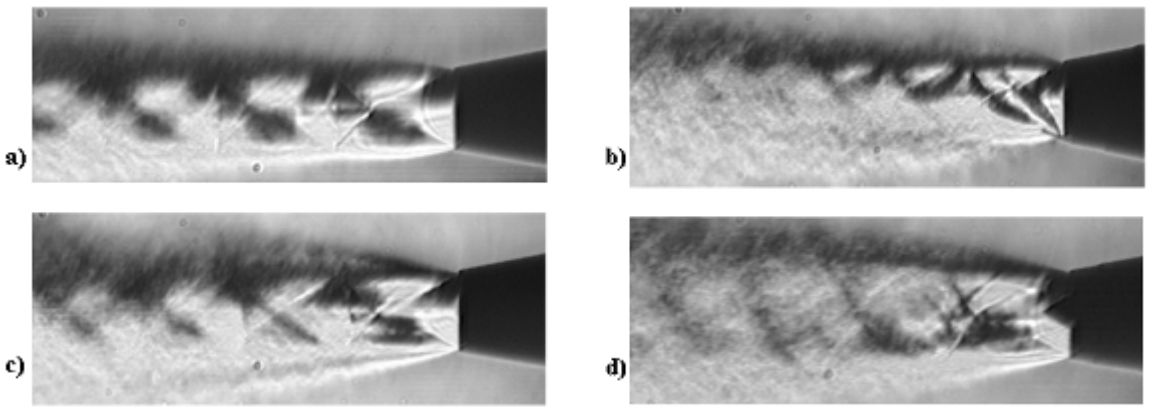

Figure **4-9**: Schlieren images of a cold jet with M_d = 1.0 and M_j = 1.5. a) clean nozzle. b) Tab2 in configuration 6. c) added roughness at the lip. d) Tab2 in configuration 2.

These screech suppression modifications, however slight, are expected to have additional effects on the OD measurements other than just a simple attenuation of the screech tone. It is expected to see the decay rates and the convection velocities affected as well. These are explored in the next section.

Finally, it is noteworthy to mention that while quality acoustic measurements are not possible while performing pitot probe surveys of the jet, the presence of the probe in the flow disrupts the feed-back loop that produces the screech tones, therefore suppressing the screech noise.

4.2.3 OD measurements in shock containing, screeching jets

Optical Deflectometry correlation measurements are made in the mixing layer of an under-expanded jet similar to the one above mentioned, with tabs and added

roughness, as well as without any screech suppression. Correlation measurements are also made with a fully expanded jet running at $M_j = 1.5$ for comparison.

The correllelogram from the fully expanded case is shown in Figure **4-10** a). Comparison can then be tentatively made to the correllelogram obtained from the under-expanded case with no screech suppression mechanism, shown in Figure **4-10** b). However, as discussed earlier, the screech tone modifies the data, affecting this comparison. In order to be able to make some comparison without having any physical alteration of the jet flow, an algorithm was written that smoothes out the cross-spectra from the PMTs where the screech tones are present, effectively removing the screech. Figure **4-11** a) shows the spectra before and after this algorithm is applied. The cross-correlation function can be computed again with the treated spectra and produces a much clearer correllelogram, as seen in Figure **4-11** b).

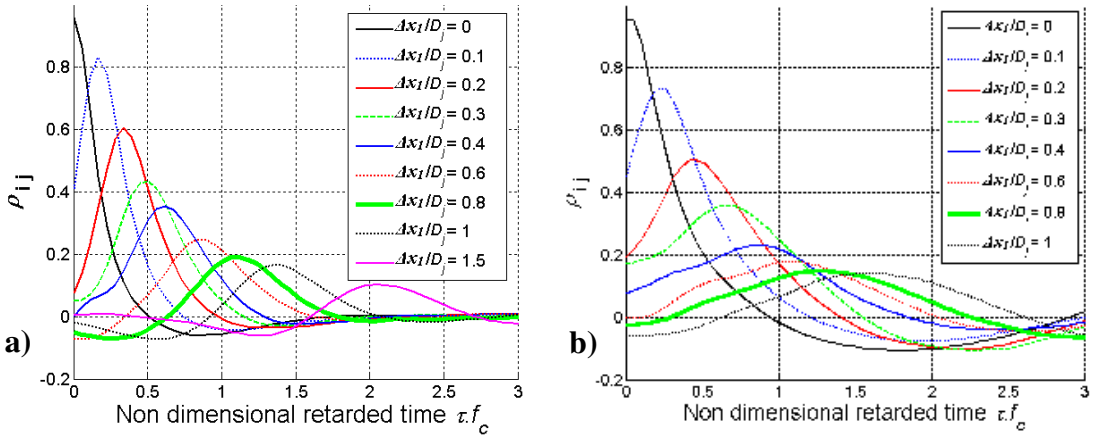

Figure **4-10**: Correllelogram of a cold jet with a) $M_d = 1.5$ and $M_j = 1.5$. b) $M_d = 1.0$ and $M_j = 1.5$ with clean lip.

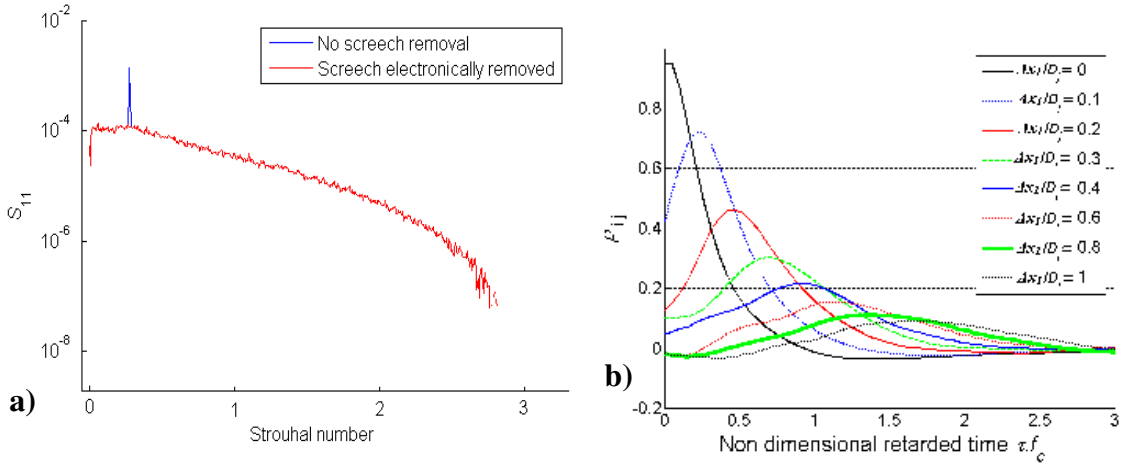

Figure **4-11**: Cold jet with M_d = 1.0 and M_j = 1.5 a) autospectra with and without electronic screech removal, b) correllelogram with the screech electronically suppressed**.**

Table **4-2** summarizes the run conditions as well as the calculated convection velocities for the data presented here. All measurements were made with a starting position $x_1 = 4.D$. In addition, some parameters need to be defined in order to make comparisons of the decay rates between the different runs. There are two parameters in addition to the convection velocity that allow for a full description of the turbulent structures. These are the length scale L_{x1} and the time scale L_τ of the convecting turbulent structure. The time scale of the turbulent structure is schematically defined in Figure **4-12** a). It can be obtained by geometric construction. The envelop of the cross-correlation functions is first drawn. Then the value of time delay for a cross-correlation peak of $1/e$ is sought on this curve. A line is drawn between this point and the starting point of the envelop: $\rho_{ij} = 1$ and $\tau = 0$. The intersection of this line with the abscissa defines the time scale L_τ. It is a measurement of how long it takes for the turbulent structure to decay. Similarly, from the correllelograms, the correlation at $\tau = 0$ can be extracted for each separation distance, producing the plot of Figure **4-12** b). A similar geometric construction allows for the determination of the length scale L_{x1}. L_{x1} is a measurement of the size of the convecting turbulent structure.

The three parameters U_c, L_τ. and L_{x1} are helpful in comparing the decay rates and the convection speed of the turbulent structures between different operating conditions.

Table **4-2**: Run Conditions and Correlation Parameters.

	Figure	M_d	M_j	U_j (m/s)	U_c (m/s)	U_c / U_j	L_τ	L_{x1} (D_j)	Screech
Fully expanded case	**4-10** b)	1.50	1.50	427.68	318.14	0.744	0.95	0.17	No
Clean nozzle	**4-10** a)	1.00	1.50	427.68	-	-	-	-	Yes
Clean nozzle	**4-11** b)	1.00	1.50	427.68	251.64	0.588	0.94	0.25	Electronically removed
Inner roughness	**4-13** a)	1.00	1.50	428.09	302.70	0.707	0.91	0.16	Reduced
Tab2 Conf1	**4-13** b)	1.00	1.50	428.09	210.35	0.491	0.88	0.21	Not measurable
Tab2 Conf2	**4-13** c)	1.00	1.50	428.09	316.43	0.739	0.85	0.19	Not measurable
Tab2 Conf6	**4-13** d)	1.00	1.50	428.09	317.42	0.741	0.86	0.28	Reduced

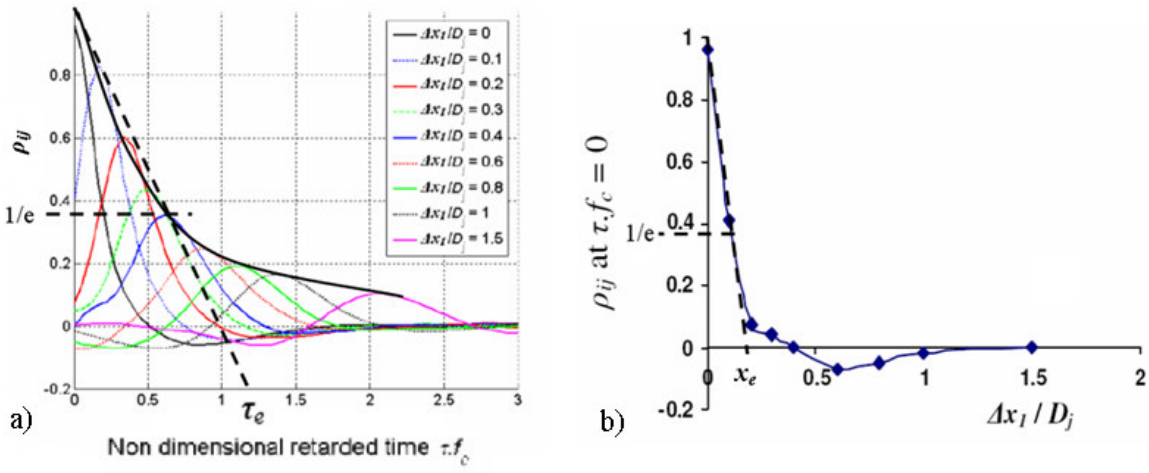

Figure **4-12**: Definition of the time scale L_τ and the length scale L_{x1} parameters from cross correlation measurements. a) Correllelograms and b) length scale measurements.

The scale parameters are not extracted from the correllogram of Figure **4-10** b) since the oscillations due to the screech tone introduce a source of error. Analysis is first made of the comparison between the scale parameters extracted from the fully expanded case (Figure **4-10** a)) and the clean nozzle operating under-expanded with electronic

suppression of the screech (Figure **4-10** b)). Firstly, the value of L_τ is very similar between the fully and the over-expanded cases. This means the decay of the turbulent structures is not affected by the presence of shock and screech in the flow. On the other hand, both the convection velocity and the length scale parameters differ between these two operating conditions. The fully expanded jet has a higher convection velocity than the shock containing case and the length scale is larger in the latter. This means that the presence of shocks induces a lower convection velocity and a larger turbulent scale: the structures present in the shock containing case are larger and travel slower in the mixing layer. However, it is not clear if the shocks are directly responsible for these effects or indirectly, via the production of screech tones. In order to know if the screech is the phenomenon responsible for these phenomena rather than the shocks, comparison should be made between a fully expanded jet $M_j = 1.5$ and a shock containing jet at the same speed that does not screech.

The same kind of correllelogram can be plotted with the different screech removal techniques in order to gain more insight on real non-screeching jet behavior. Figure **4-11** a) shows the correllelogram obtained with the roughness added inside the lip of the jet. Some screech being still present, the spectra are again electronically treated to obtain clean cross-correlations. L_τ appears to have a slightly lower value than the fully expanded case, as can be seen from the values reported in Table 3. The convection velocity is also slightly lower that the fully expanded condition and the length scale L_{x1} is the same. It was shown in section **4.2.2** that the roughness has two effects on the flow: it removes some of the screech and decreases the shock strength. So either one of these effects can explain the observations made on the decay rate and convection velocity and more experiments are needed in order to discriminate between the two.

More measurements were performed with the tab at different locations. Regarding the convection velocity, calculated from Figure **4-13** b) to d), there is a very big drop when the measurements are made at the same azimuthal location as the tab (configuration 1), which is most certainly due to the vortices shed by the protrusion of the tab in the flow. For other clocking angles of the tab, the convection velocity is very close to what is observed in a fully expanded case. The screech is mainly absent from the

correllelograms. However, careful examination of the spectra, presented in Figure **4-13** e) actually shows a small amount of screech for configuration 6. It is therefore further suppressed electronically. When looking at the schlieren image of Figure **4-9** , it becomes obvious that this side of the jet is the only location where there is a strong shock interacting with the mixing layer, hence where the feed back loop can initiate a screech tone. The time scale is changing with clocking of the tab: L_τ has higher values when measured downstream of the tab (configuration 1) than on the other side of the jet (configuration 6). L_τ is nevertheless always lower than the measurement obtained in the fully expanded jet. This means the decay of the turbulence is slightly faster in an under-expanded jet with a tab than in a fully expanded jet. L_{x1} also varies with clocking on the tab. The length scale takes the largest value when making measurement on the side of the jet opposite to the tab. The schlieren images of this jet revealed in section **4.2.2** that configuration 6 corresponds to the highest shock containing condition. Since there is shock and no screech in these configurations, the presence of screech can not be held responsible for changes in U_c and L_{x1}. Rather, the presence of shocks is most probably responsible for a larger value for L_{x1} and a lower convection velocity. This will be investigated later in Chapter **6** of this thesis.

To summarize, the convection velocity and the time and length scales of the convecting turbulent structures did not appear to be directly affected by the presence of screech in the jet. However, since the screech tones produce oscillations in the correllelograms, it is suggested that suppressing the screech with a combination of nozzle roughness and electronic processing will extract the most important turbulence properties. The strength of the shocks in a non-screeching imperfectly expanded jet seems to have little effect on the time scale of the turbulence but a strong effect on the length scale, as can be seen by examining the effect of the parameter L_{x1}. It also seems to have a strong effect on the convection velocity. For future measurements involving screech containing jets, a combination of nozzle roughness and electronic screech suppression can be used in order to produce a non screeching jet with acoustic characteristics closer to full size jet engine. As an alternative, a small tab can also be used as it does not significantly affect the BBSAN.

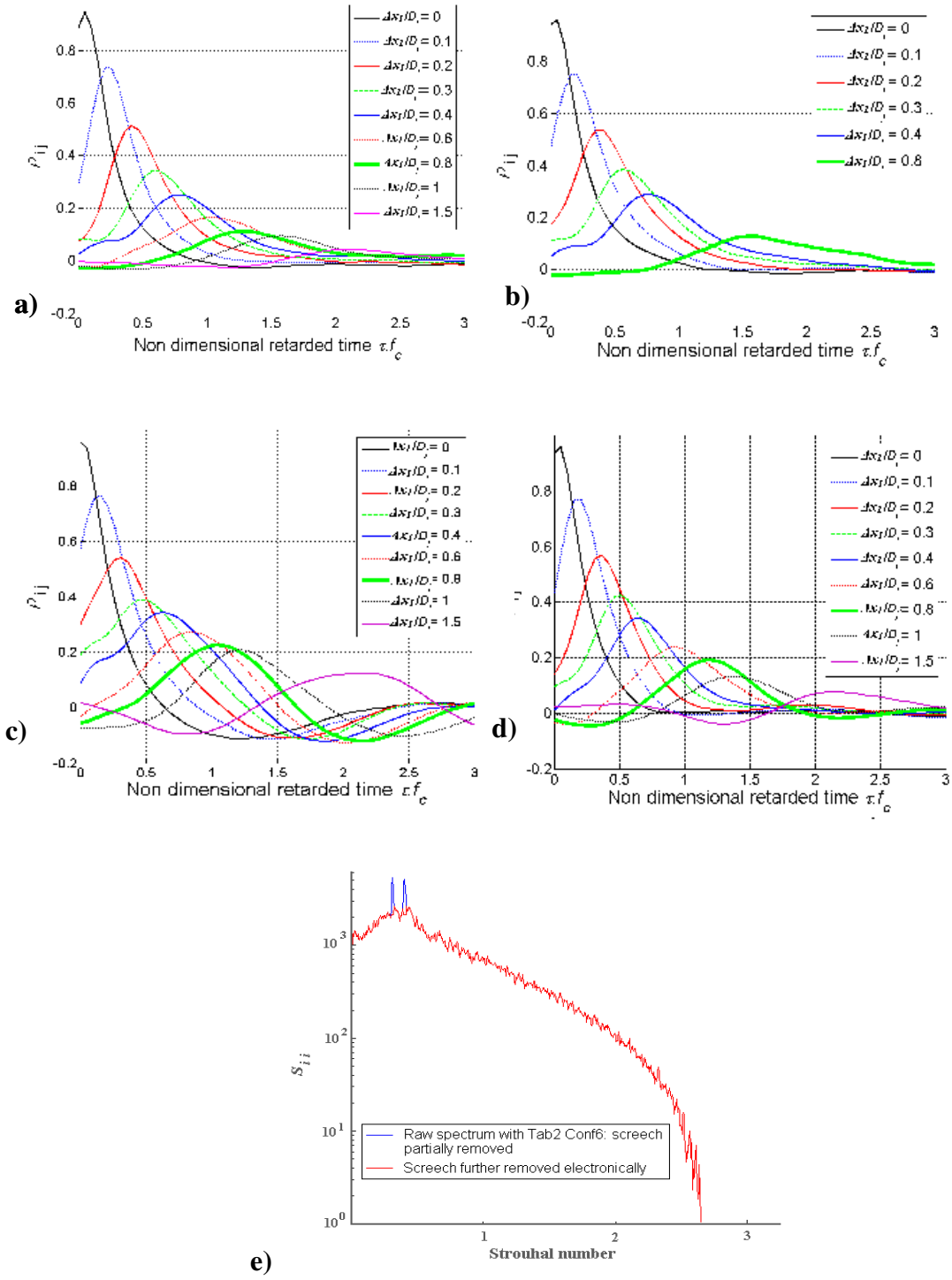

Figure **4-13**: Correllelogram of a cold jet with M_d = 1.0 and M_j = 1.5 with physical screech suppression a) roughness b)Tab2 conf1 c) Tab2 conf2 d) Tab2 conf6 e) light intensity spectra with Tab2 conf6 before and after electronic suppression of the remaining screech tones.

4.3 Optical Deflectometry qualification experiments

Before gathering optical measurements in shock containing jets and extracting data from it, a small investigation of the domain of validity of the instrument is necessary. Previous investigators [**26**], [**29**] at The Pennsylvania State University have already made qualification measurements of the setup by comparing the resulting correllelograms with hot wire measurements from Davies *et al.* [**23**]. They also uncovered limitations of the setup when the addition of helium is made to the jet. Some more qualification measurements are made in the scope of this study in order to investigate the influence of additional parameters such as the distance of the photo detectors to the knife edge, the amount of knife edge cutoff used, the diameter of the jet being investigated, and the location of the photo detectors in the image of the shear layer. It should also be noted that comparisons were made between experiments performed with Avalanche Photodiodes (APDs) and Photomultiplier tubes (PMT), since both were used in this work. Both devices proved to give near identical results as can be seen in the comparative measurements presented in Appendix **A**, where two completely different optical systems were used.

4.3.1 Effect of the distance between the knife edge and the photo detectors

When making optical measurements using a schlieren setup, many optical characteristics can reduce the quality of the measurements. One such aberration may come from the location of the optical sensors with respect to the knife edge. When trying to visualize an object that is being focused via a lens or a parabolic mirror, as is the case in the OD setup used, the thin lens formula states that for the image to be focused, the following relation between the distances should be true:

$$\frac{1}{S_1} + \frac{1}{S_2} = \frac{1}{f_m} \qquad \textbf{4.2}$$

In this equation, S_1, S_2 and f_m are defined in the diagram of Figure **4-14**.

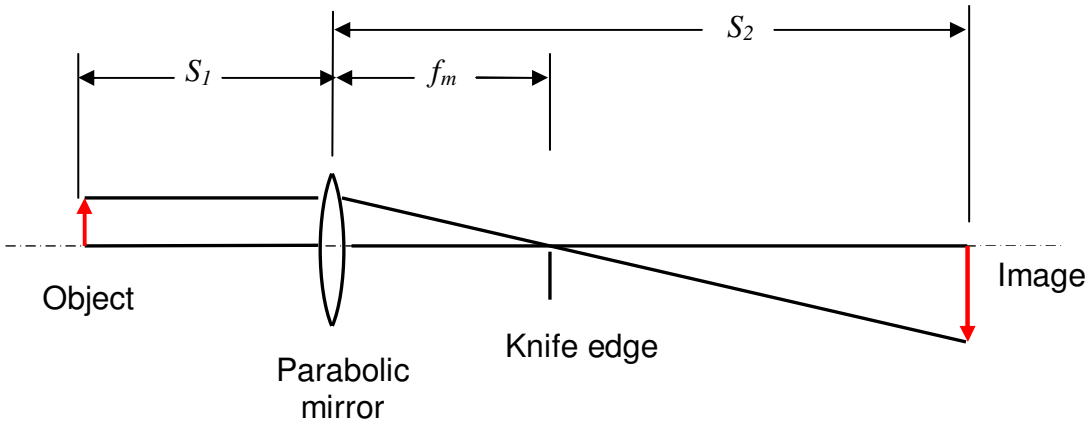

Figure **4-14**: Schematic diagram of the receiving optic.

This relation is true for an object that diffuses light in all directions. In the case of a schlieren setup, the object actually deflects one of many light beams that are initially parallel to each other, therefore the validity of this formula is in question. Measurements were hence made with the sensors set at different distances from the knife edge. Two different values of S_2 were investigated. The first value was set to 188 cm (74") since it is the distance that was used in previous experiments conducted at Penn State [**29**]. The second value investigated is the so called "focal distance", which is calculated from the formula in Eq. **4.2** with the dimensions of the setup in the Penn State facility and leads to S_2 = 210cm (82.5"). This experiment was repeated for different jet conditions and one set of representative plots of cross-correlation functions is shown in Figure **4-15**.

There is no significant change in the correllelograms, as can be seen in these plots, despite the difference in the location of the image plane. It should also be noted that moving the photo detectors down on the light path implies that the effective aperture size is decreasing: the physical dimensions of the aperture hole are kept constant while the size of the image increases.

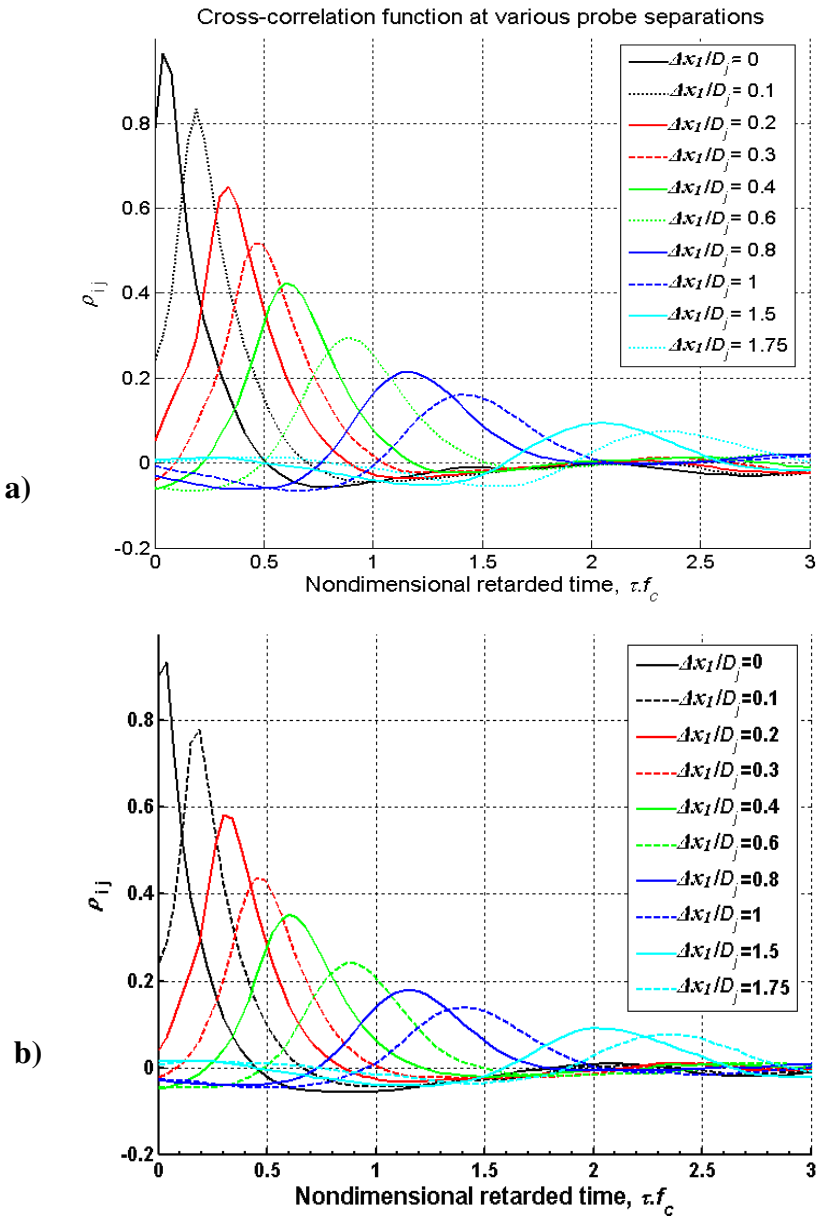

Figure **4-15**: Correllograms obtained at the lip line in a 1" jet, $M_d = 1.0$, $M_j = 0.9$ starting at $x_1/D_j = 4.0$. a) sensors at 26" from knife edge, b) sensors at 34.5".

The region of the flow scanned is therefore decreasing by a ratio equal to the ratio of the two values of S_2. Actually, for the 0.5 mm aperture holes used, the effective area scanned in the object plane decreased from 0.36 mm to 0.27 mm. Nevertheless, the correllelograms are unaffected by this, proving the robustness of the setup.

4.3.2 Influence of the knife edge cut off settings

As it was shown in section **3.3.1.3**, schlieren images taken with different knife edge settings suggest a corresponding filtering of the density gradients observed. More knife edge means that a larger density gradient is required to obtain the full illumination, and that in turns refer to the largest structures. A reasonable assumption would hence be that this affects the correlation measurements as well.

Therefore, cross-correlations measurements are made with different knife edge settings, and are shown in Figure **4-16** . The correlation presented in this figure is made at zero separation distance ($\Delta x_1 = 0$) for different knife edge settings. The knife edge cutoff percentage corresponds to the percentage of the image of the light source being obstructed by the knife edge. The cross correlation function reaches a peak as soon as the knife edge is set at a minimum of 60%. Any less knife edge cutoff produces a drop of the measured correlation between the two sensors. The same observation can be made when looking at the coherence function between the signals, with a coherence that drops as soon as the knife edge setting is lower than 60%.

However, when performing correlation measurements in a jet, typically, one of the sensors is moved downstream by a distance Δx_1. When going further downstream, the amount of knife edge required for optimum correlation increases, as can be seen in the correllelograms of Figure **4-17**. The best correlation is obtained for a large amount of knife edge cutoff, close to 100%. On the other hand, the retarded time at the correlation peak does not change. As mentioned earlier in section **3.3.1.3**, the amount of knife edge relates to specific turbulence scales. Therefore, the higher correlation obtained with higher knife edge settings underline the fact that the largest scales are propagating further (and decay slower). For proper measurement of the convection velocity in following experiments, the knife edge is set by trying to maximize the coherence (observed through a digital signal analyzer) of the two sensors with some separation distance Δx_1.

a)

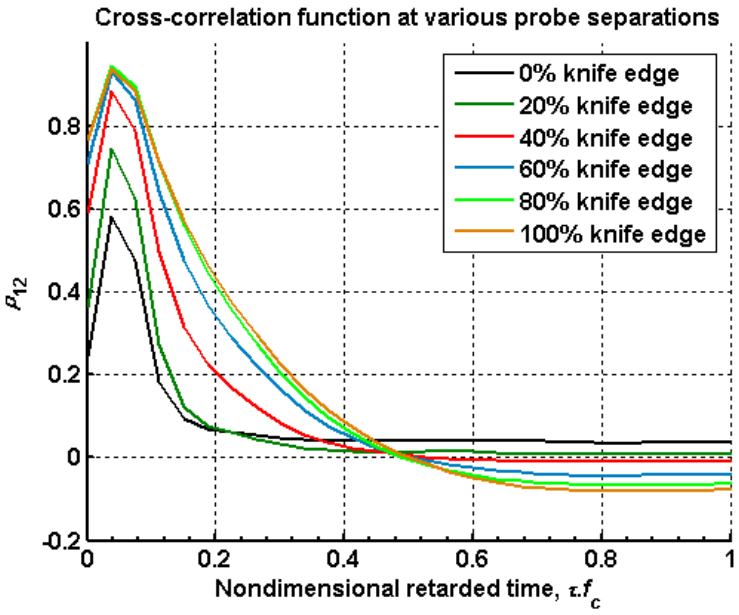

b)

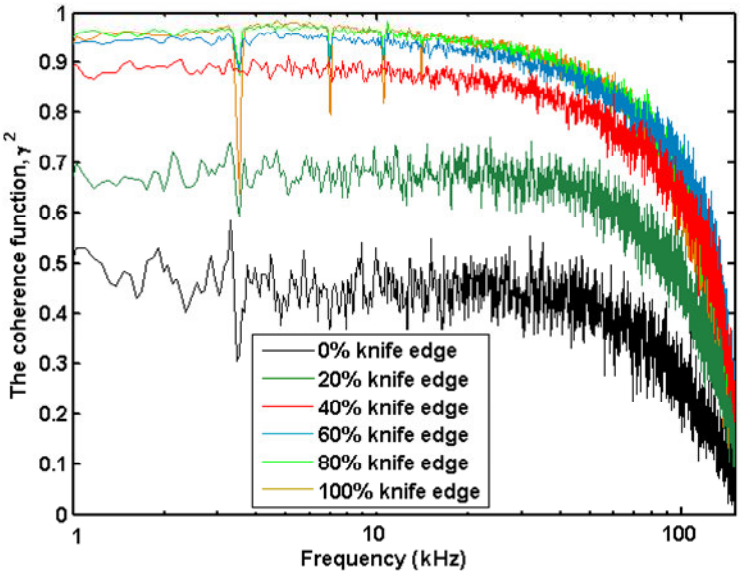

Figure **4-16**: a) cross correlation functions and b) coherence, obtained with different knife edge settings in a $M_d = 1.0$, $M_j = 0.9$ 1" jet at $x_1 / D_j = 4.0$ and with $\Delta x_1 / D_j = 0$.

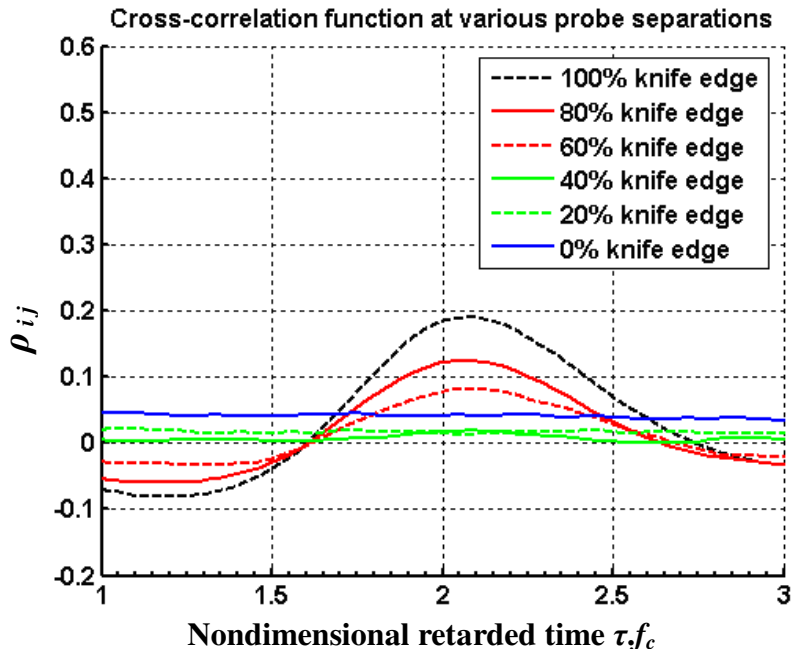

Figure **4-17**: Cross correlation functions obtained with different knife edge settings in a $M_d = 1.0$, $M_j = 0.9$ 1" jet at $x_1 / D_j = 4.0$ and with $\Delta x_1 / D_j = 1.5$.

Finally, it should be noted that the power of the light source used for illumination is important. Typical measurements are made using the light source at its full power setting (72W). Dividing that power by two to 36W still leads to accurate measurements, but decreasing it further leads to a drop of the correlation between the two photo detectors as the signal to noise ratio becomes too low. Maximizing the intensity of the point source is therefore crucial.

4.3.3 Influence of the jet diameter on the correlation measurements

In an attempt to produce more accurate measurements, optical deflectometry measurements were made in a 1" diameter jet. By increasing the diameter of the jet, the length scale of the turbulent structures decreases, as shown in the correllelograms of Figure **4-18**. By inspecting the coherence, shown in Figure **4-19,** one can see that when plotted against Strouhal number, the curves have a similar shape between measurements

made in a 0.5" and a 1" jet. However, there is a net drop of the coherence, which is presumably due to the integration length being greater when the jet diameter increases. A similar drop in the correlation was observed by Petitjean [**29**], comparing a round jet with a wider rectangular jet.

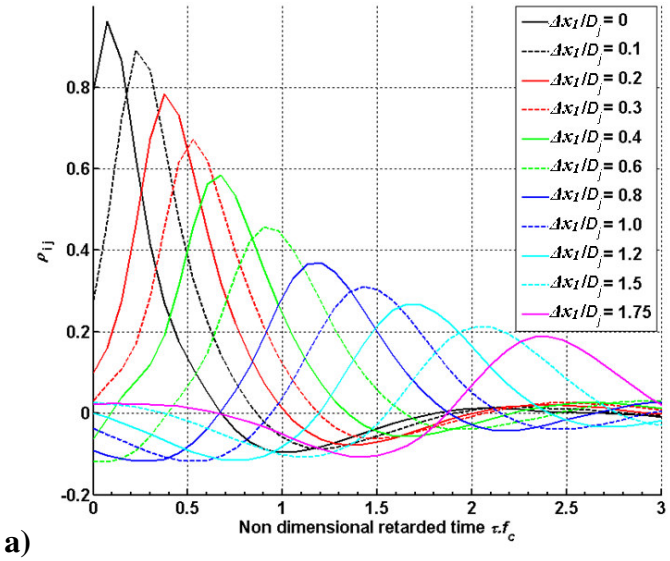

a)

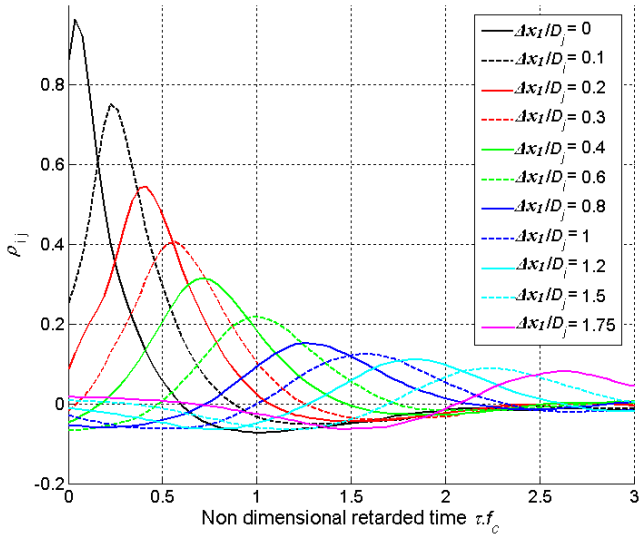

b)

Figure **4-18**: Correllelograms measured in a $M_d = 1.0$, $M_j = 0.9$ jet a) 0.5" diameter, b) 1" diameter.

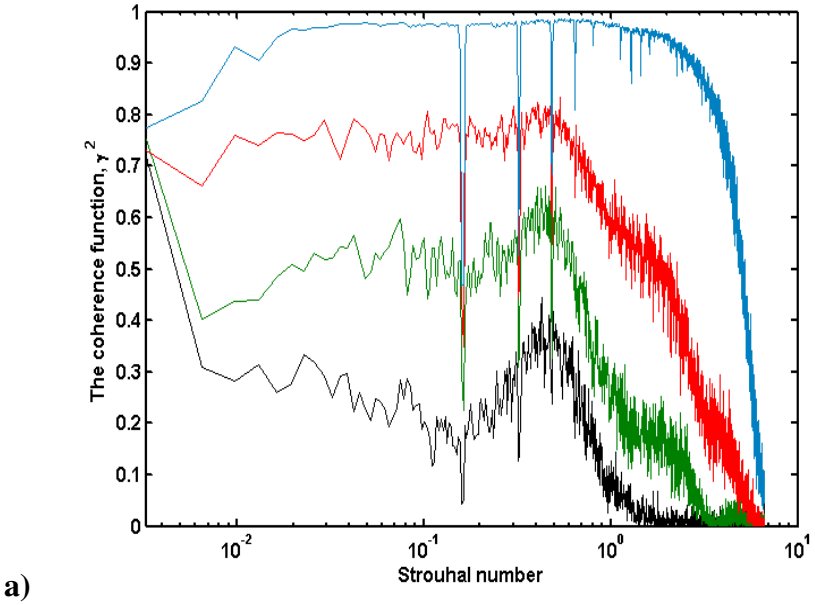

a)

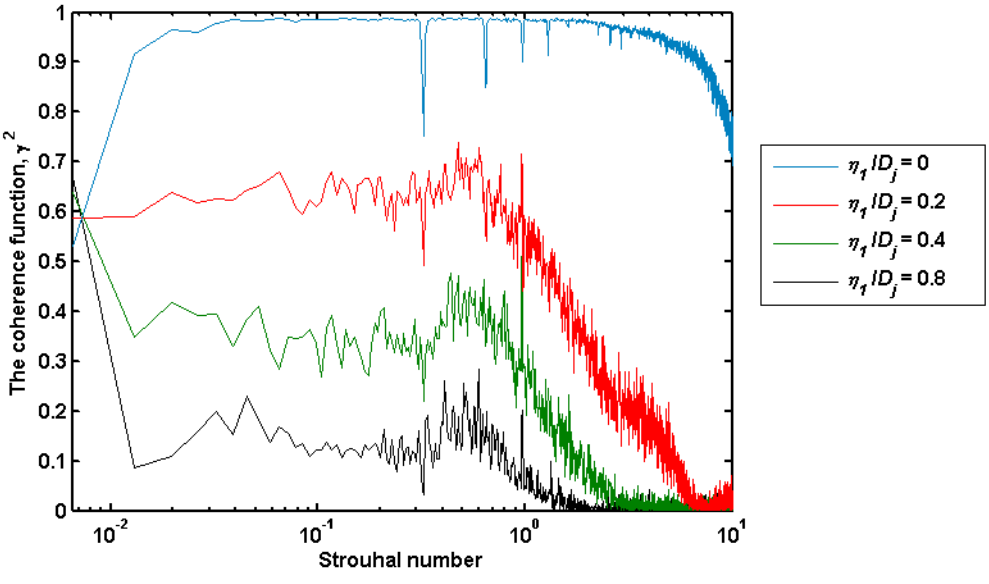

b)

Figure **4-19**: Coherence between the optical signals in a M_d = 1.0, M_j = 0.9 jet, a) 0.5" diameter, f_c = 22.5 kHz, b) 1" diameter, f_c = 11.3 kHz.

4.3.4 Limitations due to the integration effect of the OD setup

When performing correlation measurements with the Optical Deflectometer (OD), the photo sensors detect fluctuations of light intensity at one point in the image. However, the light beams cross the entire jet, leading to the measured signals being an integration of all the light fluctuations along the path of the light beam. When performing measurements in the shear layer, where the integrated length is kept presumably small, the results can easily be interpreted in terms of the convection velocity of the structures in the shear layer. However, when the focus is made lower than the shear layer, it is less easy to link the measured light fluctuation to the density fluctuations in the jet.

An assessment of the importance of the radial location when performing axial correlations has thus been performed. For that purpose, cross-correlation measurements were made at 4 diameters downstream of the nozzle exit, along, above and below the jet lip line. Figure **4-20** shows the correllelograms obtained for three different representative radial locations.

These measurements indicate a lower convection speed outside the mixing layer, but no change when moving inside the jet as summarized in Figure **4-21**. However, when moving inside the shear layer, the convection velocity is expected to increase while the turbulence intensity decreases. Such results were observed by Davies *et al.* **[23]** with hot wire anemometers. Thus the OD measurements do not represent what physically happens at the radial location that is investigated. That can be explained by the fact that the optical measurement actually measures the fluctuation of density gradient across the whole jet, as represented in the schematic of Figure **4-22** . Therefore, when the sensors are placed at a radial location located below the lip line, the density gradients traversed by the light beam being greater in the mixing layer than below it, they produce a larger deflection and dominate the measured signal. Consequently, the convection velocity measured corresponds to the turbulent structures located in the mixing layer at some out of plane azimuthal angles rather than that of the turbulent structures with lower density gradients located closer to the inside edge of the mixing layer.

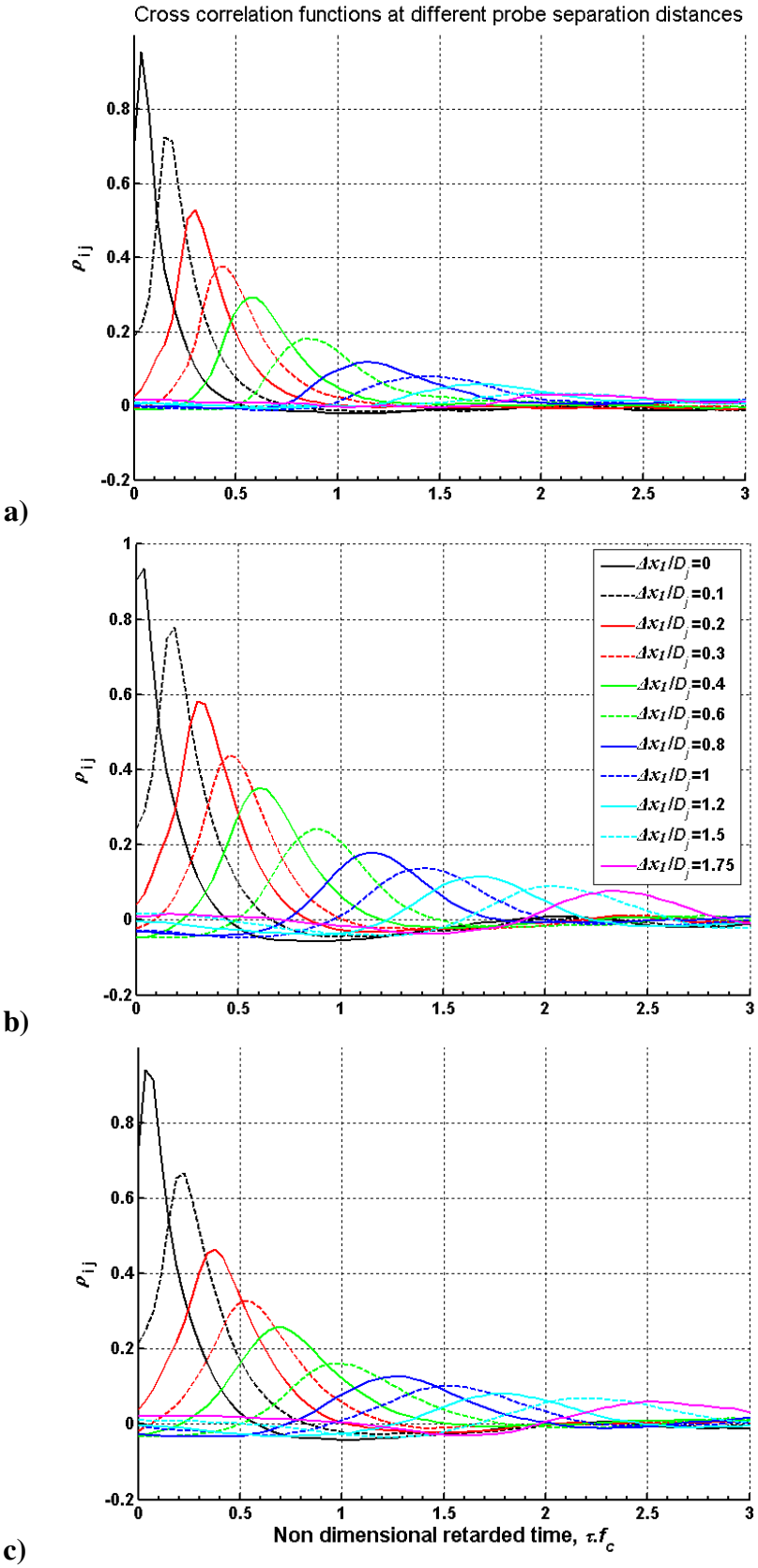

Figure **4-20**: Correllelograms for a 1" jet, M_d=1.0, M_j= 0.9 starting at $x_1 / D_j = 4.0$ and different radial locations: a) $x_2 /D_j = 0.4$, b) $x_2 /D_j = 0.5$, c) $x_2 /D_j = 0.6$.

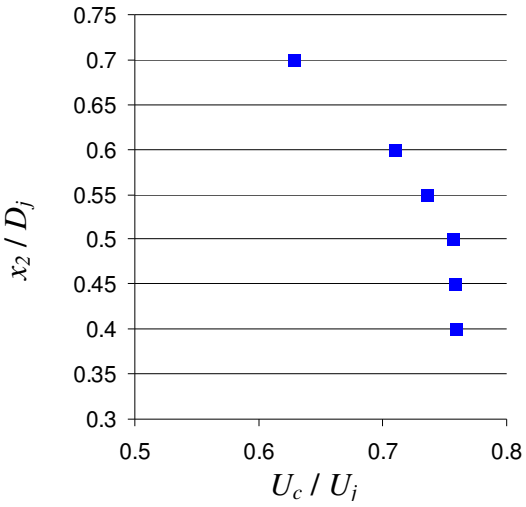

Figure **4-21**: Convection velocities for a 1" jet, M_d=1.0, M_j=0.9 starting at $x_1/D_j = 4.0$ from correllelograms obtained at different radial locations.

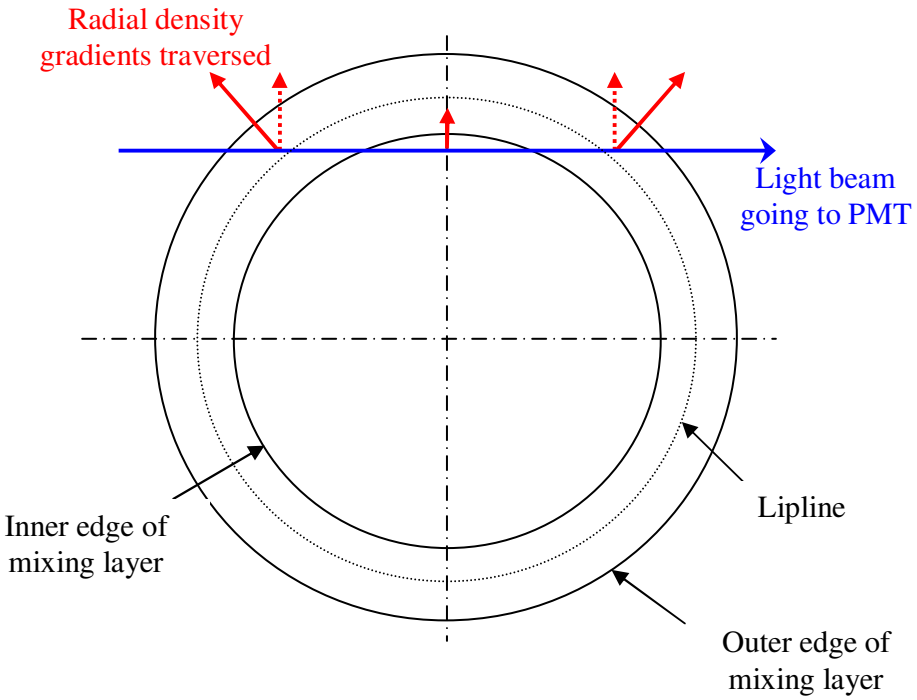

Figure **4-22**: Schematic cross-section of a jet and representation of the density gradients measured by the optical deflectometer.

In order to remain meaningful, the convection velocity measurements can thus only be obtained on or outside the lip line. Furthermore, in order to make sure that the measurements do not under-predict the convection velocity by being slightly outside of the jet, measurements should be made at radial location $x_2 / D_j = 0.48$.

4.4 Pressure survey calibration measurements

In order to gather good quality pressure data in the jets, some qualification experiments are required with the pressure probe apparatus. First of all, measurements made with the pitot rake are compared with single probe measurements in order to make sure that there is no probe interference with the flow. Then, in order to be able to simultaneously move the probe and acquire the pressure and still obtain reliable data, calibrations are made with different movement speeds. This provides a recommended highest allowable speed that will be used in order to make time efficient pitot probe measurements in helium-air mixture jets. Finally, a close look is taken at static pressure measurements and the problems associated with them.

4.4.1 Pitot rake qualification measurements

In order to validate the measurements obtained from the pitot rake, the pressure output from each individual probe was examined. Acquisition was made at different downstream locations of a shock containing jet, where high pressure gradients occur and where shocks are most likely to affect the results from one probe to another. The resulting outputs are plotted in Figure **4-23** for each pitot probe. As can be seen, the measurements from each probe are in perfect agreement with the others. These measurements also perfectly overlap with results obtained with a single pitot probe (not shown in this figure).

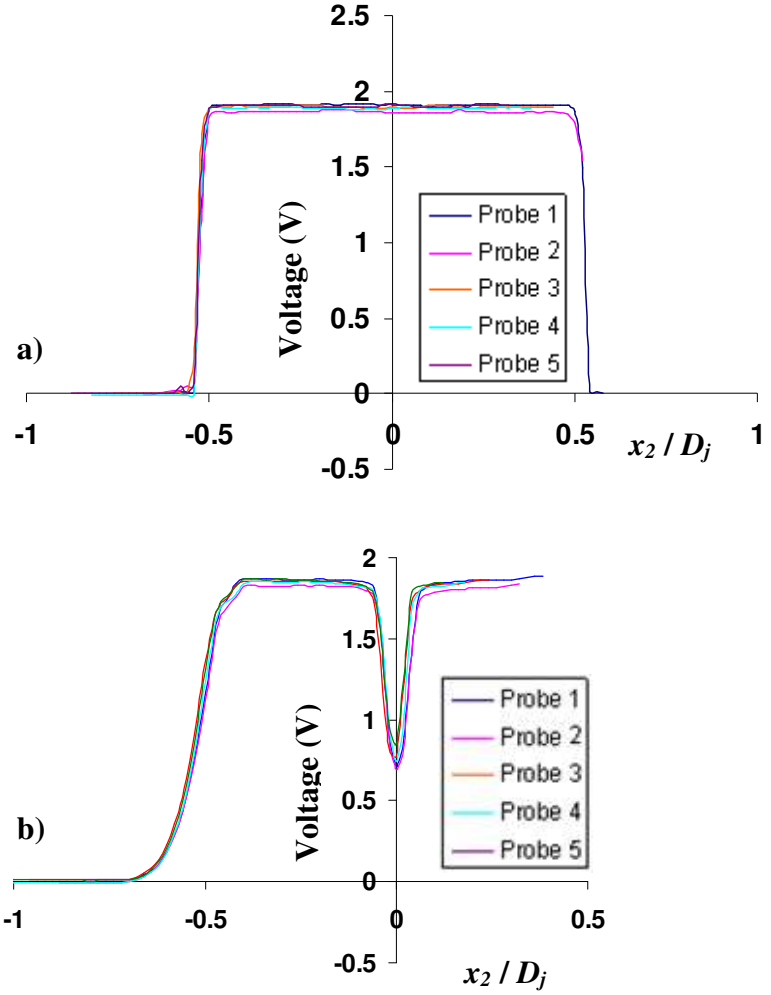

Figure **4-23**: Voltage outputs from different probes in a $M_d = 1.0$, $M_j = 1.5$, 1" jet at a) the exit plane, and b) $x_1 / D_j = 1.5$.

4.4.2 Dynamic acquisition calibration

Whenever the traverse of the jet needs to be done in a time efficient manner, the probe can be moved while simultaneously acquiring pressure data. However, due to the limited frequency response of the pressure transducers, extra care needs to be applied when making such measurement. The distance of the tubing between the probes and their respective pressure transducer is kept to a minimum in order to increase that time

response. Calculation of this time response using the volume of air contained between the tip of the probe and the diaphragm is possible. However, since the exact volume is difficult to measure precisely, the time response was determined experimentally by doing dynamic measurements at different speeds and comparing with static acquisition results (in which the probe traverse is stopped for every measurement).

Figure **4.23** shows the voltage outputs from a pressure transducer during a traverse of the shear layer at different traversing speeds. These measurements were performed in a 2.54 cm (1") diameter converging (M_d = 1.0) jet running under-expanded at M_j = 1.5. In this figure, comparison is made between the static and dynamic acquisition with the probe moving toward the center of the jet at 1.5 diameters downstream of the exit plane. From these results, it is obvious that for motor speeds higher than 100 steps per second, the dynamic acquisition measurements are lagging substantially relatively to the measurements acquired when the probe is not moving. This results in an under-prediction of the jet speed through the mixing layer.

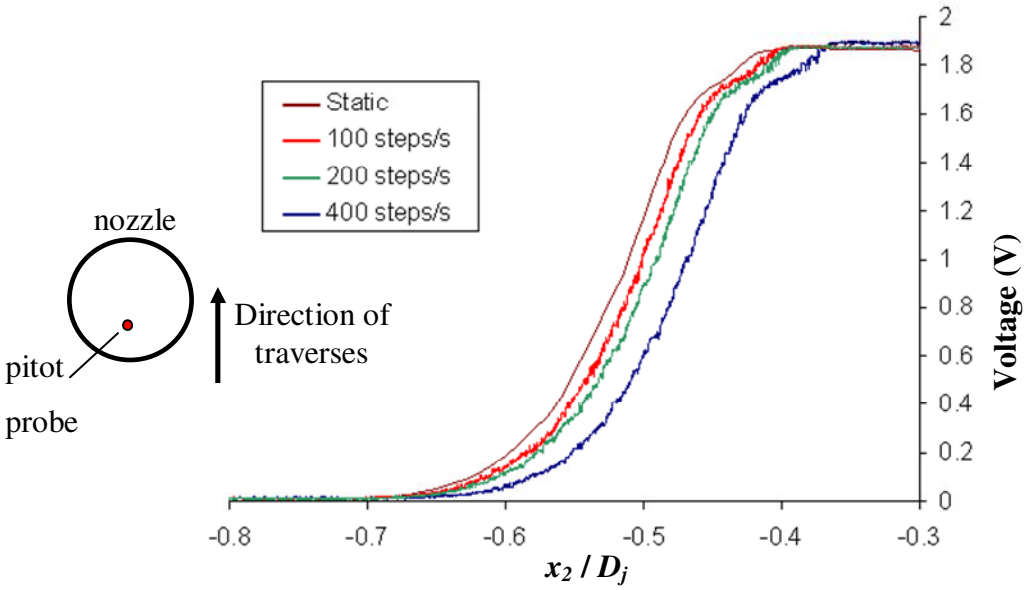

Figure **4-24**: Voltage outputs from a pressure transducer during a traverse of the shear layer at different traversing speeds toward the center of a M_d = 1.0, M_j = 1.5, 1" jet.

Figure **4-25** presents the same kind of comparison, however the probe was moving toward the outside of the jet and the measurement was performed at the exit

plane of a 1.27cm diameter converging (M_d = 1.0) jet running under-expanded at M_j = 1.5. Very similar observations can be made, with the signal measured by the dynamically moving probe lagging compared to the profile acquired statically. This results in a slight over prediction of the speed of the jet in the mixing layer region. Once again, the fastest speed adequate for good experimental uncertainty can be evaluated to 100 steps per second. Therefore, for further experiments in helium-air mixture jets, the movement of the probes will be set to 100 steps per second. This corresponds to a speed of around 0.6 mm.s^{-1} (0.025 in.s^{-1}). Higher speeds could also be used if a correction is developed from these experiments.

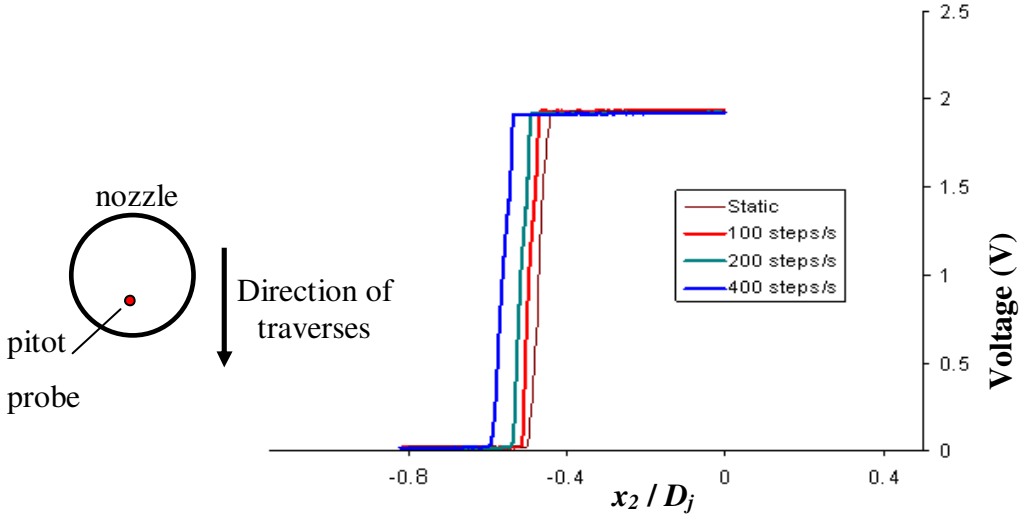

Figure **4-25**: Voltage outputs from a pressure transducer during exit plane traverses of the shear layer at different speeds toward the outside of a M_d = 1.0, M_j = 1.5, 0.5" jet.

4.4.3 Static pressure measurements

In order to uniquely specify all properties of a compressible flow, knowledge of three gasdynamic properties is required. Using the isoenergetic approximation of constant jet stagnation temperature provides the total temperature T_0 in the jet. The other quantity available is the pitot pressure and it can be combined with the static pressure to compute the local Mach number using Eq. **3.13**. For this purpose, an accurate measurement of the local static pressure P_1 is desirable.

Static pressure measurements were gathered with the static pressure probe described in section **3.4.2.** The measurements were performed with a converging contoured nozzle through which an under-expanded jet of M_j = 1.5 is produced. Figure **4-26** shows a detailed profile comparison of P_1/P_{to} between experimental data and CFD simulations. The static pressure shows very good agreement in the mixing layer and at all x_1/D_j locations smaller than x_1/D_j = 0.8. However, around the centerline, for x_1/D_j = 0.8 and greater, there are some discrepancies between the numerical and experimental solutions. Examples of the effect of this discrepancy in the static pressure measurements on the calculated Mach numbers can be found in section **5.2.2** and **5.3.3** of this thesis.

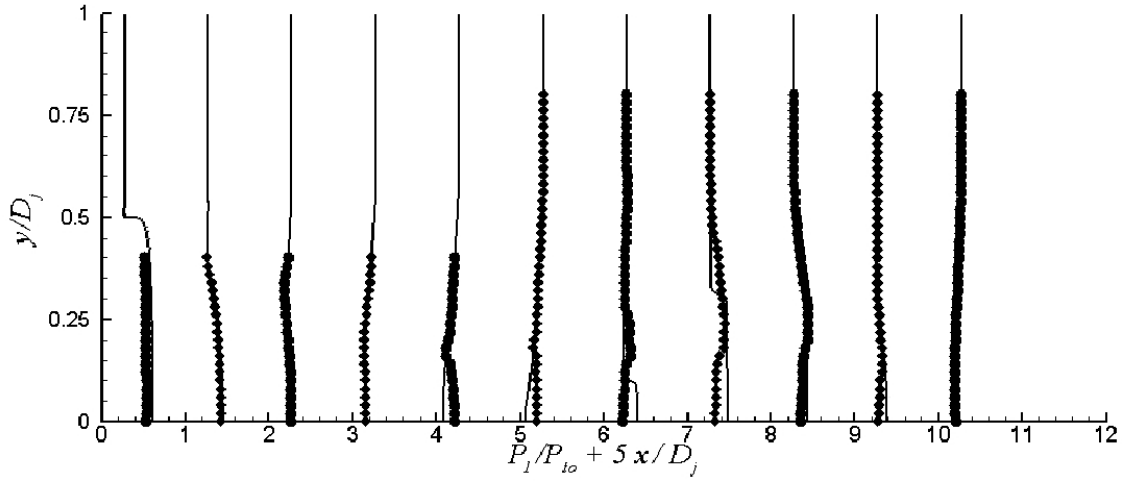

Figure **4-26**: Comparison between experimental (dots) and numerical (lines) P_1/P_{to} of a M_d = 1.0, M_j = 1.5, converging nozzle. Each set of data is separated by x_1/D_j = 0.20 starting at x_1/D_j = 0.0 at the left and stopping at x_1/D_j = 2.0 on the right.

The small discrepancies observed can be attributed to different phenomena. It is likely that the oblique shock created by the tip of the probe interacts with other flow gradients (such as the mixing layer or other shocks) and reflects back to the probe's body before the location of the static pressure hole. This can produce an error difficult to predict due to the complex shape of the mixing layer and the three dimensionality of the problem. The schlieren image shown in figure **4-27** b) offers a good visualization of this phenomenon. In this image, one can clearly see the shock wave created at the tip of the probe being reflected on the shear layer and hitting back the probe at the location of the

pressure hole. On the other hand, the presence of the probe also produces a large disturbance of the shock cell geometry when located closer to the center of the jet, as can be seen when comparing figure **4-27** a), c) and d). The shock cell pattern naturally occurring in a jet running under these conditions has been completely altered once the probe is close to the jet axis. Additionally to the shock attached at the tip of the probe, one can also notice the apparition of a shock along the body of the probe very similar to what can be observed in transonic flows.

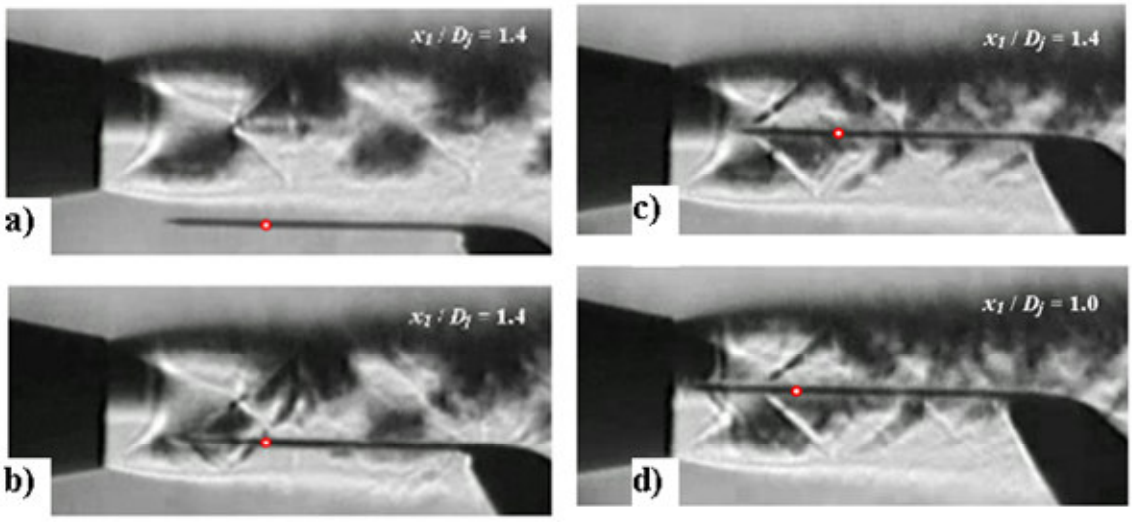

Figure **4-27**: Schlieren images of static pressure probe in a $M_d = 1.0$, $M_j = 1.5$ jet. a), b) and c): probe at $x_1/D_j = 1.4$, d) probe at $x_1/D_j = 1.0$, $D_j = 0.5$".

While all these modifications in the flow pattern would not influence pitot probe measurements, which are obtained at the tip of the probe, it does affect the results from a static probe since the holes for pressure measurements are located downstream of the tip of the probe. Therefore, in order to produce better quality predictions of Mach number and velocities, the static pressure measurement data are not relied on. Rather, the third required gas dynamic property is obtained from two assumptions: inside the shear layer and outside of the jet, the local static pressure is assumed equal to the ambient pressure, and inside the jet, assumptions are made on the value of the local total pressure P_{t1}. Only a few data points are presented later in this thesis with Mach numbers calculated from static pressure measurements.

Chapter 5

Mean flow field surveys in supersonic jets

5.1 General approach

5.1.1 Motivation

For the purpose of predicting the aeroacoustic properties of jets of various geometries, both the mean and the fluctuating parts of the flow are important to measure and compare with analytical and computational predictions. The mean flow in noise generating jets has been intensively investigated in the past years, with significant contributions from Troutt and McLaughlin [**16**]. However, measurements in shock containing jets have been limited and therefore the database needs to be extended.

Current research at Penn State aims to use three-dimensional as well as axisymmetric RANS-CFD data in the development of a BBSAN noise model, which will be less dependent on empirical data and be coupled closely to steady CFD simulations. Therefore, the ability to generate accurate Computational Fluid Dynamic (CFD) data needs to be assessed before being able to develop a new model to predict Broadband Shock Associated Noise (BBSAN) in supersonic jets.

This part of the thesis focuses on experimental results from pressure probe measurements in shock free and shock containing jets issued from nozzles of various geometries. Some of these pitot and static pressure probe measurements were compared with CFD simulations at various downstream and cross-stream locations. Quantitative comparisons were made with profiles and contour plots of the local Mach number, M_1 and local static pressure, P_1. Schlieren images of the jets were also compared with density gradients calculated from the numerical simulation data base.

5.1.2 Data processing methods

For the round under and over-expanded jet measurements, the static pressure was initially measured experimentally, and therefore, the Mach number was estimated from P_p and P_1 through Eq. **3.1**. Discrepancies appeared in these measurements and are presented and explained in section **4.4.3**.

As described earlier in section **3.4.1**, for the remainder of the data, the processing was decomposed into two domains. In the core of the jet, the normal shock relation (Eq. **3.15**) is used in order to relate the pitot pressure $P_p = P_{t2}$ and the local total pressure P_{t1} to the local Mach number M_1. Outside of the jet and in the mixing layer, the isentropic formula is used (Eq. **3.14**), relating M_1 to P_{t2} and the local static pressure P_1.

In order to use these equations, assumptions were made on both the values of P_{t1} and P_1. The first assumption made was that P_1 in the mixing layer and outside of the jet could be assumed to be equal to the atmospheric pressure P_∞. Then, the value of P_{t1} was assumed to be constant and equal to the total upstream pressure P_{to} throughout the jet and until the end of the potential core. However, after going through one or more oblique shocks, the total pressure drops locally and P_{t1} would need to be corrected for that. Calculation of that pressure drop for a 45° oblique shock with an incoming Mach number of 1.5 was made and gave a ratio of 0.9998 between the total pressure before and after the shock. While such a ratio leads to a discrepancy of 0.06 in the Mach number, this fluctuation in the value of the total pressure is well beyond the accuracy of the measurements made. Therefore, as a first approximation, the Mach number was first calculated through the whole length of the jet assuming that $P_p = P_{to}$ is constant, except in the mixing layer.

From these values of Mach number, the local speed U_1 can be computed. Using the isentropic formula the expression for U_1 can be shown to be as follows:

$$U_1 = M_1 \left[\gamma \times R \times T_\infty \times \left(1 + \frac{(\gamma - 1)}{2} M_1^{\,2} \right)^{-1} \right]^{1/2} \qquad \textbf{5.1}$$

Finally, in order to compare the profiles at different downstream locations the velocity profiles can be normalized in a manner similar to what was performed by Doty and McLaughlin [**19**] and by Kinzie and McLaughlin [**18**]. The velocity is plotted against the normalized radial distance, computed as follows:

$$\eta = \frac{x_2 - x_{2\ (0.5)}}{\delta_\omega} \qquad \textbf{5.2}$$

In this formula, δ_ω represents the vorticity thickness and is calculated as follow:

$$\delta_\omega = \frac{U_{\max}}{\left|\frac{dU}{d(x_2)}\right|_{\max}} \qquad \textbf{5.3}$$

$x_{2\ (0.5)}$ is called the half velocity point and corresponds to the radial location at which the local jet velocity is half of its maximum value.

5.1.3 Jet conditions

Different jets were investigated with the pitot probe setup described earlier in section **3.4** . First, a round contoured nozzle operating on design at M_j = 1.5 was used, providing baseline measurements in shock-free axisymmetric conditions. A survey was also performed with the same nozzle operating over-expanded at M_j = 1.3, and comparison was made with CFD predictions using Wind-US and briefly described in section **5.2.2**. Similar work was conducted with a contoured converging nozzle operating under-expanded at M_j = 1.5. Then, more realistic nozzle shapes were investigated, with measurements made in fully expanded and under-expanded jets issuing from a facetted nozzle representing a scaled model of a GE F414 jet engine exhaust nozzle. A rectangular nozzle, a replica of the F-22 nozzle was also used in under, over, and fully expanded conditions. These conditions are summarized in Table **5-1**. For the non-circular nozzles, an equivalent diameter D is calculated so that the circle of diameter D covers the same area as the exit area of the nozzle.

Table **5-1**: Jet conditions for pitot surveys.

	D (mm)	M_d	M_j	TTR	U_j (m/s)	Re	Measurements
Round nozzle cold jets	12.7	1.5	1.3	1.0	384	388,000	Static and pitot pressure, single probe
	12.7	1.0	1.5	1.0	425	738,800	
	12.7	1.5	1.5	1.0	425	681,500	
Rectangular nozzle	17.6	1.5	1.3	1.0	384	540,000	pitot pressure with 5 probe rake, minor and major axis
	17.6	1.5	1.5	1.0	425	947,000	
	17.6	1.5	1.7	1.0	470	1,285,000	
GE facetted nozzle	17.2	1.5	1.5	1.0	425	921,000	pitot pressure, single probe
	17.2	1.5	1.7	1.0	470	1,251,000	

5.2 Axisymmetric jets pressure surveys

Full pressure surveys of three different axisymmetric cold jets were first performed. A fully expanded M_j = 1.5 jet was investigated for validation of the experimental method. Then data were gathered for under and over-expanded conditions with comparison with Computational Fluid Dynamic predictions. The presence of shocks and their influence on the prediction of the local jet velocity will be discussed in the following sections.

5.2.1 Fully expanded M_j = 1.5 jet

In order to provide a check on the quality of the measurements performed, a full pitot survey of a fully expanded M_j = 1.5 jet was performed. Traverses of the jet were made at different downstream locations with refined measurements close to the exit plane.

The pitot pressure P_p, normalized with the upstream plenum pressure is shown in the contour plot of Figure **5-1** a). In this figure, the horizontal axis represents the (non-dimensionalized) downstream location x_1 / D_j and the vertical axis represents the radial direction x_2 / D_j with $x_2 / D_j = 0$ at the centerline of the jet. From these values of P_p, the local Mach number M_1 is computed as described in section **5.1.2** and plotted as a contour plot in Figure **5-1** b). Finally, the values of the local velocity U_1 are computed and plotted in Figure **5-1** c) for all available downstream locations. On these plots, the velocity is non dimensionalized with the centerline jet exit velocity U_{je}.

In order to easily compare the velocity profiles obtained at different downstream locations, the normalization scheme described in section **5.1.2** is applied, resulting in the plot of Figure **5-2**. This type of normalization was shown by Troutt and McLaughlin [**16**] and by Lau [**52**] to show a collapse of the profiles for axisymmetric jets for a wide range of downstream locations. The collapse is fairly good in the plot presented here, thus providing confidence in the quality of the data gathered and the methodology followed for calculation of the velocity. However, some discrepancies are apparent for $\eta < -0.5$. At these (non-dimensional) locations, the computed velocities are very low. These local speeds correspond to very low pressure values measured by the pitot probes through their pressure transducers. Since these transducers have a maximum range of 100 psi and have a specified accuracy of ± 1%, these low speed measurements are well below the accuracy achievable with the current setup.

Finally, the thickness parameters $x_{2\ (0.5)}$ and δ_ω can be plotted, as shown in Figure **5-3**. They are non dimensionalized with the jet diameter and δ_ω is further divided by two. As a result, the location at which the two curves intersect corresponds to the end of the potential core: the point where the centerline velocity starts decreasing. Therefore these measurements lead to $x_1 / D_j = 6.5$ for the end of the potential core. This matches with previous measurements such as the ones obtained by Zaman [**53**] who reported a potential core ending at $x_1 / D_j = 6$ for a Mach 1.4 jet.

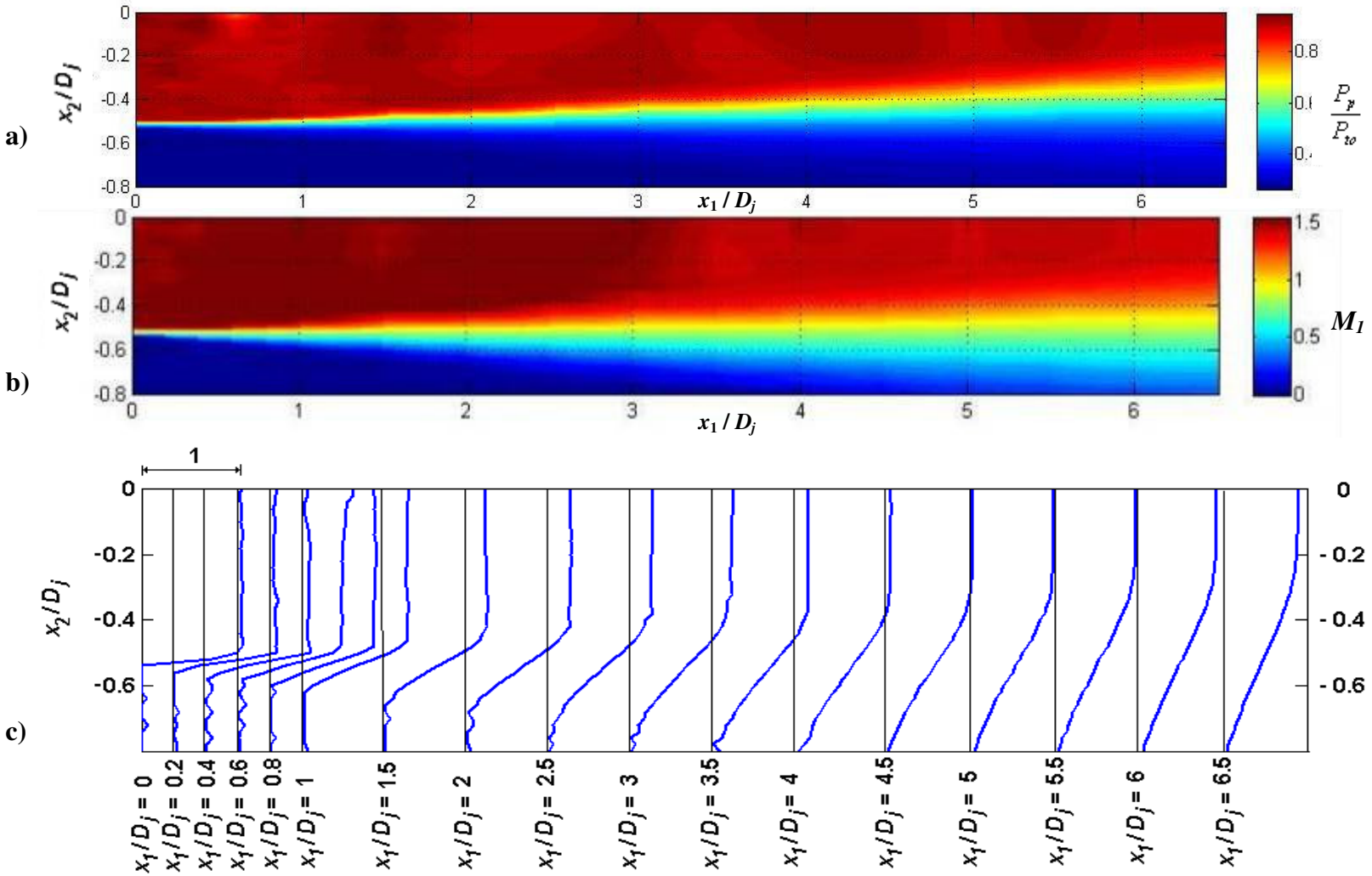

Figure **5-1**: a) contour plot of P_p / P_0 b) contour plot of local Mach number M_1, c) non dimensionalized local velocity (U_1/U_{je}) profiles at different downstream locations for a fully expanded M_j = 1.5 jet. U_{je} = 488 m/s.

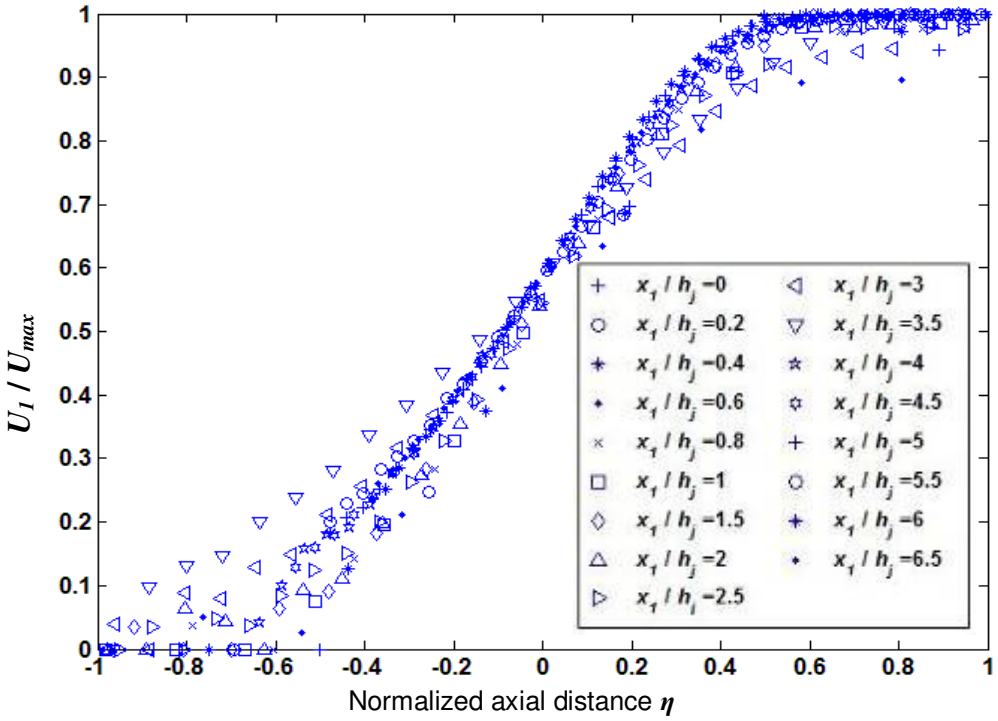

Figure **5-2**: Normalized velocity profiles of a $M_d = M_j = 1.5$ round jet.

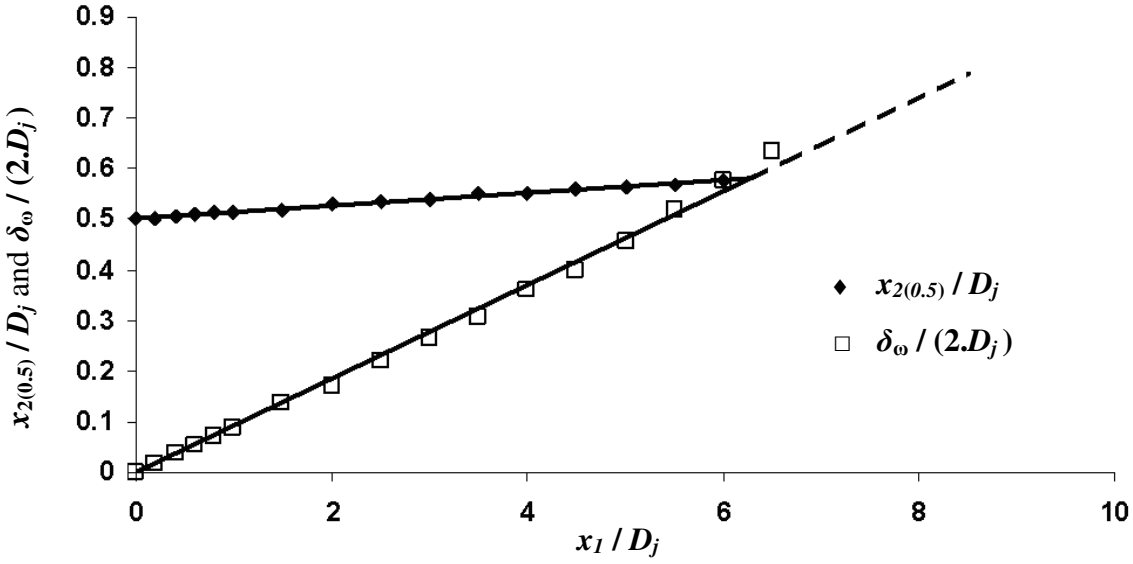

Figure **5-3**: Thickness parameters of a $M_d = M_j = 1.5$ round jet.

5.2.2 Under-expanded M_j = 1.5 jet

More measurements were performed with a purely converging contoured nozzle running an under-expanded M_j = 1.5 jet. Beyond the qualification of the CFD scheme, the purpose of these measurements was also to validate the capability of the pitot probe to accurately measure the flow despite the presence of the shocks in the jet. In order to produce some form of validation of the experimental results, direct comparison is made with the numerical predictions obtained for a jet issuing from a nozzle with the same inside contour. The CFD simulations performed by Miller [**54**] were based on Reynolds Average Numerical Simulations (RANS) and were conducted using the Wind-US code [**55**]. Wind-US is a product of the NPARC Alliance, a partnership between the NASA Glenn Research Center (GRC) and the USAF Arnold Engineering Development Center (AEDC). The boundary conditions for the solution of the problem consist of an inflow boundary at the entrance of the nozzle and the Menter k-ω turbulence model is used. More details on the simulations can be found in Miller *et al.* [**54**].

A first comparison is made of the general features of the jet flow from a schlieren image of the experimental flow and comparing it side by side with a numerical schlieren, as presented in Figure **5-4**. In this figure, the top image represents the experimental results and the bottom image shows the numerical results. The flow is from left to right in the positive x_1-direction. The lips of the nozzle at $x_2 / D_j = 0.5$ are evident by the strong shear layer emanating from these points. The sharp demarcation between dark and light regions emanating from the nozzle lip and ending on the jet centerline indicates the end of the Prandtl Meyer expansion fan and the initiation of compression waves caused by the interaction of the expansion waves with the free shear layer. Additionally, the shock waves and their corresponding angles can be seen as strong gradients of $d\rho / dx_2$. The first conical oblique shock originates at the same location in both experiment and simulation at approximately $x_1 / D_j = 1.1$. The second oblique shock waves occurs at approximately $x_1 / D_j = 2.5$. In both these figures the origin of these shock waves is the same. By inspection of this figure, the angles of both the experimental and numerical

oblique shock waves are also in agreement. This shows that the calculated and experimental shock wave strengths are equal.

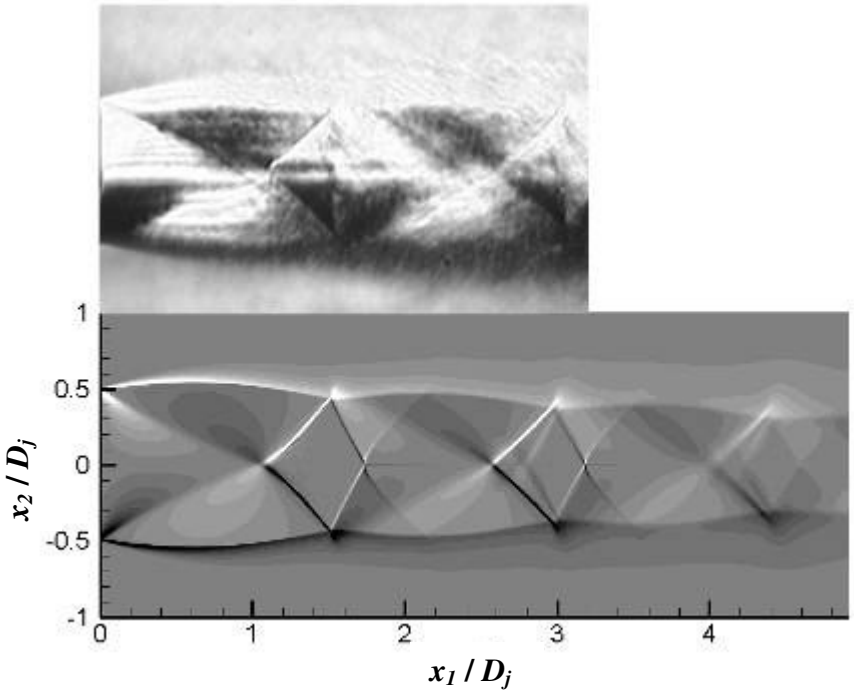

Figure **5-4**: Comparison between the experimental (top) and numerical (bottom) schlieren of the $M_d = 1.0$, $M_j = 1.5$, converging nozzle case.

Note also that the numerical contours of $d\rho/dy$ in Figure **5-4** are plotted over a very small range of negative one to one with one hundred intervals. This is done to bring out the smallest features of the density gradients and to magnify any possible imperfections in the numerical simulation. One small inaccuracy with this strategy can be seen at $x_1 / D_j = 1.8$ and $x_2 / D_j = 0$. A small line is visible along the x_1-axis. This is due to the mirroring of the data. The contours generated do not take into account the continuity of the data in the x_2-direction on the x_1-axis.

A more quantitative analysis is appropriate to evaluate the accuracy of the averaged variables of the RANS solution compared to experimental results. The formation of these data was discussed in section **5.1.2**. As noted in that section, there are some choices made in the combination of equations to be used to evaluate the flow parameters (such as the local Mach number). In these choices, the pitot pressure is always

used. For this reason the simulation data are manipulated to produce profiles of local stagnation pressure at a point that would be measured directly behind a hypothetical pitot probe. This manipulation involves using the Mach number and local static pressure ahead of the hypothetical shock that would be formed in the presence of a probe. Figure **5-5** shows profiles of these calculated data compared with the pressure measured by the pitot probe (normalized with the plenum pressure). For reference, the nozzle exit is at $x_1 / D_j = 0$ and the nozzle lip is at $x_1 / D_j = 0$ and $x_2 / D_j = 0.5$. These results show excellent agreement at all locations.

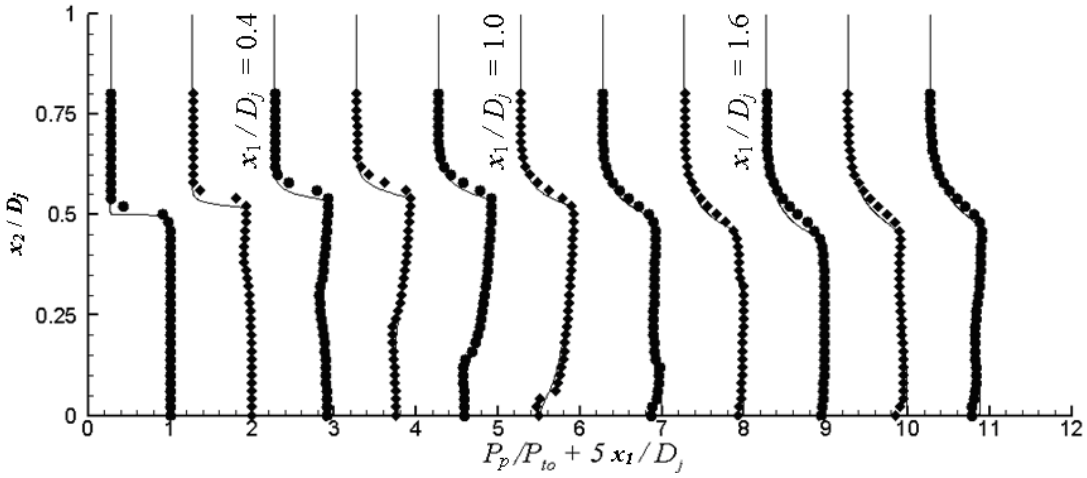

Figure **5-5**: Comparison between the experimental (dots) and numerical (lines) P_p / P_{to} of the $M_d = 1.0$, $M_j = 1.5$, converging nozzle case.

Contour plots of the total pressure are shown in Figure **5-6**. The top part of the figure, above the x_1-axis, represents the axisymmetric numerical data. The contours below the x_1-axis are generated with experimental data. The one hundred contour levels range from zero to one. In regions where there are not large gradients of total pressure, the qualitative agreement between the two plots is very good. However, in regions where shocks occur, the contour plots of the experimental data are 'smeared.' This is due to the lack of resolution of the experimental data in terms of axial spacing between experimental data points. Clearly, it is impractical to perform experimental measurements at every corresponding computational grid location. The largest separation between

experimental data points is $0.2D_j$ which is the spacing between the probe traverses in the x_1-direction. This resolution limitation did not limit the good agreement in the shear layer growth in the measured region. In particular, a place where the lack of resolution is apparent is near the oblique shocks, which are extremely thin.

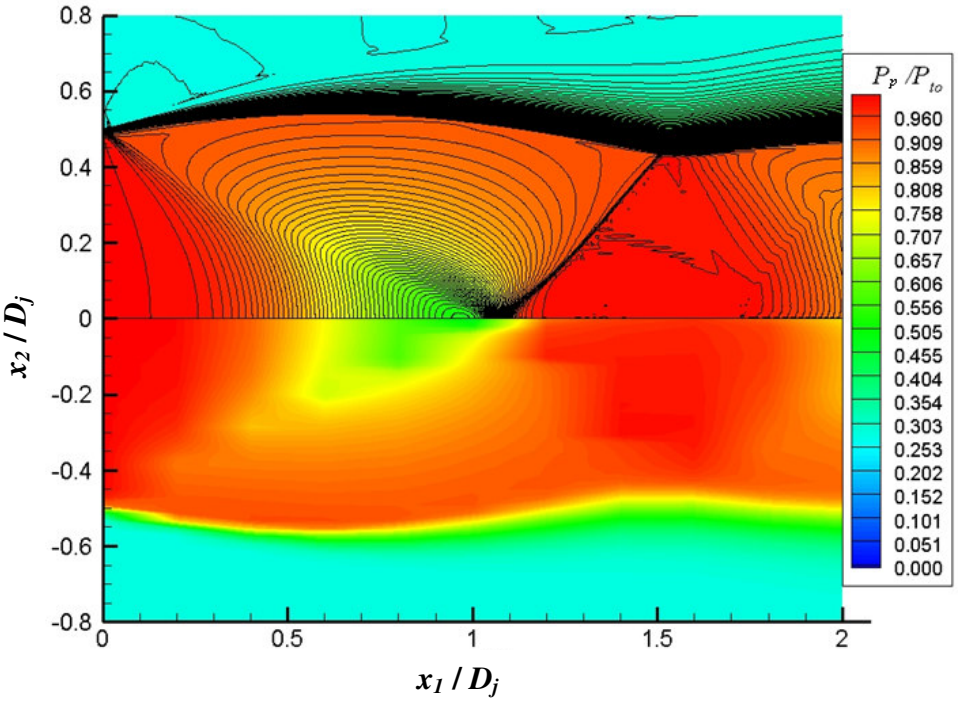

Figure **5-6**: Contour plot comparison between the experimental (bottom) and numerical (top) P_p/P_{to} of the $M_d = 1.0$, $M_j = 1.5$, converging nozzle case.

For this jet condition, the static pressure was measured and was shown in Figure **4-26** of section **4.4.3** . Discussions were also presented regarding the quality and relevance of these static pressure measurements.

Figure **5-7** shows the local Mach number, M_1, at the same locations as the previous figures. Initially all Mach number data were calculated directly from the pitot probe and static probe measurements. Since M_1 is calculated from a combination of both the pitot and static pressures, if an error occurs in one of these measurements it will show up in the comparison plots for M_1. One of these discrepancies can be seen near $x_1 / D_j = 1$, the region where the oblique shocks interact with the flow over the static pressure probe.

In an effort to obtain improved experimental estimates, the alternate approach of using the normal shock relation (Eq. **3.15**) with the assumption that the stagnation pressure is constant through the nozzle and in the jet flow inside the shear layer annulus has been used for locations x_1 / D_j = 0.8, 1.0, 1.2 and 1.4. Using this method produces improved agreement between the experimental and computational data at these points. An additional problem appears near the nozzle exit where the static pressure probe cannot traverse to the nozzle lip-line where it will encounter the nozzle. The M_1 experimental plot at $x_1 / D_j = 0$ shows a smaller radial range than its numerical counterpart. Furthermore, the numerical results at this location show that the velocity is zero on the nozzle lip; this accounts for the large gradient in the region near $x_2 / D_j = 0.5$ compared to the experimental data. The spreading rate of the jet, shown by the lower gradients of Mach number in the shear layer, is consistent with the numerical results for the range of x_1 / D_j measured.

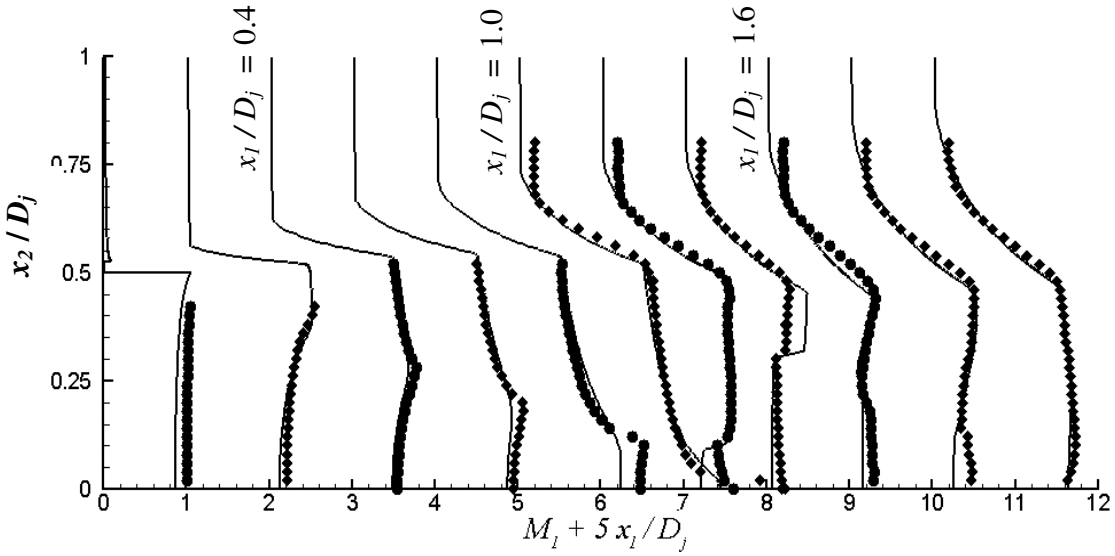

Figure **5-7**: Comparison between the experimental (dots) and numerical (lines) values of M_1 for the M_d = 1.0, M_j = 1.5, converging nozzle case.

Finally, from the experimental results, the thickness parameters $x_{2\,(0.5)}$ and δ_ω can be plotted, as shown in Figure **5-8**. Despite the fact that the measurements were not made

far enough downstream to actually observe the end of the potential core, the intersection of the trendlines of $x_{2\ (0.5)}$ and δ_ω gives an approximate location for the potential core at around $x_1 / D_j = 10$. The length of the potential core is therefore substantially longer than what was observed in the fully expanded case where it ends around $x_1 / D_j = 6.5$.

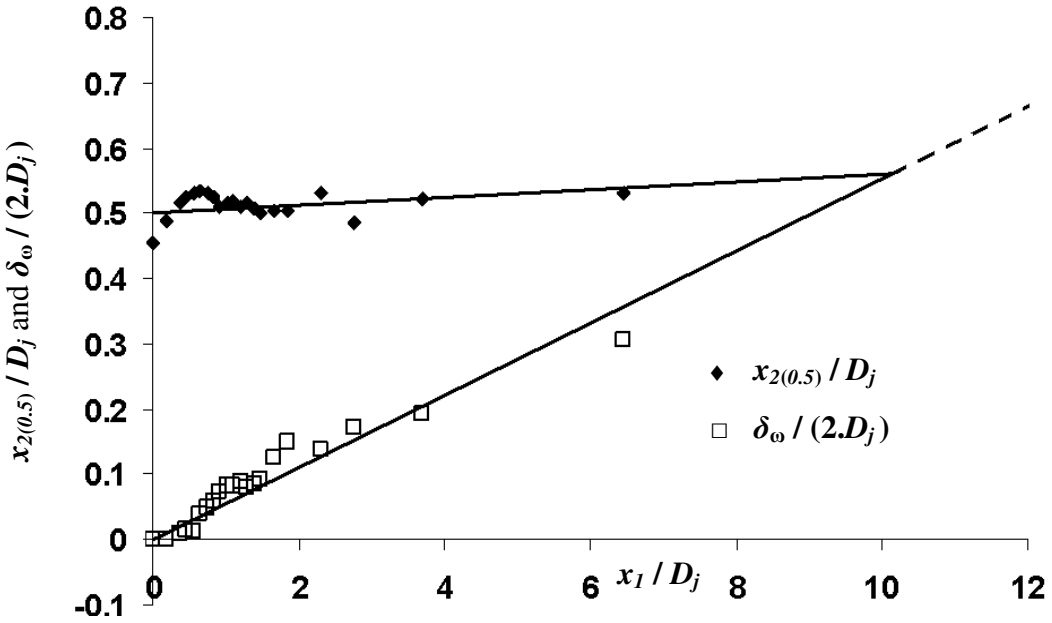

Figure **5-8**: Thickness parameters of a $M_d = 1.0$, $M_j = 1.5$ round jet.

5.3 Over-expanded $M_j = 1.3$ jet

Similar measurements were performed with a jet running at $M_j = 1.3$ from a converging-diverging nozzle designed for $M_d = 1.5$. Figure **5-9** shows the comparison between the experimental and numerical schlierens for this over-expanded case. The arrangements of the shocks are very different from the previous case because, unlike the converging nozzle case, an oblique shock wave originates at the nozzle lip and terminates as a barrel shock. The appearance of the more typical conical oblique shocks downstream ensues. A qualitative comparison of the position and angles of the shock waves shows

good agreement. In particular, the locations of the normal shock waves just after the exit of the nozzle are similar. The slip stream downstream of the normal shock is seen clearly in the simulations.

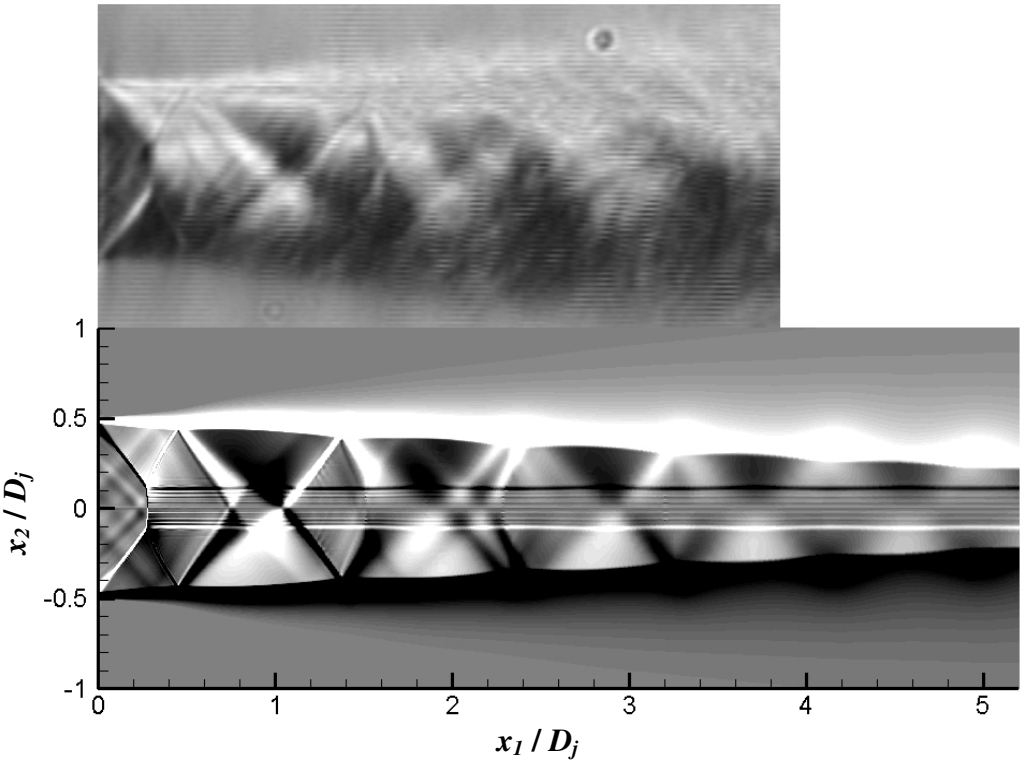

Figure **5-9**: Comparison between the experimental (top) and numerical (bottom) schlieren of the $M_d = 1.5$, $M_j = 1.3$, converging-diverging nozzle case.

The results of the probe traverses for this converging-diverging nozzle case are shown in Figure **5-10**. These experimental pitot pressure profiles show excellent agreement with the calculations for a hypothetical probe from the numerical simulations. The shear layer growth for the numerical results is slightly lower than that of the experimental results. This is most likely a problem with the turbulence model in the simulations.

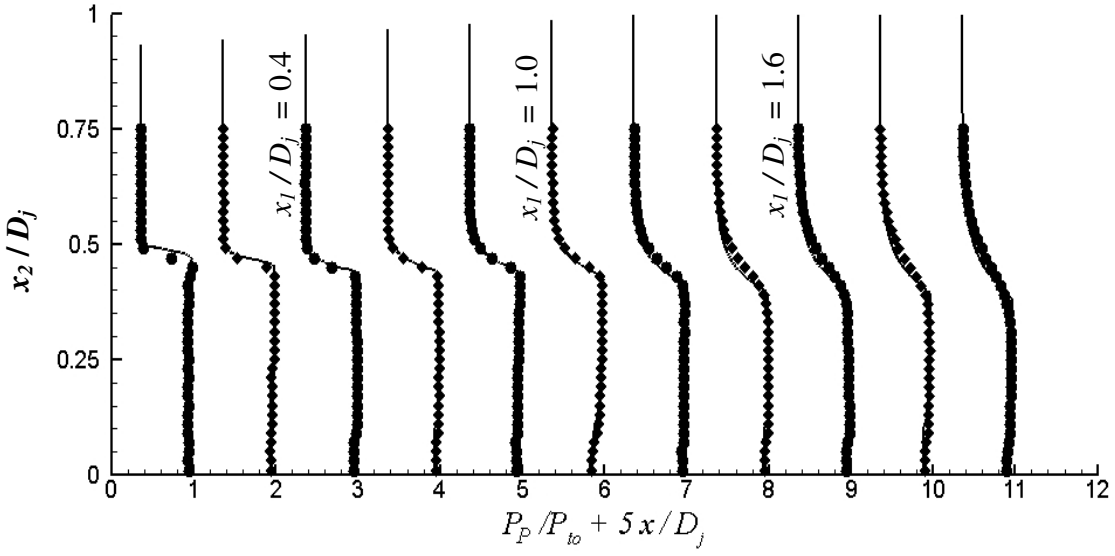

Figure **5-10**: Comparison between the experimental (dots) and numerical (lines) values of P_p/P_{to} for the $M_d = 1.5$, $M_j = 1.3$, converging-diverging nozzle case.

The same data can be presented as contour plots, as already introduced in the previous section for the under-expanded case. The resulting contour plots are shown in Figure **5-11**. The agreement is once again very good between the experiments and the computational results. In spite of the lack of resolution in the experimental data gathered, the shocks are easy to identify and the slip line downstream of the normal shock is also visible in both numerical and experimental data.

Figure **5-12** shows the corresponding static pressure measurements. These also have good agreement. However, as in the convergent nozzle case, there is one small disagreement in the static pressure data. This is at approximately $x_1 / D_j = 0.2$, which is the region located right after the normal shock, seen in the schlieren image of Figure **5-9**. Discussions over the cause for these discrepancies are presented in section **4.4.3**.

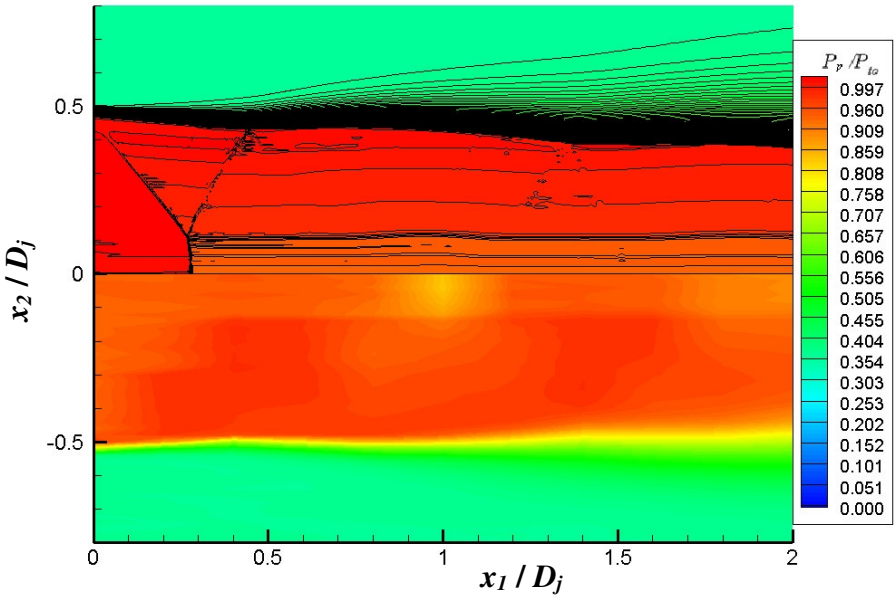

Figure **5-11**: Contour plot comparison between the experimental (bottom) and numerical (top) P_p/P_{to} of the $M_d = 1.5$, $M_j = 1.3$, converging-diverging nozzle case.

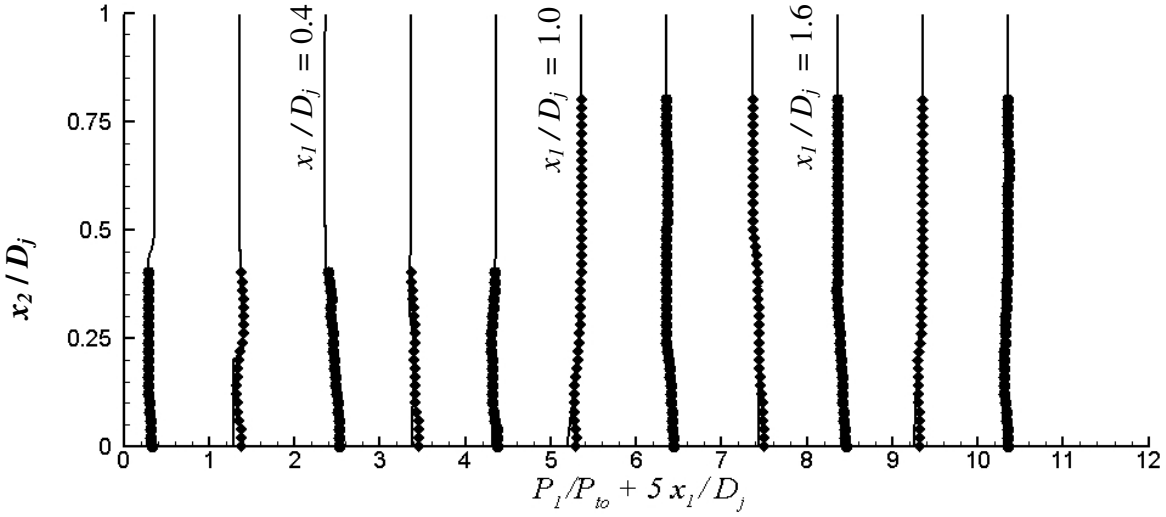

Figure **5-12**: Comparison between the experimental (dots) and numerical (lines) P_1/P_{to} of a converging-diverging nozzle with $M_d = 1.5$ running at $M_j = 1.3$.

A final comparison is made for this case between the local Mach numbers calculated from the simulation and the experimental data. The resulting plot is shown in Figure **5-13**. These Mach number estimates use the data from the static pressure probe with the Raleigh pitot formula (Eq. **3.13**) and Equation **3.14** to produce quite good agreement between experiment and computations. However, the error due to the static pressure probe interaction with barrel shock at $x_1 / D_j = 0.2$ is apparent. The static pressure measurement has altered the solution for the Mach number at this point.

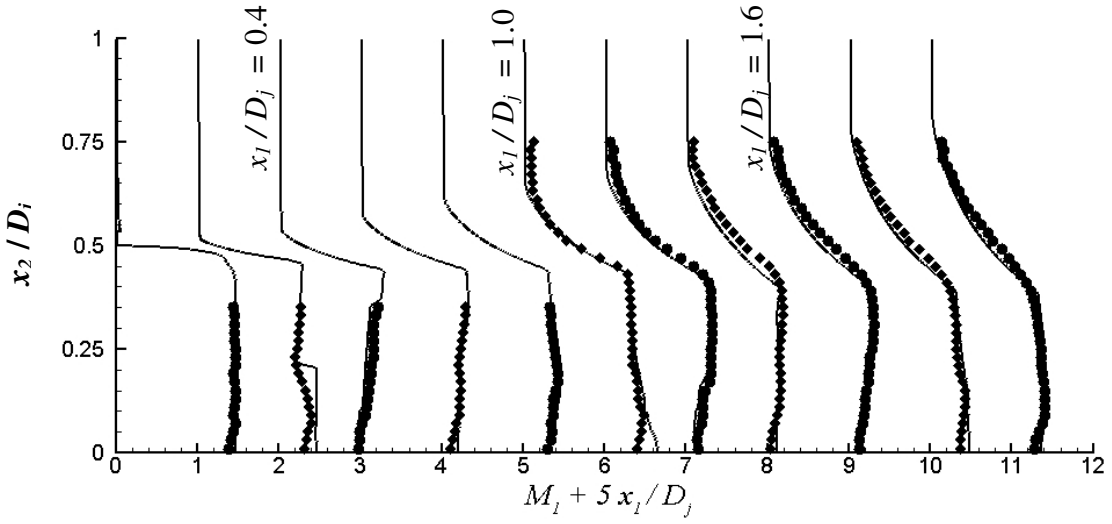

Figure **5-13**: Comparison between the experimental (dots) and numerical (lines) M_1 of the $M_d = 1.5$, $M_j = 1.3$, converging-diverging nozzle case.

Overall there is very good agreement between the numerical and experimental results for the averaged flow quantities that are measured. In some plots, it appears that the data are shifted by a very small amount in the x_2-direction. This small apparent shift, without which the results would agree even better, is due to the relatively large probe size compared to the exit diameter of the nozzle. The exit diameter of both nozzles is only 12.7 *mm* and the diameters of the total pressure probe and the static pressure probe are 5.08 and 0.9652 *mm* respectively. The relatively large diameter compared to the diameter of the nozzle and fluid dynamic structures could be the cause of this small shift. However, this error is small and the remaining agreement is excellent.

5.4 Measurements in jets issuing from facetted nozzles

In order to obtain mean flow measurements from more realistic nozzle geometries, pitot surveys were conducted in jets issuing from a facetted nozzle. The geometry of the nozzle, illustrated in figure **5-14**, is a small scale replica of existing military nozzles, with an exit to throat area ratio of approximately 1.18. The exact inner contours are the property of General Electric and were provided under an ongoing contract for the Strategic Environmental Research and Development Program (SERDP). Two similar nozzles of exit to throat area ratios of 1.07 and 1.30 were also fabricated but were not used in the present study. Acoustic measurements of these nozzles are being gathered and presented by Kuo *et al.* [**56**]. The internal contours are similar to the real aircraft engines of the F414 family. This nozzle was fabricated using rapid prototyping with a convergent and a divergent section with constant angle conical surfaces.

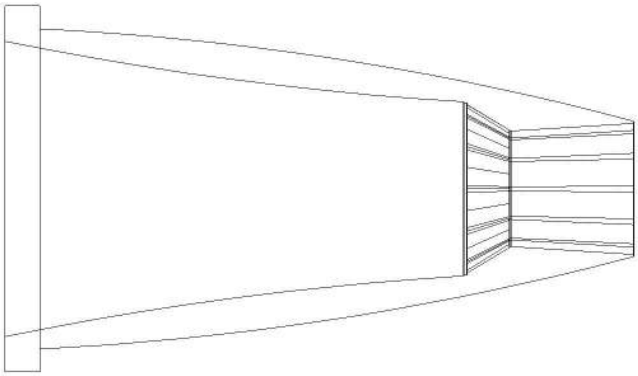

Figure **5-14**: Schematic of a GE facetted nozzle with M_d = 1.5.

Data were gathered with two different exhaust conditions. The nozzle was first operated as close as possible to the design condition, for a jet as free of shocks as possible, then measurements were made in under-expanded conditions by running a jet at M_j = 1.7 jet through this nozzle. Only pitot pressures were gathered for these jet conditions, and the Mach numbers and velocities were computed similarly to the fully expanded round jet case presented earlier in this chapter.

5.4.1 Fully expanded jet

Measurements were first gathered in fully expanded condition. Since only fairly weak shocks were expected in this case, only a small number of traverses were performed. The pitot profile contour plot as well as the computed Mach numbers and the velocity profiles are presented in Figure **5-15**. Direct comparison can be made between the contour plot of M_1 and the schlieren picture shown in Figure **5-16**. The very weak shocks that can be seen on the schlieren visualization are hardly visible in the measurements. They only appear slightly in the velocity profiles as small notches in the curves at downstream locations x_1 / D_j =0, 0.7 and 1.5.

The velocity profiles can then be collapsed using the method described in section **5.1**. The resulting plot is shown in Figure **5-17**, and the collapse of the profiles for different axial locations is fairly good. Small discrepancies are apparent directly outside of the jet, for η < -0.5 and can be most probably attributed to the presence of entrained flow. The resolution of the transducers at such low pressures is also held responsible for some of these discrepancies, as already discussed in section **5.2.1**.

Finally, Figure **5-18** presents the plots of the thickness parameters $x_{2\ (0.5)}$ and $\delta_{\omega.}$ An obvious observation from this plot is that the values of $x_{2\ (0.5)}$ are increasing faster for this nozzle than what was previously observed in the round nozzle case. This is characteristic of a larger spreading angle of the jet. The end of the potential core can also be predicted to be around 8 diameters downstream, which is substantially further than what was observed previously with the round nozzle. However, due to the small number of traverses, this prediction cannot be strongly relied on.

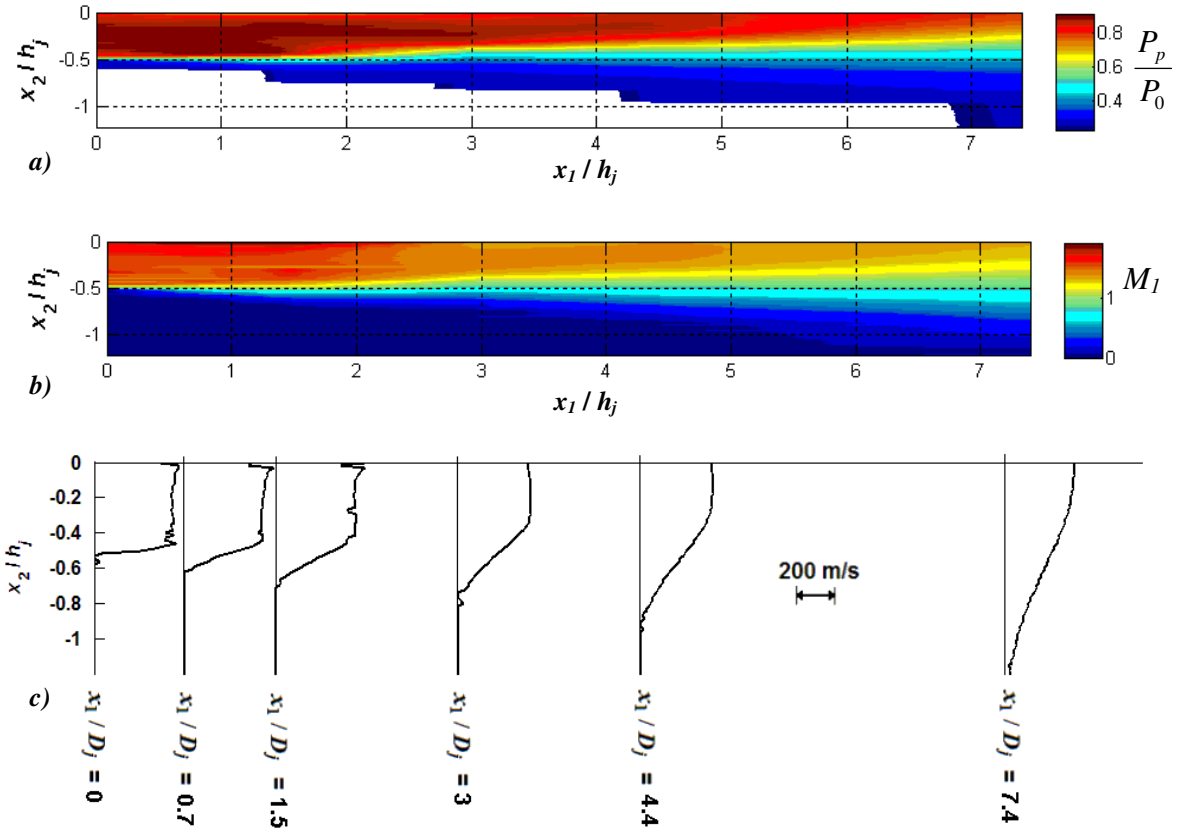

Figure **5-15**: a) contour plot of P_p / P_0 b) contour plot of local Mach number M_1, c) local velocity (U_1) profiles at different downstream locations for a M_j = 1.5 from a GE design nozzle.

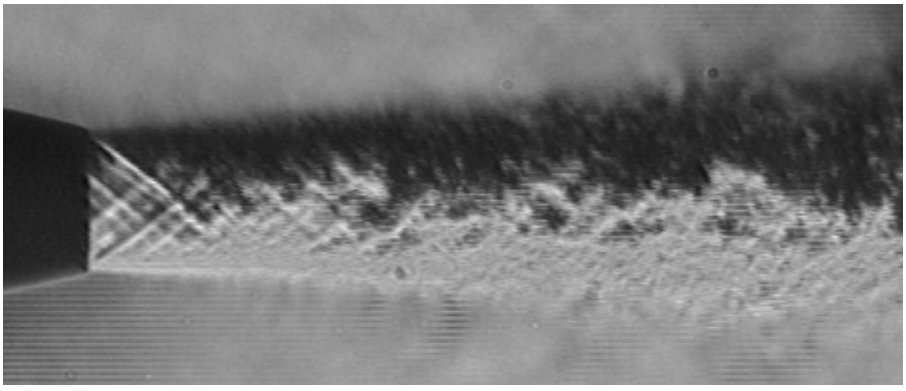

Figure **5-16**: Schlieren visualization of a M_j = 1.5 jet issuing from a GE design nozzle.

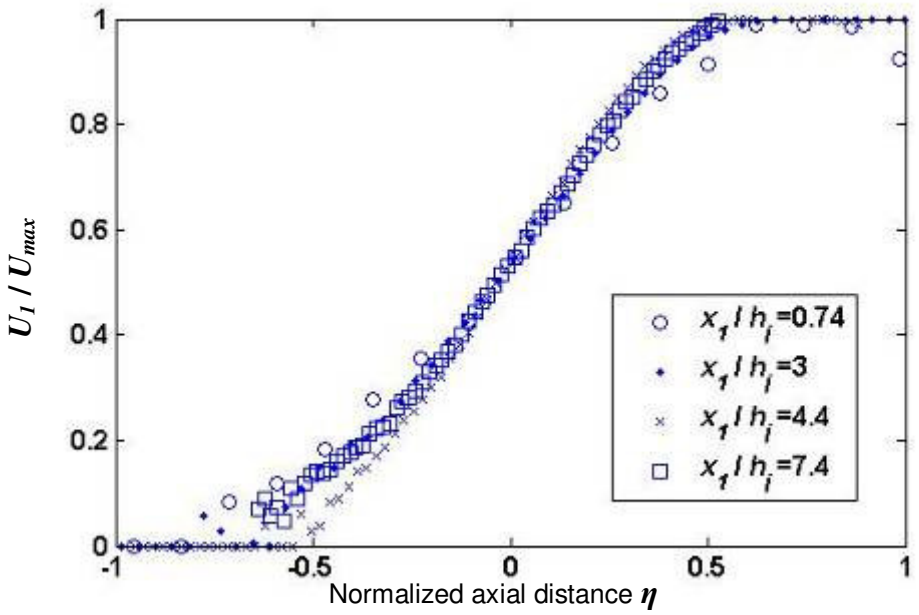

Figure **5-17**: Normalized velocity profiles for a M_j = 1.5 jet issuing from a GE nozzle.

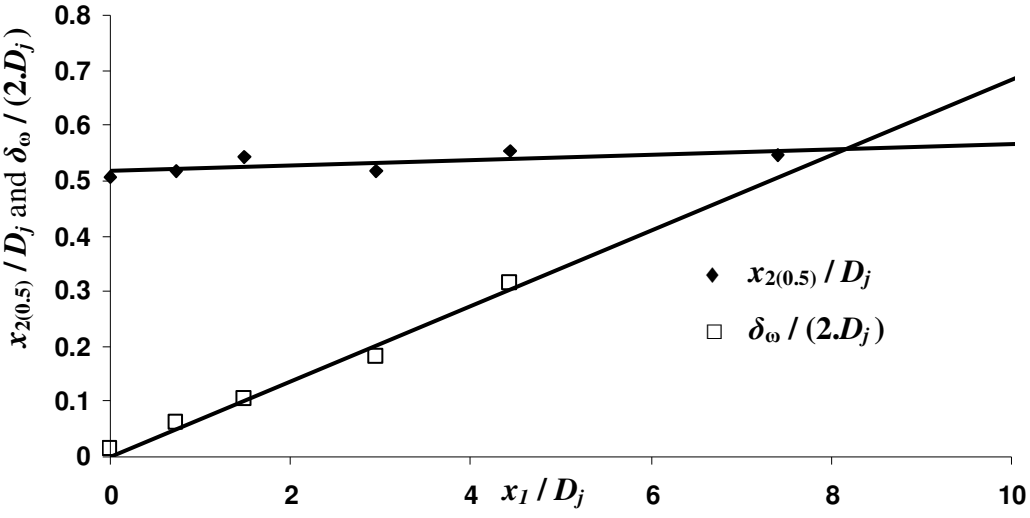

Figure **5-18**: Thickness parameters of a M_d = 1.5, M_j = 1.5 jet issuing from a GE nozzle.

5.4.2 Under-expanded jet

The same measurements were performed for an under-expanded case, with the same nozzle and $M_j = 1.7$. Due to the presence of shocks in the flow, a larger number of traverses was performed, with refined measurements close to the exit plane. Contour plots of the pitot pressure as well as the computed Mach numbers are presented in Figure **5-19**, together with the velocity profiles. Direct comparison can be made between the contour plot of M_1 and the schlieren image shown in Figure **5-20**. Strong shocks appear on the schlieren image and are clearly visible in the contour plots. The pitot measurements also capture accurately the barrel shape of the shock cell. As shown in Chapter **6**, a round jet operating at this condition has a convective velocity approximately $U_c / U_j = 0.8$. Therefore, the convection velocity of the turbulent structures is about $U_c =$ 376 m/s, leading to an acoustic Mach number $M_a = 1.1$. For such value of M_a, the Mach wave angle can be predicted to be 65° from the jet axis (from Equation **1.6**), which corresponds to the red line in Figure **5-20**. It matches very well with the schlieren visualization of the Mach waves.

The velocity profiles can then be collapsed using the method described in section **5.1**. The resulting plot is shown in Figure **5-21**, and the collapse of the profiles for different axial locations is fairly good. Once again, small discrepancies are apparent directly outside of the jet, for $\eta < -0.5$ and can be attributed to the lack of reliability in the pressure transducers at such low pressures, as already discussed in section **5.2.1**.

Finally, Figure **5-22** plots the thickness parameters $x_{2\ (0.5)}$ and $\delta_{\omega..}$ The measurements were not performed far enough downstream to produce very reliable prediction of the end of the potential core. Nevertheless, its location is at approximately $x_1 / D_j = 7.0$.

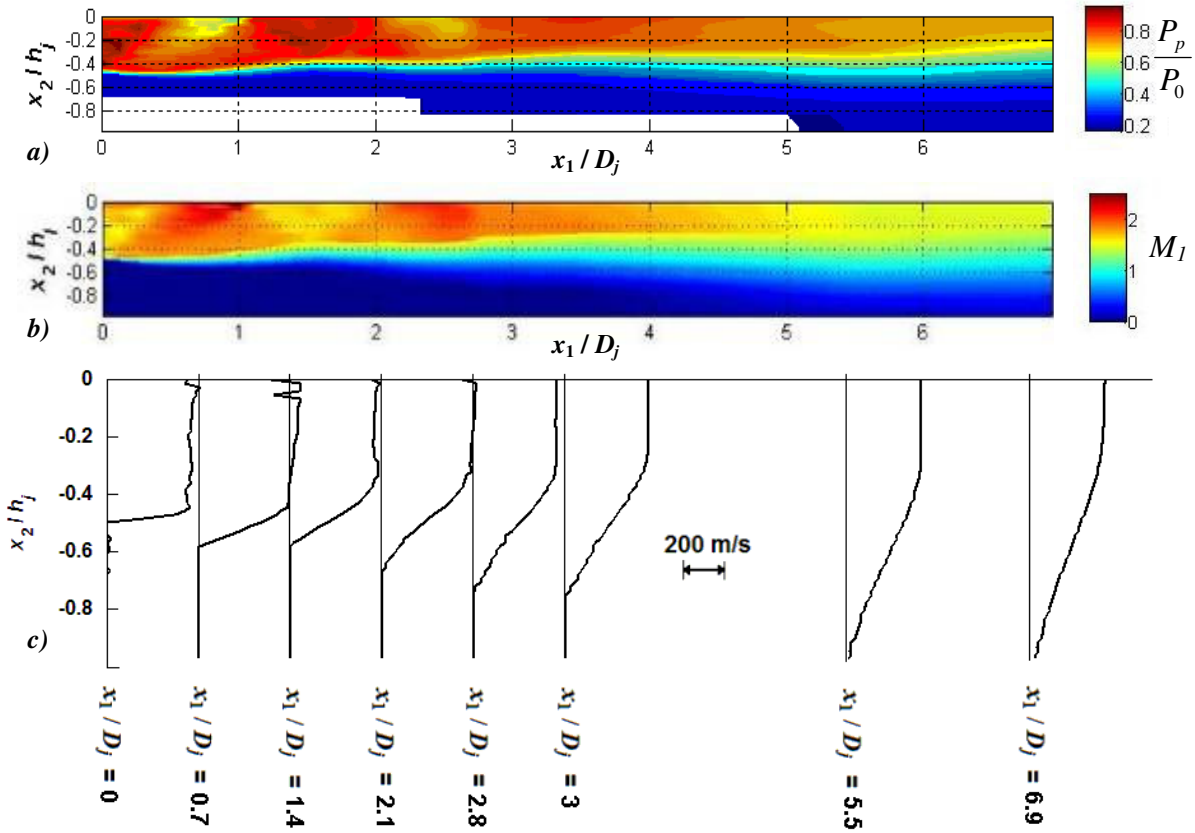

Figure **5-19**: a) contour plot of P_p / P_0 b) contour plot of local Mach number M_1, c) local velocity (U_1) profiles at different downstream locations for a M_j = 1.7 from a GE nozzle.

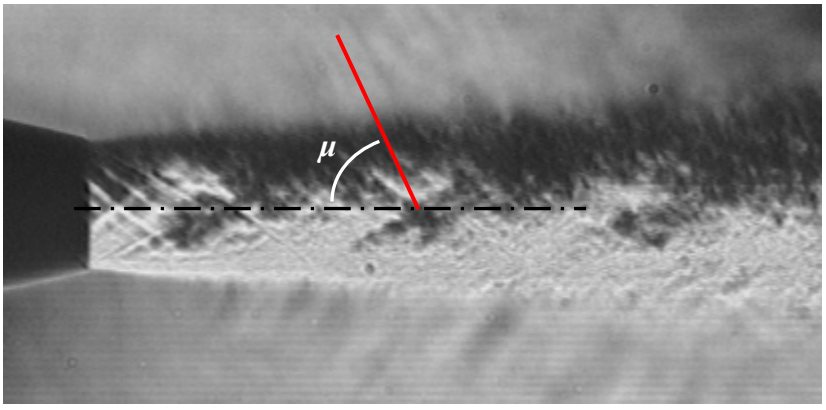

Figure **5-20**: Schlieren visualization of a M_j = 1.7 jet issuing from a GE design nozzle.

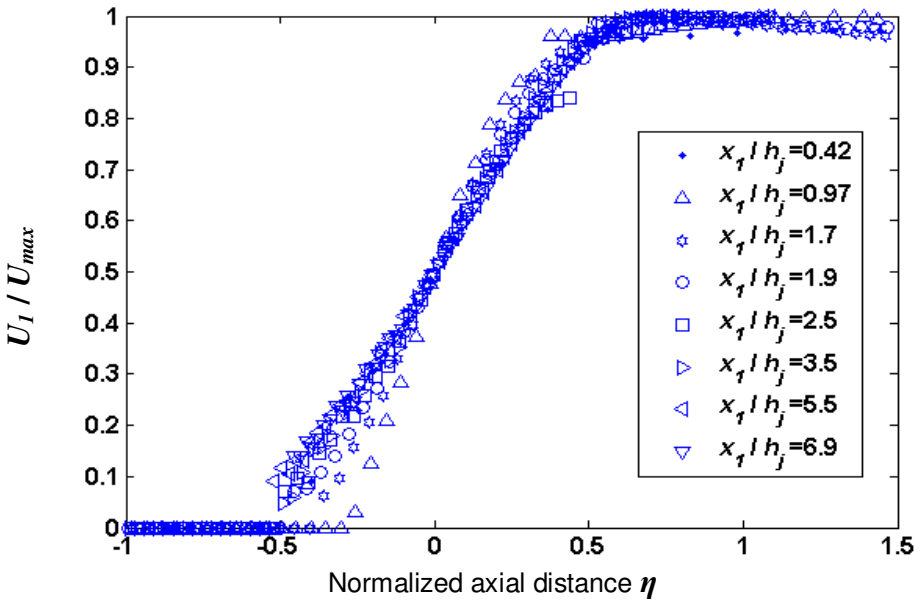

Figure **5-21**: Normalized velocity profiles for a M_j = 1.5 jet issuing from a GE nozzle .

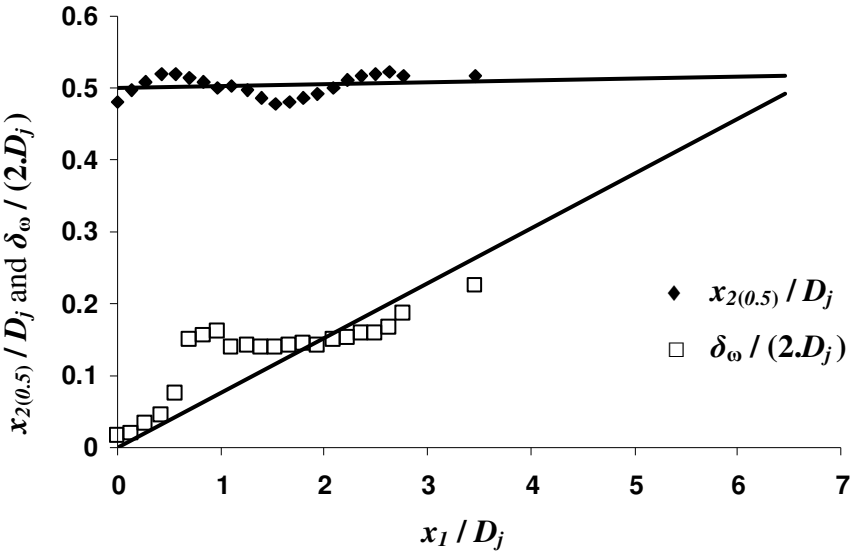

Figure **5-22**: Thickness parameters of a M_d = 1.5, M_j = 1.7 jet issuing from a GE nozzle.

5.5 Pitot surveys in rectangular jets

Rectangular nozzles also constitute a geometry of interest due to the existence of aircraft with rectangular jet exhausts and the notable noise reductions observed with such geometries. Comprehensive reviews of these findings can be found in Morris [**57**] and in Tam [**58**].

Therefore, measurements were made with a M_d = 1.5 rectangular nozzle that was designed to be a small scale replica of a F-22 jet engine. Some previous acoustic measurements were taken at Penn State with this nozzle and can be found in Lee *et al.* [**51**], together with more details on the exact geometry of the nozzle. For these flow field measurements, three conditions were investigated: a fully expanded condition with a minimum amount of shocks in the jet, an under-expanded and an over-expanded condition. Measurements were made both along the minor and the major axes of the jet to obtain as complete a survey as possible. The schematic for minor axis traverses is presented in Figure **5-23** and the one for major axis traverses was shown earlier, in Figure **3-15**.

For measurements performed in a cold rectangular jet, the pitot rake was mounted horizontally, providing 5 profiles at different x_3 locations during each motorized movement. Depending of the orientation of the rectangular nozzle, the traverses were performed successively along the minor and the major axes. The direction x_3 was kept fixed relative to the traverse movement and depending on the clocking of the nozzle x_3 corresponds either to the minor or to the major axis.

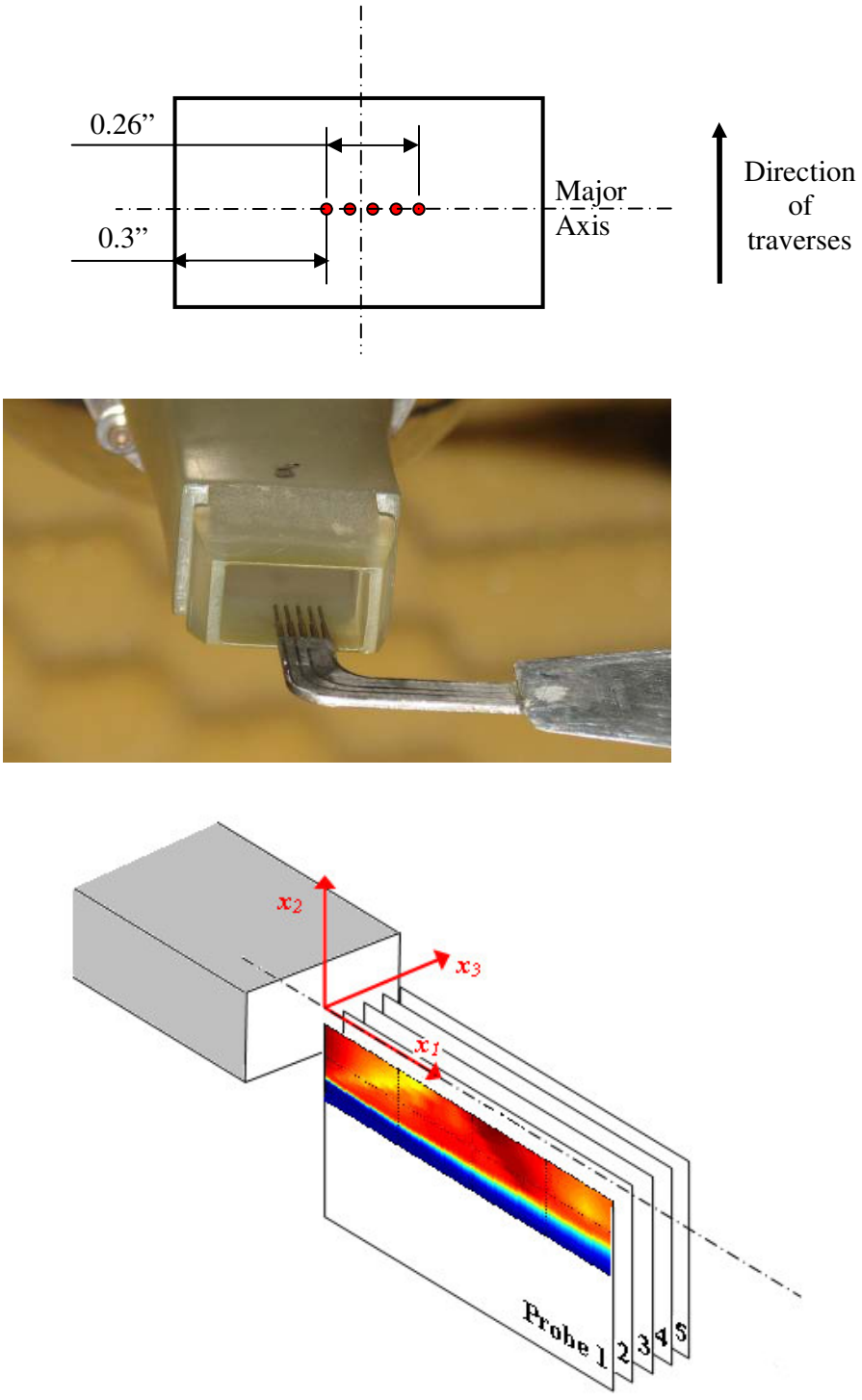

Figure **5-23**: Location of pitot probes during vertical traverses of a rectangular jet along the minor axis.

Since the shock patterns are mainly dependant on the height h of the jet, and are fairly insensitive to its width w, h is used as non-dimensionalization parameter. When the flow is not fully expanded, the actual average height of the rectangular jet issuing from the nozzle is written h_j and can be computed from isentropic relations. Since the growth of the jet is mainly along h, a 2D assumption is made in calculating h_j, leading to the following expression:

$$\left(\frac{h_j}{h}\right)_{2D} = \left[\frac{1+\frac{\gamma-1}{2}M_j^{\,2}}{1+\frac{\gamma-1}{2}M_d^{\,2}}\right]^{\frac{\gamma+1}{2(\gamma-1)}} \left(\frac{M_d}{M_j}\right) \qquad \textbf{5.4}$$

This expression leads to the following values of h_j for the three chosen rectangular jet conditions:

- Fully expanded jet: $M_d = 1.5$, $M_j = 1.5$: $h_j = 0.46$”
- Over-expanded jet: $M_d = 1.5$, $M_j = 1.3$: $h_j = 0.417$”
- Under-expanded jet: $M_d = 1.5$, $M_j = 1.7$: $h_j = 0.523$”

5.5.1 Fully expanded $M_j = 1.5$ rectangular jet

The first measurements were performed in a fully expanded jet. A total of 24 traverses was obtained along the major axis and 28 along the minor axis. The traverses were finely separated close to the jet exit (every 0.1 h_j) and further apart downstream. The measured pitot pressures from the 5 probes in each nozzle orientation are presented in Figure **5-24**. The contour plots presented are plotting the value of P_p / P_0 in term of downstream (x_1 / h_j) and vertical (x_2 / h_j) locations for all 5 planes x_3 / h_j available.

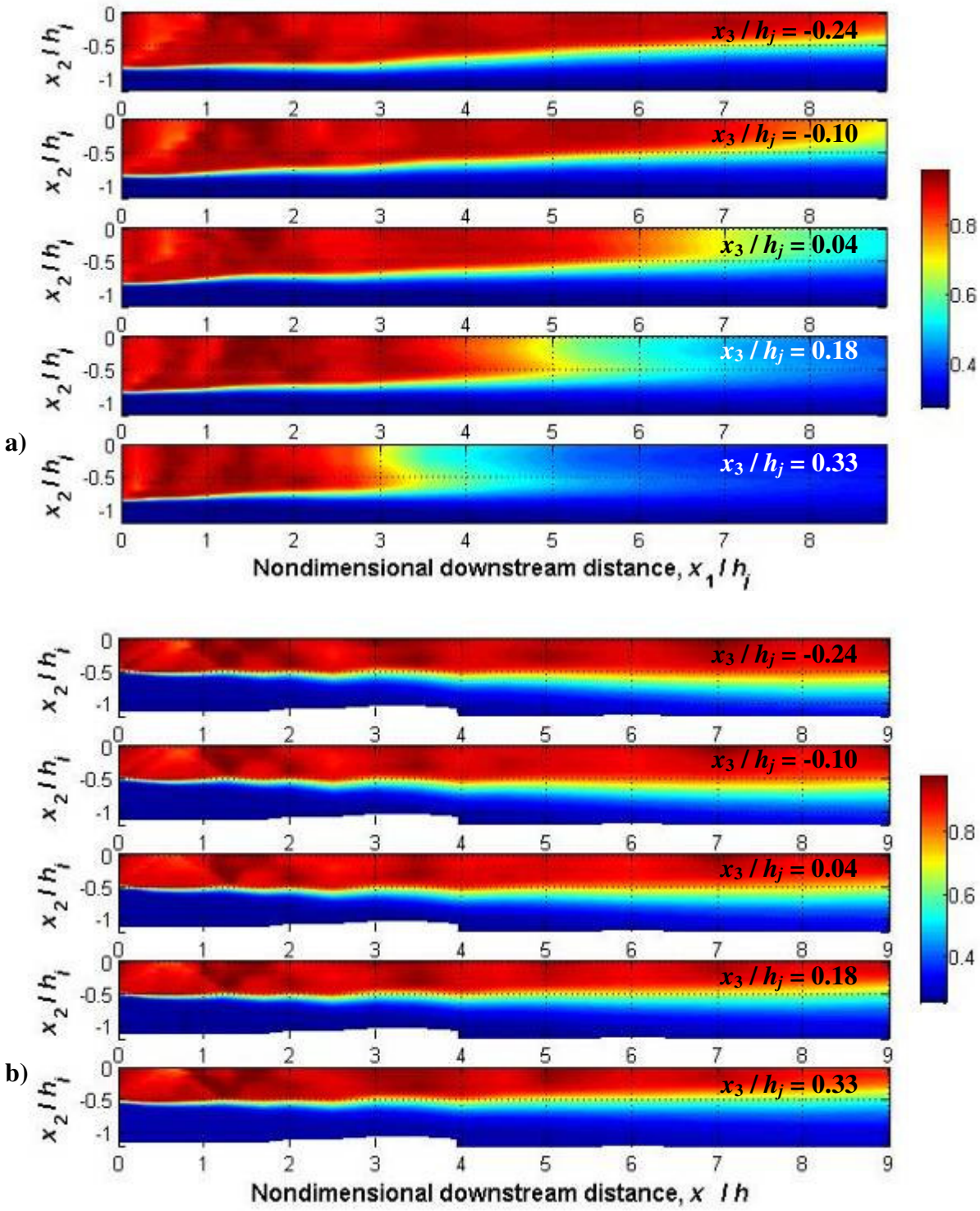

Figure **5-24**: Contour plots of the measured values of P_p / P_0 in a rectangular jet at different x_3 locations. M_d = 1.5, M_j = 1.5. a) nozzle oriented vertically: x_2 along major axis, x_3 along minor axis, b) nozzle oriented horizontally: x_2 along minor axis, x_3 along major axis.

As can be seen from these contour plots, the pitot probe located at $x_3 / h_j = -0.24$ was the one that measured the largest values of pressure far downstream. This suggests that this probe was actually the one located closest to the center line $x_3 / h_j = 0$ when far downstream. Since it was not at the centerline when located at the exit plane, this shows there is a misalignment between the x_1 motorized traverse and the jet axis. This discrepancy did not appear when the nozzle was oriented horizontally. Therefore, it seems the jet issuing from the nozzle was at a slight angle relative to both the plenum and the x_1 traverse. However, this angle is very small (1.6 degree) and after shifting the profiles the quality of the data should not be affected. Furthermore, since the pressure measurements close to the nozzle exit are indiscernible between probe 0, 1 and 2, one can make the assumption that the first probe gives a good representation of the pressure profile along the major axis along the whole jet.

Some more observations can be made from Figure **5-24**. Measurements along both axes clearly reveal the presence of shocks of limited strength in the flow. These can be compared to schlieren images taken for the same jet conditions and presented in Figure **5-25**, showing good overall agreement.

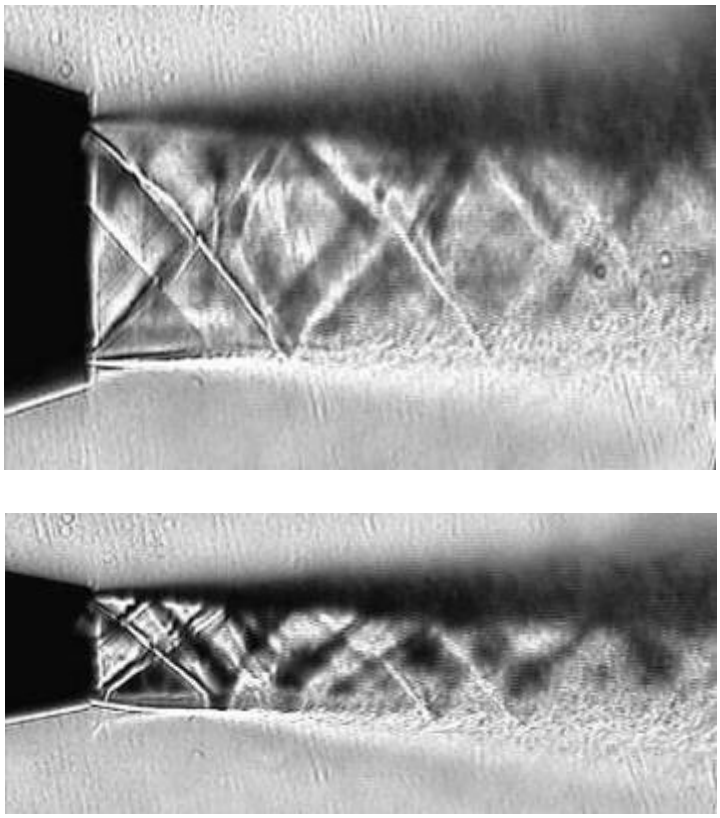

a)

b)

Figure **5-25**: Schlieren images of a rectangular $M_d = 1.5$, $M_j = 1.5$ jet taken along a) the minor axis, b) the major axis. Taken with 100 Hz stroboscopic light and 25 Hz camera.

In order to obtain more valuable insight into the jet's behavior, the local Mach number M_1 and the local velocity U_1 were computed as described in section **5.1.2.** The velocity profiles were then collapsed and are presented in Figure **5-26** for both the minor and the major axes. The collapse is quite good, in spite of the presence of some shocks. The velocity profiles were then plotted for both the minor and the major axes of the jet, as shown in Figure **5-27**. From these profiles, it is quite obvious that there is some axes switching: after a downstream distance of around $x_1 / h_j = 6$, the velocity profiles obtained along the minor axis extend to a larger vertical range than the ones obtained along the major axis. This phenomenon of axes switching was already observed in rectangular and elliptic jets by Zaman [**53**]. The half velocity point $x_{2\,(0.5)}$ and the vorticity thickness δ_ω were then plotted as a function of the downstream location, as shown in Figure **5-28**. In this figure, the $x_{2\,(0.5)} / h_j$ curves obtained for both axes intersect, showing the downstream

location at which the axis switching occurs. This location is at an approximate distance of 8.5.h_j downstream of the exit plane. The δ_ω / (2.h_j) curves are very similar between the minor and the major axes of the jet. However, the jet spreads more rapidly in the minor axis direction.

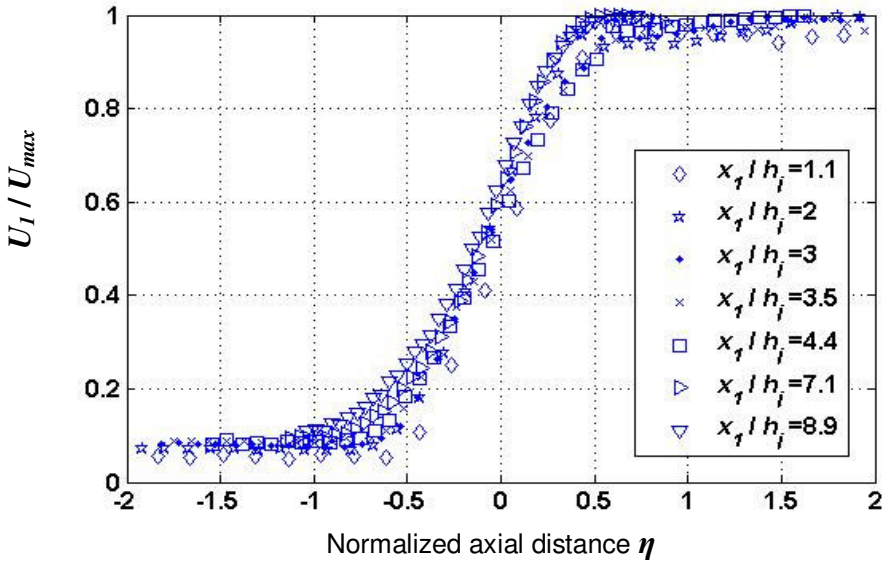

Figure **5-26**: Normalized velocity profile for a rectangular jet M_d = 1.5, M_j = 1.5 along the major axis.

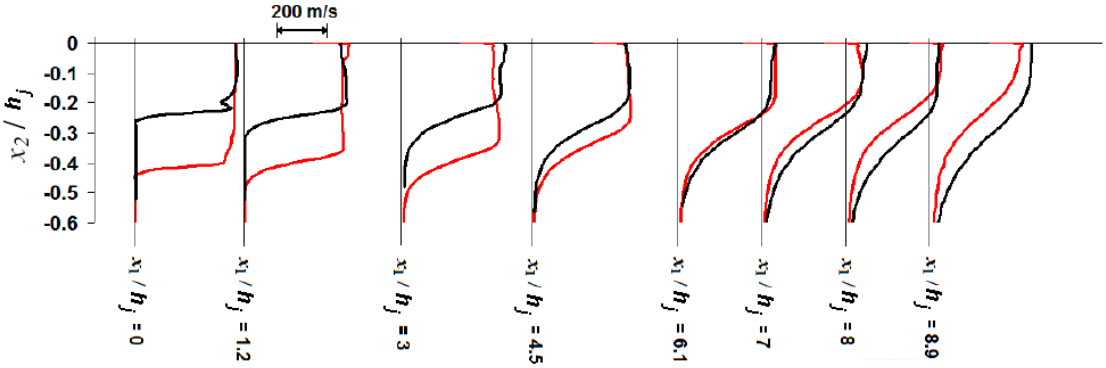

Figure **5-27**: Velocity profiles for different downstream location along both major (red) and minor (black) axis of a rectangular jet M_d = 1.5, M_j = 1.5.

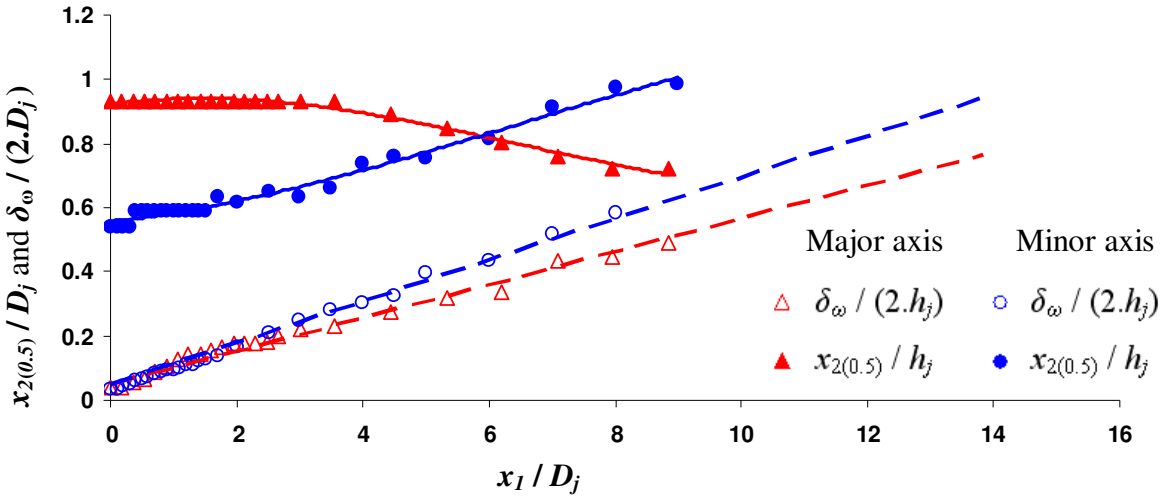

Figure **5-28**: Thickness parameters of a rectangular jet M_d = 1.5, M_j = 1.5.

5.5.2 Over-expanded M_j = 1.3 rectangular jet

Similar measurements were performed with an over-expanded jet issuing from the same nozzle. The resulting pitot pressure and Mach number contour plots are shown in Figure **5-29**. Once again, from these plots, the presence of shocks is clearly visible on traverses along both axes. The probe initially positioned at x_3 / h_j = -0.24 also seems to be actually located along the centerline of the jet and will be considered as such for the remaining of the analysis. The schlieren images obtained from this jet show good qualitative agreement with these pitot profiles, as can be seen from Figure **5-30**. While it is difficult to compare the spreading angles, the shock pattern looks similar between the two. The collapse of the velocity profiles obtained in Figure **5-31** also suggests that in spite of the asymmetry of the jet, there is an element of self similarity along the range of the measurement. The presence of weak shocks however deteriorates somewhat the collapse of the profiles.

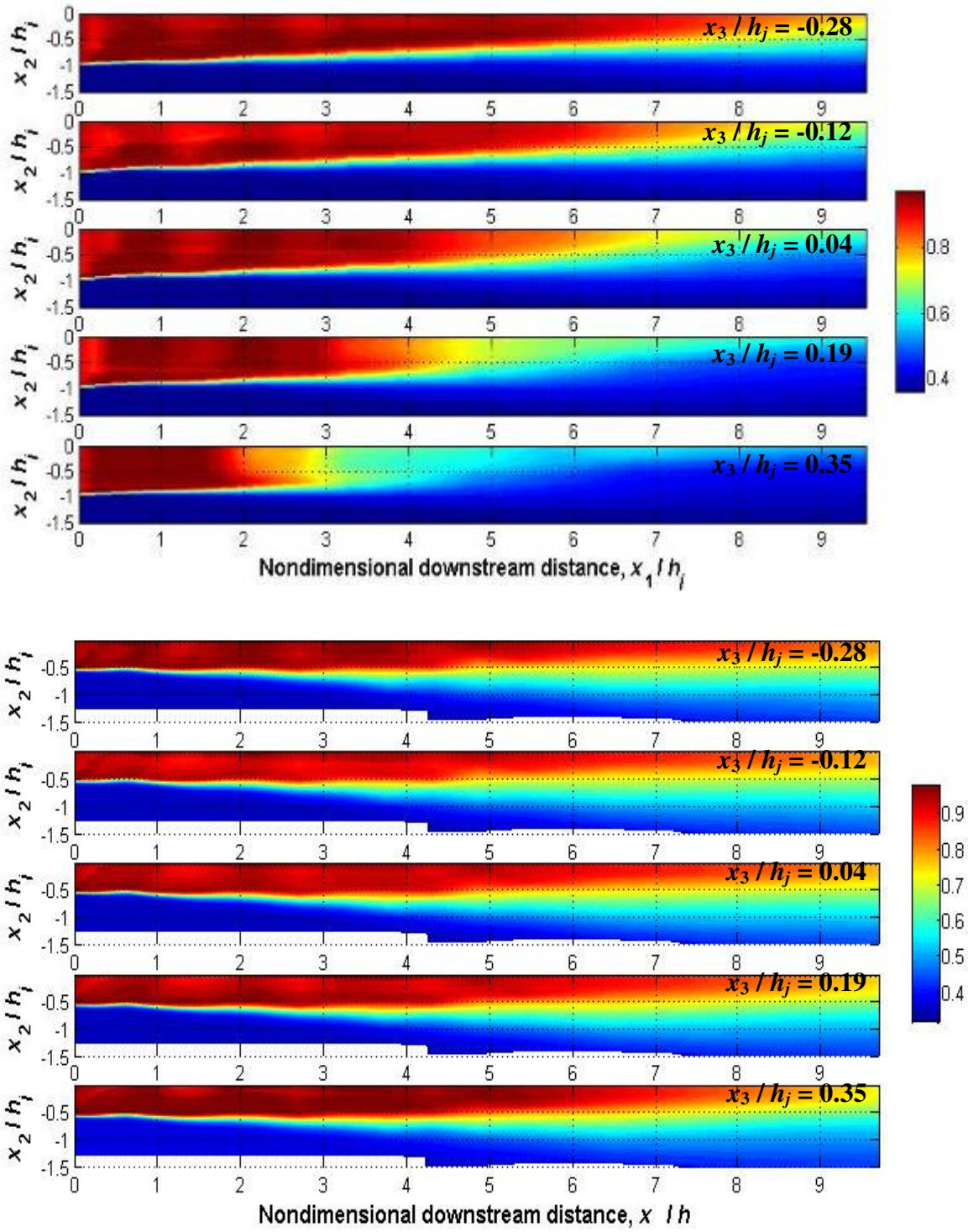

Figure **5-29**: Contour plots of the measured values of P_p / P_0 in a rectangular jet at different x_3 locations. M_d = 1.5, M_j = 1.3. a) nozzle oriented vertically: x_2 along major axis, x_3 along minor axis, b) nozzle oriented horizontally: x_2 along minor axis, x_3 along major axis.

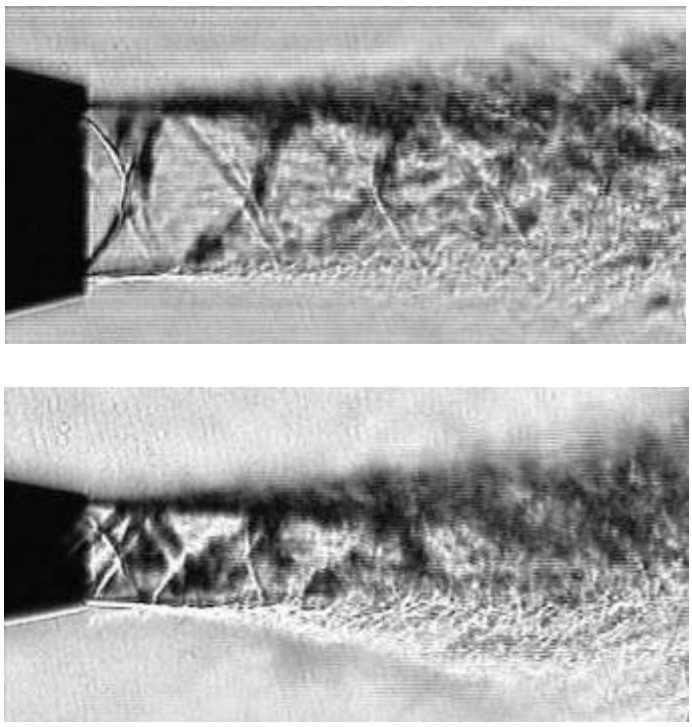

Figure **5-30**: Schlieren images of a rectangular $M_d = 1.5$, $M_j = 1.3$ jet taken along a) the minor axis, b) the major axis. Taken with 100 Hz stroboscopic light and 25 Hz camera.

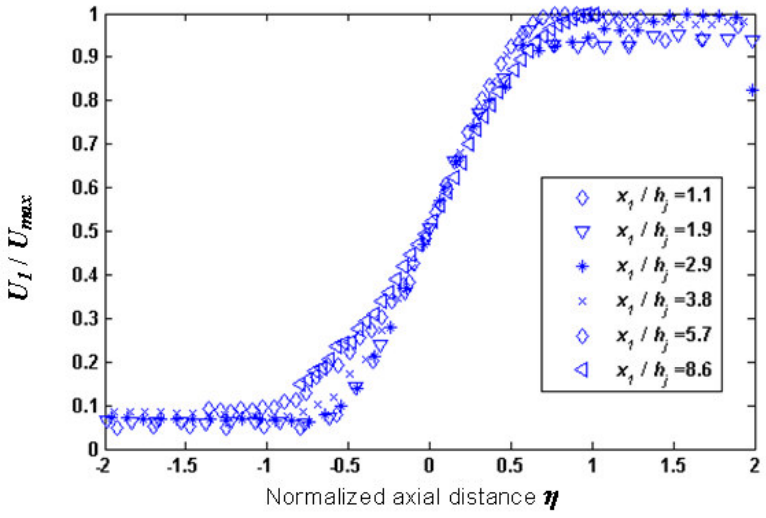

Figure **5-31**: Normalized velocity profile for a rectangular jet $M_d = 1.5$, $M_j = 1.3$ along the major axis.

The thickness parameters used for plotting of these non dimensionalized velocities are then plotted, non dimensionalized with h_j and divided by 2 for the vorticity thickness. The resulting graph of Figure **5-32** shows a switch of the axes, similar to what was observed in previous jet conditions. However the downstream location of this axes switching is changing to $x_1 / D_j = 4.5$, which is substantially earlier than in the fully expanded case.

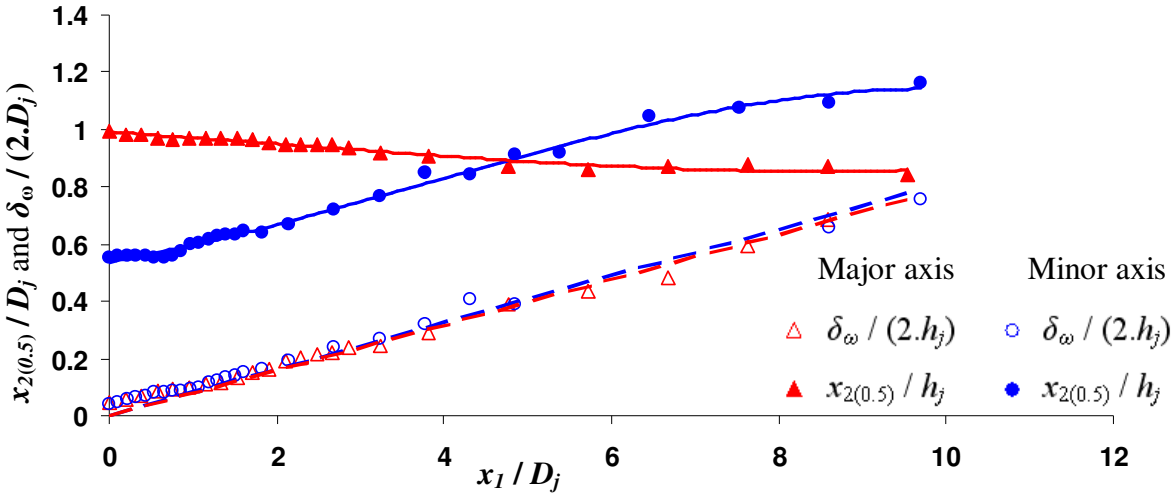

Figure **5-32**: Thickness parameters of a rectangular jet $M_d = 1.5$, $M_j = 1.3$.

5.5.3 Under-expanded $M_j = 1.7$ rectangular jet

The last condition investigated consists of an under-expanded case, $M_j = 1.7$. In this case, the traverses were performed at very similar downstream locations and the resulting pitot pressure and Mach number contours are presented in Figure **5-33**. The shock cell structure is very sharply defined in these measurements, as well as the barrel shape associated with it. It is visually in agreement with the schlieren images obtained in the same flow and shown in Figure **5-34**. One other observation from these images is the presence of Mach wave radiation. The convection velocity of such a high speed jet is bound to be supersonic (relative to the ambient speed of sound), therefore the convecting structures generate Mach waves.

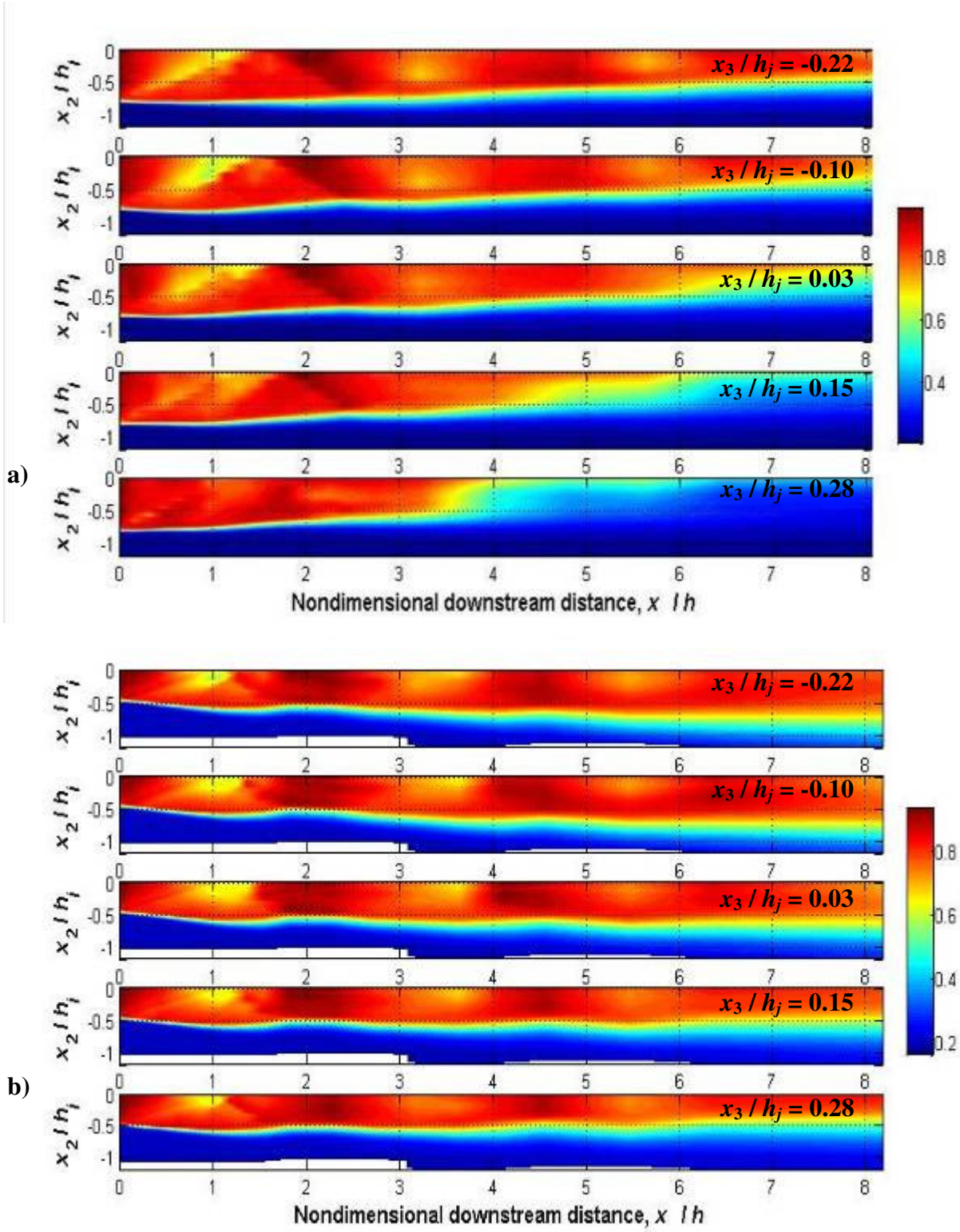

Figure **5-33**: Contour plots of the measured values of P_p / P_0 in a rectangular jet at different x_3 locations. M_d = 1.5, M_j = 1.7. a) nozzle oriented vertically: x_2 along major axis, x_3 along minor axis, b) nozzle oriented horizontally: x_2 along minor axis, x_3 along major axis.

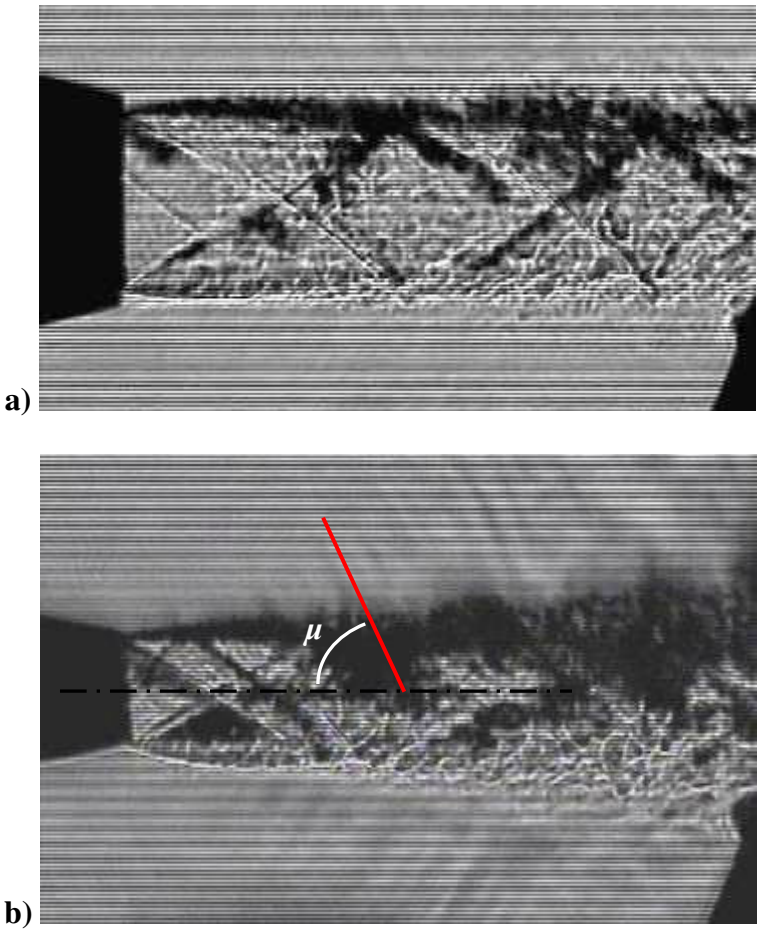

Figure **5-34**: Schlieren images of a rectangular M_d = 1.5, M_j = 1.7 jet taken along a) the minor axis, b) the major axis. Taken with 100 Hz stroboscopic light and 25 Hz camera.

Interestingly enough, the radiated Mach waves are only apparent along the minor axis, suggesting a different convection speed for each axis. As previously shown in section **5.4.2**, the convection velocity of the turbulent structures being about U_c = 376, the acoustic Mach number is M_a = 1.1. For such value of M_a, the Mach wave angle can be predicted to be 65° from the jet axis, which corresponds to the red line in Figure **5-34**. It matches very well with the visualization of the Mach waves. Future optical measurements in a rectangular jet will confirm this result.

Finally, the normalized velocity profiles were plotted, as shown in Figure **5-35**. In spite of the presence of strong shocks, the collapse is fairly good along the downstream

locations of the measurements. The thickness parameters used for plotting of these non dimensionalized velocities are again plotted, non dimensionalized with h_j and divided by 2 for the vorticity thickness. The resulting graph of Figure **5-36** shows a switch of the axes, similar to what was observed in previous jet conditions. The minor axis becomes the major axis at aproximately 4.5 h_j downstream, at the same distance as the over-expanded case.

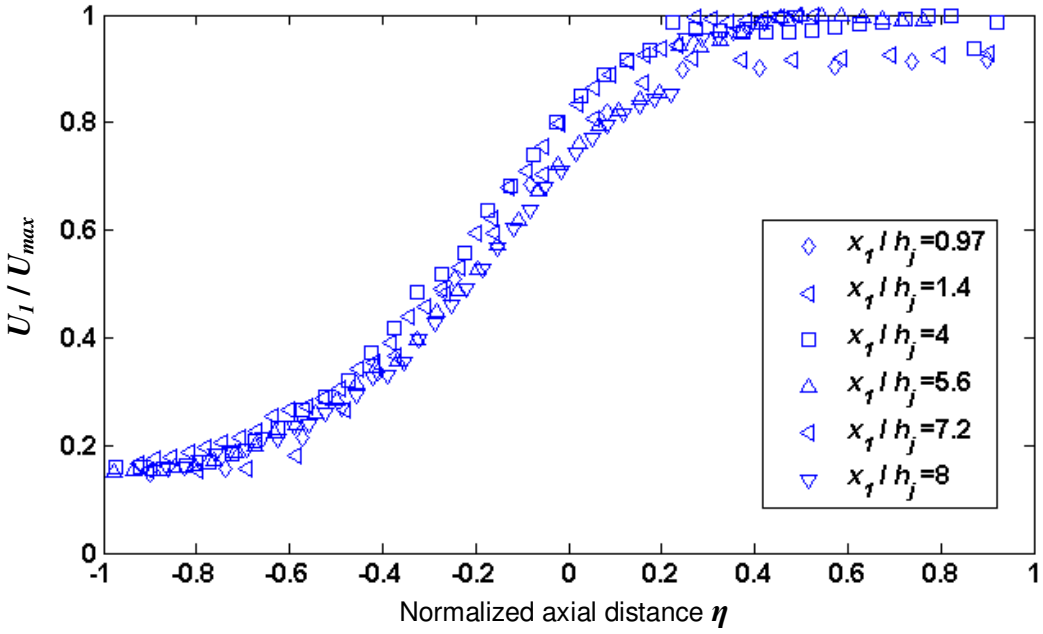

Figure **5-35**: Normalized velocity profile for a rectangular jet $M_d = 1.5$, $M_j = 1.7$ along the major axis.

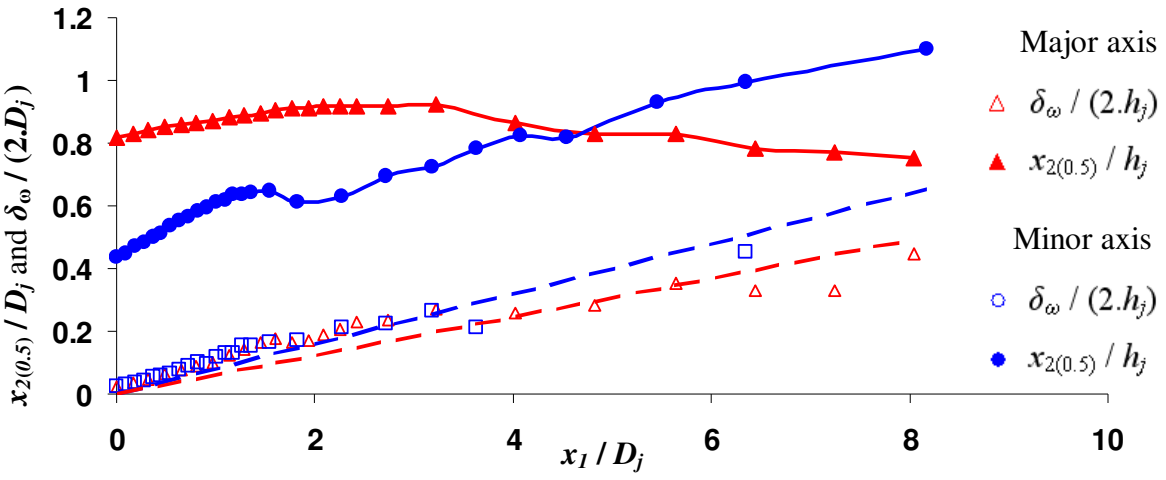

Figure **5-36**: Thickness parameters of a rectangular jet M_d = 1.5, M_j = 1.7.

5.6 Summary

Pressure surveys were performed in the flow field of jets of different conditions. Measurements were obtained with an axisymmetric converging-diverging (CD) nozzle producing a supersonic $M_j = M_d = 1.5$ fully expanded jet in order to gain confidence in the setup. Favorable results were obtained. An over-expanded $M_j = 1.3$ condition was chosen with the same CD nozzle and the resulting measurements were compared to CFD predictions. Static pressure measurements were tentatively conducted with a static probe but failed to produce accurate results due to the probe interference in the flow. A different approach was then chosen in order to calculate the local Mach number in the jet, making assumption on the total pressure and the static pressure. Good comparisons with the numerical results were obtained with this method. The same exercise was repeated with an under-expanded round jet $M_d = 1.0$ $M_j = 1.5$ and lead to the same observations. In both cases, the shock cell structure was accurately captured by the pitot probe, as well as the shape of the mixing layer.

Surveys were then performed with jets issuing from nozzles replicating real jet engines. A conical converging-diverging $M_d = 1.5$ GE nozzle which internal contoured is

composed of 12 facets was used in both fully expanded M_j = 1.5 condition and an under-expanded M_j = 1.7 condition. Finally, a rectangular nozzle, replica of a F-22 aircraft engine and designed for M_d = 1.5 was used with three different pressure ratios: M_j = 1.3, 1.5 and 1.7. Measurements along both axes were performed and lead to the observation of axes switching of the jet. This axes switching occurs further in the fully expanded case than in the two imperfectly balanced cases.

Chapter 6

Optical Deflectometry Results

Since Lighthill's first developments of the acoustic analogy, one of the main goals of the jet noise community has been to develop aeroacoustic theories that will enable an accurate prediction of the radiated noise. Since the far-field noise is produced by a turbulent flow contained in a mixing layer and downstream in a fully developed jet, accurate knowledge of the turbulent properties is a key parameter for proper results.

Two point space-time correlations of velocity, pressure and density have been measured extensively in order to gain knowledge of the length scale and decay rate of the turbulent structures, parameters of the noise generation process. Previous experimentalists have used hot wire anemometry extensively in order to measure the velocity fluctuations. However, the method is usually limited to subsonic jets and is difficult to apply to heated jets. Laser velocimetry and Rayleigh scattering techniques have also been used for this purpose. These techniques rely on particle seeding of the flow, which raises issues such as non-uniform seeding and bad flow representation due to the inertia of the particles. In spite of these difficulties, very good results were obtained with laser velocimetry by Lau [**20**] and more recently by Kerhervé *et al.* [**59**], and with Rayleigh scattering by Panda *et al.* [**60**] and Panda and Seasholtz [**61**]. PIV measurements have also been used extensively for that purpose by Bridges [**21**] and by Kastner *et al.* [**62**] to name only a few. However, while spatial resolution is no issue for this technique, the time resolution remains insufficient to produce accurate time correlations in supersonic jets.

As described earlier, Optical Deflectometry (OD) is used in The Pennsylvania State University jet noise laboratory in order to measure the turbulence properties necessary for proper modeling of the noise generation. As described in section **3.3.2.2**, the main type of measurement one can obtain from the OD system is a simple correlation of the time signal with different separation distance Δx_1 between the two optical sensors.

Recommendations were given in Chapter **5** on how to obtain meaningful measurements in shock containing jets as well as words of caution regarding the limitations of the system. A particularity of the OD setup is that it produces two point correlation measurements with very high frequency response. However, the nature of the system makes it difficult to interpret the light fluctuation to obtain specific values for the density (gradient), and while not impossible, calibration of the system in order to obtain a direct measurement of the density is still challenging. Another limitation of the system was uncovered by Doty and McLaughlin [**37**] who underlined the difficulties of obtaining meaningful measurements in hot and heat simulated jets. Therefore, this study focuses solely on cold jets.

While numerous measurements have been made in subsonic jets and in supersonic fully expanded jets, the database of correlation measurements in shock containing jets is very scarce. One of the most significant pieces of work on this topic was carried out by Harper-Bourne and Fisher [**8**], where correlations were obtained in a supersonic under-expanded jet. However, the specifics of the technique used raises questions regarding the nature of the correlations obtained.

The work presented in this part of this thesis investigates the influence of the shocks appearing in over- and under-expanded jets on the correlation of the turbulent structures. Radial correlations are first investigated in order to gain knowledge of the shape of the turbulent structures. Then axial correlations and convection velocities under different jet conditions are presented. In addition, direct correlations are made between measurements obtained in the flow field via the optical sensors and microphone measurements in the far field, providing some source localization of the noise radiated. Finally, measurements are made with the optical sensors in the near field, showing that detection of the sound via optical deflectometry is possible and can provide some correlation between the near field and the far field acoustic fields.

6.1 Correlation of optical measurements

Radial and axial correlations of the optical signals in the jet are first presented. The table below summarizes the jet conditions investigated in this part of the study. A variety of pressure ratios was investigated as well as two different 0.5" diameter nozzles: a contoured converging nozzle (M_d = 1.0) and a contoured converging-diverging nozzle (M_d = 1.5). Different axial ($\Delta x_1 / D_j$) and radial ($\Delta x_2 / D_j$) separations of the sensors were used as well as different starting axial locations (x_1 / D_j) of the correlations.

Table **6-1**: Table of conditions for OD measurements

M_d	M_j	x_1 / D_j	$\Delta x_1 / D_j$	$\Delta x_2 / D_j$
1.0	1.5	4.0	0	-.012 → 0.12
1.0	0.9	2.0, 4.0	0	-.01 → 0.1
1.5	1.5 & 1.7	4.0	0	-.012 → 0.12
1.5	1.3	4.0, 4.6	0	-.012 → 0.12
1.0	0.9	4	0.5	-.01 → 0.1
1.0	1.5	2.0, 4.0	0.5	-.01 → 0.1
1.0	0.7 → 1.56	4.0	0 → 1.5	0
1.5	1.0 → 1.65	4.0	0 → 1.5	0

As an example of correlation measurements the correllelograms of Figure **6-1** a), c) and d) represent the cross correlation functions obtained in jets of different conditions with an optical sensor fixed in the shear layer at x_1 / D_j = 4.0 and another one scanning in the x_1 direction. As an alternative to this representation, the length scale alone can be plotted by extracting from these cross-correlation functions the value of the correlation at zero delay time as a function of separation distances. The resulting plots are presented in Figure **6-1** b), d) and f). From these plots, the time scale L_{x1} and length scale L_τ of the turbulent structures can be evaluated as described in section **4.2.2**.

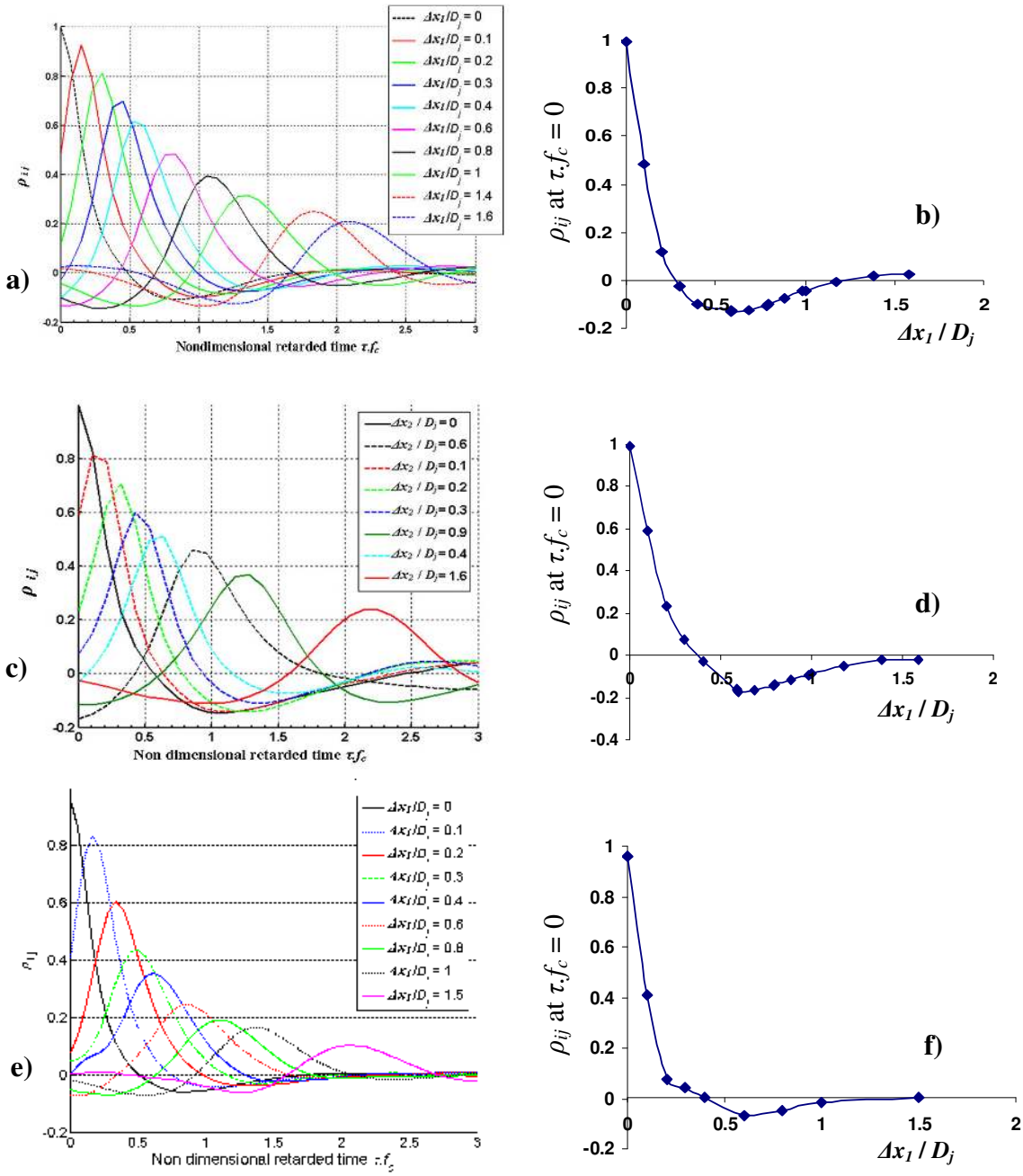

Figure **6-1**: Correllelograms and length scale measurements for a) and b) $M_d = 1.0$ and $M_j = 0.9$, c) and d) $M_d = 1.5$, $M_j = 1.3$, e) and f) a $M_d = 1.5$, $M_j = 1.5$ fully expanded jet. $x_1 / D_j = 4.0$, measurement along the lipline.

6.1.1 Radial correlation measurements

While the convection speed of the turbulent structures provides important information when modeling the flow field, some knowledge of the shape of the turbulent structures is required too. For that purpose, radial correlation measurements are performed for different jets and different downstream locations.

Cross-correlations are made across the mixing layer, by scanning in the radial direction in order to obtain some knowledge of the thickness and shape of the turbulence structures. For this purpose, the first photomultiplier was focused at the lip line of the nozzle ($x_2 / D_j = 0.5$), 4 diameters downstream of the exit plane ($x_1 / D_j = 4$). The second one was first positioned at the same downstream location and then moved up and down through the mixing layer. The resulting correllelograms are shown in Figure **6-2** for two different jet conditions. Their shape is very different from the typical measurements where the photomultiplier is moved in the downstream direction. The first thing that can be observed from these measurements is a change of sign of the time delay with different direction of displacement. When the second photomultiplier is displaced toward the center of the jet, the time delay at the peak of the correlation, τ_{peak} becomes negative. When it is moved outward, τ_{peak} becomes positive. This happens more or less symmetrically around x_2. Moreover, the magnitude of the correlation peak decreases with increasing distance between the two photomultipliers, in a way very similar to what is observed during axial correlations.

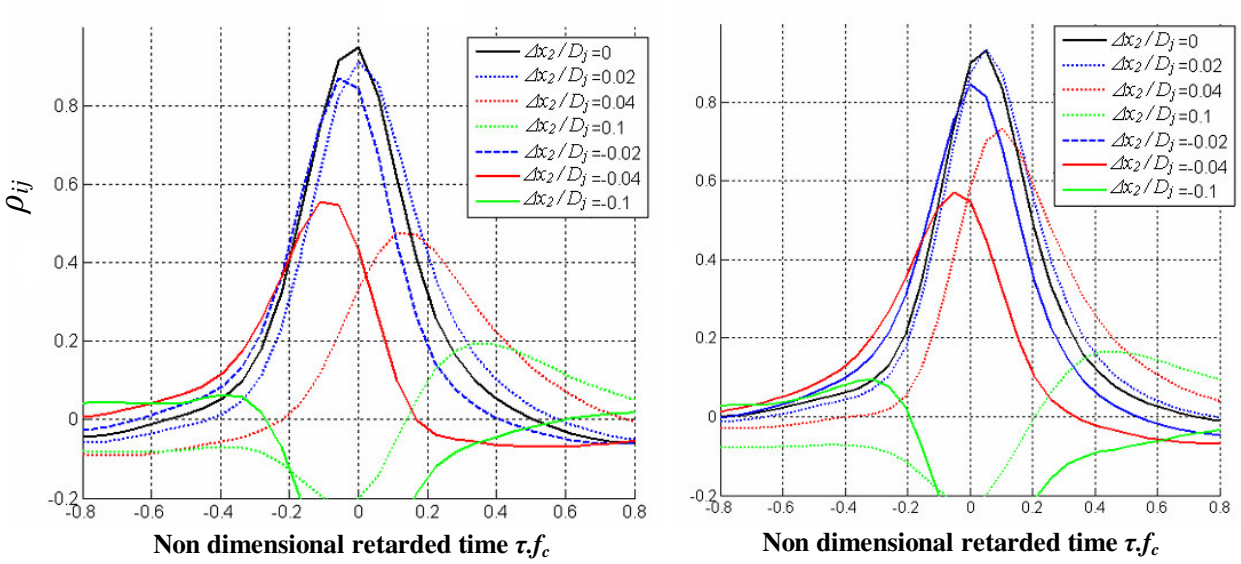

Figure **6-2**: Correllelograms across the mixing layer a) M_d = 1.0, M_j = 1.5 b) M_d = 1.5, M_j = 1.5.

In order to better understand the significance of these results, the non-dimensional radial displacement $\Delta x_2 / D_j$ can be plotted against the time delay at the peak of the correlation , τ_{peak}. Moreover, knowing the convection velocity of the turbulent structure U_c. , τ_{peak} can be interpreted as a non-dimensional axial displacement around x_1, $\Delta x_1 / D_j$, calculated as follow:

$$\Delta x_1 / D_j = -\tau_{peak} . U_c / D_j \qquad \textbf{6.1}$$

This results in a spatial correlation plot, shown in Figure **6-3** , where the correlation peaks follow a diagonal with an approximate angle of 16°. The fact that the peaks of correlation are along a diagonal means that the turbulent structures are strongly distorted along this line. In other words, the correlation "volume" of the turbulence in the shear layer distorts or shears as it convects axially downstream, and the radial length scale is very small. This supports the idea that the source can be treated as compact in the radial direction. This result is consistent with measurements made by Harper-Bourne [**63**] with hot wires in a M_j = 0.18 jet. In their measurements, a 2 to 3 ratio was found between the radial and axial correlation length, leading to an angle very similar to the one observed in the present study. It is also consistent with results obtained with PIV by

Fleury *et al.* [**64**] who observed an angle of 18° all over the shear layer of subsonic jets at $M_j = 0.6$ and $M_j = 0.9$. This pattern can be attributed to the effect of the mean shear flow on the turbulence, producing some anisotropy.

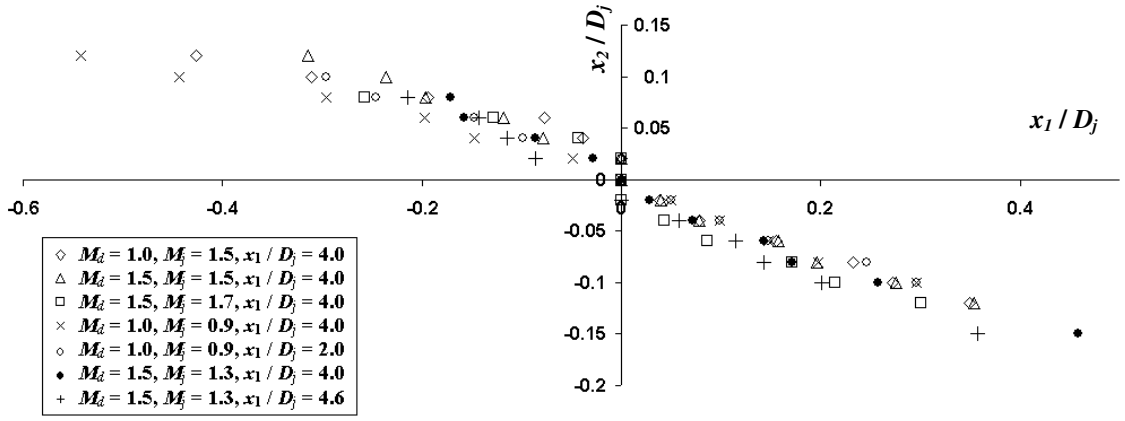

Figure **6-**3: Spatial distribution of the correlation peak through the shear layer of different jets

Moreover, for all the jet conditions shown in Figure **6-3**, the angle at which these structures are skewed is the same. Two of these conditions correspond to under-expanded jets, where strong shocks are present in the flow and interact with the mixing layer, while the last conditions correspond to an over-expanded jet. They all match well with the measurements made in fully expanded jets, despite different downstream locations (ranging between 2 and 4 jet diameters). Therefore, multiple shock interactions with the mixing layer do not affect the shape of the turbulent structures.

6.1.2 Axial correlation measurements

Axial correlation measurements are very important for modeling of the noise generated. They enable the speed of the convecting turbulent structures to be determined, which in turn provides information on the large scale turbulence noise production and the emission of Mach waves. These turbulent structures also interact with the shock cells in imperfectly expanded jets, producing the broad band shock associated noise.

Measurement of axial correlations was obtained for different jet conditions following the methodology described in section **3.3.2.2**. Qualification experiments made in under-expanded M_j = 1.5 jets and presented in section **4.2** underlined the importance of screech suppression in order to obtain quality correllelograms. The results presented here were obtained with a combination of physical screech suppression and electronically removed screech, as prescribed earlier in section **4.2**.

The first observation one can make when making this kind of measurement in a shock containing jet is that the mixing layer does not have a simple conical shape, as is the case in a fully expanded jet. The presence of barrel shocks in strongly shock containing cases increases the difficulty of the measurements. The cross-correlation functions presented in Figure **6-4** offer a representation of the variation in the cross-correlation with small radial displacement of the downstream sensor. These measurements were obtained in a M_d = 1.0, M_j = 0.9 jet at x_1 / D_j = 4.0 and an axial separation distance of the sensors $\Delta x_1 / D_j$ = 0.5 for different radial displacements values $\Delta x_2 / D_j$.

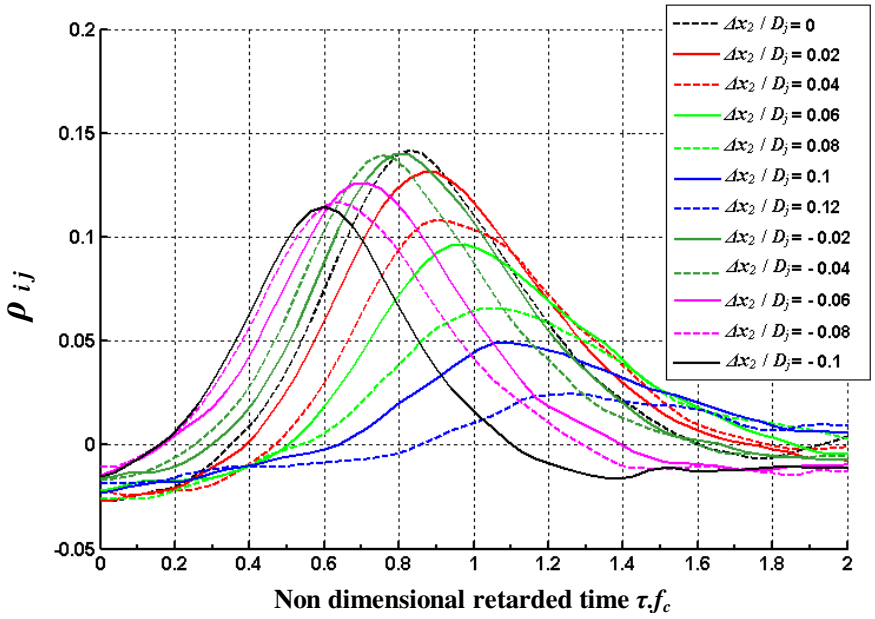

Figure **6-4**: Correlation functions recorded in an M_j = 0.9 jet with $\Delta x_1 / D_j$ = 0.5 and various $\Delta x_2 / D_j$ values and x_1 / Dj =4.0.

In this subsonic jet, the maximum of correlation is obtained for $\Delta x_2 / D_j = 0$. This means that in order to perform proper axial correlation measurements and extract from it a meaningful convection velocity, the moving optical sensor can simply be moved in the downstream direction, following the mixing layer.

Similar measurements were then made in a shock containing jet. Figure **6-5** a) presents cross correlation curves obtained in a $M_d = 1.0$, $M_j = 1.5$ jet at $x_1 / D_j = 2.0$ and an axial separation distance of the sensors $\Delta x_1 / D_j = 0.5$ for different radial displacements $\Delta x_2 / D_j$. As can be seen, this time, the maximum of correlation is not obtained for $\Delta x_2 / D_j = 0$ but rather for $\Delta x_2 / D_j = -0.04$. This means that the convecting turbulent structures have moved in the radial direction too and therefore proper convection speed measurement can only be achieved by using the peak correlation value at this radial displacement. The schlieren image of Figure **6-5** b) shows the location of the sensors in the jet, and it is clear that this radial displacement is due to the barrel shape of the shock cell structure. Such shapes only appear in strongly under-expanded cases.

While the presence of barrel shocks is problematic when making axial correlation measurements at small x_1 / Dj locations, their effect is less visible on the correlation further downstream. Figure **6-6** presents cross correlation curves obtained in a $M_d = 1.0$, $M_j = 1.5$ jet at $x_1 / D_j = 4.0$ and an axial separation distance of the sensors $\Delta x_1 / D_j = 0.5$ for different radial displacements $\Delta x_2 / D_j$. From this graph, it is quite clear that the peak of correlation is not obtained for $\Delta x_2 / D_j = 0$, however, it is difficult to precisely locate the exact position at which the peak of correlation is maximized. This may be due to the thickening of the mixing layer, and the fact that the barrel shape is less sharply defined this far downstream. Therefore, caution should be applied when trying to explain the convection velocity measurements in shock containing jets.

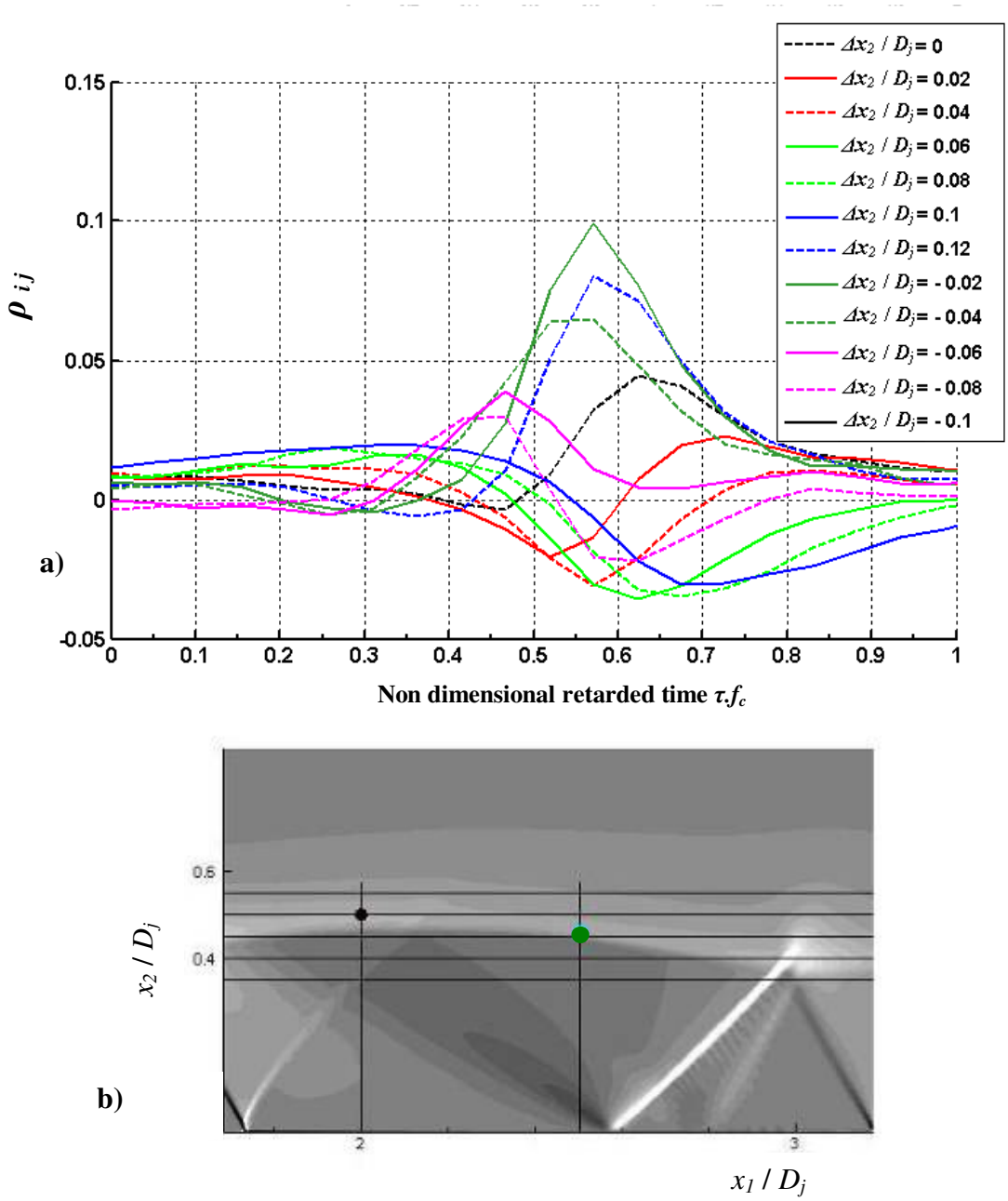

Figure **6-5**: a) Correlation functions in an $M_d = 1.0$, $M_j = 1.5$ jet with $\Delta x_1 / D_j = 0.5$ and various $\Delta x_2 / D_j$ and $x_1 / Dj = 2.0$. b) location of fixed sensor (black) and sensor with maximum correlation (green).

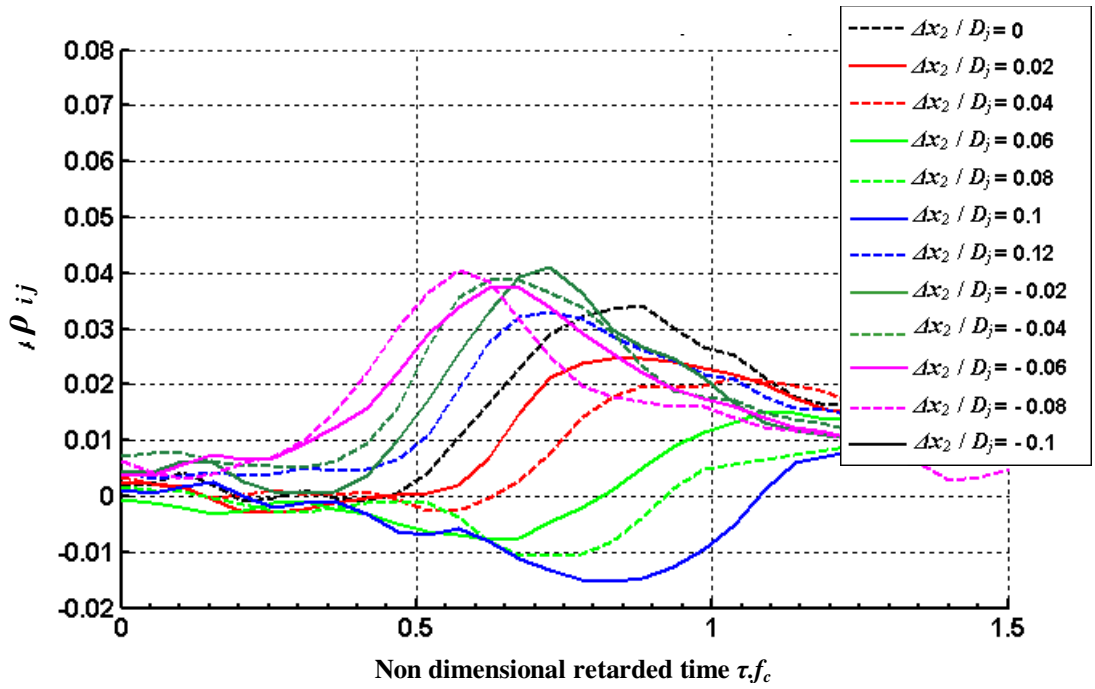

Figure **6-6**: Correlation functions recorded in an $M_d = 1.0$, $M_j = 1.5$ jet with $\Delta x_1 / D_j =$ 0.5 and various $\Delta x_2 / D_j$ and $x_1 / Dj = 40$.

Bearing in mind the difficulties in gathering reliable convection velocity measurements in shock containing jets, data were obtained for a variety of jet conditions. Sample correllelograms obtained for a $M_d = 1.5$, $M_j = 1.3$ jet is presented in Figure **6-7**. From these correllelograms, the convection velocity varies with both the jet Mach number and the design Mach number of the nozzle. Therefore, the convection velocity is tentatively plotted against the off-design parameter β defined in Equation Eq. **1.7**. For more general nozzle geometries and operating conditions, β is defined as follow:

$$\beta = \sqrt{\left| M_j^{\,2} - M_d^{\,2} \right|} \qquad \textbf{6.2}$$

The resulting plot is shown in Figure **6-8.** Part of the data was acquired with a purely converging nozzle running at different pressure ratios resulting in a range of M_j values between 0.7 and 1.56. The other part represents measurements made with a converging-diverging $M_d = 1.5$ contoured nozzle running at pressure ratios leading to a range of M_j between 1.0 and 1.5.

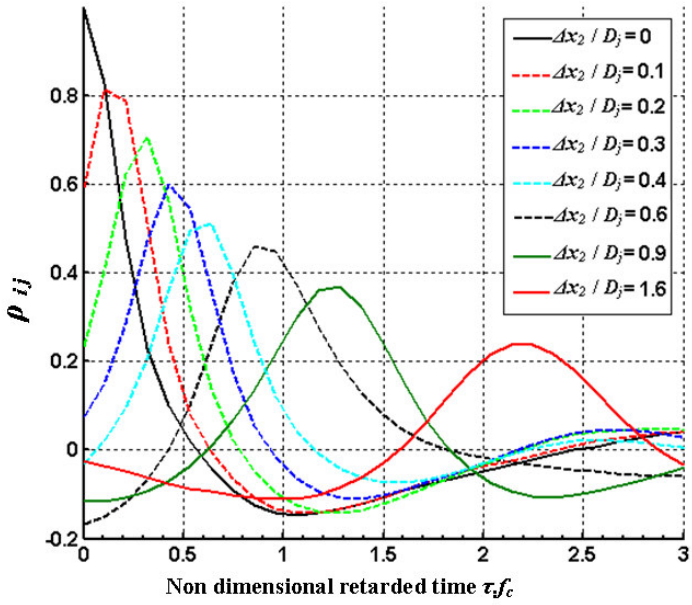

Figure **6-7**: Cross-correlation functions measured at the lipline and $x_1 / Dj = 4.0$ in a $M_d = 1.5$, $M_j = 1.3$ jet.

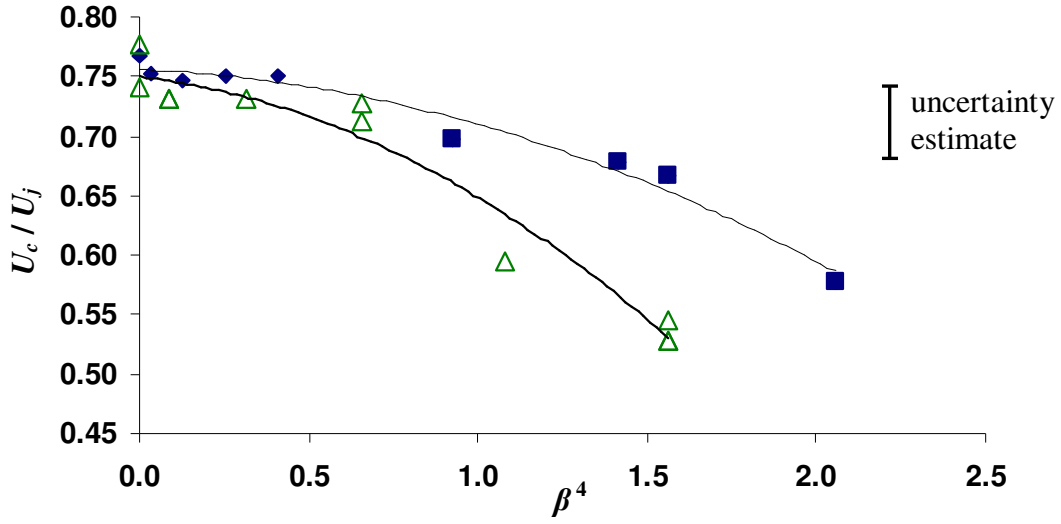

Figure **6-8**: Measured convection velocity as a function of β^4 for different jet pressure ratios and design Mach number Δ $M_d = 1.5$ over-expanded, ♦ $M_d = 1.0$ under-expanded, ■ $M_d = 1.0$ under-expanded.

These plots show that the convection velocity gradually decreases with the pressure imbalance parameter. This decrease is stronger for jets emanating from choked M_d = 1.0 nozzles as discussed by Veltin and McLaughlin [**65**]. However these results have experimental uncertainties that prevent us from drawing definitive conclusions.

6.1.3 A closer look at the convection velocity

In a flow with different turbulence scales, proper modeling can only be achieved if information is gathered for the entire frequency range. Therefore, in a convective mixing layer that radiates noise, it is important to gain knowledge on the relative speed of the frequency components of the turbulence. For that purpose, one can examine the phase of the cross spectra, noted $\Phi_{Sij}(f)$, between the fixed sensor and the one that is moved downstream. $\Phi_{Sij}(f)$ can be computed for each frequency band and plotted for every available separation distances of the two probes, as shown in Figure **6-9** for four different jet conditions. On these plots, the phases are shown in radians and the measurements were made at a downstream location $x_1 / D_j = 4.0$ and on the lipline.

From these measurements of $\Phi_{Sij}(f)$, the convection velocity can be calculated as a function of frequency. The convection velocity is calculated from the change of phase with separation distance as follow:

$$U_c(f) = \omega \Big/ \left(\frac{d\,\Phi_{S_{ij}}(f)}{d\,x_1} \right)$$
$$\text{or} \quad U_c(f) = 2\pi.f \Big/ \left(\frac{d\,\Phi_{S_{ij}}(f)}{d\,x_1} \right) \qquad \textbf{6.3}$$

In the case of these experimental data, the slope of the phase is evaluated at each frequency for all available separation distance and averaged as follows:

$$\left(\frac{d\,\Phi_{S_{ij}}(f)}{d\,x_1} \right) = \left[\sum_{k=1}^{n} \left(\Phi_{S_{ij}}(f) \right)_{\eta_{1k}} \Big/ \Delta x_{1k} \right] \Big/ n \qquad \textbf{6.4}$$

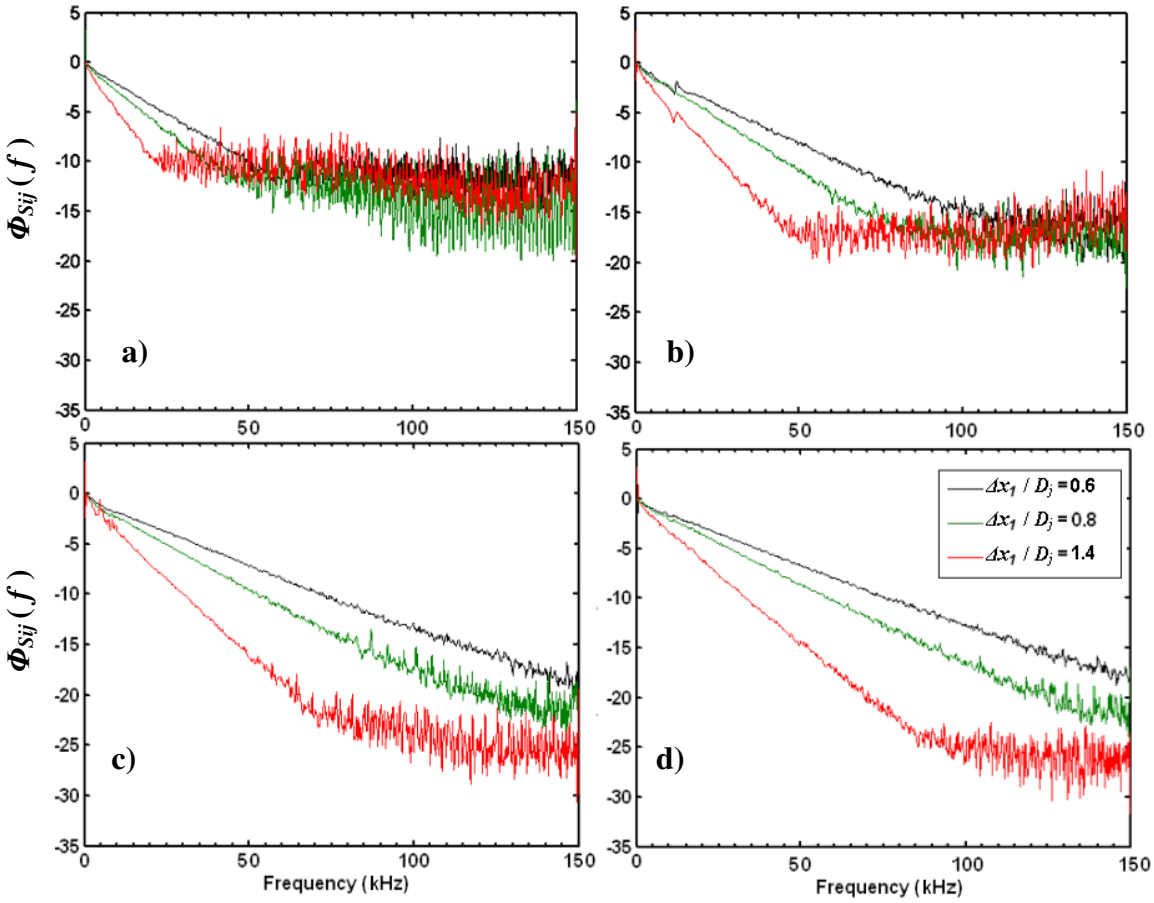

Figure **6-9**: Phase in radians as a function of frequency for 3 different separation distance of the optical sensors in jets issuing from a M_d =1.5 nozzle at a) M_j = 1.1, b) M_j = 1.3 c) M_j = 1.5, d) M_j = 1.65. Measurements at x_1 / D_j = 4.0 on the lipline.

The resulting convection velocity $U_c(f)$ is plotted in Figure **6-10** for several jet Mach number conditions and the CD nozzle designed at M_d = 1.5 at a downstream location x_1 / D_j = 4.0 and on the lipline. In this figure, comparison is made with similar measurements obtained by Troutt and McLaughlin [**16**] with a M_j = 2.0 jet. Their convection velocity measurements are in general agreement with the results obtained in the highest speed case, M_j = 1.65. The general logarithmic shape of these results also matches closely to results obtained by Harper-Bourne [**63**] with hot wire anemometers in a M_j = 0.18 jet, in spite of the large difference in Mach number and by Kerhervé [**59**]

with $M_j = 0.75$ and $M_j = 0.9$ jets. The results presented here also highlight some variation with the speed of the jet. Higher speed jets have a higher convection velocity (normalized with the jet velocity) on the whole frequency range of the measurement.

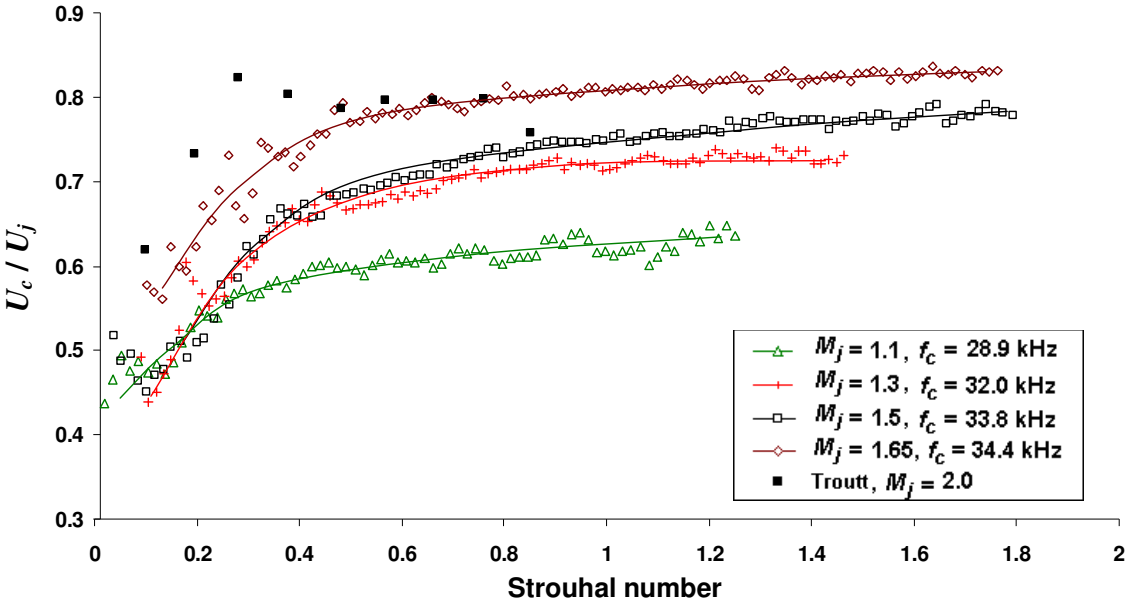

Figure **6-10**: Convection velocity as a function of frequency for jets of different speed issuing from a $M_d = 1.5$ contoured nozzle.

6.2 Flow field correlation with near field and far field acoustics

In an attempt to provide direct evidence of the noise generation inside the jet and possibly some localization of the noise generators, simultaneous measurements of the flow field fluctuating properties and the acoustic far field are made. While testing for the new Optical Deflectometry system described in section **3.3.2.4** and in Appendix **A**, four sensors were used to make simultaneous acquisition and correlations between optical sensors in the jet and in the near field with microphones in the far field. Data were first gathered at the Penn State facility. Later experiments were conducted at the University of California Irvine by the author and Dr. Papamoschou and his team. Some of the most important results from these experiments are highlighted in the following pages.

Most experiments reported here were conducted with a supersonic contoured converging-diverging (CD) nozzle designed for shock free flow at M_d = 1.5. The nozzle was operated over a range of pressure ratios yielding average Mach numbers on the centerline for the first several diameters of M_j = 0.5 to 1.8. In addition, a purely converging nozzle was operated over a similar range of pressure ratios in order to investigate strongly shock containing jets. The matrix of experimental conditions for these experiments is presented in Table **6-2**.

Table **6-2**: Experimental conditions for correlation measurements between OD sensors and far field microphones.

Nozzle		**Conditions**		**Mic Array**	**APD Location**
Shape	M_d	M_j	T_0/T_a		
Round D = 0.5"	1.50	0.9 -> 1.8	1.0	Configuration 1	Configuration 1
Round D = 0.5"	1.50	0.5 -> 1.8	1.0	Configuration 1	Configuration 2
Round D = 0.5"	1.00	1.3 -> 1.8	1.0	Configuration 2	Configuration 2

Each conducted experiment involves acquiring data from the 4 avalanche photo diodes (APDs) in the optical deflectometer system and 4 microphones on a polar array in the far-field. At this point, it is important to note that the acoustic measurements obtained during these experiments were compared to typical acoustic measurements and did not show any sign of contamination due to the presence of the OD setup in the anechoic chamber. Two different configurations of the microphone array and optical sensors are presented in this part of the thesis, as illustrated in Figure **6-11**. The first microphone configuration (Configuration 1) has microphones in the rear arc arranged at polar angles of 24˚, 27˚, 34˚, and 45˚ at a radius of 50 diameters centered around 5 diameters downstream on the centerline of the jet. The second configuration has microphones placed in the forward arc with polar angles of 104˚, 109˚, 119˚, 134˚ at a radius of 42 diameters centered on a point 5 diameters downstream of the nozzle exit. Both configurations have microphones in the same plane as the OD sensors.

The first configuration of optical sensors has the first pair of sensors along the lipline of the jet and the other pair outside of the jet in an attempt to capture signals from the near field sound. The second configuration has all 4 sensors along the lipline of the jet, in the mixing layer.

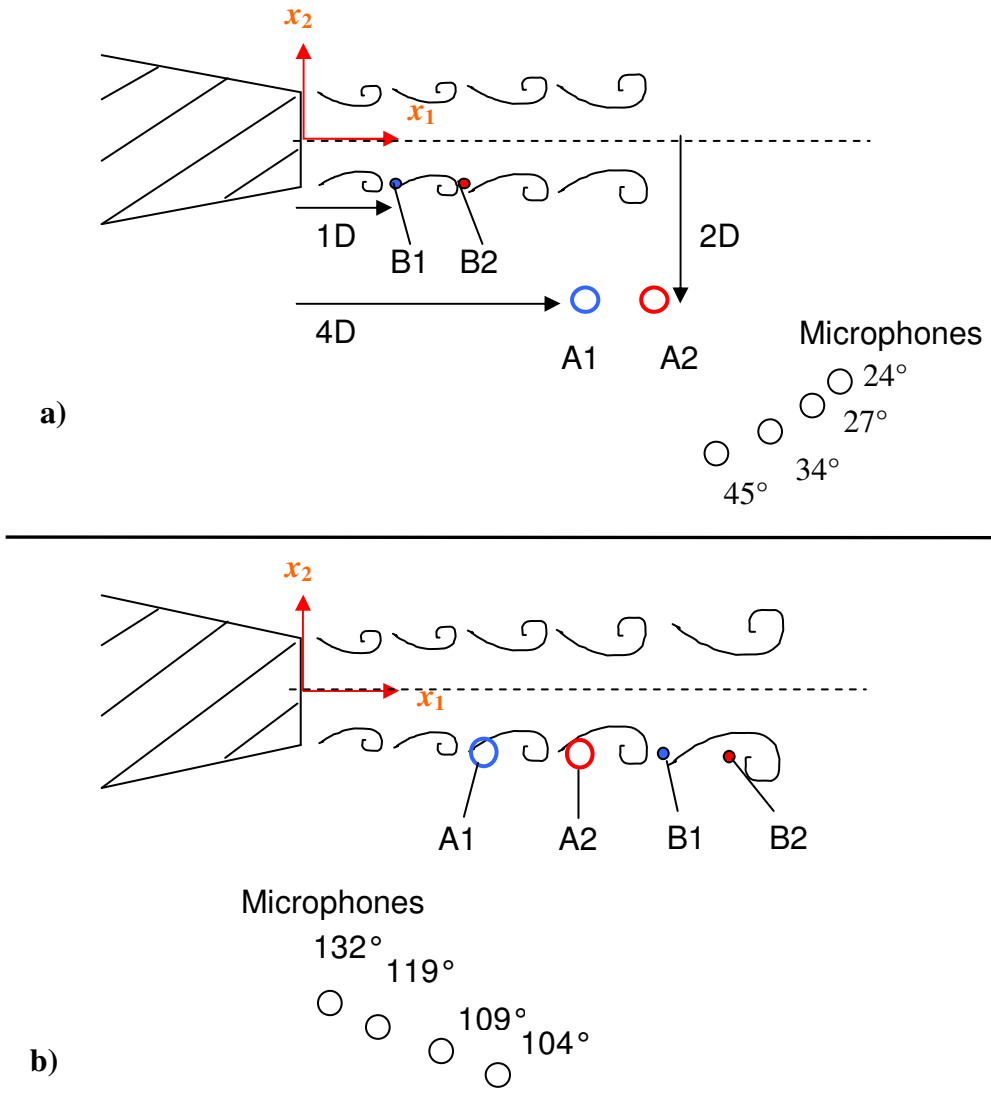

Figure **6-11**: Configurations of the microphones and APDs. a) microphones and APDs in configuration 1, b) microphones and APDs in configuration 2. (Not to scale)

6.2.1 OD-correlation with microphones in the rear arc

As a first try of flow field versus far field acoustic correlations, experiments were conducted on the correlation between the OD sensors in the shear layer of the jet and a polar microphone array in configuration 1. Four correllelograms comparing each OD sensor to the microphones in the rear arc for a jet with M_d = 1.5 M_j = 1.5 are shown in Figure **6-12**. Correlation peaks are obtained between the APDs in the flow and the microphones in the far field. The maximum peak of correlation found in this configuration is approximately 0.1.

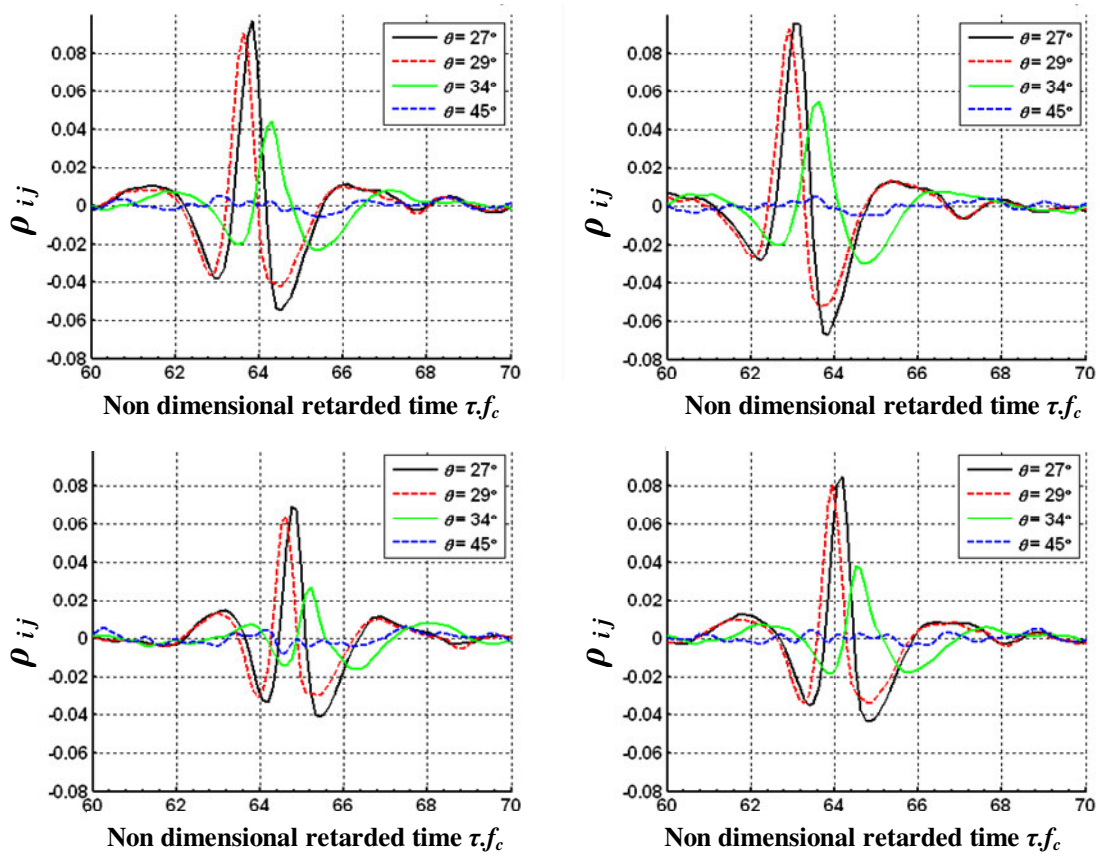

Figure **6-12**: Correlations between each OD sensor and microphones in the rear arc for M_d = 1.5, M_j = 1.5, f_c = 34.1 kHz.

Each OD sensor shows the same pattern of correlation with the microphones. They each showed the highest correlation with microphones at 27 and 29 degrees, roughly half as much correlation at 34 degrees, and nothing at 45 degrees. It is quite interesting that there is such a noticeable difference between these correlations across such a small range of polar angles (as little as 10 degrees from 30°).

In an attempt to find a trend in the peak correlation values and microphone polar angle, a plot of the two values was generated and is shown in Figure **6-13**. In this figure, each line consists of the peak correlations obtained with the OD sensor across the range of microphone polar angles, and each group of lines corresponds to a different jet Mach number. This attempt is complicated by the fact that many of the conditions are shock containing jets. Since the OD sensors are fixed and the shock patterns change with the jet Mach number, the relative position of the APDs to the shocks is changing.

One trend is quite clear from these measurements: the correlation peak between the APDs and the microphones shifts to higher value of polar angle with increasing jet speed. For the two highest jet conditions, one could therefore argue that this peak corresponds to the propagation angle of Mach waves radiated by the jets. However, non negligible amount of correlation are also obtained in the jets with speed lower than M_j = 1.2, suggesting that some of the physical phenomena responsible for the generation of the turbulent mixing noise is captured by the APDs and subsequently correlate with the measured noise.

Changes in peak correlation with axial location of the OD sensor was more closely investigated in the perfectly expanded condition. A plot showing the peak correlation obtained with each of the 4 microphones and OD sensors at several axial locations is shown in Figure **6-14**. These results underline the increase of correlation between the optical sensors and the microphones for microphones located at shallow angles. However, definitive conclusions will only be possible with more refined measurements of similar jets and with the positioning of the OD sensors further downstream.

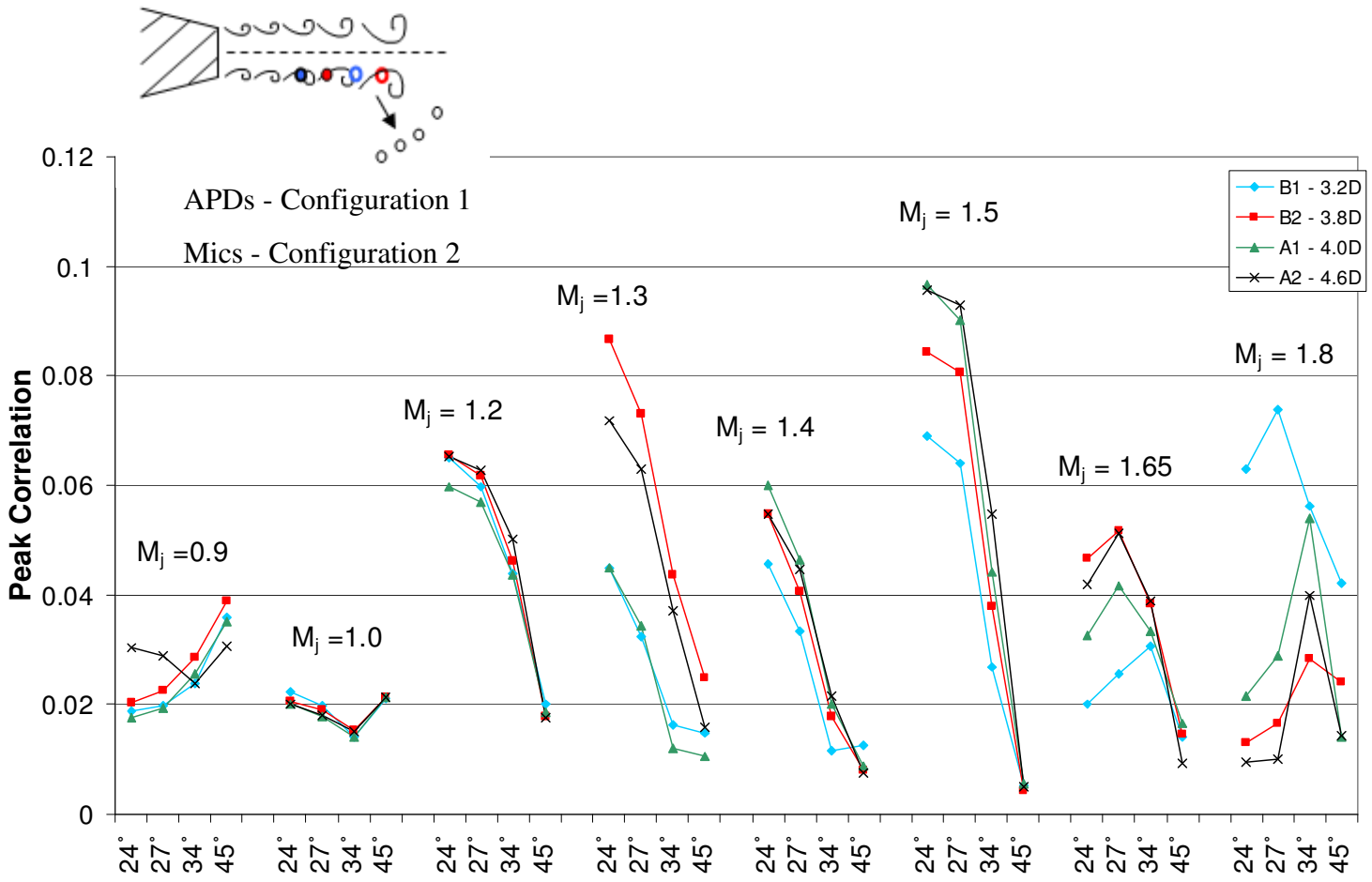

Figure **6-13:** Peak correlation between OD sensors in the shear layer and microphones in the rear arc for M_d = 1.5, operating at various pressure ratios (and M_j values).

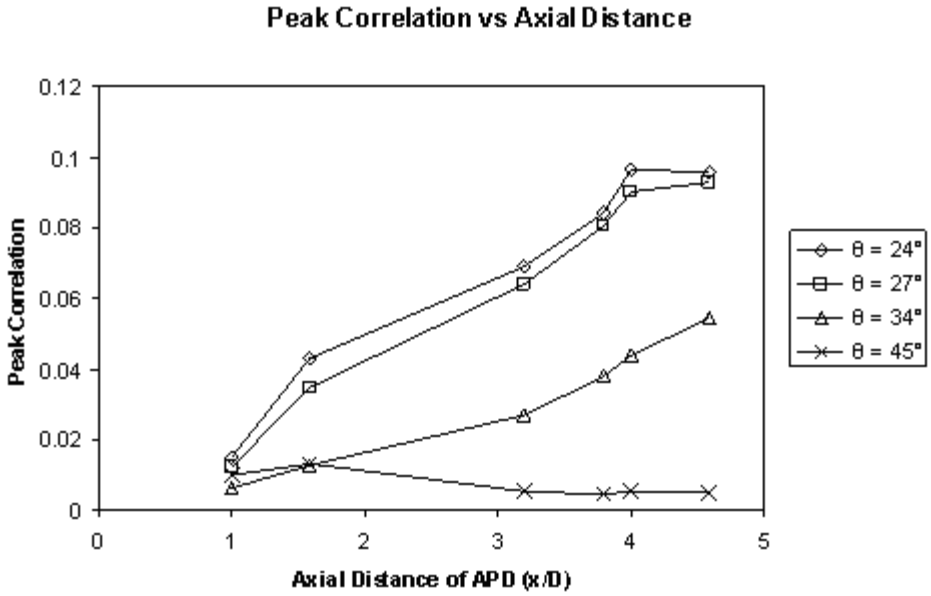

Figure **6-14:** Peak correlation between OD sensors and microphones in the rear arc with OD sensor at various axial locations in $M_d = 1.5$, $M_j = 1.5$ jet.

Experiments were also conducted with 2 of the OD sensors (A1 and A2) located outside of the jet (configuration 1 of the APD, as shown in Figure **6-11**). These sensors were located at 4 and 5 diameters downstream from the nozzle exit and 2 diameters from the jet centerline. The sensors were positioned outside the jet in an attempt to capture Mach wave radiation. The 2 other OD sensors (B1 and B2) were located at 1 and 2 diameters from the nozzle exit at the lip line.

With this configuration, higher correlations were recorded with the OD sensors positioned outside the flow than with the sensors in the shear layer. A correllelogram showing this result for a $M_j = 1.8$ jet is shown in Figure **6-15** . Sensor A2 outside of the flow displays a much higher correlation than sensor B2 in the jet for every polar angle of the microphones. No trend between jet Mach number and correlation level was observed, as can be seen from the plot of Figure **6-16**. Similar levels of correlation are measured when the large scale turbulence convection velocities are supersonic and subsonic. This

suggests that Mach waves may not need the (average) turbulence convection Mach number to exceed unity.

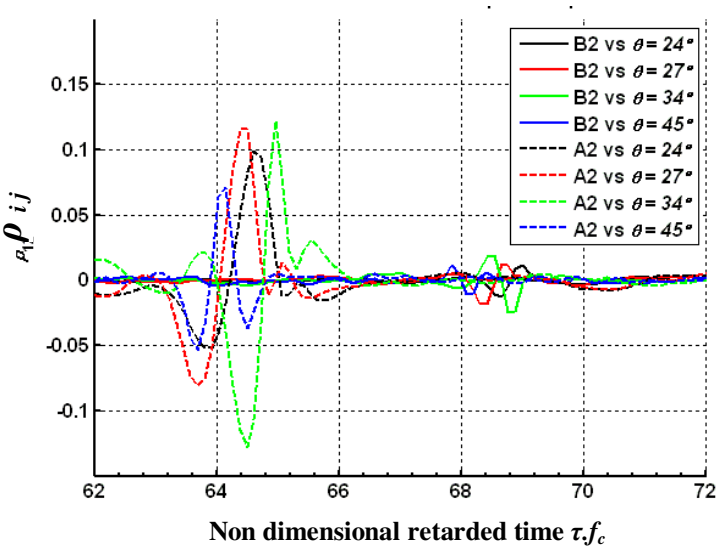

Figure **6-15**: Correllelogram for microphones and OD sensors positioned in the shear layer and outside of the jet with M_d = 1.5, M_j = 1.8. Microphones in the rear arc.

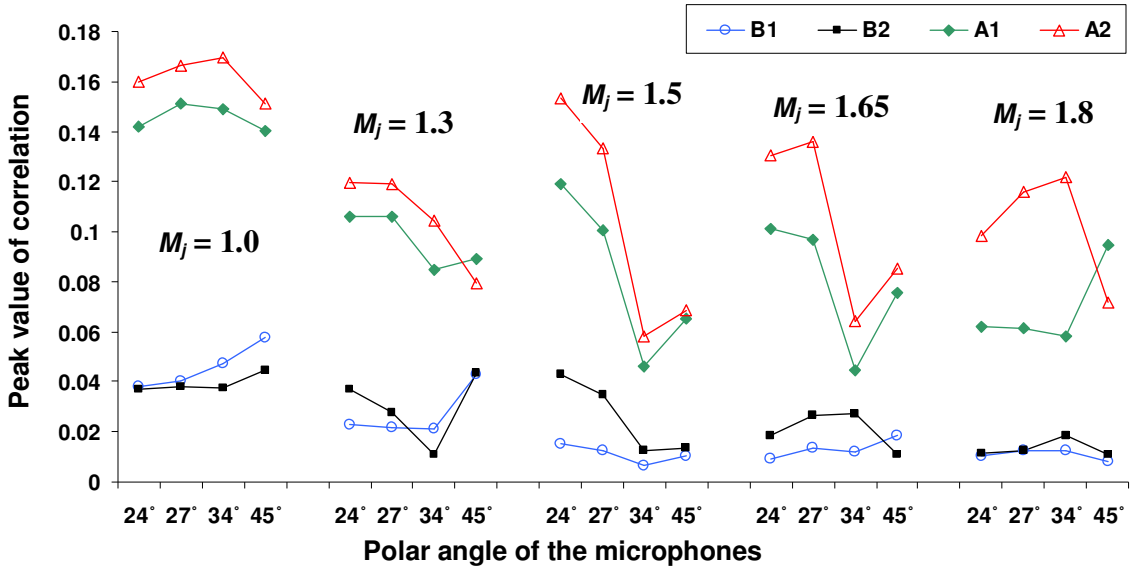

Figure **6-16**: Peak values of the correlation between APDs in configuration 1 (A pair in the near field, B pair in the shear layer) and microphones in the rear arc. M_d = 1.5.

6.2.2 OD correlations with microphones in the forward arc

Another set of experiments was conducted to study shock associated noise. The experiments were done with the microphone array repositioned in the forward arc – configuration of the microphones, as shown in Figure **6-11**. The OD sensors A2 and B2 were approximately positioned on the second and third shock-shear layer interaction points as represented by points marked on the schlieren photograph shown in Figure **6-17** (configuration 2 of the APDs as shown in Figure **6-11**). A second experiment moved a pair of OD sensors to the first shock layer interaction point with these points labeled as B1' and B2' in the figure. The sensors were positioned at 1.5, 2.1, 2.7, 3.3, 4.2, and 4.8 diameters downstream from the nozzle.

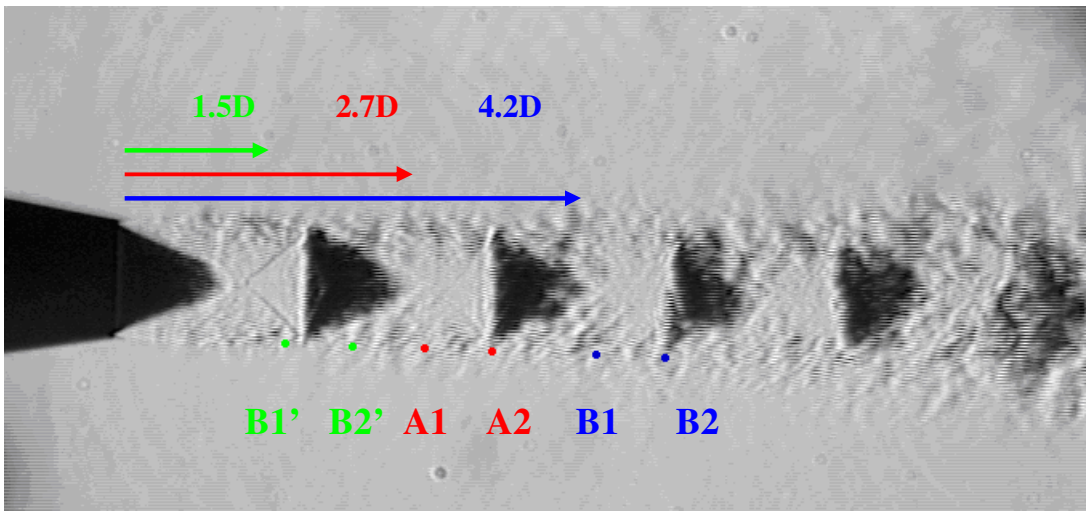

Figure **6-17:** Schlieren photograph of M_d = 1.0, Mj = 1.5 jet with APD sensor locations marked.

The OD sensors in the flow field were successfully correlated with microphones in the forward arc. The highest correlation obtained with this configuration was only 0.037 though. The sensor with the highest correlation is located between the second and third shocks. There is not a strong trend for the sensors at the shock – shear layer interaction point correlated better than the ones positioned between shocks. Four correllelograms comparing each OD sensor to the microphones in the forward arc in a

Mach 1.5 jet can be seen in Figure **6-18** . Once again the trend between axial location of the OD sensors and peak correlation was investigated. The change in peak correlation with axial distance of the OD sensor is shown in Figure **6-19** for a jet with M_d = 1.0 and M_j = 1.5. Peak correlation is seen to increase as axial distance increases until 4 diameters downstream.

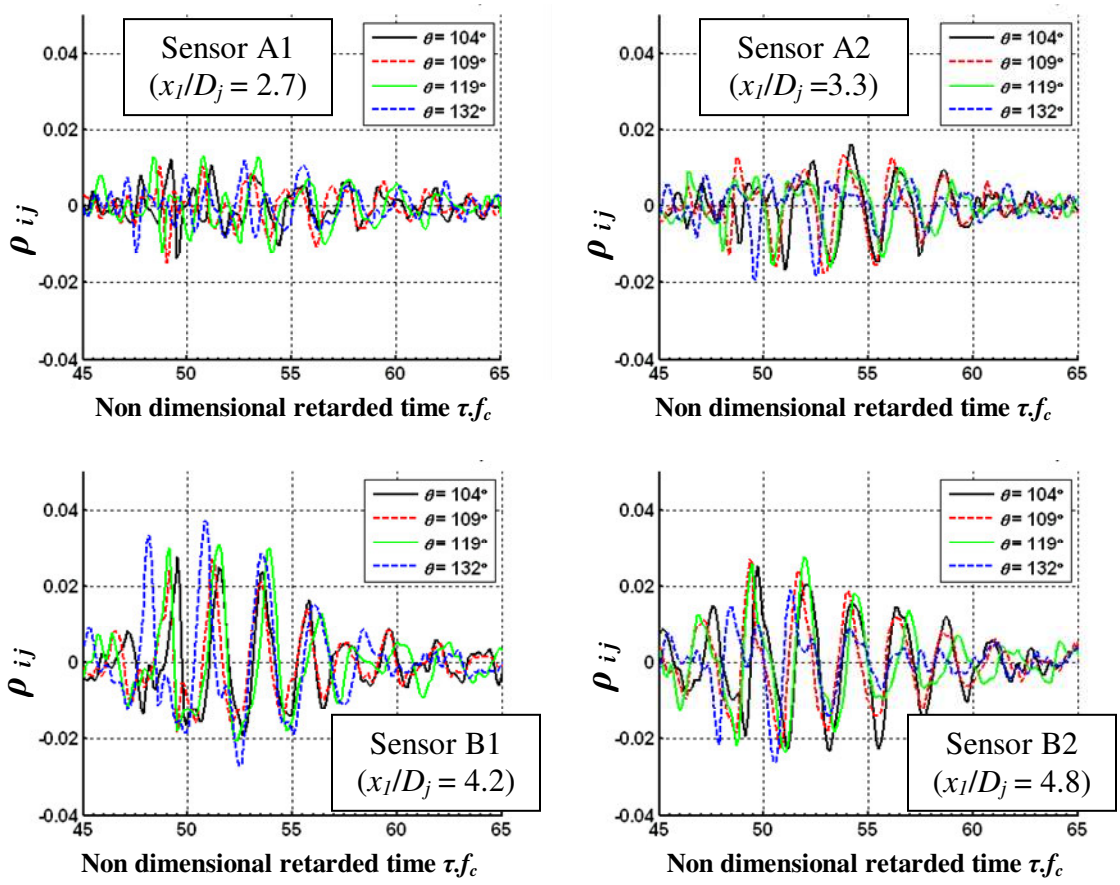

Figure **6-18**: Correlations between each OD sensor and microphones in the forward arc for M_d = 1.0, M_j = 1.5, f_c = 31.2 kHz.

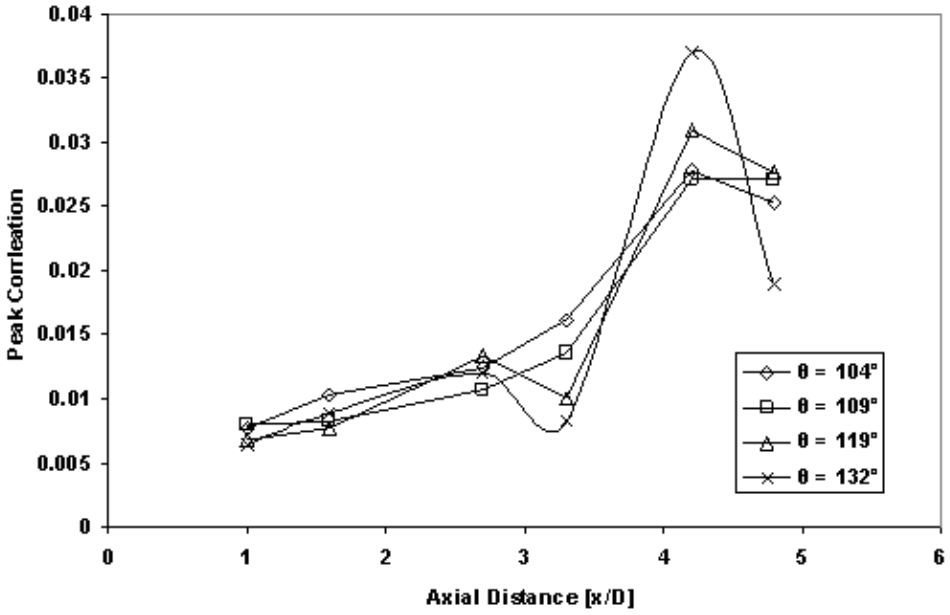

Figure **6-19**: Peak correlation between OD sensors at different axial locations and microphones in the forward arc for M_d = 1.0, M_j = 1.5.

The peak of correlation can also be plotted for different off-design conditions, as shown in Figure **6-20**. In this plot, there is not a strong trend between the value of the peak of correlation and the polar location of the microphones. There isn't any strong trend either with changes of Mach number of the jet, except maybe a slightly higher correlation for the APDs furthest downstream (B pair) in the M_j = 1.5 case than in any other off-design conditions. This might be due to the location of this pair of sensors relative to the shock cell patterns. Much more refined measurements will be necessary to obtain definite results.

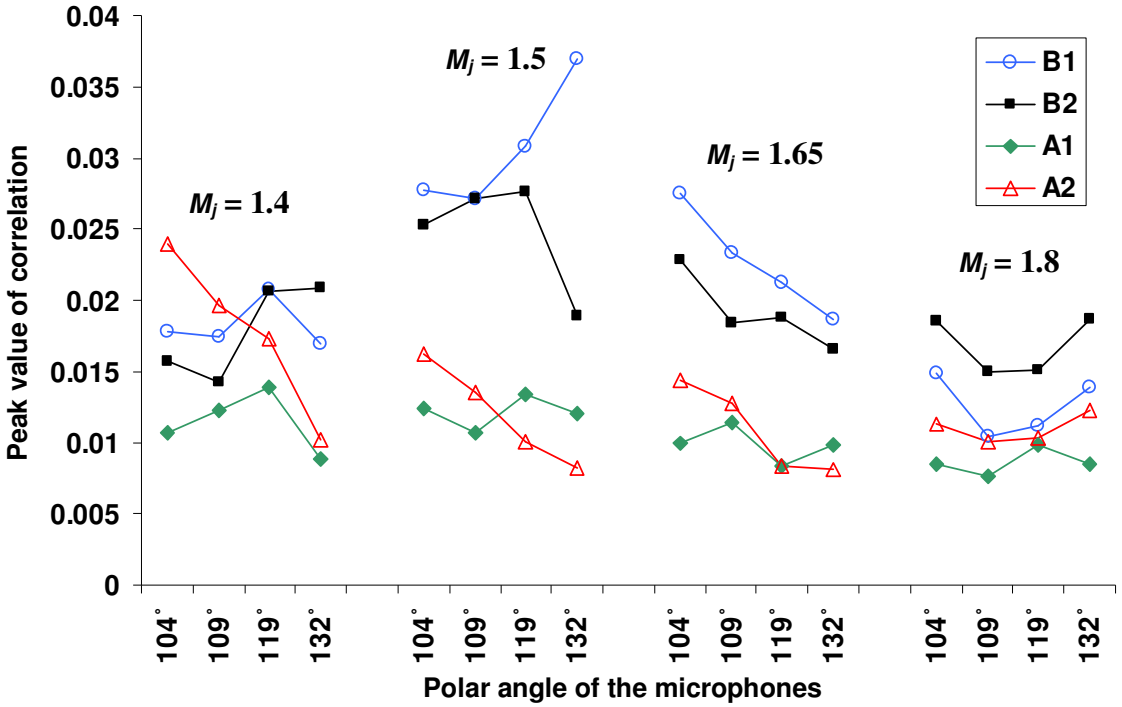

Figure **6-20**: Peak values of the correlation between APDs in the shear layer and microphones in the forward arc. M_d = 1.0.

Overall, less correlation was found between OD sensors in the shear layer and microphones in the forward arc than with microphones in the rear arc. The auto and cross spectra between an OD sensor and microphones in the rear arc and in the forward arc are shown in Figure **6-21** . The difference in spectral shape is clearly visible between the two microphone locations. The APDs spectra are identical since they are almost located at the same location in both cases, but the cross-spectra clearly show which part of the APD signals are correlating with the acoustic measurements. The microphones in the forward arc show correlation over a different frequency range than microphones in the rear arc. The correlating part of the signal corresponds to the shock associated noise for microphones in the forward arc and to broad band mixing noise for the rear arc measurements.

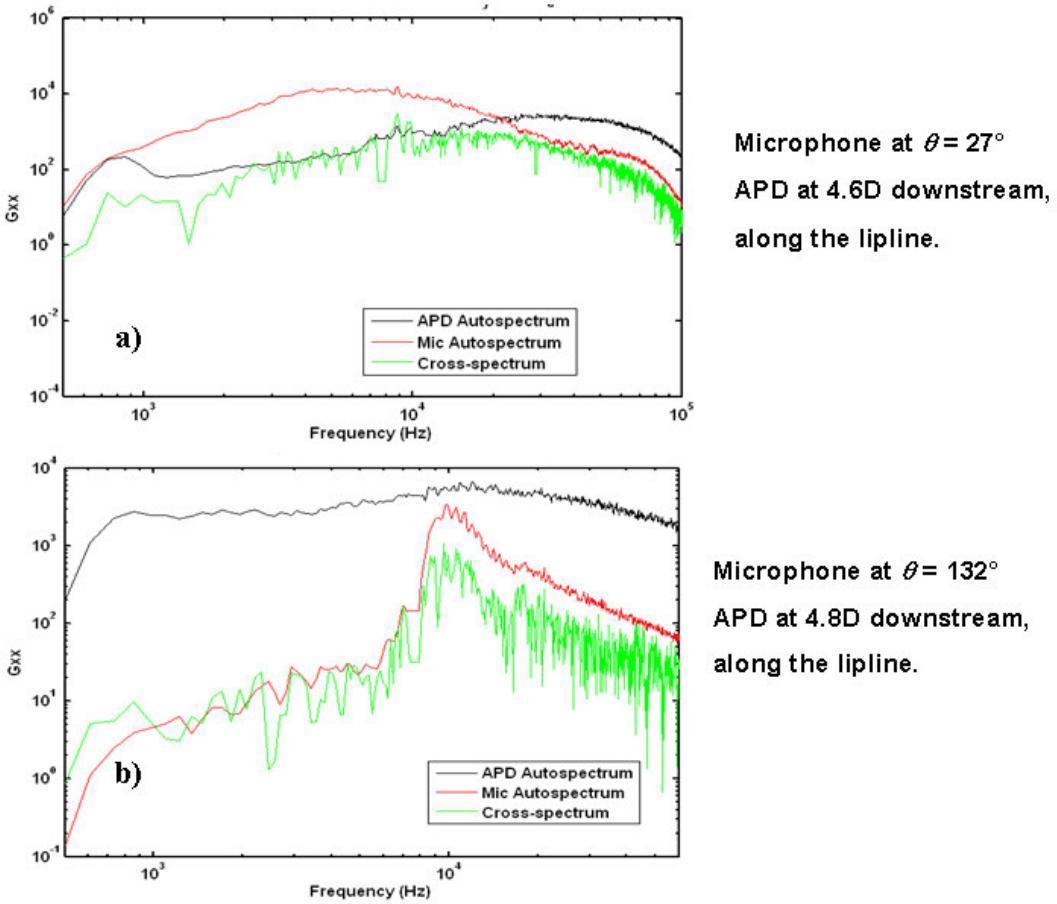

Figure **6-21**: M_d = 1.5, M_j = 1.8, auto and cross correlation of an APD and a microphone in the a) rear arc b) forward arc.

6.3 Investigation of a fully expanded M_j = 1.75 jet

6.3.1 Preliminary results

Following the successful correlation of the flow features with the propagated noise at The Pennsylvania State University, similar measurements were performed with the same setup in the Jet Noise Facility of the University of California Irvine. The four optical sensors were located inside and outside of the jet, and simultaneous acquisition

was obtained with an 8 microphones polar array located 70 jet diameters from the jet exit plane. A complete survey of a fully expanded M_j = 1.75 jet (U_j = 474 m/s) was performed, with the optical sensors scanning the jet centerline, lipline, and the near field around the jet. Figure **6-22** below offers a representation of the locations of the APDs used for the measurements. The microphones (in green) are fixed, the red pair of APDs is fixed for one set of experimental data and the blue pair is moved around the flow field.

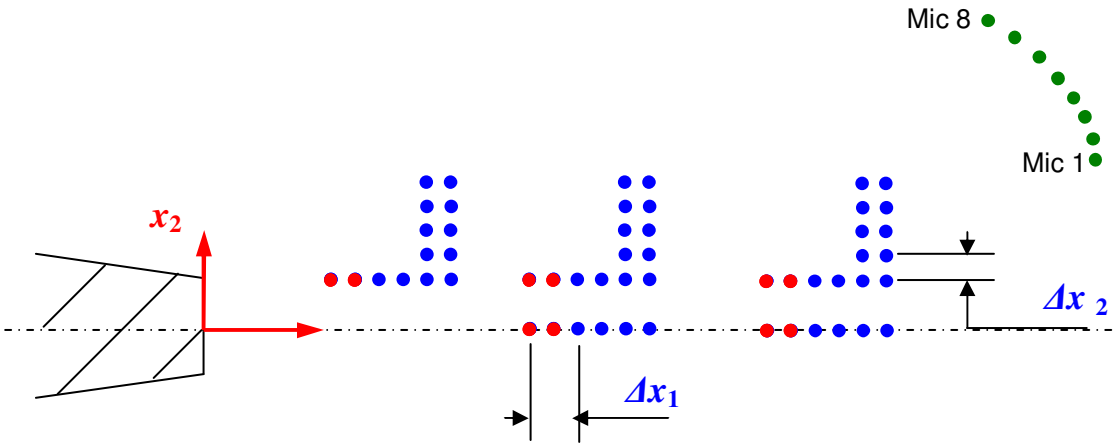

Figure **6-22**: Schematic drawing of the optical sensor locations.

Typical cross-correlation function curves can be extracted from these data in order to produce a correllelogram, shown in Figure **6-23** . The decay rate is consistent with previous measurements and the convection velocity calculated from these correlations is approximately 402 m/s, leading to U_c / U_j = 0.85. This in turn results to predicted Mach wave radiation at an angle μ = 58° from the jet axis. The resolution of the correllograms is slightly less accurate than the ones typically produces at Penn State due to the limited acquisition speed of 160 kHz. This reduced acquisition speed was necessary in order to be able to simultaneously acquire data from the 4 optical sensors and the 8 microphones. Therefore, some curve fitting was applied between the data points. The resulting correllelogram looks very similar to the prvious measurements. The increase in phase shift with increasing frequency is also consistent with previous measurements.

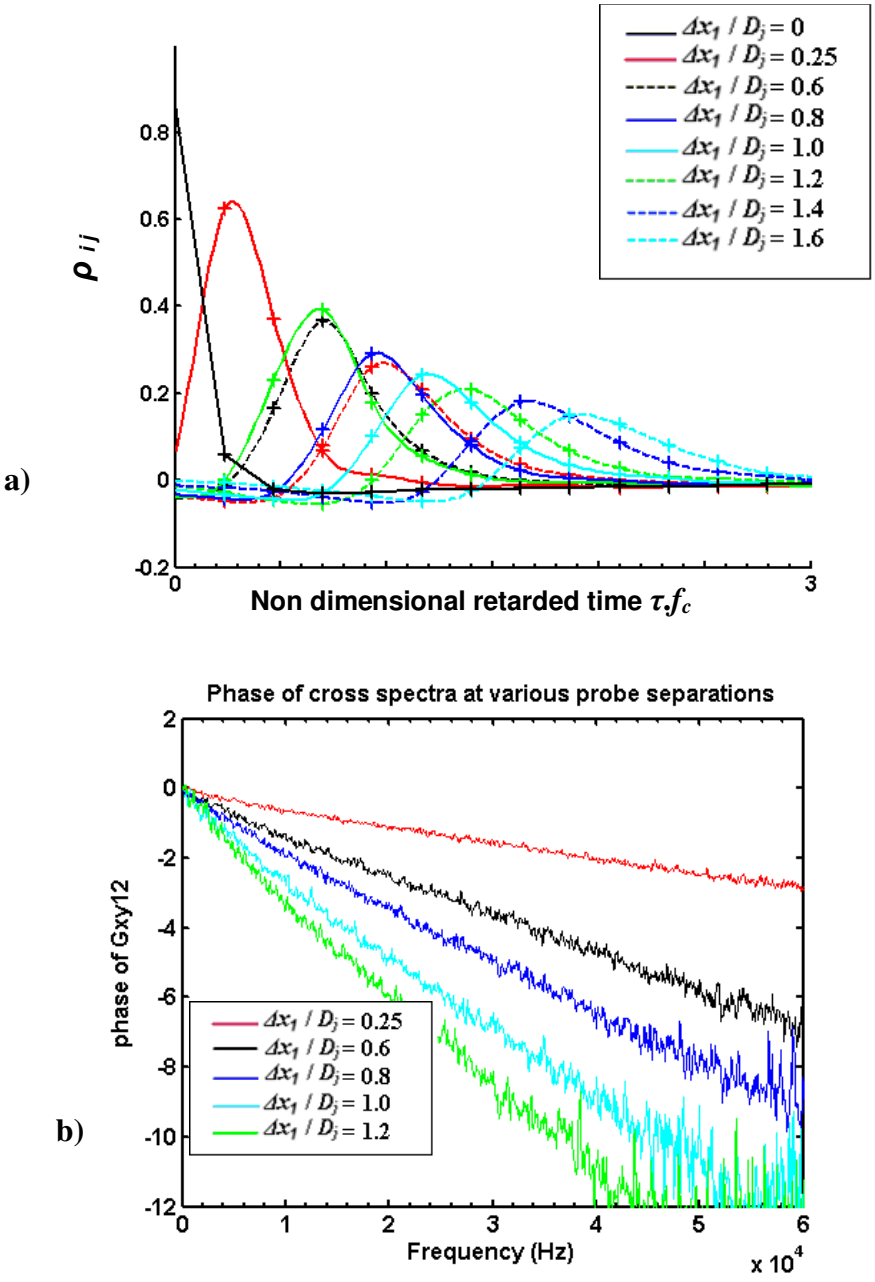

Figure **6-23**: Cross correlation functions and phase of the cross spectra measured in a fully expanded $M_j = 1.75$ jet.

Different quantities are extracted from these experiments in order to localize the noise generation in the jet. In a jet with such high speed, the turbulence convects at a supersonic speed, producing Mach wave radiation that results in a peak in the OASPL. Furthermore, a clear signature of the presence of Mach waves in the measured noise is the

presence of a strong positive skewness (defined in Eq. **3.9**). The value of the skewness as well as the OASPL are calculated for each microphone and plotted in Figure **6-24**. The skewness reaches a peak around 30 degrees, while the OASPL is the highest for that same polar angle value. This concurs with the prediction of the Mach wave radiation angles computed from the convection velocity that gave μ = 58°, which corresponds to a polar angle θ = 32°.

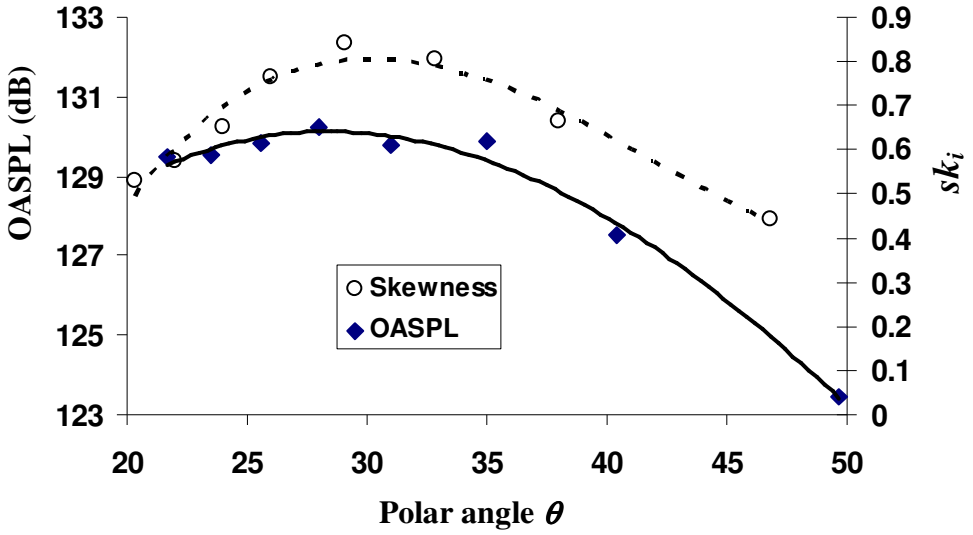

Figure **6-24**: Skewness and OASPL as a function of polar angle for a $M_d = M_j = 1.75$ jet.

6.3.2 Optical signals in the jet

The rms value of the APD signals can then be examined in order to try and visualize the parts of the flow with high fluctuations of density. This in turn gives a measurement of the amount of turbulence in the jet for different locations. The rms is plotted along the centerline and the lipline of the jet and presented in Figure **6-25**. Words of caution were expressed in section **4.3.3** regarding the usage of the OD system slightly inside of the jet. When making measurements on the centerline, the sensing volume

traverses the whole jet. However, the density gradients in the mixing layers being mainly in the radial direction, they do not dominate the signal, as it was the case when making measurements slightly below the mixing layer. The centerline measurements can therefore be considered to represent to some extend the light fluctuations induced by the density gradients in the core of the jet. The signal strength shown in Figure **6-25** reaches a peak at about $x_1/D_j = 9$ on the lipline, while on the centerline, this maximum occurs at around $x_1/D_j = 13$. Therefore, one would expect the noise generation at the centerline and the lipline to reach a peak at these same locations. Another observation that can be made from this plot is that the maximum rms value of the signal measured on the lipline of the jet is noticeably higher than the maximum value of the signal measured on the centerline. On the other hand, when the rms of the OD signal measured along the centerline reaches its maximum, it is higher than at the corresponding lipline location. Therefore, one would expect the noise generation location to progressively switch from the centerline to the lipline between $x_1/D_j = 9$ and $x_1/D_j = 13$.

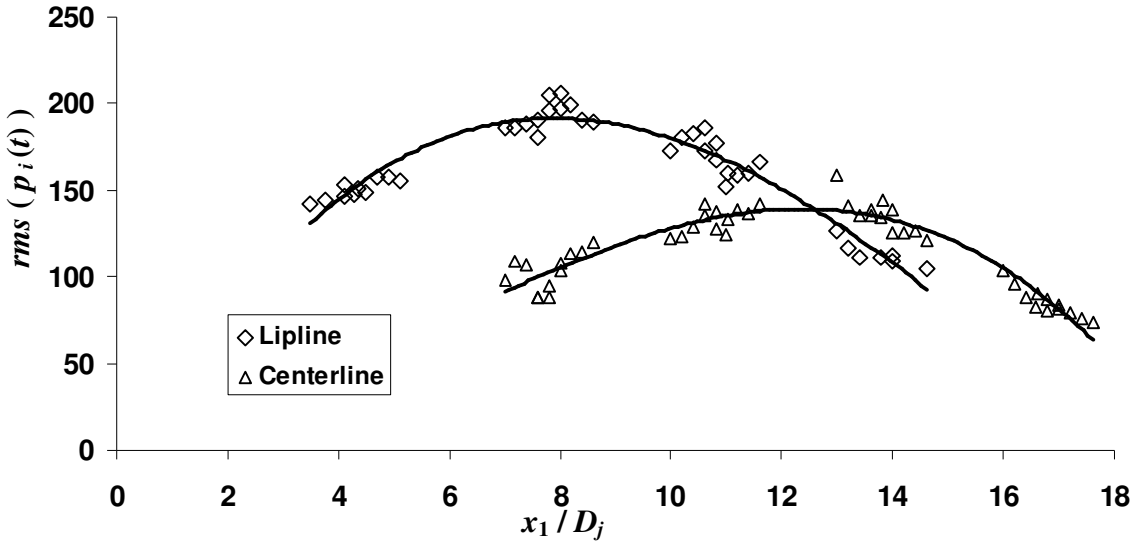

Figure **6-25**: rms values of the OD signals along the axial direction in a fully expanded $M_j = 1.75$ jet.

The correlation between the optical sensors in the flow and the far field microphones can then be investigated. While the microphones are directly measuring pressure fluctuation, the physical meaning of the signal from the optical sensor is less clear. The measurement relates to fluctuations of density gradient and it is not clear if a positive or a negative correlation should be expected with microphone measurements. Therefore, both the negative and the positive peaks are plotted, as shown in Figure **6-26.** This graph presents the correlation peaks between an optical sensor scanning the jet shear layer and a microphone fixed at approximately $\theta = 22.5°$. Obviously, for this polar angle, there are two peaks of correlation: around $x_1 / D_j = 4$ and $x_1 / D_j = 10$. The strength of these peaks varies whether the negative or positive peaks are considered. However, the trend is relatively similar.

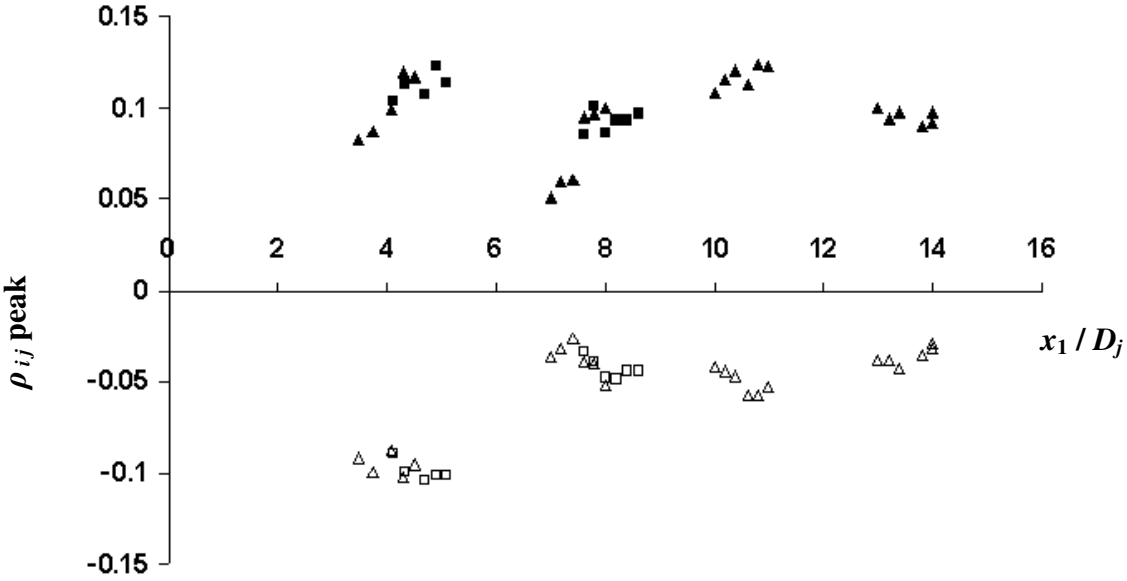

Figure **6-26**: positive(■ ▲) and negative (□ Δ) values of the peak of correlation between an optical sensor scanning the jet lipline and a microphone at $\theta = 22.5°$.

Next, the positive peak of correlation between the far field microphones and the optical sensor at the lipline and the centerline is plotted for different polar location of the microphones. Due to the presence of Mach wave radiation, the peak of correlation is expected to be obtained for the microphones located at the polar angle at which the Mach waves propagate. The resulting graphs are presented in Figure **6-27** and show these

correlations for both the lipline and the centerline of the jet. The amount of correlation does not vary strongly with microphone polar angle between 20 and 30 degrees. However, it does decrease significantly for larger polar angles of the microphone. It also varies significantly with downstream location. On the lipline, the correlation reaches a peak at about 10 jet diameters downstream of the exit plane. On the centerline, the peak of correlation also appears further downstream, at around 13 diameters. These distances approximately match the locations observed earlier in Figure **6-25** for the maximum rms value of the OD signals.

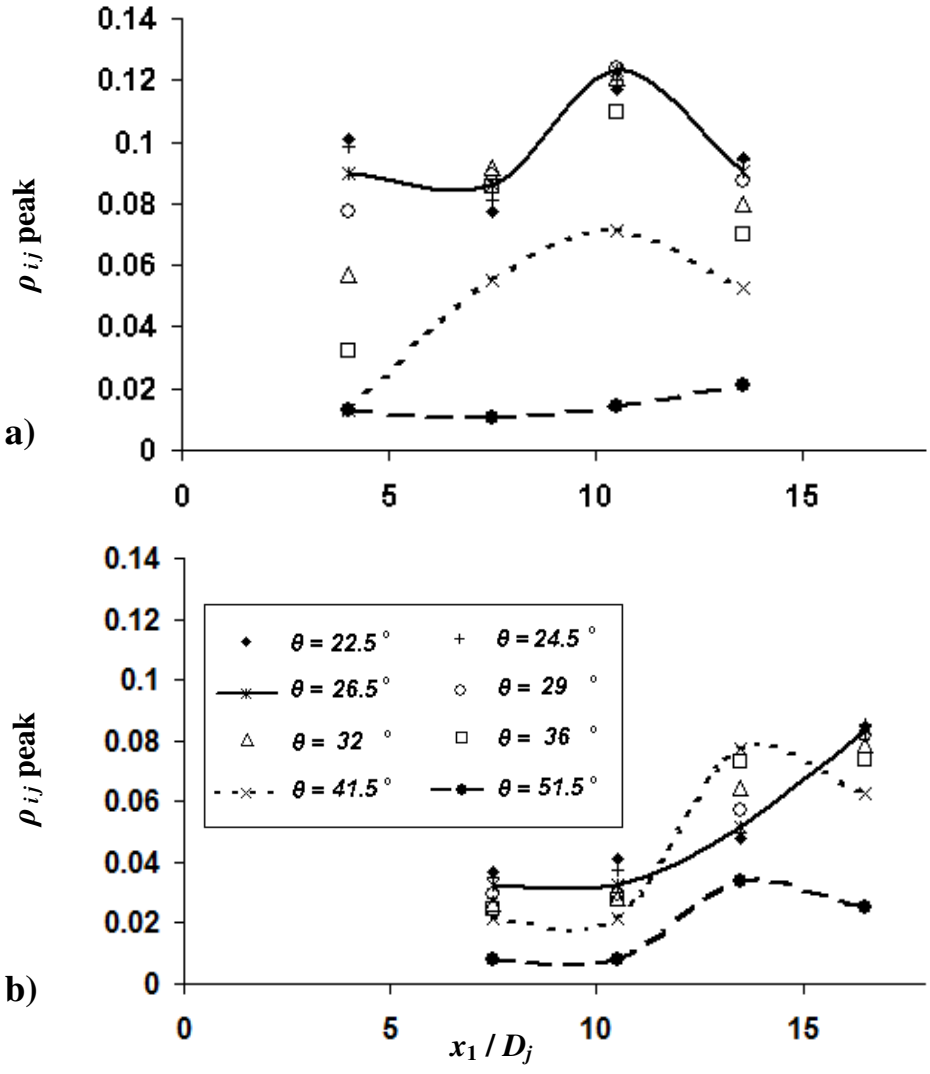

Figure **6-27**: Correlation peaks between microphones at different polar angle and OD sensors at a) the lipline b) the centerline of a $M_d = M_j = 1.75$ jet.

The coherence between the optical signal and the microphones can also give some relevant information concerning the frequency bands that correlate. Figure **6-28** presented below shows the coherence between an optical sensor at the lipline of the jet and different downstream locations and a microphone fixed at $\theta = 32°$. A first obvious observation from these cross-coherence functions is that there is a change of the amplitude of the coherence. The highest coherence is obtained for $x_1 / D_j = 10$ and significantly lower coherence is observed for the other downstream locations. This confirms the observations made in Figure 6-26 where it was observed that the cross-correlation function was the highest for $x_1 / D_j = 10$. Then, one can observe that the frequency at which the coherence peaks varies with downstream location. The peak is very broad for $x_1 / D_j = 3.5$, and centered around $St = 0.6$, while it shifts to a much lower value, around $St = 0.25$ for $x_1 / D_j = 13$. While this shows that the sound measured by the far field microphones correlates with the turbulence measurement in a very wide region of the jet, it also demonstrates that the frequency components of the propagated sound are generated in a specific region of the flow. The highest frequencies are generated close to the exit plane while larger frequencies issue from further downstream. This concurs with results obtained by Papamoschou and Dadvar [**66**] who used a polar microphone phased array to localize the sound sources in the jet as a function of frequency bands. There again, the high frequencies of the generated sound were seen to be generated close to the nozzle exit plane and the lower frequencies further downstream.

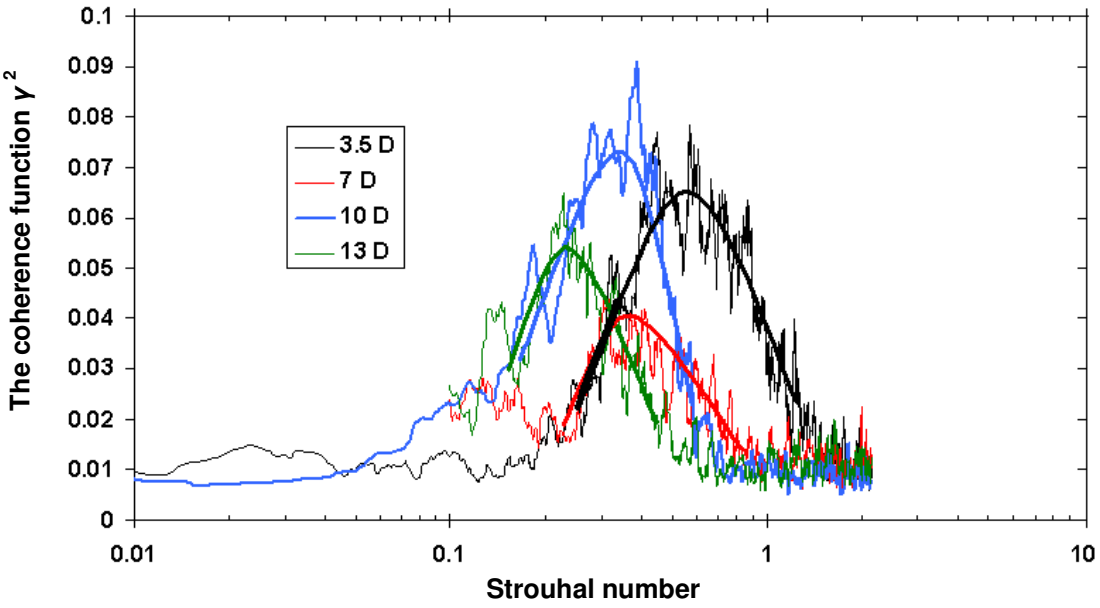

Figure **6-28**: Coherence function between OD sensors on the lipline at varying x_1 / D_j locations and a microphone in the acoustic far field at $\theta = 32°$. $M_d = M_j = 1.75, f_c = 37.3$ kHz.

6.3.3 Optical measurements in the near acoustic field

Scanning of the near field is obtained with the optical sensors, as was previously presented in the diagram of the experiments shown in Figure **6-29**. The rms values of the optical signals is first calculated and plotted against the axial location x_2 / D_j. As expected the strength of the signals drops significantly when the sensors exit the jet, reaching very small values when $x_2 / D_j > 1.5$. The same observation is true for all downstream locations, with a change of the rms value for different x_1 / D_j locations, as was observed earlier in Figure **6-25**.

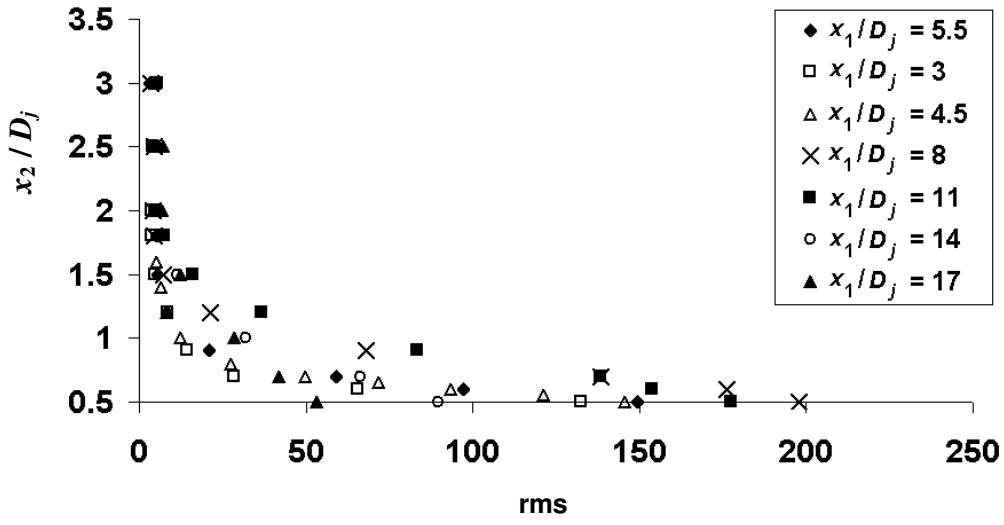

Figure **6-29**: rms values of the optical signals at different axial locations (x_1 / D_j) and radial positions (x_2 / D_j).

The peaks of correlation can be calculated between optical sensors in the jet with the ones that scan the near field. Figure **6-30** presents the value of the correlation between an optical sensor located at different positions x_1 / D_j along the lipline of the jet and another optical sensor located a distance $\Delta x_1 / D_j = 1$ downstream of the first sensor and scanning the near field in the radial direction. There is obviously some high correlation for no radial displacement of the second sensor, since it measures the propagation of the flow structures. With increasing values of $\Delta x_2 / D_j$, the amount of correlation first drops as the sensor exits the jet and then increases again, showing correlation peaks as high as 0.25. Since the sensor is now in the near acoustic field, this tends to show that this correlation corresponds to noise radiated by the structures passing through the location of the first sensor. With increasing axial locations of the pair of sensors, this correlation peak flattens in the radial (x_2) direction and disappears all together at $x_1 / D_j = 7$. This shows that the part of the sound that dominates the near acoustic field and is measured by the sensor that is outside of the jet is only produced at distances relatively close to the jet exit plane.

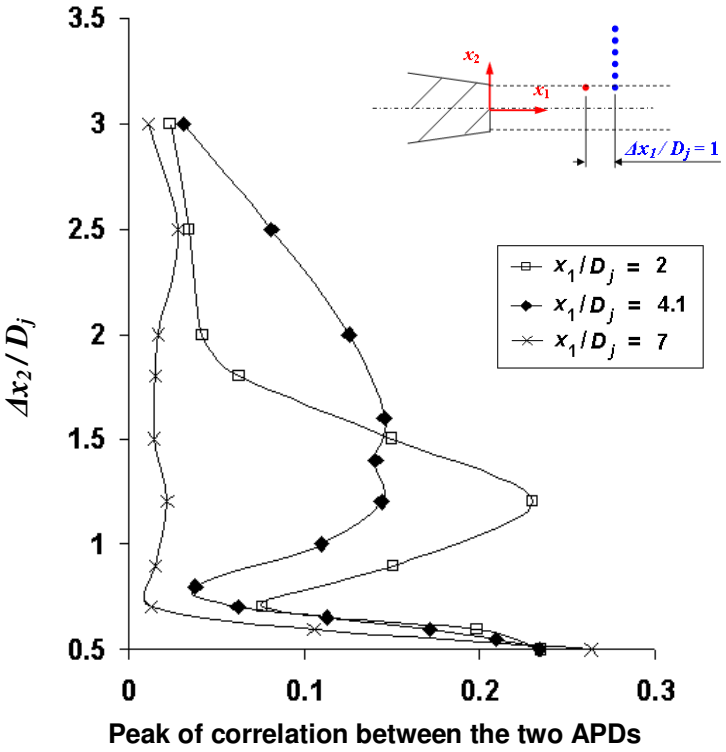

Figure **6-30**: Correlation peaks between one APD at the lipline ($x_2 = 0.5$) and different axial locations with an APD scanning radially outward, 1 diameter further downstream ($\Delta x_1 / D_j = 1$ and different values of $\Delta x_2 / D_j$). $M_d = M_j = 1.75$.

Correlation between the near field optical sensors and microphones at different polar locations is made, resulting in the plot of Figure **6-31.** The peak values of the correlation are once again larger than what is observed with sensors in the jet, as previously observed in section **6.2**. This is attributed to the fact that the optical sensors are recording the propagation of a sound wave rather than a fluctuating property of the jet. The correlations also reach a maximum for microphones located at polar angles around 30 degrees, because that is the direction of the Mach wave propagation. The peaks are also obtained at larger radial location for increasing axial locations, which tends to indicate that the Mach waves are radiated only very close to the nozzle exit plane. The maximum correlation obtained is around 0.4, which is notably higher than what was previously observed with sensors inside the jet.

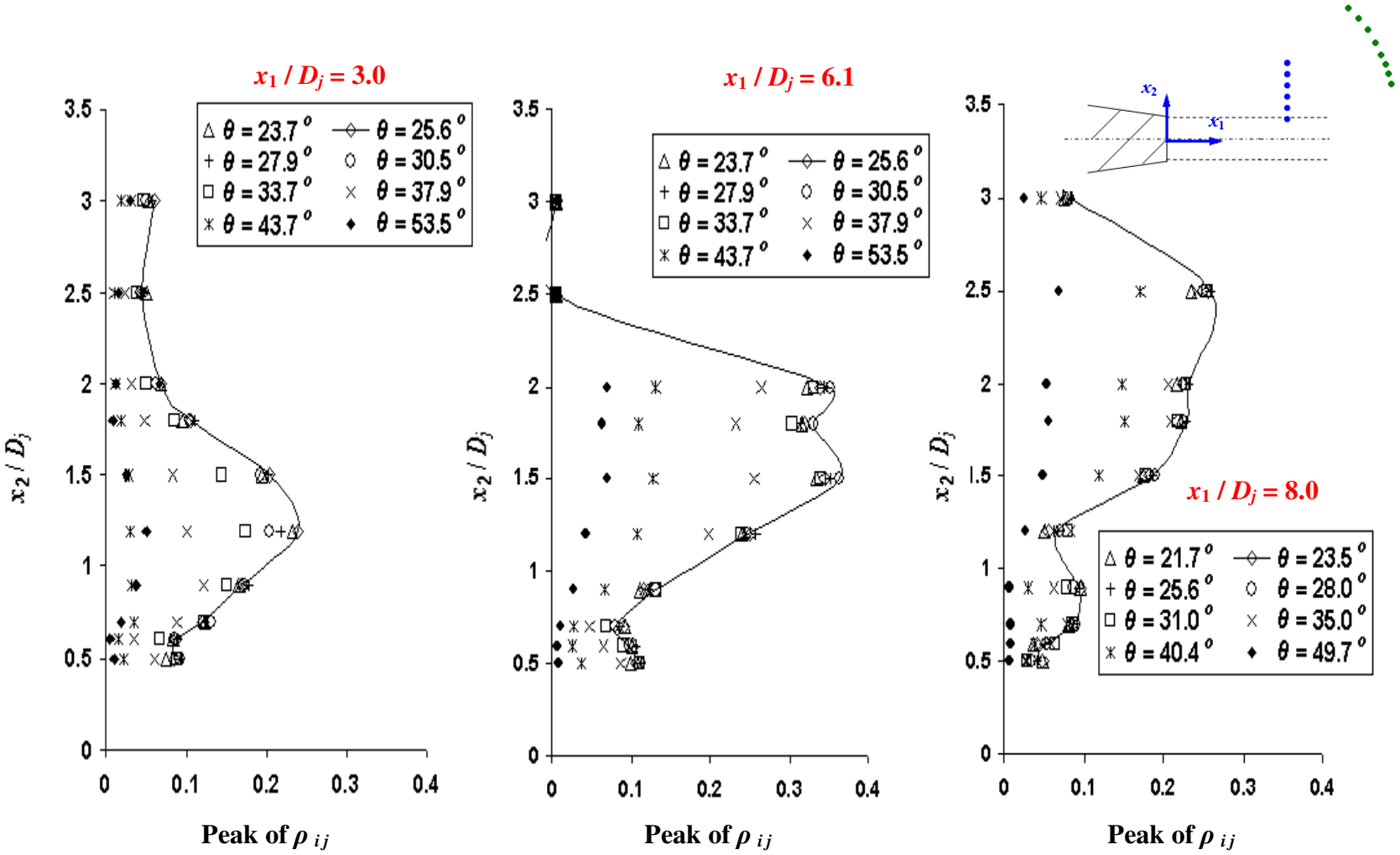

Figure **6-31**: Correlation peak value between an optical sensor at different x_1 and x_2 locations outside a M_j= 1.75 fully expanded jet and far field microphones at different polar angles.

The coherence function between an OD sensor scanning radially the acoustic near field and a microphone at $\theta = 30.5°$ is plotted in Figure **6-32**. This polar angle of the microphone was chosen since it is the direction with highest OASPL and highest correlation with the near field optical measurements. As can be seen, the coherence is very high, peaking at 0.7 for $x_2/D_j = 1.5$. The peak frequency of the coherence also shifts with x_2/D_j locations from $St = 0.3$ close to the lipline to $St = 0.5$ at the maximum coherence location. The coherence drops suddenly to 0 after the peak value is reached. The diagram of Figure **6-32** shows the acoustic paths from a microphone located at $\theta = 30.5°$ and different radial position of the OD sensor (blue dots) at $x_1/D_j = 1.5$. From this geometric construction, one can easily realize that the correlation measured at small values of x_2/D_j (close to the jet lip line) corresponds to sound issuing from downstream locations close to the measurement plane: $x_1/D_j = 1.5$. Going further from the jet in the radial direction, the correlation is made between the fixed microphone and sound that is generated closer to the exit plane (blue and black lines and coherence functions). The fact that the peak of frequency is increasing with radial position therefore means that the highest frequencies are generated closer to the jet exit plane, as already observed and reported in section **6.3.2**. The coherence is however much larger for a very well defined frequency range, which tends to underline the directivity of the radiated noise. The correlation suddenly drops when the acoustic path between the microphone and the OD sensor does not intersect the jet but hits the nozzle itself.

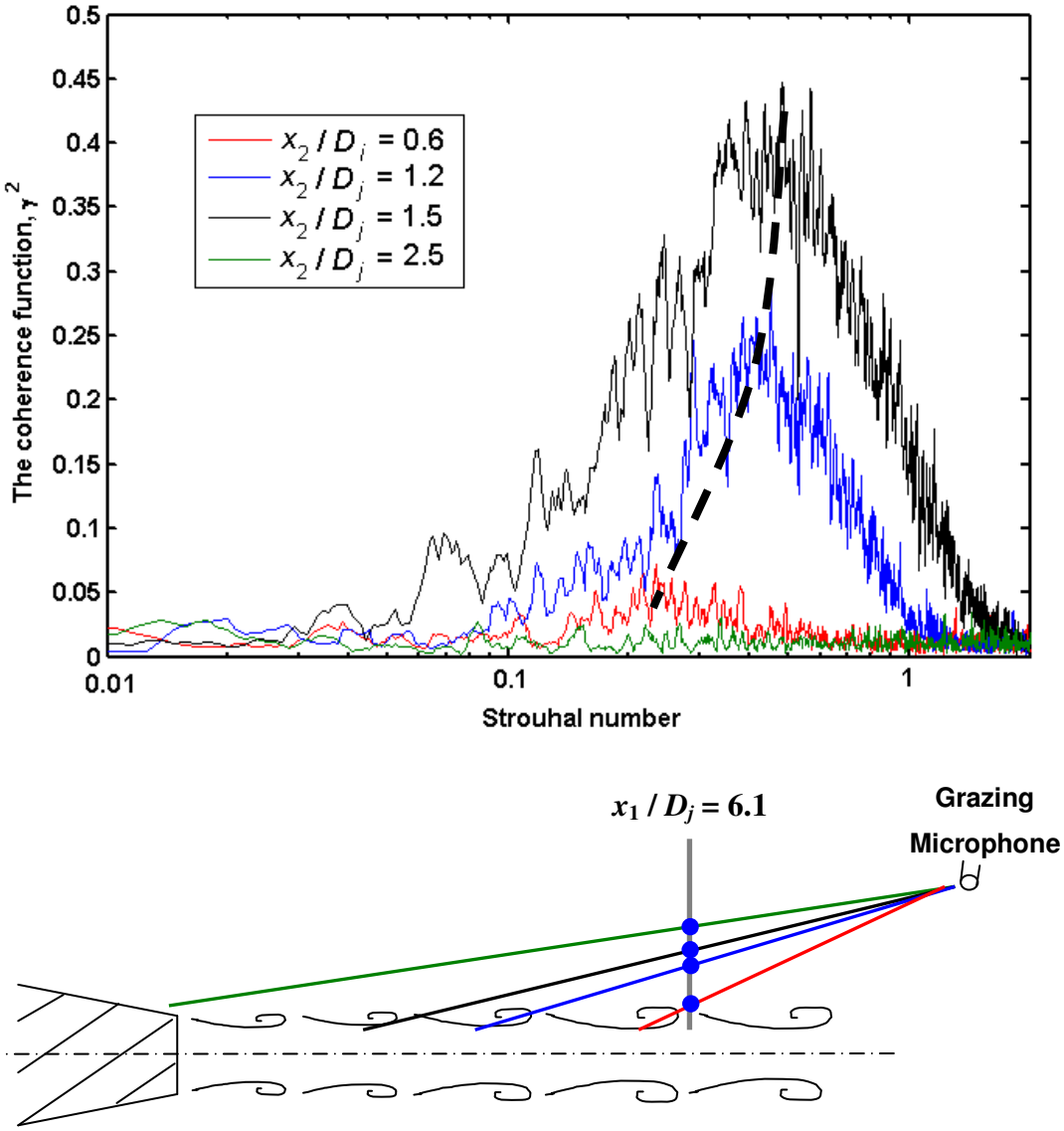

Figure **6-32**: Coherence function between a microphone at $\theta = 30.5°$ and OD measurements at $x_1/D_j = 6.1$ and various x_2/D_j locations for a fully expanded $M_j = 1.75$ jet, $f_c = 37.3$ kHz.

6.4 Summary

This chapter presents the main results obtained using the optical deflectometry technique. Radial and axial correlation measurements were made in shock free and shock containing supersonic jets. The turbulence structures across the shear layer were seen to exhibit a distortion, with an angle of approximately 16 degrees relative to the jet axis. This angle did not change over a wide range of jet velocities and with the presence of shocks. The convection velocity was calculated for many different jet conditions and evaluated as a function of frequency. The presence of shocks affects the value of the convection velocity. However it is very difficult to obtain reliable measurements due to the complex shape the mixing layer acquires when the jet is shock containing.

Correlation between optical sensors in the flow and far field microphones showed a direct relation between the flow features in the jet and the radiated sound. Localization of the noise generation regions was shown to be possible. High frequency noise was observed to be generated close to the exit plane while lower frequencies are produced further downstream. Optical sensors were also used to measure sound propagation in the acoustic near field of the jets. To the author's knowledge, it is the first time such measurements have been made. It enables accurate measurements of the acoustic near field to be obtained and showed very high correlation with both the flow field measurements and the acoustic far field. It also enables the localization of the noise generation by frequency band. It will be very interesting to gather more of this type of measurements in order to fully understand the noise generation process and produce a mapping of the sound sources in the flow.

Chapter 7

Conclusions and future work

7.1 Summary of objectives

This thesis has reported on the aeroacoustic properties of supersonic jets issuing from axisymmetric and military style nozzles. The objectives of the current work were detailed in chapter **1** and are restated here to facilitate the conclusion.

The major goal of this thesis was to investigate the noise generation mechanisms in supersonic shock containing and shock free jets and gather data relevant to the prediction of the acoustic far field. The database for flow quantities in shock containing jets being very scarce, this study brings some relevant data points that will help in defining the parameters of a model for Broad Band Shock Associated Noise. Building on past experiences in the Penn State jet noise facility, experiments were designed to provide information regarding the turbulence quantities in the jet and the way they are affected by the presence of shock cells. These measurements were performed in conjunction with acoustic measurements designed to record the major features of the acoustic fields. These data are part of a parallel analytical and computational modeling effort being conducted by Prof. P.J. Morris and his research assistants developing a prediction scheme for BBSAN.

The specific goals included:

1. To produce a Schlieren flow visualization database for extraction of the main features of the flows considered.

2. To develop the capability to make reliable pitot probe measurements in shock containing jets and use it for the evaluation of a CFD model.
3. To measure the properties of the flow field turbulence with an optical deflectometry system for jets of varying conditions.
4. To correlate the flow field fluctuations with the acoustic far field.
5. To investigate on the influence of the screech on the measured flow properties and eventually to develop techniques to suppress it.

The first objective was successful and schlieren images were presented throughout the entire thesis as a complement to other measurement techniques. It brought insight to the study by providing a visual help to the interpretation of the data. The second objective constitutes the first major goal of this research and was met by showing reasonable agreement between the pitot measurements and the CFD predictions produced by Miller *et al.* [**54**]. The third objective was the second main goal of this thesis and was reasonably successful. The optical deflectometry technique was refined to a point where it could produce reliable measurements in both shock free and shock containing jets. The properties measured match very well with previous studies and some conclusions were drawn on the influence of shock cells and screech tones on the characteristics of the turbulence. The fourth objective was met by obtaining strong correlations between OD sensors in the flow and microphones in the acoustic far field. In addition, OD sensors were positioned in the acoustic near field and were shown to provide a measurement of the propagating sound waves. Finally, the fifth objective was successful and recommendations were given on the most suitable techniques to remove screech in shock containing jets. A more detailed summary of the results is now presented.

7.2 Acoustic measurements

Acoustic measurements were performed first to assure that data was obtained with precisely the same nozzles and jets with which flow field data were being obtained. Secondly, such measurements were performed to assess the amount of screech

suppression obtained with different concepts. The different techniques investigated gave very good results but most were observed to produce a non-insignificant impact to the remainder of the spectra, mainly the broad band shock associated noise. More refined concepts will be investigated based on these findings whenever there is a need for screech suppression.

Additional acoustic measurements were performed after the many modifications applied to the jet noise facility in order to qualify the rig. Favorable comparisons were obtained with previous measurements at Penn State. Spectral comparisons with data reported in the open literature also proved successful and enhanced our confidence in the quality of the data. Finally, acoustic spectra were acquired simultaneously with the optical deflectometry setup in order to provide acoustic measurements to correlate the flow field measurements to.

7.3 Mean flow measurements

Pressure probe measurements were performed with a 5 pitot probe rake in order to gain information on the mean quantities of the flow field of jets of different conditions. Some preliminary data were gathered for jets issuing from a converging-diverging (CD) round nozzle designed for producing a shock free supersonic jet at M_j 1.5. Favorable results were obtained with a fully expanded M_j = 1.5 jet. An over-expanded M_j = 1.3 condition was then run with the same CD nozzle and the resulting measurements were compared to CFD predictions. Static pressure measurements were measured with a static pressure probe but failed to produce accurate results due to the probe interference in the flow. A different approach was then chosen in order to determine the Mach number distributions in the jet, making assumptions regarding the total pressure and the static pressure. Good comparisons with the numerical results were obtained with this method. The same exercise was repeated with an under-expanded round jet M_d = 1.0 M_j = 1.5 and lead to the same observations. In both cases, the shock cell structure was accurately captured by the pitot probe, as well as the shape and growth of the mixing layer.

Surveys were then performed with jets issuing from nozzles replicating real jet engine exhausts. A conical converging-diverging M_d = 1.5 GE nozzle whose internal contoured is composed of 12 facets was used in both fully expanded M_j = 1.5 and under-expanded M_j = 1.7 conditions. Finally, a rectangular nozzle, a replica of a F-22 aircraft engine exhaust and designed for M_d = 1.5 was used with three different pressure ratios corresponding to fully expanded Mach numbers M_j = 1.3, 1.5 and 1.7. Traverses with the pitot rake were performed to map the full jet at numerous downstream locations. These measurements lead to the observation of axes switching of the jet. This axes switching occurred further downstream in the fully expanded case than in the two imperfectly balanced cases.

7.4 Optical Deflectometry diagnostics of the flow

The optical deflectometry technique has been used extensively in this research. Limitations of the system as well as words of cautions have been expressed during the analysis of the preliminary measurements presented in Chapter **4**. Use was made of two completely different systems, one of them being a brand new design fabricated for the University of California Irvine and using different kinds of optical sensors. This provided a check on the quality of the data gathered.

Two point correlation measurements were performed in both the radial and the axial direction of the jet. Shock free and shock containing conditions were investigated in an attempt to assess the influence of the shocks on the correlation measurements. Radial measurements lead to a measurement of the angle at which the turbulence structures across the shear layer are skewed. This angle was found to be around 16 degrees relative to the jet axis and was observed to be constant through the jet and did not change with the presence of shocks or with variations of the jet velocity. This result is consistent with measurements obtained with lower speed jets, like the one reported by Fleury *et al.* [**64**].

The convection velocity was calculated from axial correlation measurements for many different jet conditions and evaluated as a function of frequency. The occurrence of

screech was observed to have a minimal effect on the length and time scales of the convecting turbulent structures. The presence of shocks affected the value of the convection velocity, however it is very difficult to obtain very accurate measurements due to the complex shape that the mixing layer acquires when the jet is shock containing.

Correlation was attempted between optical sensors in the flow and far field microphones. They showed some level of coherence, providing evidence that there is a direct relation between the flow features in the jet and the radiated sound. These measurements were attempted with a wide range of jet conditions for a finite set of OD sensor locations in an attempt to obtain trends of correlations in term of the jet conditions. The amount of correlation with microphones in the forward arc was found to be higher in strongly shock containing cases, when the broad band shock associated noise is dominant. Correlations with microphones in the rear arc peak in the direction of Mach wave radiation. However, reasonable correlation levels were also obtained with jets with subsonic convection velocity. Refined measurements were performed at UCI on one jet condition in order to try to localize the noise generation regions. High frequency noise is generated close to the exit plane while lowest frequencies are produced further downstream, a feature that has been well established with earlier studies.

Finally, optical sensors were used to measure the sound propagation in the acoustic near field of the jets. To the author's knowledge, it is the first time such measurements were made. A significant amount of correlation was obtained with both the far field microphone measurements and the OD measurement simultaneously acquired in the flow. This also facilitates the localization of the centroids of the generation of noise by frequency band.

7.5 Future work

There are existing data from measurements that were made in the scope of this research that require additional analysis in order to provide definitive conclusions. The pitot probe measurements that were obtained for round and asymmetric jets were only

partially compared with the results from numerical simulations. More comparisons will be necessary to validate both the CFD results and the quality of the experimental data gathered. Measurements in heat simulated jets are also scheduled. While the preparation work for these measurements has been completed and the qualification measurements have been made, the actual experiments still need to be performed. These will provide insightful data on the nature of the effect of heat on the mean flow properties of the jet. They are especially important due to the fact that measurement of the fluctuating quantities in a heat simulated jet is difficult with the OD setup. On the other hand, the mean flow measurements in cold rectangular jets can be completed by OD measurements along the lip line of the jet, bringing more insight on the mechanisms behind the noise generation processes.

The results obtained for the convection velocity in shock containing jets will need to be completed by more refined measurements in order to be really conclusive. The phase plots and the variation of the convection velocity with wavelengths need to be investigated further for the same reasons. After the successful fabrication of the upgraded optical system for the University of California Irvine and the very good results obtained from it, a similar upgrade on the Penn State setup seems appropriate. Replacing the aging photomultipliers by more accurate and smaller photodiodes is an option that could upgrade the current measurement capabilities and the quality of the measurements. It also seems productive to keep performing more correlation measurements with the far field noise, with sensors both in the jet and in the near acoustic field. A comprehensive survey of selected jet conditions could provide a mapping of the sound sources in the flow. One condition of special interest would be a strongly shock containing jet (for example $M_d = 1.0$, $M_j = 1.5$) with microphones located in the forward arc.

Finally, completion of the forward flight capability will be pursued throughout the spring of 2009 and subsequent calibration of the facility will provide valuable data on the effect of forward flight on the acoustic of jets. Mean flow measurements as well as optical deflectometry measurements will also be performed with the simulated forward flight in order to observe the effect of the low speed flow on the mean and fluctuating properties of the mixing layer.

Bibliography

1 Shivashankara, B. N. and Bhat, T. R. S., "Outlook on jet noise". 1999, AIAA 99-1841, 1999.

2 Lighthill, M. J., "On sound generated aerodynamically", *Proc. Roy. Soc. London*, Ser .A, 211, 1952, pp564-587

3 Tam, C. K. W., Golebiowski, M. and Seiner, J. M., "On the two components of turbulent mixing noise from supersonic jets", AIAA 96-1716.

4 Tanna, H. K., "An experimental study of jet noise Part I: turbulent mixing noise", *Journal of Sound and Vibration*, 1977.

5 Krothapalli, A., Arakeri V. and Greska B., "Mach wave radiation: a review and an extension", AIAA-2003-1200.

6 Ahuja, K.K.. "Correlation and prediction of jet noise", *Journal of Sound and Vibration*, **29**(2), 1973, pp.155-168.

7 Tanna, H. K., "An experimental study of jet noise Part II: shock associated noise", *Journal of Sound and Vibration*, 1977.

8 Harper-Bourne, M. and Fisher, M. J., "The noise from shockwaves in supersonic jets", AGARD-CP-131, 1974.

9 Seiner, J.M., "Advances in high speed jet Aeroacoustics", AIAA-84-2275, 1984

10 Shen, H. and Tam, C.K.W., "The effects of jet temperature and nozzle lip thickness on screech tones", AIAA-1999-1860, 1999

11 Panda, J., "Shock oscillation in underexpanded screeching jets", *Journal of Fluid Mechanics*, **363**, 1998.

12 Norum, T.D., "Screech suppression in supersonic jets", *AIAA Journal*, **21**(2), 1983, pp.235-240.

13 Raman, G., "Cessation of screech in underexpanded jets", *Journal of Fluid Mechanics*, **336**, 1997, pp.69-90.

14 Tam, C. K. W., "Stochastic model theory of broadband shock associated noise from supersonic jets," *Journal of Sound and Vibration*, **116**(2), 1987, pp. 265-302.

15 Morris, P.J., Boluriaan, S., Lilley, G.M. and Long, L.N., "Two-point cross correlations of turbulence and noise predictions- analysis and simulation", AIAA-2002-0071.

16 Troutt, T.R. and McLaughlin, D.K., "Experiments on the flow and acoustic properties of a moderate-Reynolds-number supersonic jet", *Journal of Fluid Mechanics*, **116**, 1982, pp.123-156.

17 Morris P.J., Bhat T.R.S., "The spatial stability of compressible elliptic jets", *Phys. Fluids*, **7**, pp 185-194.

18 Kinzie, K.W. and McLaughlin, D.K., "Aeroacoustic properties of supersonic elliptic jets", *Journal of Fluid Mechanics*, **395**, 1999, pp1-28.

19 Doty, M. J. and McLaughlin, D. K, "Acoustic and mean flow measurements of high speed helium air mixture jets", *International Journal of Aeroacoustics*, **2**, No.3&4, 2003, pp293-334.

20 Lau, J.C., "Laser velocimeter correlation measurements in subsonic and supersonic jets", *Journal of Sound and Vibration*, **70**(1), 1980, pp.85-101

21 Bridges, J., "Effect of heat on space-time correlations in jets", AIAA-2006-2534-924.

22 Doty, M. J. and McLaughlin, D. K, "Space-time correlation measurements of high-speed axisymmetric jets using optical deflectometry", *Experiments in Fluids*, **38**, 2005, pp415-425.

23 Davies, P. O. A. L, Fisher, M. J., and Barratt, M. J., "The characteristics of the turbulence in the mixing region of a round jet", *Journal of Fluid Mechanics*, **15**, 1963, pp337-367.

24 Norum, T.D., Garber, D.P., Golub, R.A., Santa Maria, O.L. and Orme J.S., "Supersonic jet exhaust noise at high subsonic flight speed", NASA-2004-TP212686.

25 Viswanathan, K., "Does a model scale nozzle emit the same jet noise as a jet engine", *AIAA Journal*, **46**(2), 2008, pp336-365.

26 Doty, M., "An experimental investigation of the aeroacoustic properties of high-speed, helium/air mixture axisymmetric jets", PhD Thesis, 2002, The Pennsylvania State University.

27 Bridges, J. and Brown, C. A., "Validation of the small hot jet acoustic rig for aeroacoustic research", AIAA 2005-2846.

28 Papamoschou, D, "Acoustic simulation of coaxial hot air jets using cold helium–air mixture jets", *Journal of Propulsion and Power*, **23**, No. 2, March–April 2007.

29 Petitjean, B. P., "On the nonlinearities in the noise radiated from high-speed model jets", PhD Thesis, 2006, The Pennsylvania State University.

30 Kinzie, K.W. and McLaughlin, D. K., "Measurements of supersonic helium/air mixture jets", *AIAA Journal*, **37**, (11), 1999, pp. 36-41.

31 Reynolds, W.C., Perkins, H.C., "Engineering Thermodynamics", McGraw-Hill, New York, 1977.

32 Gabrielson, T.B., Marston, T. M. and Atchley, A.A., "Non linear propagation modeling-guidelines for supporting measurements", Noise-con 2005

33 Kuo, C.W, personal communication

34 Petitjean, B.P., McLaughlin, D.K. and Morris, P.J., "On the nonlinear propagation of shock-associated jet noise", AIAA 2005-2930-830, 2005.

35 McIntyre, S.S., "Optical experiments and instrument development for compressible turbulent mixing layers", PhD Thesis, 1994, The Pennsylvania State University

36 Papamoschou, D, "Mach wave elimination in supersonic jets", *AIAA Journal*, **35**, (10), 1997, pp1604-1611

37 Doty, M. and McLaughlin, D.K., "Two-point correlations of density gradient fluctuations in high speed jets using optical deflectometry", AIAA-2002-0367

38 Petitjean, B.P., Viswanathan, K. and McLaughlin, D.K., "Space-time correlation measurements in subsonic and supersonic jets using optical deflectometry", AIAA Paper No 2007-3613-510.

39 McLaughlin, D.K., Carter, J.E., Finston, M. and Forney, J.A., "Experimental investigation of the mean flow of the laminar supersonic cone wake", *AIAA Journal*, **9**, (3), March 1971, pp. 479-484

40 Liepman, H. W. Roshko A., Dhawan S., "On reflection of shock waves from boundary layers", NACA Rep. 1100, 1952

41 Patel, U., "The mapping of supersonic flow and calibration of a four element hot-film probe", Master Thesis, 2008, The Pennsylvania State University

42 Ahuja K.K., "Designing clean jet-noise facilities and making accurate jet-noise measurements", *International Journal of Aeroacoustics*, **2**, (3-4), 2003 , pp. 371-412.

43 Tanna, H. K., Dean, P. D., and Burrin, R. H., "The generation and radiation of supersonic jet noise, Volume III: turbulent mixing noise data," Tech. Rep. AFAPL-TR-74-24, Lockheed-Georgia Company, Marietta, GA, September 1976.

44 "Gas Turbine jet exhaust noise prediction," Tech. Rep. SAE ARP876-D, Society of Automotive Engineers, 1994.

45 Veltin, J., McLaughlin, D.K. and Morris P.J., "Improvement of acoustic models for community noise exposure prediction", AIAA-2008-12-485.

46 Paliath, U., "Numerical simulation of jet noise", PhD Thesis, 2006, The Pennsylvania State University

47 Bridges, J., personal communication

48 Kuo C-W, Veltin J. and McLaughlin D.K., "Methods to improve the accuracy of acoustic measurements in small-scale high speed jets", 15th AIAA/CEAS Aeroacoustics Conference, 2009

49 Kerhervé, F., Jordan, P., Gervais, Y., Valiere, J.-C and Braud, P., "Two point laser Doppler velocimetry measurements in a Mach 1.2 cold supersonic jet for statistical aeroacoustic source model", *Experiments in Fluids*, **37**, 2004, pp419-437.

50 Tam, C. K. W., Seiner, J. M. and Yu, J. C., "Proposed relationship between broadband shock associated noise and screech tones", *Journal of Sound and Vibration*, **110**(2), 1986, pp309-321.

51 Lee, J., Goss, A. and McLaughlin, D.K, "Experiments on high-speed jets from thrust vectoring rectangular nozzles", .AIAA-2006-2704-995

52 Lau J., "Effects of exit Mach number and temperature on mean flow and turbulence characteristics in round jets", *Journal of Fluid Mechanics*, **105**, 1981, pp. 193-218.

53 Zaman, K.B.M.Q., "Axis switching and spreading of an axisymmteric jet – role of vorticity dynamics", AIAA- 95-0889, 1995.

54 Miller, S.A.E., Veltin, J., Morris, P.J. and McLaughlin, D.K., "Validation of computational fluid dynamics for supersonic shock containing jets", AIAA-2008-2988.

55 Nelson, C., Power, G., "The NPARC alliance flow simulation system," AIAA Paper 2001-0594 , 2001.

56 Kuo, C-W, Veltin, J. and McLaughlin, D.K., "Acoustic measurements of models of military style supersonic sozzle jets", 47th AIAA Aerospace Sciences Meeting, 2009

57 Morris, P.J., "Noise radiation from non-circular supersonic jets" AIAA92-02-061

58 Tam, C.K.W., "Influence of nozzle geometry on the noise of high speed jets". *AIAA Journal*, **36**(8), 1998

59 Kerhervé, F., Fitzpatrick, J. and Jordan, P., "The frequency dependence of jet turbulence for noise source modeling", *Journal of Sound and Vibration*, **296**, 2006, pp. 209-225.

60 Panda, J., Seasholtz, R.G. and Elam, K.A., "Measurement of correlation between flow density, velocity and density * velocity with far field noise in high speed jets", AIAA-2002-2485

61 Panda, J., Seasholtz, R.G, "Experimental investigation of density fluctuations in high-speed jets and correlation with generated noise", *Journal of Fluid Mechanics*, **450**, 2002, pp97-130.

62 Kastner, J., Kim, J.H. and Samimy, M., "Correlation of large scale structure dynamics and far-field radiated noise in a Mach 0.9 jet", AIAA-2007-830.

63 Harper-Bourne, M., "Jet noise turbulence measurements", AIAA paper No 2003-3214

64 Fleury, V., Bailly, C., Jondeau, E., Michard, M. and Juve, D., "Space–time correlations in two subsonic jets using dual Particle Image Velocimetry measurements", *AIAA Journal*, **46**(10), 2008

65 Veltin, J. and McLaughlin, D.K., "Noise mechanisms investigation in shock containing screeching jets using optical deflectometry", AIAA-2008-288

66 Papamoschou, D. and Dadvar, A., "Localization of multiple types of jet noise sources", AIAA-2006-2644.

67 Morrison, G.L. and McLaughlin, D.K., "Noise generation by instabilities in low Reynolds number supersonic jets", *Journal of Sound and Vibration*, **65**, pp 177-191.

Appendix A

Facilities pictures and drawings

A.1 Penn State jet noise facility upgrades

Some drawings and photographs of the upgraded facility are provided in this part of the appendix. The newly redesigned plenum is first presented, with a general drawing presented in Figure **A-1**. As can be seen in this drawing, turbulence management was achieved via a perforated plate (picture in Figure **A-4**) and honeycomb. The perforated plate is made of stainless steel for corrosion resistance and was designed to break the jet issuing from the upstream pipe into the plenum. It also provides enhance mixing between helium and air when gas mixtures are used. The honeycomb then breaks the largest turbulent structures present in the flow. The pressure and temperature probes are not represented in this general drawing of the plenum, but shown on the picture of Figure **A-3**. On this image are also visible the supports for the plenum. They consist of two 1.27cm (0.5") thick and 15.2cm (6") wide Aluminum plates that are screwed on a cradle in which the plenum rests. The overall arrangement was designed bearing in mind that it should not produce much drag once the forward flight capability described in sections **2.3** and **A.2** is operational. Horizontal streamlined strengthening member (visible on Figure **A-3**) were added to provide rigidity to the structure.

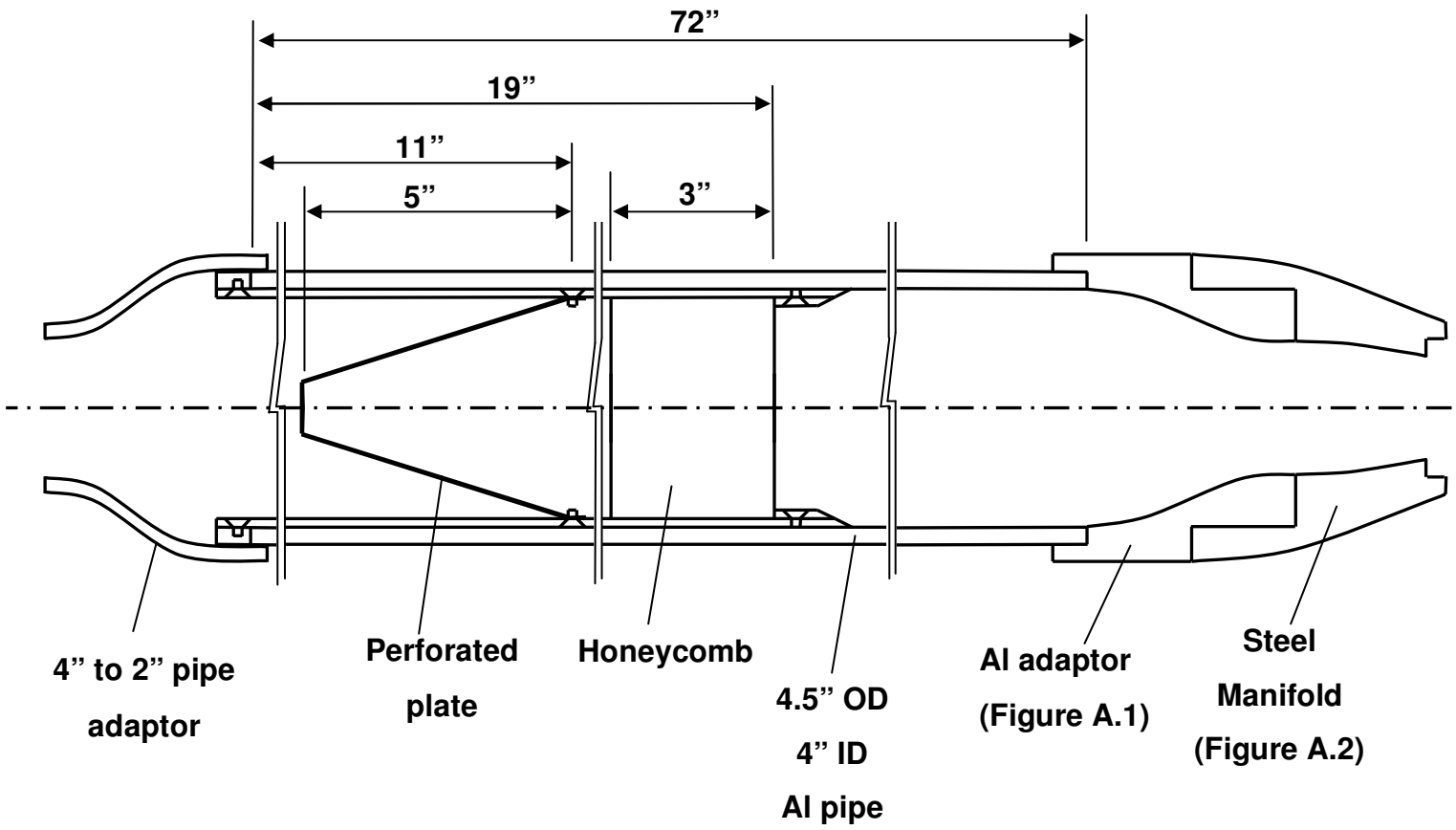

Figure **A-1**: Assembly drawing of the plenum arrangement.

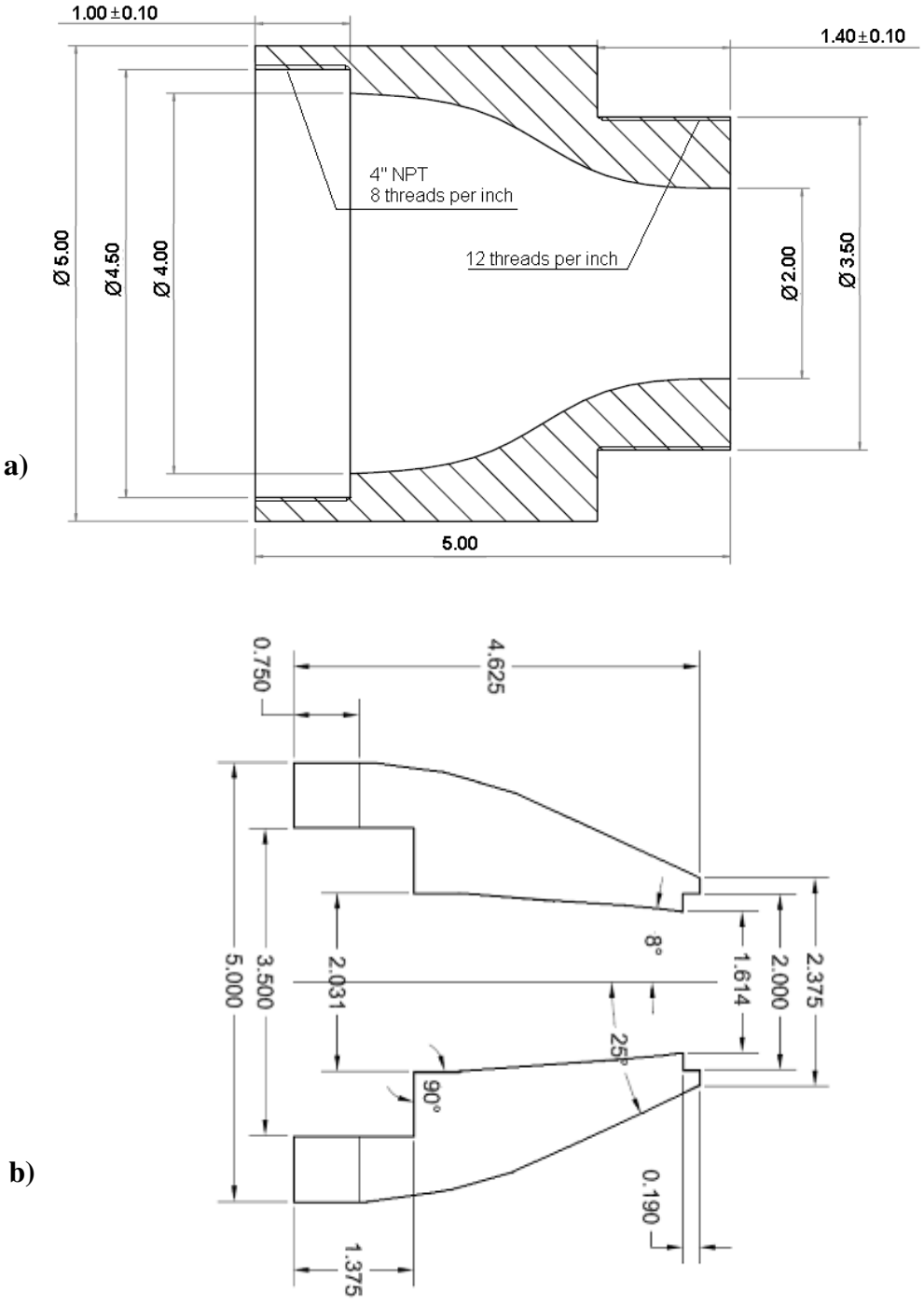

Figure **A-2**: a) Adaptor between the plenum and the manifold, b) manifold at the end of which the nozzles are mounted

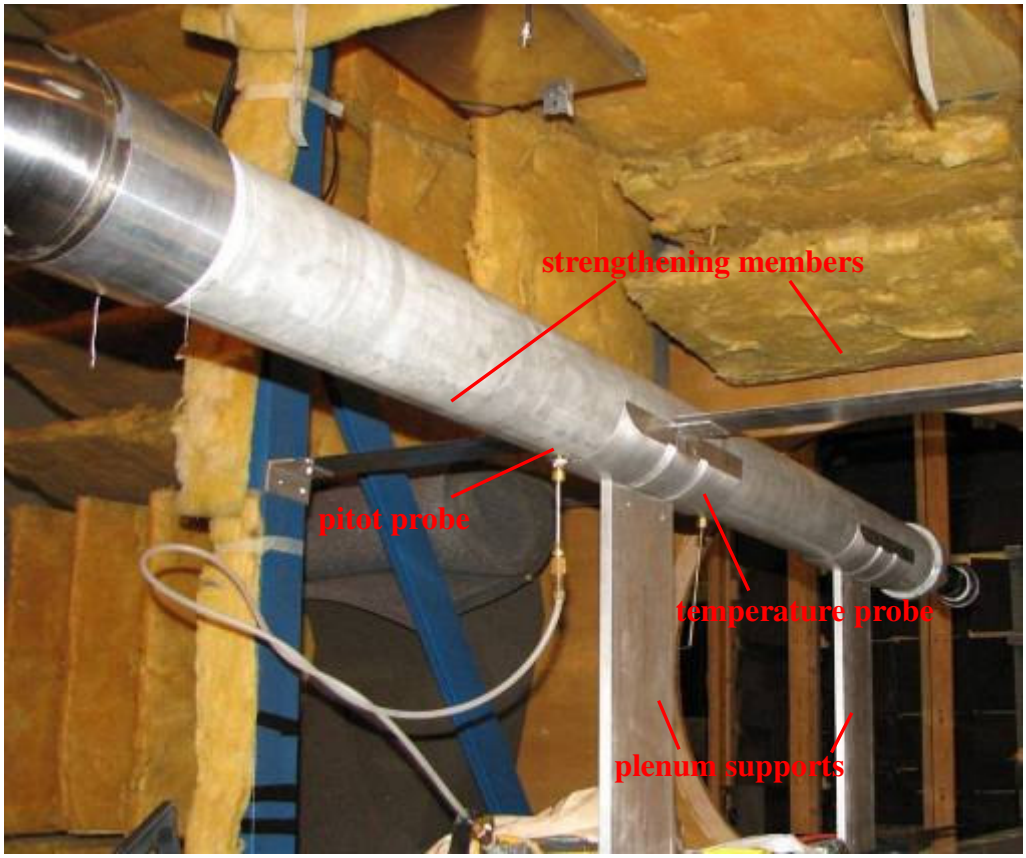

Figure **A-3**: Picture of the new plenum and it supports

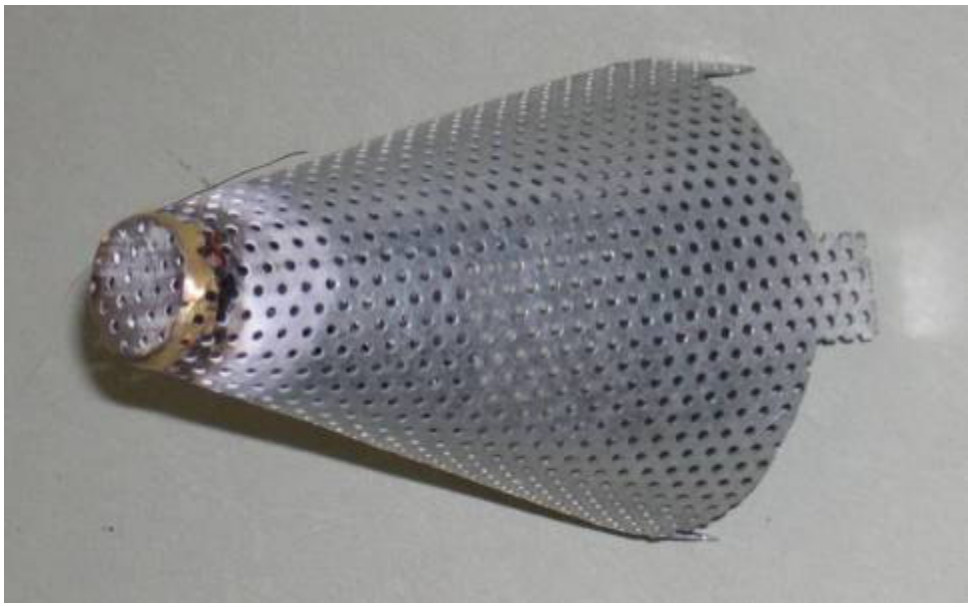

Figure **A-4**: Plenum screen: stainless steel conical perforated plate.

Additional pictures of the new helium-air mixture piping arrangement described in section **2.2.1** are also presented here. Figure **A-5** shown below offers a view of the piping cabinet without the front panel on. Figure **A-6** shows the cabinet in its final location in the control room. The front panel was designed to the image of the diagram of Figure **2-4**. To the left of the cart, one can see the helium farm. The setup now offers the possibility to draw helium from 6 helium canisters simultaneously in order to perform longer measurements with larger jets.

Figure **A-5**: Piping inside the cabinet

Figure **A-6**: Finalized version of the piping cabinet with helium farm.

A.2 Addition of a forward flight simulation capability

A major upgrade was undertaken, starting in the fall semester 2006 and consisting of the addition of a forward flight capability. In order to do so, usage can be made of the fan that was installed [**26**] at the back end of the anechoic chamber and currently used for ventilating the room during helium usage and in order to avoid pressure build up during the experiments. By running that fan at full power and creating an opening around the plenum, one can expect to create a flow velocity able to simulate the forward flight effect. However, this fan mass flow rate does not allow to reach sufficiently high air velocity. It also creates a large amount of disturbance inside the control room, which is not acceptable if we are to run that kind of experiment routinely.

Some upgrade is thus needed. The adopted solution is to provide additional ducting, from the inlet surrounding the plenum, to the windows in the back wall of the control room, as shown in Figure **2-5** of section **2.3**. Addition of a second fan compresses the air upstream of the anechoic chamber and hence provides the additional pressure drop required for high air speed. The whole system looks very similar to the existing exhaust system located in room 26.

Work has been carried out in order to seal as best as possible the anechoic chamber and hence reduce the pressure losses due to any leak. Purchase of a new fan has been made, together with its controller and an appropriate muffler. The volume flow rate necessary in order to reach the target speed is around $6.6m^3/s$ (14,000 CFM). On the other hand, obtaining a 70 m/s (230 ft/s) flow also requires a pressure drop of 2,500 Pa (10" of water). Following summer 2006 experiments on the fan currently used for the exhaust system, the maximum conditions reached for a similar exhaust area are around $2.4m^3/s$ (5,000 CFM) with a pressure drop of around 625 Pa (2.5" of water). All these observations are helpful in dimensioning the inlet fan so that it can reach the desired amount of pressure drop and flow rate. The fan chosen is a mixed flow fan model QSL270, from *Twin City Fan & Blower*, and is specifically designed for minimal noise production. In order to further decrease the noise level, a muffler is installed downstream of the fan, and the ducts leading to the anechoic chamber and manufactured by *Sheet Metal Connectors, Inc.* are acoustically treated. An assembly drawing of the whole upgrade is shown in Figure **A-7**.

As of fall 2008, most of the acoustic ducting has been installed, as well as the fan and the muffler, as shown in Figure **A-8**. This installation prompted a complete reorganization of the workspace in the control room and was done with as little disruption as possible to the ongoing works in the jet noise facility. Figure **A-9** shows the facility at different stage of the assembly process. In Figure **A-9** a), only the fan, the round to square transition and the muffler have been installed. In Figure **A-9** b), an additional straight duct element is assembled, as well as an elbow with turning vanes for reduced head loss.

Figure **A-10** below shows images of the inlet to the forward flight fan. A round section is attached to the flange of the fan, and transition is made to a square section. There, louvers are attached before the bell inlet that increases the flow area to a 5’ by 4’ rectangular area. The whole inlet is acoustically treated with the usage of perforated plates and fiberglass.

Finally, the picture of Figure **A-10** presents the remaining piece of the forward flight duct that consists of a straight section of 36” by 36” Aluminum duct and a nozzle. The straight duct was designed with an patch panel for easy access to the plenum piping. The nozzle was built in two distinct sections and the convergent section ends with a 15” by 15” square area that will be about 1 foot recessed with respect to the high speed jet nozzle exit plane.

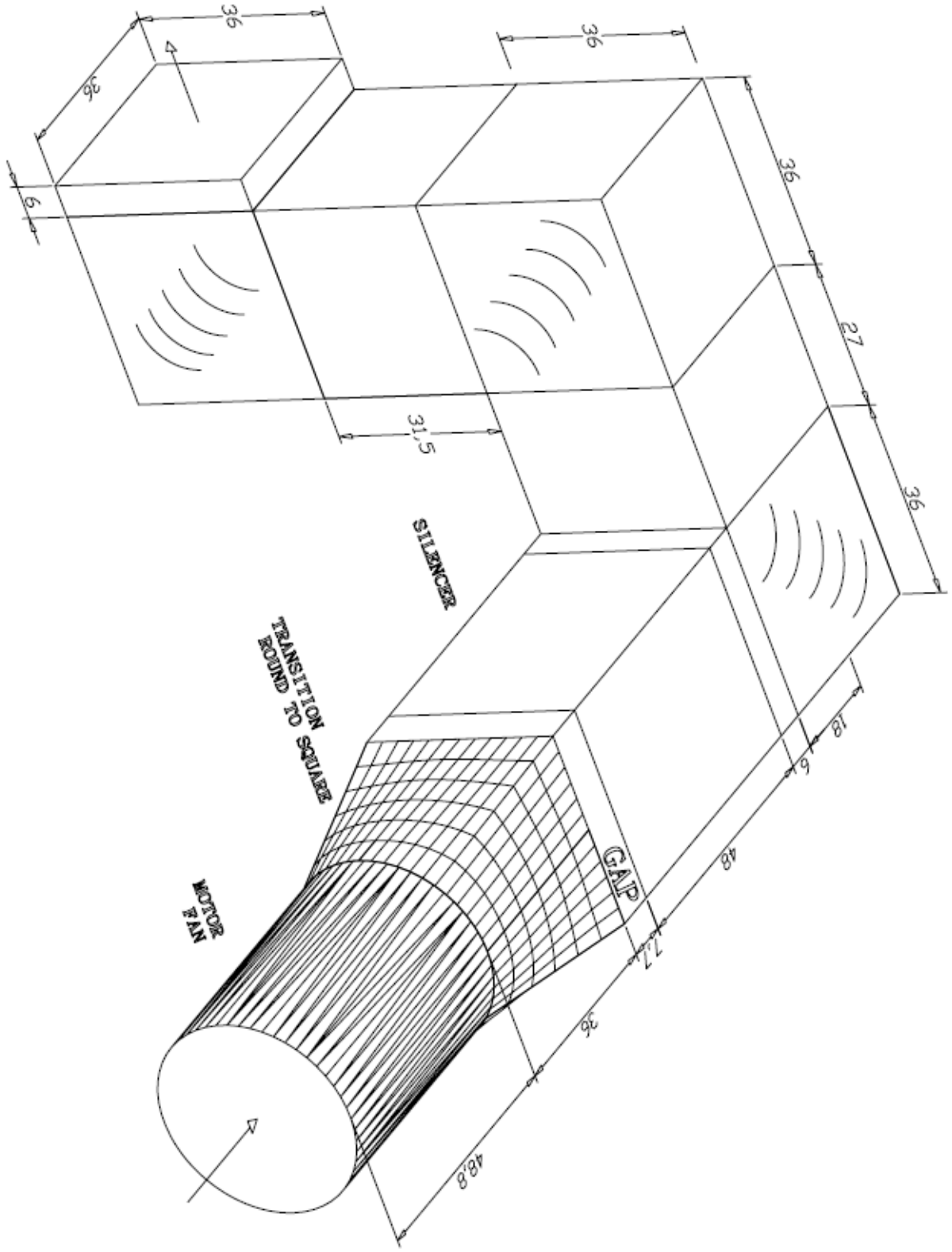

Figure **A-7**: Assembly drawing of the forward flight ducting

Figure **A-8**: a) forward flight duct as of November 2008. b) yet to be installed forward flight nozzle and inlet to the fan.

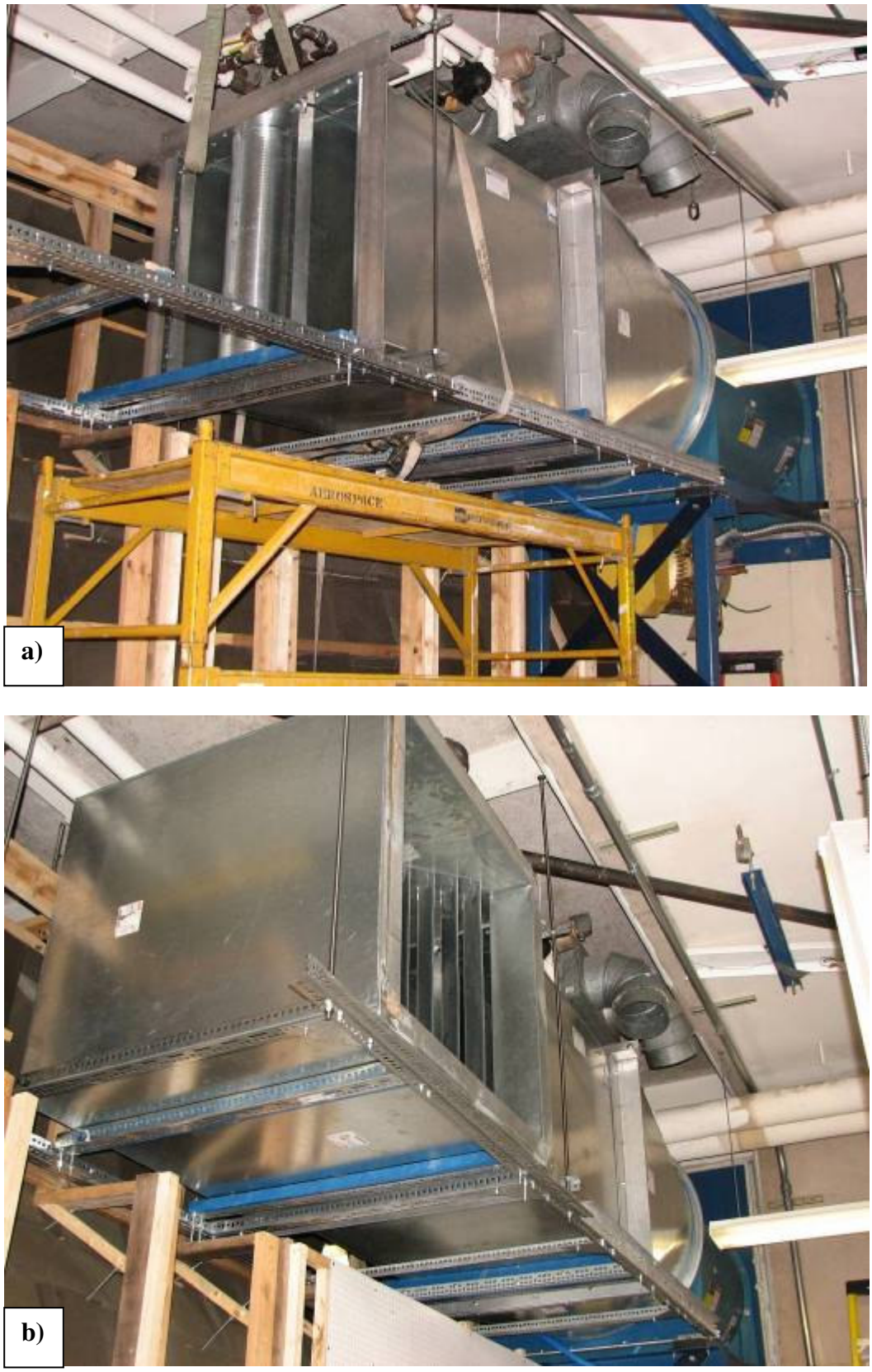

Figure **A-9**: Forward flight duct at different stages of the assembly process.

a)  b) 

Figure **A-10**: Two views of the inlet of the fan. a) transition going to the fan flange b) bell inlet section.

Figure **A-11**: Remaining duct and forward flight nozzle

A.3 OD setup for the UCI Jet noise facility

Development of a new Optical Deflectometry system was undertaken under an ongoing contract for NASA. The setup is very briefly described in section **3.3.2.4** and was tested in The Pennsylvania State University jet noise laboratory before shipping to the University of California, Irvine. Measurements performed at Penn State are presented in section **6.2** and some of the data gathered at UCI are shown in section **6.3**. Additional drawings of the setup and some qualification measurements are presented here.

A full design process was undertaken for this project. The main characteristics of the setup and its requirements were defined in order to make optimal use of the limited facility space. One of the main criteria for the new design was that the system provides measurements of comparable quality to the Penn State system, operates with as limited a setup time as possible and requires only few adjustment and alignment before each run. The whole setup obviously also had to be easy to ship and had a limited budget and allowable development time.

A.3.1 Design of the new OD setup

One main constraint on the optical deflectometer system is the limited amount of space available at the UCI facility. A schematic of the UCI anechoic chamber is presented in Figure **A-12**, together with the overall arrangement of the optical system. Since the anechoic chamber is too small to house the whole optical setup, decision was taken to leave the sending and receiving plates outside of the facility. A small perforation was done in the chamber's wall on the sending side to allow for the light beam passage. On the receiving side, the door of the chamber was kept open without deterioration of the quality of the acoustic measurements.

Building on experience acquired with the Penn State setup, the new optical setup was designed for maximized sensitivity. When making optical measurements of a flow, the size of the image (relative to the size of the object) is an important factor in the

system sensitivity. A larger image allows for smaller probe volume in the flow but it also significantly reduces the intensity of the light measured.

The image size is affected by parameters such as the size and focal length of the mirrors and the distance from the jet exit to the receiving mirror. The limited facility space requires placement of the sending and receiving optics outside of the anechoic chamber. Therefore, in order to keep noise to a minimum and to avoid natural convection in the facility to decrease the quality of the optical signals, he receiving optic plate is placed as closely as possible outside of the chamber.

Then different focal lengths of the parabolic mirrors were investigated, as well as the possibility to fold some of the optic to allow for a larger image size while still meeting the space requirements. Two views of a detailed drawing of the receiving optics are shown in Figure **A-13** and Figure **A-14**. The whole arrangement is set up on an optical bread board with threaded holes every 1" allowing for adjustment of the system. The parabolic mirror is 4.5" in diameter with a focal length of 34". At its focal distance is located the knife edge. Then the light beam hits a flat surface mirror before being split in two images. Each component is mounted on traverses to allow for some vertical and horizontal adjustment

In order to provide an upgrade on the capability of the system as a whole, the possibility to use 4 simultaneous channels of acquisition was investigated. Due to the limited space available on the receiving side, smaller sensors than the current photo multiplier tubes were required. Hamamatsu model C5460-01 Avalanche Photo-Diodes were selected for the UCI optical deflectometer. To verify that the APD units were appropriate replacements for the PMTs a series of experiments were performed to measure the APDs frequency response and signal to noise performance.

Finally, the prism system that allow for both APDs to sense volumes closer than the physical diameter of the APD sensor itself is described in section **3.3.2.4**. The whole system can be seen installed at the UCI facility in Figure **A-15**.

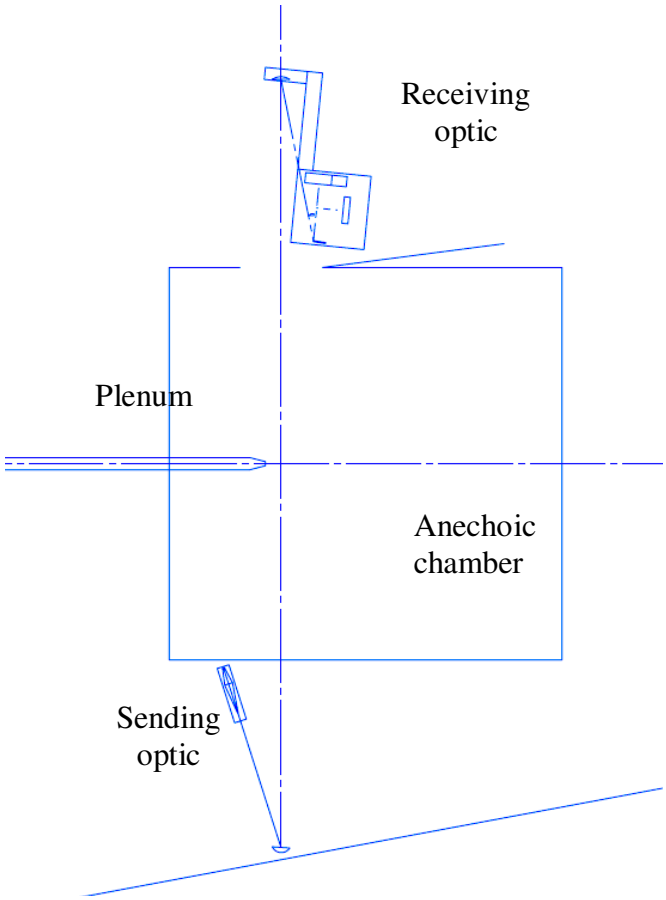

Figure **A-12**: Diagram of the OD setup in the UCI jet noise facility

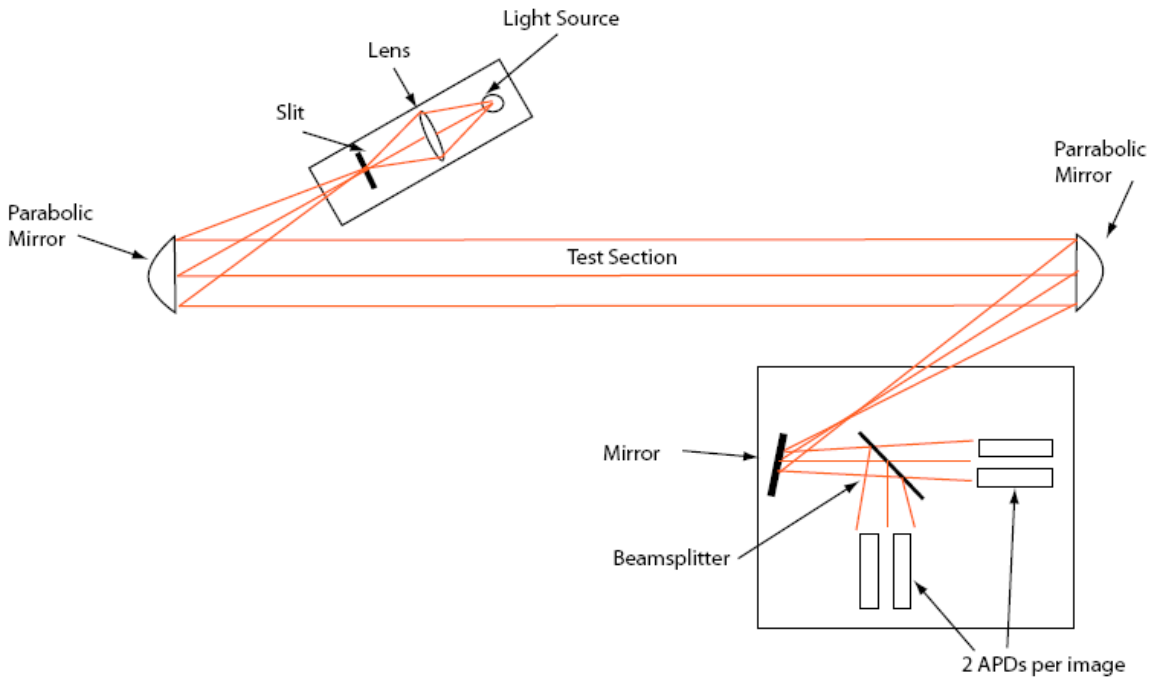

Figure **A-13**: Optical setup diagram

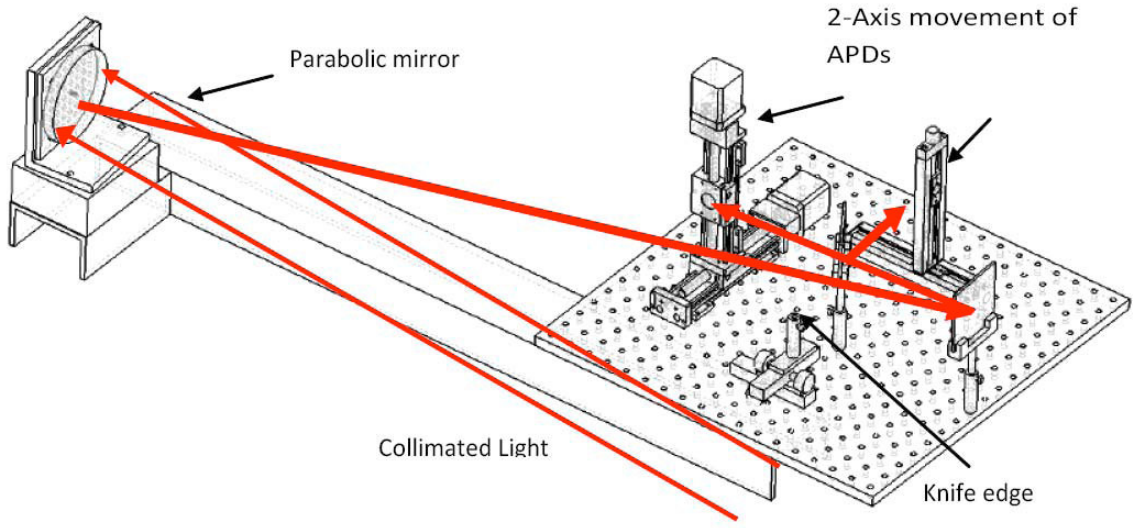

Figure **A-14**: Isometric view of the UCI OD receiving optic

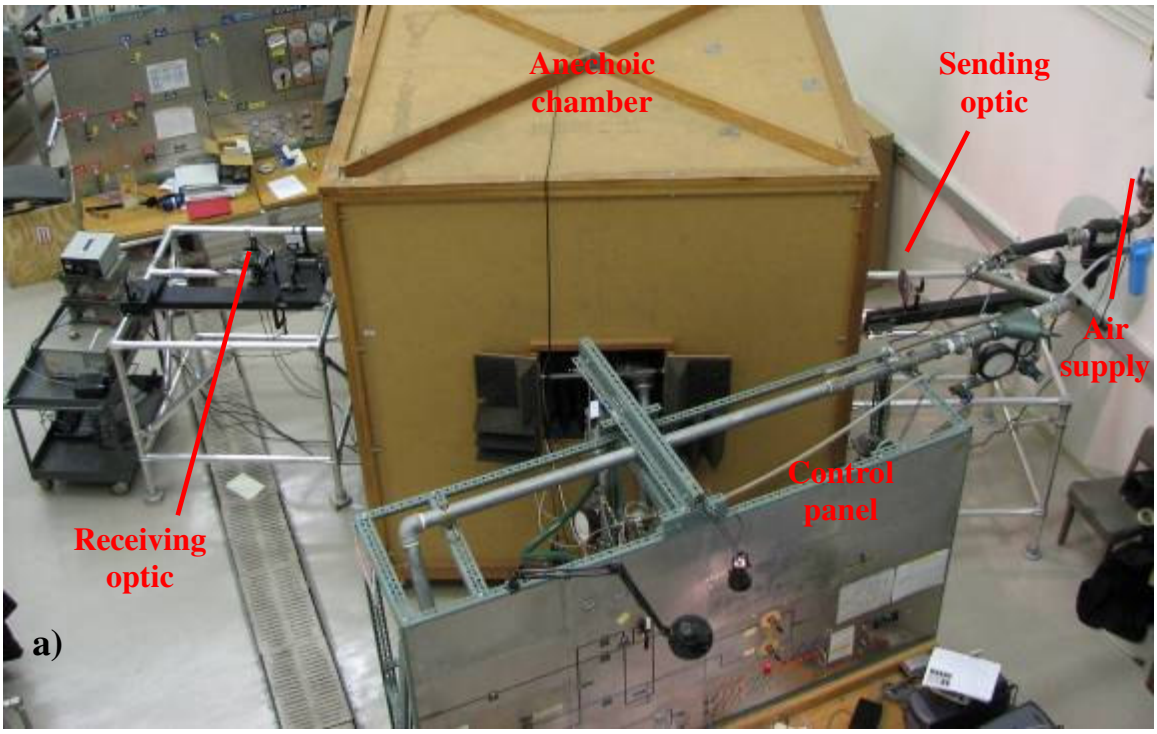

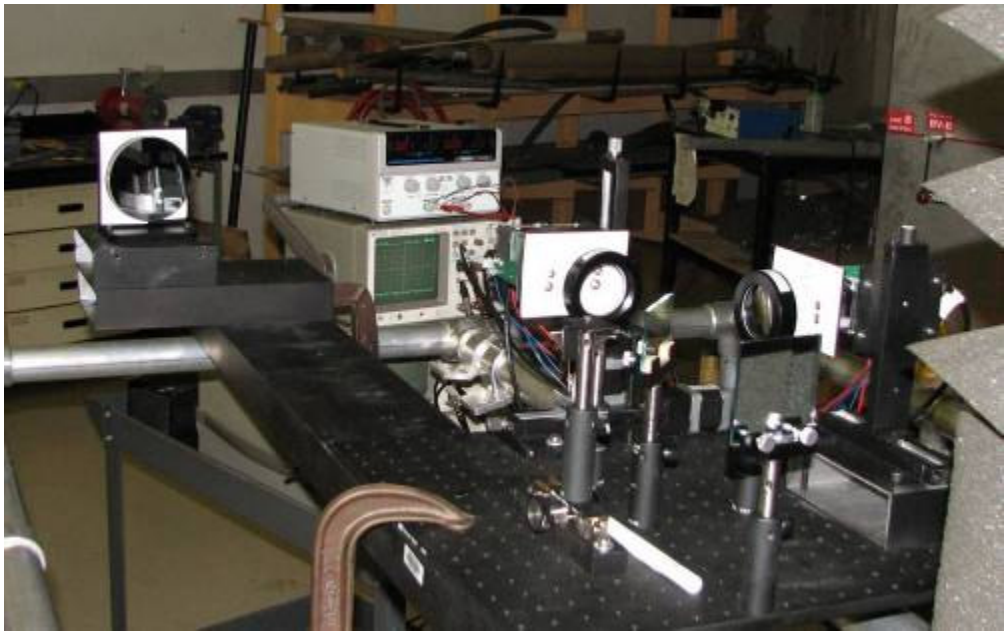

Figure **A-15**: Pictures of the OD system installed in the UCI facility. a) overview picture, b) details of the receiving optic plate.

A.3.2 Qualification measurements

Correllelograms obtained with the Penn State setup and with the newly designed UCI setup are presented in Figure **A-16.** These were acquired both in the Penn State jet noise facility with the same jet conditions: $M_d = 1.0$, $M_j = 0.9$. As can be seen, the results are nearly identical.

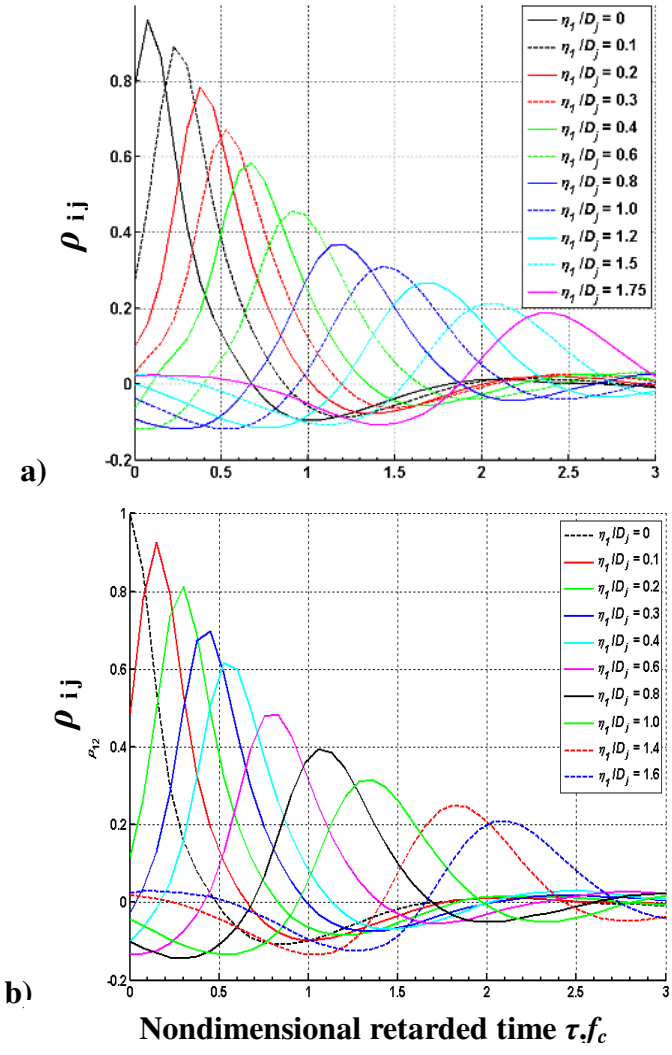

Figure **A-16**: Correllelograms for $M_d = 1.0$, $M_j = 0.9$, cold jet a)Previously obtained data with PSU Optical Deflectometer b)Data obtained with UCI system

Appendix B

Processing codes

This appendix contains a listing of the main codes used for the processing of the data

B.1 Acoustic processing code: JNA_CPSD_Vb.m

```
%*********************************************************************
%
%   HIGH SPEED JET NOISE FACILITY
%
%   The name of this program is JNA_CPSD_Vb.m
%
%   This Matlab code processes time series data and outputs corrected
PSD.
%   Input to this code comes from
%        K:\CWK\JNA_Code\Matlab_Code\Data_Process\filename.txt
%
%   It processes the data by making the following corrections:
%   - Microphone corrections (actuator + free-field)
%   - Atmospheric attenuation
%   - 1 Hz frequency binwidth reduction
%   - Strouhal number scaling
%   - Given measurement location scaling
%
%   Modified by Jeremy Veltin on                    February 20, 2007
%   Developed by Ching-Wen Kuo                          July 11, 2007
%   Derived from 4CH_MIC_PSD_dir_Va.m
%   Originally Written by Jeremy Veltin                 July 10, 2006
%
%
%*********************************************************************

clear all
close all
clc;
```

```
disp(' ');
disp('************************************************************');
disp('POWER SPECTRAL DENSITY FOR 4 MICROPHONES WITH ATMOSPHERIC
ATTENUATION,');
disp('              FREEFIELD AND ACTUATOR CORRECTIONS');
disp('************************************************************')
;
disp(' ');
disp(' ');
disp('This Matlab code is the second step in the processing of the time
signal data measured by the microphones in the anechoic chamber. It
takes as an input a text file containing the 4 time data from the
microphones, with the microphone calibration constants already applied
via the labview code "Convert BIN into TXT v00.vi". Another input file
named "input_dir.dat" located in the same folder as this code should
contain the experimental conditions. Two other input files containing
respectively the actuator correction and the freefield correction
should be contained in a "Correction Factors" subdirectory under the
names "actuator_cor.txt" and "freefield_fi.txt". This code calculates
the SPL per unit resolution bandwidth and adds to it the atmospheric
attenuation and microphone calibrations in order to obtain lossless
SPL. It can also be used to calculate the SPL per Hz or even per unit
Strouhal number. A graph and an output text file are used as an output
for these lossless SPL. The text file can be used by an excel sheet for
advance graphing.');
disp(' ');
disp('Please make sure the input file "input_dir.dat" is properly
filled before running the program');
disp(' ');
%
%
%*********************************************************************
***
%                                   NOMENCLATURE
%
% Ntotal is the total number of data points in the time signal
% fs is the sampling frequency
% ch1data is the voltage time histories recorded on channel #1
% ch1out_hw is the windowed piece of channel #1 signal used for FFT
% N_PointFFT is the number of points used for each Fourier transform
% N_avg is the number of averages used to compute the psd, taking into
% account overlap by 1/2
% DFT1 is the discrete fourier transform calculated from ch1out_hw
% psd1 is the power spectral density calculated from DFT1
% PSD1_avg is the power spectral density of channel#1 after averaging
on
% all the windows
% spl1 is the sound pressure level of channel#1
% LS_spl1 is the sound pressure level of channel#1 after applying the
% microphone and atmospheric corrections
% St_spl1 is the sound pressure level of channel#1 per unit Strouhal
number
% f_bin is the frequency bin width
% D_noz is the nozzle diameter
% Mj is the jet Mach number
```

```
% TR is the temperature ratio (Tj/Tamb)
% D_eff is the equivalent fully epanded jet diameter
% Md is the design Mach number of the nozzle
% Uj is the jet velocity
% fc is the characteristic frequency
% propag is the propagation distance in R/Dj
%*****************************************************************
******

format long e;

%_____________________________________________________________________
%   Reading of the inputs

%inputtype=(input('Input is time signal in Pa (time), SPL lossless
(lossl), raw SPL (SPLr) or per unit Strouhal number (St) ? : ','s'));
disp('');
disp('************************************************************');
disp('      Choose the input file name containing the microphone time
signals      ');
disp('************************************************************');
disp(' ');
disp('                          Press any key to continue
');
disp('');
pause
[filename1, pathname] = uigetfile( {'*.txt'} ,'Open' );
[ch1data, ch2data, ch3data, ch4data] = textread(filename1,'%f %f %f
%f');
clc


%_____________________________________________________________________
% Reading the conditions from the input file.

disp('');
disp('************************************************************');
disp('    Choose the input file name containing the conditions for this
data set   ');
disp('************************************************************');
disp(' ');
disp('                          Press any key to continue
');
disp('');
pause

[filename2, pathname] = uigetfile( {'*.dat'} ,'Open' );
fid1 = fopen(filename2);
buffer = fscanf(fid1,'%f');
fclose(fid1);
clc
```

```
%_____________________________________________________________________
%   Corrections to produce lossless data

% Microphone Corrections
cd 'Correction Factors';

disp('');
disp('*****************************************************************');
disp(' Choose the input file name containing the mic corrections for
this data set ');
disp('*****************************************************************');
disp(' ');
disp('                          Press any key to continue
');
disp('');
pause

[filename3, pathname] = uigetfile( {'*.txt'} ,'Open' );
fid2 = fopen(filename3);
% fid4 = fopen('actuator_resp_30.txt','rt');
[act1, act2, act3, act4] = textread(filename3,'%f %f %f %f');
st1 = fclose(fid2);
clc

disp('');
disp('*****************************************************************');
disp('       Choose the file for the free-field correction for this
data set       ');
disp('*****************************************************************');
disp(' ');
disp('                          Press any key to continue
');
disp('');
pause
[filename4, pathname] = uigetfile( {'*.txt'} ,'Open' );
fid3 = fopen(filename4);
[ff_fi] = textread(filename4,'%f');
st2 = fclose(fid3);
clear filename pathname
clc

cd ..


% output = input('Enter output file name, with extension: ','s');
% disp(' ');
disp(' ');
disp('*****************************************************************');
disp(' ');
disp1 = strcat ('   The input file for microphone time signals :',
filename1);
disp(disp1);
disp(' ');
```

```
disp2 = strcat ('   The input file for data conditions :', filename2);
disp(disp2);
disp(' ');
disp3 = strcat ('   The input file for microphone corrections :',
filename3);
disp(disp3);
disp(' ');
disp4 = strcat ('   The input file for free-field correction :',
filename4);
disp(disp4);
disp(' ');
disp('************************************************************');
disp(' ');

disp('Enter the propagation distance in r/D where you want the
measurements propagated');
propag = input('(0 if no propagation is required) : ');
disp(' ');

dimension=(input('Result per frequency (fq) or per unit Strouhal number
(St) ? : ','s'));
resolution = '  ';
if (dimension=='fq')
    resolution = (input('Result per unit resolution bandwidth (bw) or
per Hertz (Hz) ? : ','s'));
    if (and((resolution~='Hz'),(resolution~='bw')))
       disp(' ');
       disp('Error in the inputs!');
       disp('Do not trust the results');
    end
end
if (and((dimension~='fq'),(dimension~='St')))
    disp(' ');
    disp('Error in the inputs!');
    disp('Do not trust the results');
end

disp(' ');
disp('Type in the file name of the output data, FILENAME');
disp('The file will be named as FILENAME_001.txt to FILENAME_004.txt');
outfile = input('  ','s');
disp(' ');


disp('');
disp('Wait for the "end of code" message....');
disp(' ');
Ntotal = length(ch2data);



% Ambient Conditions
T_inp = buffer(1);
```

```
P_inp = buffer(2);
rh = buffer(3);

fs = buffer(4);
N_PointFFT = buffer(5);
N_avg = 2*floor(Ntotal/N_PointFFT)-1;
f_bin = fs/N_PointFFT;
freq = 0:f_bin:(floor(N_PointFFT/2)-1)*f_bin;

% Read microphone distances and put them in SI
r1 = buffer(6)*0.0254;
r2 = buffer(7)*0.0254;
r3 = buffer(8)*0.0254;
r4 = buffer(9)*0.0254;

% Signal conditioning
m1 = mean(ch1data);
ch1data = ch1data - m1;
m2 = mean(ch2data);
ch2data = ch2data - m2;
m3 = mean(ch3data);
ch3data = ch3data - m3;
m4 = mean(ch4data);
ch4data = ch4data - m4;

% Jet running conditions
gamma = 1.402;
R = 286.7;

D_noz = buffer(10)*0.0254;
Md = buffer(11);
Mj = buffer(12);
TR = buffer(13);
D_eff=D_noz*sqrt(Md/Mj)*((1+Mj*Mj*(gamma-1)/2)/(1+Md*Md*(gamma-
1)/2))^((gamma+1)/(4*(gamma-1)))
% We transform the input temperature from Farenheit to Kelvins...
T_amb = 273.16 + (5.0/9.0)*(T_inp - 32.0);
% ...we compute the jet velocity...
Uj = Mj*sqrt(gamma*R*TR*T_amb);
% ...and the characteristic frequency.
fc = Uj/D_eff;

angle1=buffer(14);
angle2=buffer(15);
angle3=buffer(16);
angle4=buffer(17);

%_____________________________________________________________________
%   Windowing

hw = hanning(N_PointFFT-2);

for i = 1:N_PointFFT,
```

```
   sum1(i) = 0.0;
   sum2(i) = 0.0;
   sum3(i) = 0.0;
   sum4(i) = 0.0;
end


%_____________________________________________________________________
%   Beginning of main loop

for k = 1:N_avg,

    for i = 1:N_PointFFT,
        ch1out_hw(i) = 0.0;
        ch2out_hw(i) = 0.0;
        ch3out_hw(i) = 0.0;
        ch4out_hw(i) = 0.0;
    end

    for j = 1:N_PointFFT-2,
        ch1out_hw(j+1) = ch1data(j+1+(k-1)*(N_PointFFT/2))*hw(j);
        ch2out_hw(j+1) = ch2data(j+1+(k-1)*(N_PointFFT/2))*hw(j);
        ch3out_hw(j+1) = ch3data(j+1+(k-1)*(N_PointFFT/2))*hw(j);
        ch4out_hw(j+1) = ch4data(j+1+(k-1)*(N_PointFFT/2))*hw(j);
    end

% ch1out_hw contains the windowed pressure time history over N_PointFFT
scans
% for channel 1

%_____________________________________________________________________
DISCRETE FOURIER TRANSFORM

        DFT1 = fft(ch1out_hw);
        DFT2 = fft(ch2out_hw);
        DFT3 = fft(ch3out_hw);
        DFT4 = fft(ch4out_hw);

%_____________________________________________________________________
%   Power spectral density calculation

    for n = 1:N_PointFFT,

      psd1(n) = 2*DFT1(n)*conj(DFT1(n))/(N_PointFFT)^2;
      sum1(n) = sum1(n) + psd1(n);

      psd2(n) = 2*DFT2(n)*conj(DFT2(n))/(N_PointFFT)^2;
      sum2(n) = sum2(n) + psd2(n);

      psd3(n) = 2*DFT3(n)*conj(DFT3(n))/(N_PointFFT)^2;
      sum3(n) = sum3(n) + psd3(n);
```

```
      psd4(n) = 2*DFT4(n)*conj(DFT4(n))/(N_PointFFT)^2;
      sum4(n) = sum4(n) + psd4(n);

   end


end
% End of the main loop

%_____________________________________________________________________
%   Calculation of the Sound Pressure Level

%   Hanning window correction
for i=1:N_PointFFT/2
    sum1(i)=sum1(i)*8/3;
    sum2(i)=sum2(i)*8/3;
    sum3(i)=sum3(i)*8/3;
    sum4(i)=sum4(i)*8/3;
end

%   Calculation of PSD per unit bandwidth
for i=1:N_PointFFT/2
    PSD1_avg(i)=sum1(i)/N_avg;
    PSD2_avg(i)=sum2(i)/N_avg;
    PSD3_avg(i)=sum3(i)/N_avg;
    PSD4_avg(i)=sum4(i)/N_avg;
end

%   Calculation of PSD per Hz if applicable
if or((resolution=='Hz'),(dimension=='St'))
   for i=1:N_PointFFT/2
        PSD1_avg(i)=PSD1_avg(i)/(f_bin);
        PSD2_avg(i)=PSD2_avg(i)/(f_bin);
        PSD3_avg(i)=PSD3_avg(i)/(f_bin);
        PSD4_avg(i)=PSD4_avg(i)/(f_bin);
   end
end

%   Calculation of Sound Pressure Level
for i = 1:N_PointFFT/2;
      spl1(i) = 10.0*log10(PSD1_avg(i)/(0.00002^2));
      spl2(i) = 10.0*log10(PSD2_avg(i)/(0.00002^2));
      spl3(i) = 10.0*log10(PSD3_avg(i)/(0.00002^2));
      spl4(i) = 10.0*log10(PSD4_avg(i)/(0.00002^2));
end


% Atmospheric Attenuation coefficients

P0 = 1.0;
T0 = 293.15;
T_tp = 273.16;
% T_amb has already been evaluated
```

```
P_amb = P_inp/1013.25;

% Equilibrium speed of sound
c_ss = sqrt(gamma*R*T_amb);

% Maximum absorption per wavelength associated with the Ox/Ni
relaxation process
a_ox = 0.0011;
a_ni = 0.0002;

% Frozen speed of sound
c_0 = c_ss/(1.0 + (a_ox + a_ni)/pi);

beta (1:floor(N_PointFFT/2)) = 0.0;

%P_sat1 = 10.79586*(1.0 - (T_tp/T_amb));
%P_sat2 = - 5.02808*log10(T_amb/T_tp);
%P_sat3 = 1.50474*10.0^(-4)*(1.0 - 10.0^(-8.29692*((T_amb/T_tp) -
1.0)));
%P_sat4 =  - 4.2873*10.0^(-4)*(1.0 - 10.0^(-4.76955*((T_tp/T_amb) -
1.0)));
%P_sat = P0*10.0^(P_sat1 + P_sat2 + P_sat3 + P_sat4 - 2.2195983);

%Make use of equivalent expresion:
P_sat = P0*10.0^( -6.8346*((T_tp/T_amb)^1.261) + 4.6151);
h = (rh/P_amb)*P_sat;

fr_ox = (P_amb/P0)*(24.0 + 4.04*10.0^4*h*((0.02 + h)/(0.391 + h)));

fr_ni = (P_amb/P0)*(T0/T_amb)^0.5*(9.0 + (280.0*h)*exp(-
4.17*((T0/T_amb)^(1/3) - 1.0)));

alpha_1 = 1.84*10^(-11)*(P0/P_amb)*(T_amb/T0)^0.5;

alpha_2 = (T0/T_amb)^2.5*(0.01275*exp(-
2239.1/T_amb)./(fr_ox+((freq).^2/fr_ox)));

alpha_3 = (T0/T_amb)^2.5*(0.1068*exp(-
3352.0/T_amb)./(fr_ni+((freq).^2/fr_ni)));

alpha = (freq).^2.*(alpha_1 + alpha_2 + alpha_3);

% Final correction coefficients (in dBs per meter)

alpha_dB = 10.0*log10((exp(alpha*1.0)).^2);


% We apply all appropriate corrections to the sound pressure levels

LS_spl1 = spl1 - act1.' - ff_fi.'+ alpha_dB*r1 ;
LS_spl2 = spl2 - act2.' - ff_fi.'+ alpha_dB*r2 ;
```

```
LS_spl3 = spl3 - act3.' - ff_fi.'+ alpha_dB*r3 ;
LS_spl4 = spl4 - act4.' - ff_fi.'+ alpha_dB*r4 ;

% LS_spl1 = spl1 - act1.' - ff_fi.'+ alpha_dB*r1 +
20.0*log10(r1/dist_sc(1));
% LS_spl2 = spl2 - act2.' - ff_fi.'+ alpha_dB*r2 +
20.0*log10(r2/dist_sc(2));
% LS_spl3 = spl3 - act3.' - ff_fi.'+ alpha_dB*r3 +
20.0*log10(r3/dist_sc(3));
% LS_spl4 = spl4 - act4.' - ff_fi.'+ alpha_dB*r4 +
20.0*log10(r4/dist_sc(4));

% Linear propagating of the results if applicable
propag = propag*D_noz;
if (propag~=0);
    LS_spl1 = LS_spl1+20*log10(r1/propag);
    LS_spl2 = LS_spl2+20*log10(r2/propag);
    LS_spl3 = LS_spl3+20*log10(r3/propag);
    LS_spl4 = LS_spl4+20*log10(r4/propag);
End

%_____________________________________________________________________
%   Strouhal number adjustment

Strouhal = freq/fc;

St_spl1 = LS_spl1 + 10.0*log10(fc);
St_spl2 = LS_spl2 + 10.0*log10(fc);
St_spl3 = LS_spl3 + 10.0*log10(fc);
St_spl4 = LS_spl4 + 10.0*log10(fc);


%_____________________________________________________________________
%   Plots of the acoustic spectra and writing of the output text file

if (dimension=='St')
    res = [Strouhal ; St_spl1 ; St_spl2 ; St_spl3 ; St_spl4];
else
    res = [freq ; LS_spl1 ; LS_spl2 ; LS_spl3 ; LS_spl4];
end

figure(1)
hold on
xlabel('Frequency (Hz)');
ylabel('SPL per unit bandwidth');
xlim([0,150000]);
set(gca,'xtick',[1000 10000 150000]);
set(gca,'xscale','log');
set(0,'DefaultLineLineWidth',2);
grid on;
plot
(res(1,:),res(2,:),res(1,:),res(3,:),res(1,:),res(4,:),res(1,:),res(5,:
),'--');
```

```
title('Corrected Power Spectra, {\itM_j} = 1.5, Cold Jet, {\itR /D_j} =
80');
legend( ['{\it\theta} = {\circ}'],['{\it\theta} =
{\circ}'],['{\it\theta} = {\circ}'],['{\it\theta} = {\circ}']);

[M,N] = size(res);

cd CPSD_Data
if (propag~=0);
    for i = 2:M
        spl = [res(1,:) ; res(i,:)];
        filename = strcat(outfile,'_00',num2str(i-1),'.txt');
        fid2 = fopen(filename,'wt');
        fprintf(fid2,'%16.10f\t%16.10f\t\n',spl);
        fclose(fid2);
    end;
else
    for i = 2:M
        spl = [res(1,:) ; res(i,:)];
        filename = strcat(outfile,'_00',num2str(i-1),'.txt');
        fid2 = fopen(filename,'wt');
        fprintf(fid2,'%16.10f\t%16.10f\t\n',spl);
        fclose(fid2);
    end;
end
cd ..

disp('END OF CODE')
```

B.2 Optical Deflectometry processing code: *OD_process_JV_V10.m*

```
clear all;
close all;
clc;

%
%**********************************************************************
******
%
disp('                    |-------------------------------|');
disp('                    | HIGH SPEED JET NOISE FACILITY |');
disp('                    |-------------------------------|');
disp(' ');
%   The name of this code is "OD process JV V9.m"
%   Modified from OD process JV V8.m
```

```
%   This Matlab code processes time series data from two
photomultipliers recorded from channels 1 and 2

disp('Developed by Jeremy Veltin                                February
26th, 2008');
disp('Last updated                                              June 28th,
2008');
%
%   Checked by Ching Wen kuo and partly by P.J. Morris
%
%*********************************************************************

disp(' ');
disp('************************************************************');
disp('           CROSS CORRELATION AND CROSS SPECTRA CALCULATIONS');
disp('              FROM OPTICAL DEFLECTOMETRY MEASUREMENTS.');
disp('************************************************************');
disp(' ');
disp(' ');
disp('This Matlab code takes as an input a text file containing
informations on the conditions of the experiment. The time series (in
text format) are then read for each photomultiplier location and the
distance between the two photomultipliers needs to be input. ');
disp(' ');
disp('This code calculates the cross spectrum for each separation
distance as well as the cross-correlation function. It plots them and
saves them as separate text files in the "Results" folder that needs to
be created in the working directory. In addition, the convection
velocity is calculated, and an option was added in order to numerically
remove the screech tones from a screeching jet (in a way similar to
what was first done by S. Saxena and B. Day in Fall 07).
disp('Please make sure the input file is properly filled before running
the code. The original file "input.dat" contains a description of the
needed inputs.');
disp(' ');

%

%*********************************************************************
%                                  NOMENCLATURE
%
% - Ntotal is the total number of data points in the time signal
% - fs is the sampling frequency
% - Ch1 is the voltage time histories recorded on channel #1
% - ch1out_hw is the windowed piece of channel #1 signal used for FFT
% - N_PointFFT is the number of points used for each Fourier transform
% - N_avg is the number of averages used to compute the psd, taking
into
%    account overlap by 1/2
% - DFT1 is the discrete fourier transform calculated from ch1out_hw
% - psd1 is the double sided power spectral density calculated from
DFT1
% - PSD1_avg is the double sided power spectral density of channel#1
%    after averaging on all the windows
```

```
% - PSD12_avg is the double sided cross spectral density between
channels 1
%    and 2
% - Gxx1 and Gxx2 are the single sided power spectral density of
channels 1
%    and 2
% - Gxy is the single sided cross spectral density between channels 1
and 2
% - Rxx1 and Rxx2 are the auto correlations of channels 1 and 2
% - Rxy is the cross correlation between channel 1 and 2
% - Cross is a vector that stores the cross correlation functions for
each
%    probe location. The cross correlation functions are Rxy normalized
by
%    the values of the autocorrelation peaks (max(Rxx1) and max(Rxx2))
% - f_bin is the frequency bin width
% - D_noz is the nozzle diameter
% - Mj is the jet Mach number
% - TR is the total temperature ratio (To/Tamb)
% - TRs is the static temperature ratio (Tj/Tamb)
% - D_eff is the equivalent fully epanded jet diameter
% - Md is the design Mach number of the nozzle
% - Uj is the jet velocity
% - fc is the characteristic frequency
%
%*********************************************************************
%_____________________________________________________________________
% Reading the conditions from the input file.

disp('');
disp('*************************************************************');
disp('    Choose the input file name containing the conditions for this
data set   ');
disp('*************************************************************');
disp(' ');
disp('                          Press any key to continue
');
disp('');
pause

[filename_input, pathname] = uigetfile( {'*.dat'} ,'Open' );

fid1 = fopen(filename_input);
buffer = fscanf(fid1,'%f');
fclose(fid1);
clc

disp('');
disp('*************************************************************');
disp('                    Reading of time series fom files      ');
disp('*************************************************************');
disp(' ');
nb_file = (input('Type in the number of raw time series files : '));
clc
```

```
%%new with version 10%%
disp('');
disp('************************************************************');
disp('                    Select which of the channels you would like to
use        ');
disp('************************************************************');
disp(' ');
primary_chan = (input(' Please input the channel number of your Primary
Channel: '));
secondary_chan = (input(' Please input the channel number of your
Secondary Channel: '));
clc

%%End of new part


for i=1:nb_file,
    disp('');

disp('************************************************************');
    disp('                    Reading of time series fom files      ');

disp('************************************************************');
    disp(' ');
    disp1 = strcat('File number: ',num2str(i));
    disp(disp1);
    disp(' ');
    distance(i) = (input('Distance between 2 photomultipliers (in
Diameters): '));
    disp(' ');

disp('************************************************************');
    disp('             ');
    disp('                  Press any key to choose the file name
');
    disp(' ');
    pause
    [filename_time(i,:), pathname] = uigetfile( {'*.*'} ,'Open' );
    clc
    disp('             ');
    disp('          Reading file, please wait ...
');
    disp(' ');
    %open binary file as read only big-endian
    fid = fopen(filename_time(i,:),'r','b');
    fseek(fid,0,'eof'); %seek to end of file
    file_size = ftell(fid); %get file size
    fseek(fid,0,'bof'); %go back to begining of file
    %get header length
    header_size = fread(fid,1,'int32');
    %get number of channels from channel string
    channel_str_len = fread(fid,1,'int32');
    channel_str = fread(fid,channel_str_len,'*char');
```

```
    num_channels = str2num(channel_str(channel_str_len))+1;
    hardware_config_len = fread(fid,1,'int32');
    %move to end of hardware confid and back up 8 bytes
    fseek(fid,hardware_config_len-8,'cof');
    scale_factor = fread(fid,1,'float32');
    scale_offset = fread(fid,1,'float32');
    sample_rate = fread(fid,1,'float32');
    interchannel_delay = fread(fid,1,'float32');
    %skip past header to data part of file
    fseek(fid,header_size+4,'bof');
    data_size = file_size - header_size - 4; %calc how much data there
is
    num_samples = (data_size/2)/num_channels;
    %read data into array
    data = zeros(num_samples,num_channels);
    dataread = zeros(num_samples*num_channels,1);
    %i think this is faster
    dataread =
fread(fid,num_samples*num_channels,'int16')*scale_factor*1000;
    data = (reshape(dataread,num_channels,num_samples))';
    %close the file
    fclose(fid);

    %Save the two channels that were selected earlier
    Ch1(i,:)=data(:,primary_chan);
    Ch2(i,:)=data(:,secondary_chan);

    clc
    disp('              ');
    disp('          Please wait ...                          ');
    disp(' ');
end

%_____________________________________________________________________
% Interpretation of inputs

Ntotal = length(Ch1(1,:));

% Ambient Conditions
T_inp = buffer(1);
P_inp = buffer(2);
rh = buffer(3);

fs = buffer(4);
N_PointFFT = buffer(5);
N_avg = 2*floor(Ntotal/N_PointFFT)-1;
f_bin = fs/N_PointFFT;
freq = 0:f_bin:(floor(N_PointFFT/2)-1)*f_bin;
dt = 1/fs;

% Jet running conditions
gamma = 1.402;
R = 286.7;
```

```
D_noz = buffer(6)*0.0254;
Md = buffer(7);
Mj = buffer(8);
TR = buffer(9);
screech_removal = buffer(12);
channel=buffer(11);
XoverD = buffer(10);
D_eff=D_noz*sqrt(Md/Mj)*((1+Mj*Mj*(gamma-1)/2)/(1+Md*Md*(gamma-
1)/2))^((gamma+1)/(4*(gamma-1)));
% We transform the input temperature from Farenheit to Kelvins...
T_amb = 273.16 + (5.0/9.0)*(T_inp - 32.0);
% We calculate the static temperature ratio
TRs = TR / (1+(gamma-1)/2*Mj*Mj);
% ...we compute the jet velocity...
Uj = Mj*sqrt(gamma*R*TRs*T_amb);
% ...and the characteristic frequency.
fc = Uj/D_eff;
St=freq/fc;
filt = (input('Type in the filtering frequency for cross-correlation
calculation : '));
disp('              ');

color = strvcat('k', '--k', 'r', '--r', 'g', '--g', 'b', '--b', 'c','--
c', 'm', '--m', 'k', '--r', 'g', '--b', 'c', 'm', '--c', 'm', '--m',
'k', '--r', 'g', '--b', 'c', 'm','--b', 'c', 'm', '--c', 'm', '--m',
'k', '--r', 'g', '--b', 'c', 'm');
color2 = [[0, 0, 0]  ;[0, 0.5, 0]; [1 ,0, 0] ;[0.04, 0.52 ,0.78]; [0, 1
,0]; [0.87, 0.49, 0] ;[0.48, 0.06, 0.89] ;[0, 0, 1] ;[0.32, 0.19
,0.19];[0, 1, 1];[0.75,0,0.75];[0, 0, 0]  ;[0, 0.5, 0]; [1 ,0, 0]
;[0.04, 0.52 ,0.78]; [0, 1 ,0]; [0.87, 0.49, 0] ;[0.48, 0.06, 0.89]
;[0, 0, 1] ;[0.32, 0.19 ,0.19];[0, 1, 1];[0.75,0,0.75];[0, 0, 0]  ;[0,
0.5, 0]; [1 ,0, 0] ;[0.04, 0.52 ,0.78]; [0, 1 ,0]; [0.87, 0.49, 0]
;[0.48, 0.06, 0.89] ;[0, 0, 1] ;[0.32, 0.19 ,0.19];[0, 1,
1];[0.75,0,0.75];[0, 0, 0]  ;[0, 0.5, 0]; [1 ,0, 0] ;[0.04, 0.52
,0.78]; [0, 1 ,0]; [0.87, 0.49, 0] ;[0.48, 0.06, 0.89] ;[0, 0, 1]
;[0.32, 0.19 ,0.19];[0, 1, 1];[0.75,0,0.75]];

%_____________________________________________________________________
% Calculation of Cross-correlation functions, spectra and cross spectra
cd Results

%   Windowing

hw = hanning(N_PointFFT-2);

% Looping through each PM location
for position=1:nb_file

distance(position)=distance(position)*D_eff;
disp(' ');
disp1 = strcat('   Processing file number: ',num2str(position));
disp(disp1);
```

```
for i = 1:N_PointFFT,
   sum1(i) = 0.0;
   sum2(i) = 0.0;
   sum12(i) = 0.0;
end

% Beginning of loop on windows

for k = 1:N_avg,

    for i = 1:N_PointFFT,
        ch1out_hw(i) = 0.0;
        ch2out_hw(i) = 0.0;
    end

    for j = 1:N_PointFFT-2,
        ch1out_hw(j+1) = Ch1(position,j+1+(k-1)*(N_PointFFT/2))*hw(j);
        ch2out_hw(j+1) = Ch2(position,j+1+(k-1)*(N_PointFFT/2))*hw(j);
    end

% ch1out_hw contains the windowed pressure time history over N_PointFFT
% scans for channel 1


%   DISCRETE FOURIER TRANSFORM

    DFT1 = fft(ch1out_hw);
    DFT2 = fft(ch2out_hw);


%   Power spectral density calculation (double sided, per unit
bandwidth)

    for n = 1:N_PointFFT,

      psd1(n) = DFT1(n)*conj(DFT1(n))/(N_PointFFT)^2;
      sum1(n) = sum1(n) + psd1(n);

      psd2(n) = DFT2(n)*conj(DFT2(n))/(N_PointFFT)^2;
      sum2(n) = sum2(n) + psd2(n);

    if channel
        psd12(n) = DFT2(n)*conj(DFT1(n))/(N_PointFFT)^2;
    else
        psd12(n) = DFT1(n)*conj(DFT2(n))/(N_PointFFT)^2;
    end
      sum12(n) = sum12(n) + psd12(n);

    end
```

```
end
% End of the windows loop

% Hanning window correction
for i=1:N_PointFFT
    sum1(i)=sum1(i)*8/3;
    sum2(i)=sum2(i)*8/3;
    sum12(i)=sum12(i)*8/3;
end

% Calculation of averaged double sided PSD per unit bandwidth
for i=1:N_PointFFT
    PSD1_avg(i)=sum1(i)/N_avg;
    PSD2_avg(i)=sum2(i)/N_avg;
    PSD12_avg(i)=sum12(i)/N_avg;
end

% Removal of the screech tones, if applicable
if screech_removal
loop=true;
% Plot the unmodified PSD
figure(8)
hold on
for i=1:N_PointFFT/2
    Temp(i)=2*PSD12_avg(i);
end
plot(freq,Temp);
% cycle through all screech tones
iter=1;
while loop
    [tone,freq_tone(iter)]=max(PSD1_avg(8:N_PointFFT));
    freq_tone(iter)=freq_tone(iter)+7;
    average1=0;
    average2=0;
    average3=0;
    for j=1:5
         average1=average1+PSD1_avg(freq_tone(iter)-j-2)/5;
         average2=average2+PSD2_avg(freq_tone(iter)-j-2)/5;
         average3=average3+PSD12_avg(freq_tone(iter)-j-2)/5;
    end
    % Smooth out if the peak is too much above the rest of the spectrum
    if tone>average1+tone/5
        for k=-2:2
            PSD1_avg(freq_tone(iter)+k)=average1;
            PSD2_avg(freq_tone(iter)+k)=average2;
            PSD12_avg(freq_tone(iter)+k)=average3;
        end
        iter=iter+1;
    else
        loop=false;
    end
end
% Plot the modified PSD in red
figure(8)
```

```
hold on
for i=1:N_PointFFT/2
    Temp(i)=2*PSD12_avg(i);
end
plot(freq,Temp,'r');
end

% Calculate filtered PSD for cross-correlation
max_freq=floor(filt/f_bin);
for i=1:max_freq;
    PSD12_filt(i)=PSD12_avg(i);
    PSD1_filt(i)=PSD1_avg(i);
    PSD2_filt(i)=PSD2_avg(i);
end
for i=1:max_freq;
    PSD12_filt(i+max_freq)=PSD12_avg(length(PSD12_avg)-max_freq+i);
    PSD1_filt(i+max_freq)=PSD1_avg(length(PSD1_avg)-max_freq+i);
    PSD2_filt(i+max_freq)=PSD2_avg(length(PSD2_avg)-max_freq+i);
end

% Calculation of single sided PSD per unit bandwidth
for i=1:max_freq
    Gxx1(i)=2*PSD1_filt(i);
    Gxx2(i)=2*PSD2_filt(i);
    Gxy12(i)=2*PSD12_filt(i);
end


% Calculation of auto and cross-correlation functions
    Rxy=ifft(PSD12_filt)/(f_bin*dt);
    Rxx1=ifft(PSD1_filt)/(f_bin*dt);
    Rxx1 = fftshift(Rxx1);
    Rxx2=ifft(PSD2_filt)/(f_bin*dt);
    Rxx2 = fftshift(Rxx2);
    cross(position,:)=Rxy/(max(Rxx1)*max(Rxx2))^0.5;

    for j=1:max_freq*2
        if j>max_freq
            temp(j-max_freq)=cross(position,j);
        else
            temp(j+max_freq)=cross(position,j);
        end
        % Calculation of retarded time, non-dimensionalized with fc
        Ret_time(j) = (j-max_freq-1)/(2*max_freq*f_bin)*fc;
    end
    for j=1:max_freq*2
        cross(position,j) = temp(j);
    end
    for j=1:max_freq
        freq2(j)=f_bin*j;
    end

    St2=freq2/fc;
```

```
% Save cross-spectra to text file
totextfile = [freq2 ; Gxy12];
filename = strcat('Cross-spectrum at position
',num2str(position),'.txt');
fid2 = fopen(filename,'wt');
fprintf(fid2,'Distance between the two photomultipliers: %1.2f
D\n',distance(position)/D_eff);
fprintf(fid2,'Total number of photomultiplier locations used in this
processing: %i \n',nb_file);
fprintf(fid2,'Filename of the time serie file: %s
\n',filename_time(position,:));
fprintf(fid2,'Filename of the input file: %s \n\n',filename_input);
fprintf(fid2,'%16.10f\t%16.10f\t\n',totextfile);
fclose(fid2);

% Plot magnitude of auto and cross spectra
figure(5)
hold on
set(gca,'XMinorTick','on','LineWidth',2,'FontWeight','bold','FontSize',
12);
title('Auto and cross spectra at various probe separations');
xlabel('Frequency (Hz)');
ylabel('Gxx');
plot(freq2,abs(Gxx1),color(1,:));
plot(freq2,abs(Gxx2),color(3,:));
plot(freq2,abs(Gxy12),color(5,:));
box('on');
xlim([0,60000]);

%plot the magnitude and auto and cross spectra at EACH LOCATION
figure(20+position)
hold on
set(gca,'XMinorTick','on','LineWidth',2,'FontWeight','bold','FontSize',
12);
title(strcat('Auto and cross spectra at separation
{\Delta}{\itx}/{\itD} =', num2str(distance(position)/D_eff)));
xlabel('Frequency (Hz)');
ylabel('Gxx');
plot(freq2,abs(Gxx1),color(1,:));
plot(freq2,abs(Gxx2),color(3,:));
plot(freq2,abs(Gxy12),color(5,:));
box('on');
xlim([0,60000]);
saveas(gcf,strcat('Auto-cross-
spectra',num2str(distance(position)/D_eff),'D.fig'));


% Plot phase of cross-spectra
figure(6)
hold on
title('Phase of cross spectra at various probe separations');
xlabel('Frequency (Hz)');
ylabel('phase of Gxy12');
```

```
xlim([0,150000]);
phase(position,:) = angle(Gxy12);
for i = 1:length(phase(position,:))
   phase_shifted(position,i)=phase(position,i);
end
test=1;
for l=1:5
for i = 41:length(phase(position,:))
   if phase_shifted(position,i)>pi+mean([phase_shifted(position,i-30)
phase_shifted(position,i-40)]) ;
       phase_shifted(position,i)=phase_shifted(position,i)-2*test*pi;
   end
end
end
for i = 5:length(phase)-5
    phase_shifted(position,i)=mean([phase_shifted(position,i-2)
phase_shifted(position,i-1) phase_shifted(position,i+1)
phase_shifted(position,i+2)]);
end
set(gca,'FontSize',12);
plot(freq2,phase_shifted(position,:),'Color',color2(position,:));
set(gca,'XMinorTick','on','LineWidth',2,'FontWeight','bold','FontSize',
12);
box('on');
figure(1)
hold on
title('Phase of cross spectra at various probe separations');
xlabel('Frequency (Hz)');
ylabel('phase of Gxy12');
xlim([0,150000]);
set(gca,'FontSize',12);
plot(freq2,phase(position,:),'Color',color2(position,:));
set(gca,'XMinorTick','on','LineWidth',2,'FontWeight','bold','FontSize',
12);
box('on');

% calculate and plot the coherence
figure(7)
hold on
gamma = sqrt((conj(PSD12_avg).*PSD12_avg)./(PSD1_avg.*PSD2_avg ));
xlabel('Strouhal number');
ylabel('The coherence function, \gamma ^2');
xlim([0,10]);
set(gca,'xscale','log');
set(gca,'FontSize',12);
for k=1:max_freq
    gamma2(position,k)=gamma(k)^2;
end
plot (St2,gamma2(position,:),'Color',color2(position,:));
set(gca,'XMinorTick','on','LineWidth',2,'FontWeight','bold','FontSize',
12);
box('on');
```

```
% Plot and save cross-correlations to text file
figure(2)
hold on
plot (Ret_time(:),cross(position,:),color(position,:),'LineWidth',2)
totextfile = [Ret_time ; cross(position,:)];
filename = strcat('Cross-correlation at position
',num2str(position),'.txt');
fid2 = fopen(filename,'wt');
fprintf(fid2,'Distance between the two photomultipliers: %1.2f
D\n\n',distance(position)/D_eff);
fprintf(fid2,'Total number of photomultiplier locations used in this
processing: %i \n',nb_file);
fprintf(fid2,'Filename of the time serie file: %s
\n',filename_time(position,:));
fprintf(fid2,'Filename of the input file: %s \n\n',filename_input);
fprintf(fid2,'%16.10f\t%16.10f\t\n',totextfile);
fclose(fid2);

figure(3)
hold on
plot (Ret_time(:),Rxx2/max(Rxx2))
set(gca,'XMinorTick','on','LineWidth',2,'FontWeight','bold','FontSize',
12);
% Look for the peak of correlation, record the peak value and the
% corresponding retarded time.
max_time(position) = 0.0;
[cor_max(position), timebin_peak(position)]=max(cross(position,:));
max_time(position)=Ret_time(timebin_peak(position))/fc;

end
% End of loop on PM locations
%_____________________________________________________________________
____


% Format the graphs
figure(2)
grid on;
xlim([0.0,3.0]);
ylim([-0.2,1.0]);
set(gca,'XMinorTick','on','LineWidth',2,'FontWeight','bold','FontSize',
12);
title('Cross-correlation function at various probe separations');
xlabel('Nondimensional Time, {\it\tau} = {\itt} \times {\it{f_c}}');
ylabel('{\it{\rho}}_{12}');
leg='';
leg2='';
for position=1:nb_file
    leg=strvcat(leg,strcat('{\Delta}{\itx}/{\itD} =
',num2str(distance(position)/D_eff)));
    leg2=strvcat(leg2,strcat('Gxx at {\Delta}{\itx}/{\itD} =
',num2str(distance(position)/D_eff)));
    leg2=strvcat(leg2,strcat('Gyy at {\Delta}{\itx}/{\itD} =
',num2str(distance(position)/D_eff)));
```

```
    leg2=strvcat(leg2,strcat('|Gxy| at {\Delta}{\itx}/{\itD} =
',num2str(distance(position)/D_eff)));
end
legend(leg,1)
saveas(gcf,strcat('Correllelogram.fig'));

figure(3)
set(gca,'XMinorTick','on','LineWidth',2,'FontWeight','bold','FontSize',
12);
title('Auto-correlation function at various probe locations');
legend(leg,1)
saveas(gcf,strcat('Autocorrelations.fig'));
figure(1)
legend(leg,1)
figure(4)
legend(leg,1)
figure(5)
legend(leg2,1);
figure(6)
legend(leg,1)
saveas(gcf,strcat('Phase.fig'));
figure(7)
legend(leg,1)
saveas(gcf,strcat('Coherence.fig'));
allfigs = dir('*.fig');
% save all the figs as bmp pictures
for n = 1:length(allfigs)
        openfig(allfigs(n).name);
        print( '-dbitmap',
strcat(allfigs(n).name(1:length(allfigs(n).name)-4),'.bmp'));
        close
        disp(strcat(allfigs(n).name(1:length(allfigs(n).name)-4), '.bmp
saved'))
end

figure(4)
[p, S] = polyfit(max_time, distance, 1);
plot(max_time, distance, '-b');

% Statistics
time_avg = mean(max_time);
dist_avg = mean(distance);
st_sq = 0.0;
sd_sq = 0.0;
s_td = 0.0;

for i = 1:nb_file,
    st_sq = (1.0/(8.0 - 1.0))*(max_time(i) - time_avg)^2 + st_sq;
    sd_sq = (1.0/(8.0 - 1.0))*(distance(i) - dist_avg)^2 + sd_sq;
    s_td = (1.0/(8.0-1.0))*(max_time(i) - time_avg)*(distance(i) -
dist_avg) + s_td;
end;

% % Correlation coefficient
```

```
r = s_td/sqrt(st_sq*sd_sq);
r_sq = r^2;
R = corrcoef(max_time, distance);

% Convection velocity:
Uc = p(1);

% Convection velocity ratio
ratio = Uc/Uj;

% Display results
fprintf('\nJet Exhaust Velocity\t = '); disp(num2str(Uj));
fprintf('Jet Convection Velocity\t = '); disp(num2str(Uc));
fprintf('Ratio Uc/Uj\t\t\t\t = '); disp(num2str(ratio));
fprintf('Correlation Coefficient\t = '); disp(num2str(r));

save results;
```

B.3 Sample input files

B.3.1 Sample input file for *JNA_CPSD_Vb.m*

```
70.0
975.0
42.0

300000
4096

69.5
68.5
68.25
69.0

0.5
1.0
1.5
0.69

80
90
100
110


% The first 3 elements are related to ambient conditions in the chamber
% Temperature (in F)
% Pressure (in mBar)
% Percentage relative humidity (%)
%
% The next two figures are the sampling frequency (in Hz) and the total number of points
% to be used for Discrete Fourier Transform.
%
% The next four numbers are microphone distances (in inches).
%
% The following four numbers are the jet running conditions. The nozzle diameter (in
% inches) then, the jet Mach design, the jet Mach number and the temperature ratio.
%
% Finally, the next 4 numbers are the polar angle at each microphone
```

B.3.2 Sample input file for *OD_process_JV_V10.m*

```
71.0
977.0
43.0

300000
4096

1.0
1.0
0.9
1.0

4.0

0
0

% Temperature (in F) in the chamber
% Pressure (in mBar) in the chamber
% Percentage relative humidity (%) in the chamber
%
% Sampling frequency (in Hz)
% Total number of points to be used in one window for Discrete Fourier Transform.
%
% Nozzle diameter (in inches)
% Jet Mach design
% Jet Mach number
% Total temperature ratio (1 for cold jets)
%
% Starting distance of OD measurement: X/D
%
% Put 0 if the PMT that moves is on channel0, 1 if on channel1
% Put 1 if computational removal of the screech tones is required, 0 otherwise
```

Appendix C

Additional screech tone suppression measurements

The main results of the research made on screech tone suppression are presented in section **4.2**. Some additional measurements are presented here, including different tab sizes and penetration angles, noise from a jet issuing from an imperfectly round nozzle and the addition of a foam baffle around the nozzle.

The results of these experiments are very similar to what was summarized before. The ring with added roughness behaved in a same way than the roughness added at the lip, reducing the screech intensity with little effect on the shock associated noise and no effect on the rest of the spectra. The out of round nozzle behaved pretty poorly in term of screech suppression. The different tabs showed very good results as far as screech removal is concerned, with the biggest tabs (Tab1 and Tab2) removing the screech best, especially with higher penetration angle (Tab2). However, they affected the magnitude of the BBSAN significantly. Smaller tabs (Tab 3 and 4) affected less the spectra but failed to completely remove the screech. Usage of two small tabs showed results very similar to the usage of one big tab, with good screech suppression and some effect on the BBSAN. Clocking of the tab affects the results but not significantly, despite the strong impact the presence of the tabs had on the shock cell geometry (shown in section **4.2**).

Finally, a 2” thick 6” sided square foam baffle surrounding the jet was used as screech suppressor. It performs some screech suppression since some of the tones completely disappeared. No effect on the rest of the spectra was observed. However some of the tones were not affected at all by the baffle and were still at very high amplitude. Different foam densities may produce a better suppression, as well as different shapes of the baffle.

These results are very positive and will be used in the future any time screech suppression is required for accurate measurement of any other property of the jets.

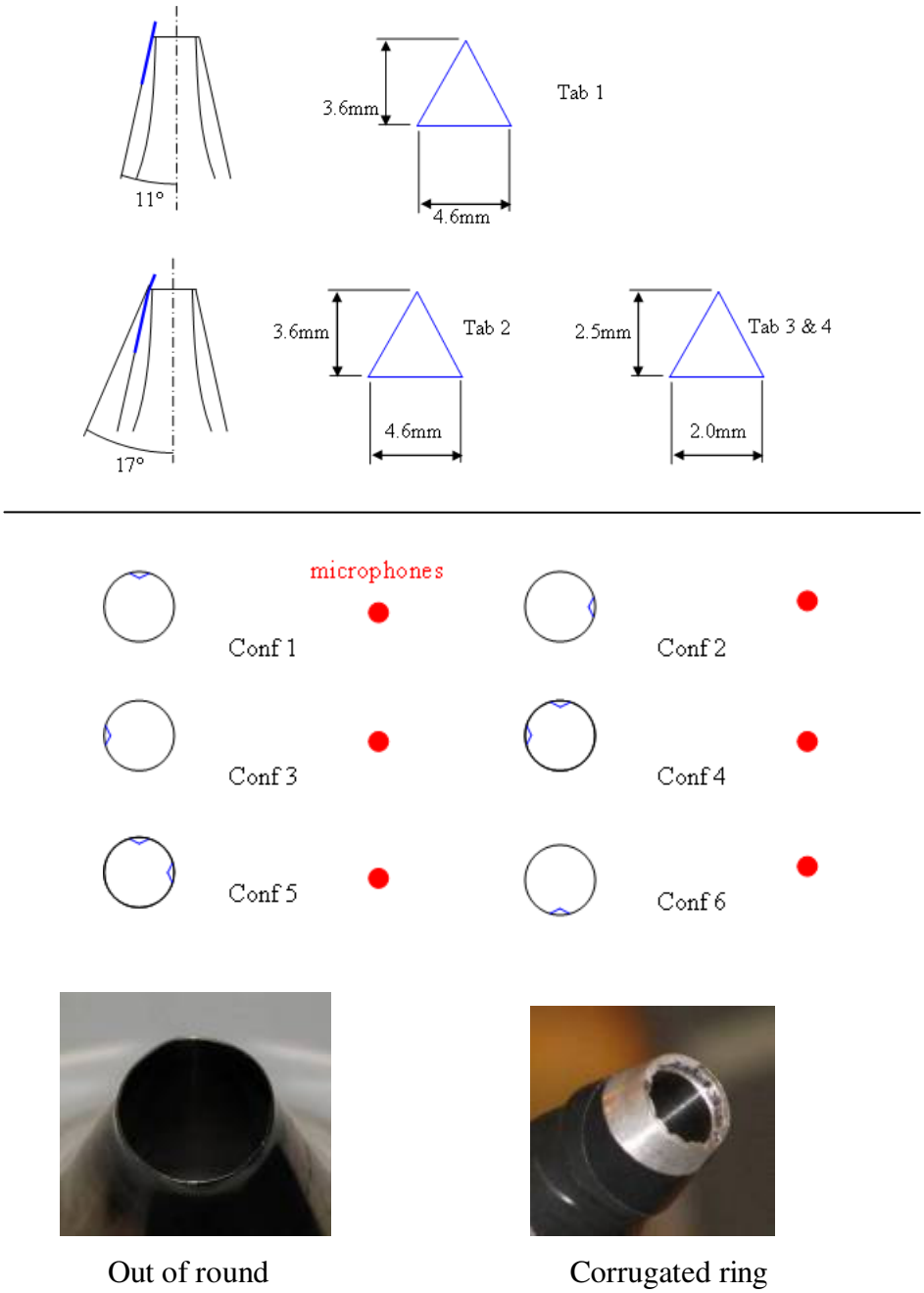

Figure **C-1**: Drawing of the different tabs used for screech suppression, definition of the tab location with respect to the microphones, and pictures of the out or round and of the corrugated ring

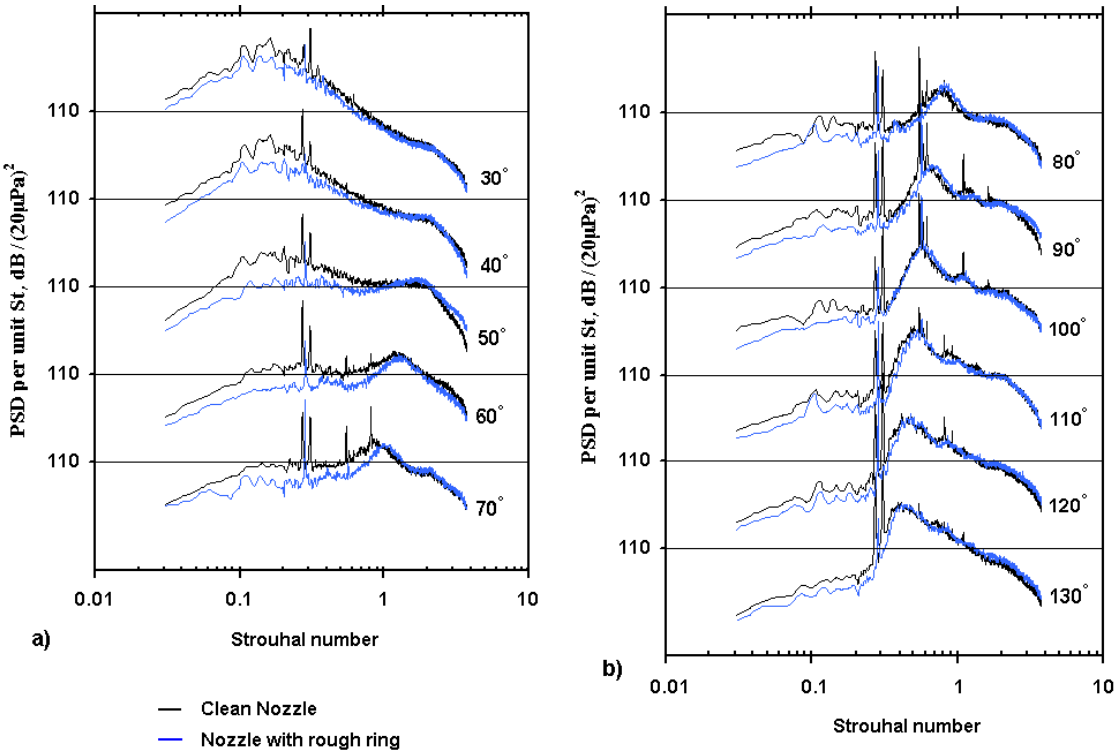

Figure **C-2**: Comparison between a clean nozzle and one with a rough ring for a cold jet, $M_d = 1.0$ and $M_j = 1.5$. a) θ from 30° to 70° . b) θ from 80° to 130°.

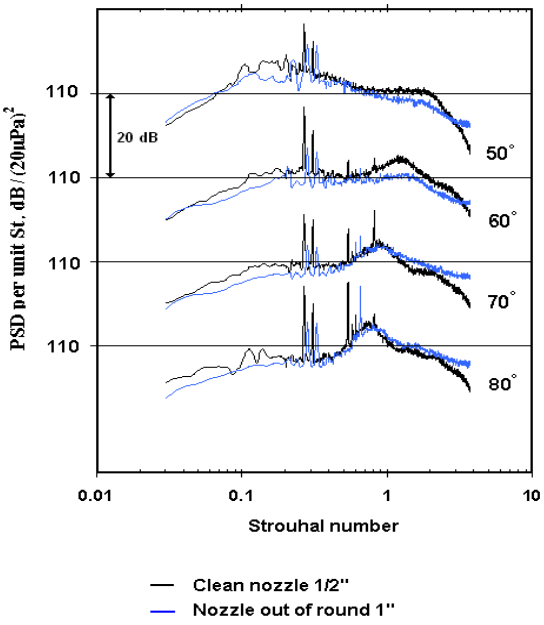

Figure **C-3**: Comparison between a clean nozzle and one with am out of round lip for a cold jet, $M_d = 1.0$ and $M_j = 1.5$. a) θ from 30° to 70° . b) θ from 80° to 130°.

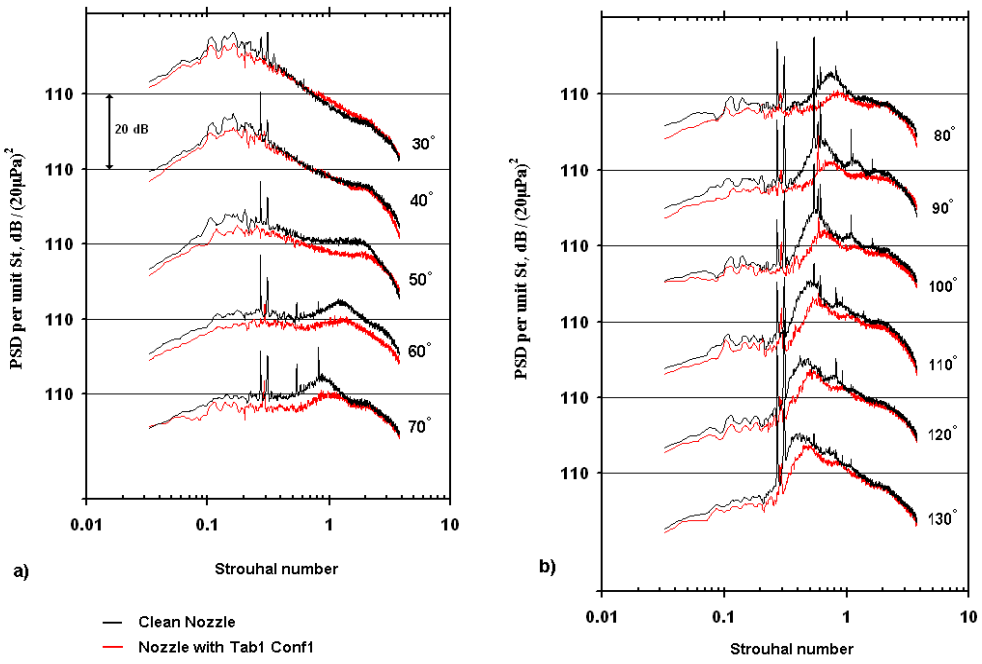

Figure **C-4**: Comparison between a clean nozzle and one with a Tab1 in configuration 1 for a cold jet, M_d = 1.0 and M_j = 1.5. a) θ from 30° to 70° . b) θ from 80° to 130°.

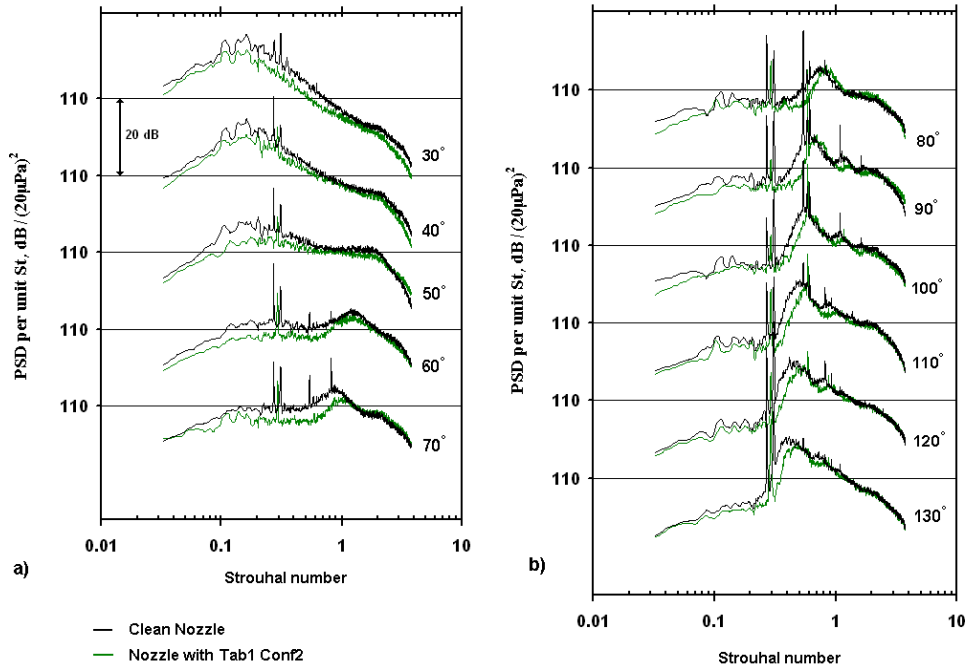

Figure **C-5**: Comparison between a clean nozzle and one with a Tab1 in configuration 2 for a cold jet, M_d = 1.0 and M_j = 1.5. a) θ from 30° to 70° . b) θ from 80° to 130°.

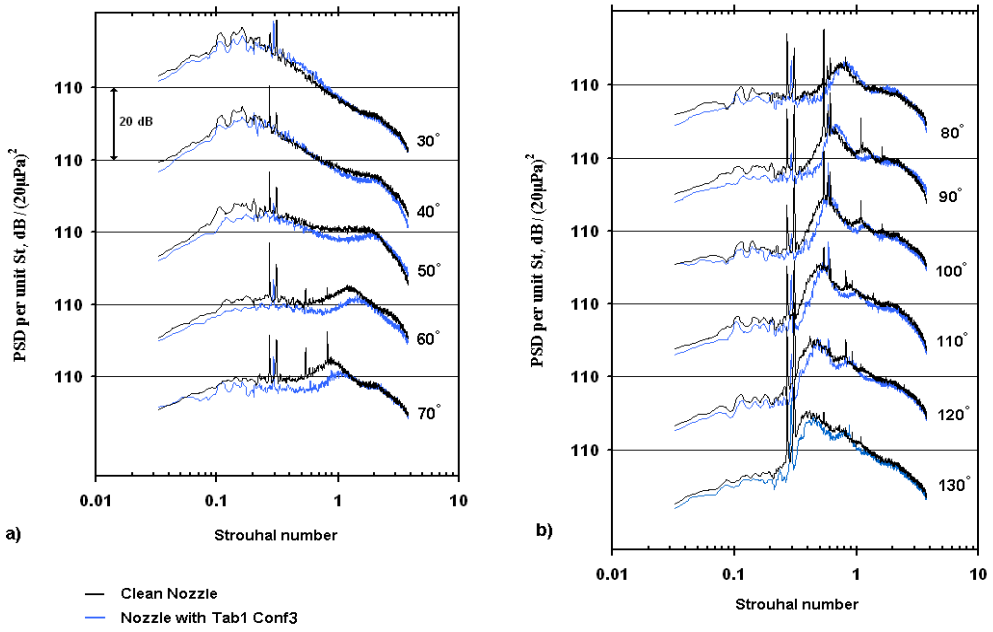

Figure **C-6**: Comparison between a clean nozzle and one with a Tab1 in configuration 3 for a cold jet, M_d = 1.0 and M_j = 1.5. a) θ from 30° to 70° . b) θ from 80° to 130°.

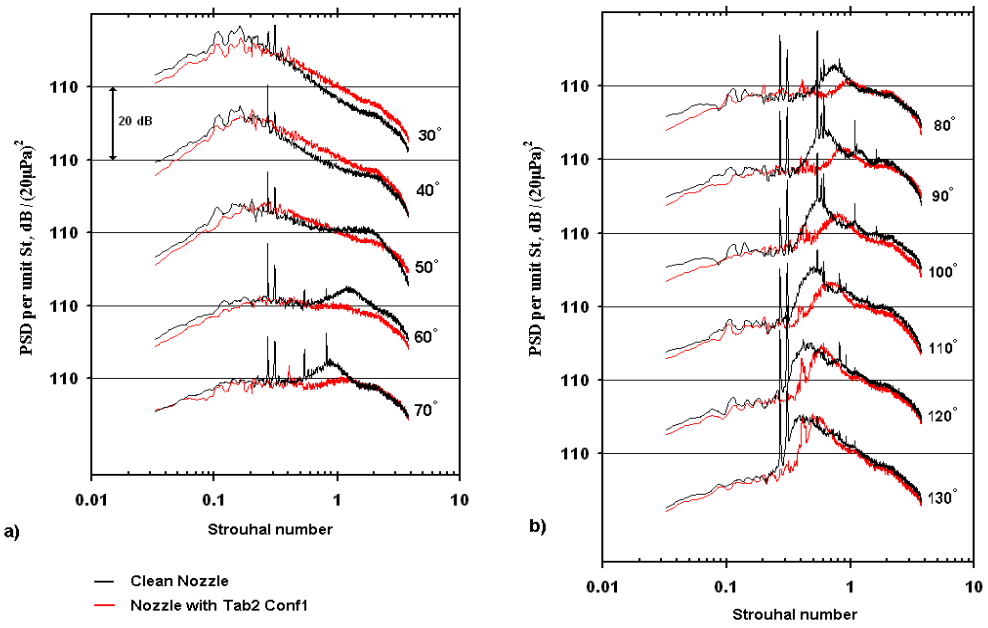

Figure **C-7**: Comparison between a clean nozzle and one with a Tab2 in configuration 1 for a cold jet, M_d = 1.0 and M_j = 1.5. a) θ from 30° to 70° . b) θ from 80° to 130°.

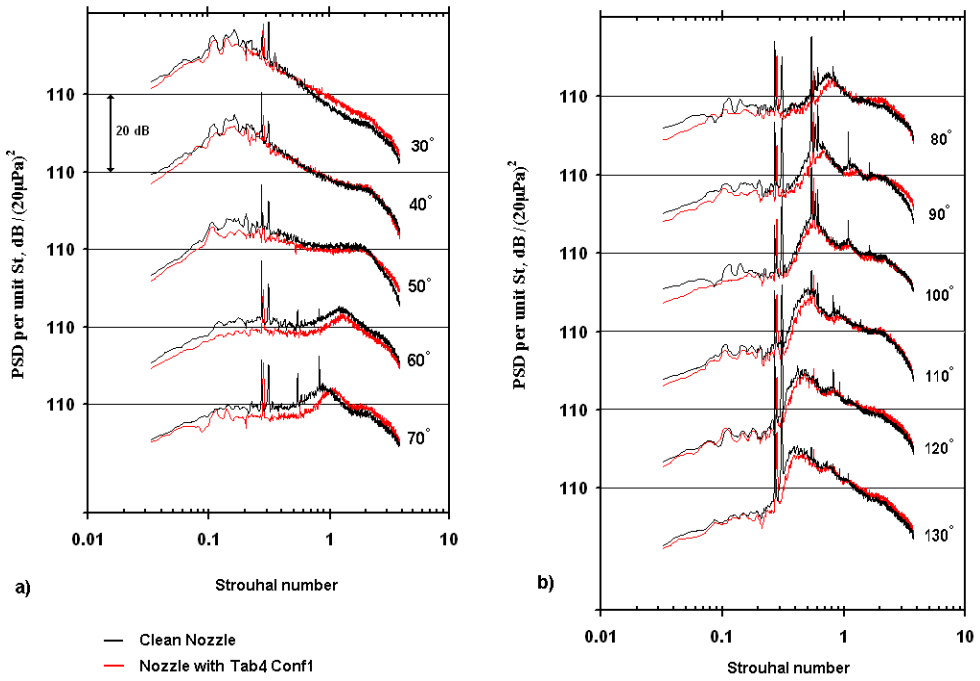

Figure **C-8**: Comparison between a clean nozzle and one with a Tab4 in configuration 1 for a cold jet, M_d = 1.0 and M_j = 1.5. a) θ from 30° to 70° . b) θ from 80° to 130°.

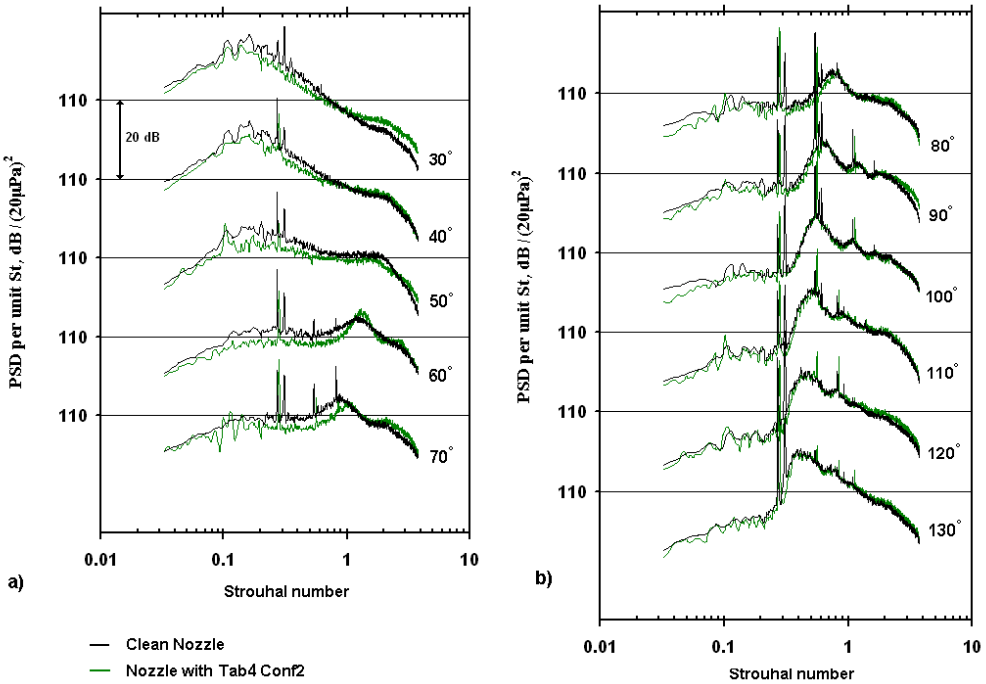

Figure **C-9**: Comparison between a clean nozzle and one with a Tab4 in configuration 2 for a cold jet, M_d = 1.0 and M_j = 1.5. a) θ from 30° to 70° . b) θ from 80° to 130°.

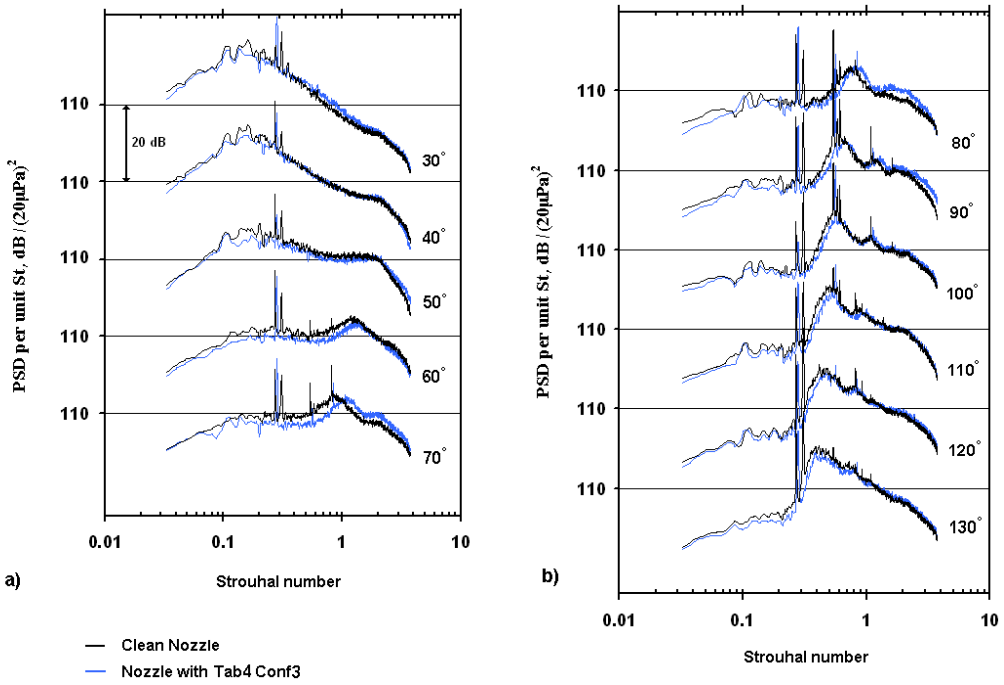

Figure **C-10**: Comparison between a clean nozzle and one with a Tab4 in configuration 3 for a cold jet, M_d = 1.0 and M_j = 1.5. a) θ from 30° to 70° . b) θ from 80° to 130°.

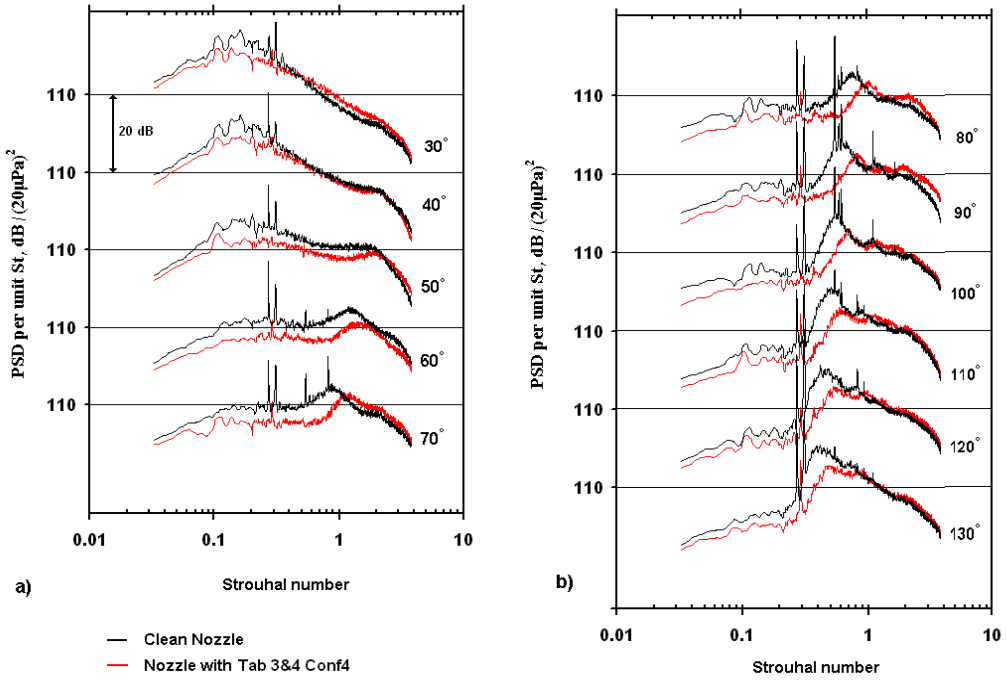

Figure **C-11**: Comparison between a clean nozzle and one with Tabs 3&4 in conf 4 for a cold jet, M_d = 1.0 and M_j = 1.5. a) θ from 30° to 70° . b) θ from 80° to 130°.

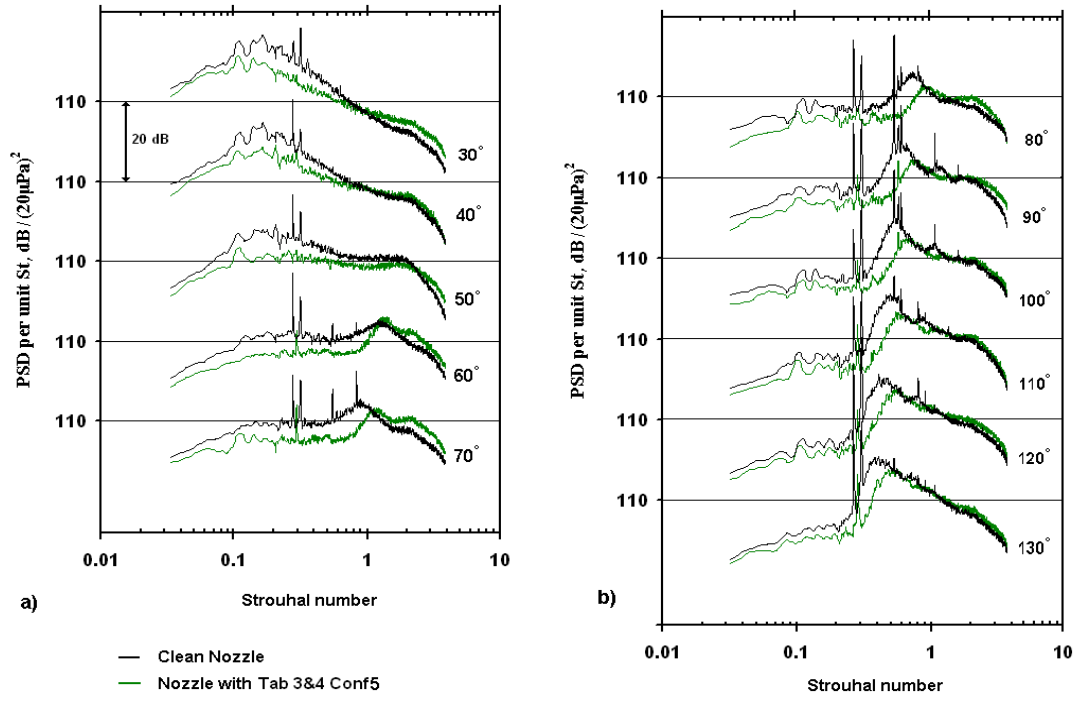

Figure **C-12**: Comparison between a clean nozzle and one with Tabs 3&4 in conf 5 for a cold jet, M_d = 1.0 and M_j = 1.5. a) θ from 30° to 70° . b) θ from 80° to 130°.

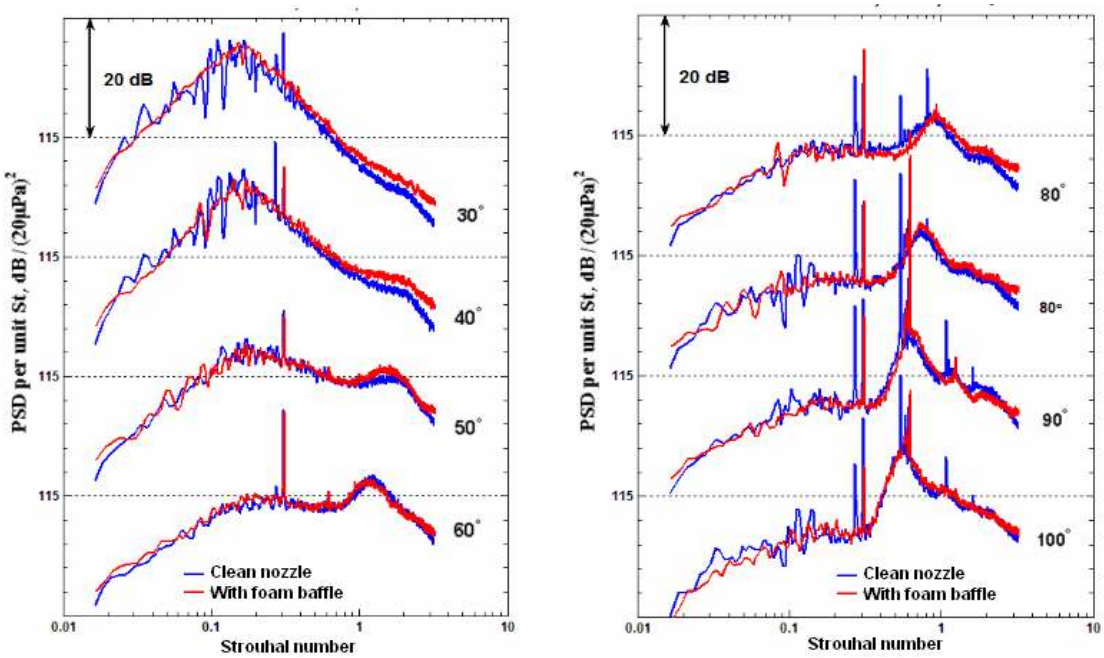

Figure **C-13**: Comparison between a clean nozzle and one with Tabs 3&4 in conf 5 for a cold jet, M_d = 1.0 and M_j = 1.5. a) θ from 30° to 70° . b) θ from 80° to 130°.

VITA

Jérémy Veltin

Jérémy Veltin was born on January 31st 1981 in Woippy, France to Francis and Fabienne Veltin. He graduated from Lycée (High School) Henri Poincaré (Nancy, France) in June 1998. He then attended the Ecole Supérieure des Ingénieurs de Nancy (E.S.S.T.I.N.) where he obtained in July 2003 his Master of Science in Fluid Mechanics. During his studies, he spent an academic year (2000-2001) at the Queen Mary College (London, England) and a semester (Spring 2003) at the Von Karman Institute for Fluid Dynamics (Brussels, Belgium). He spent the following year working for Aircelle (formerly Hurel-Hispano, Safran group) in Le Havre (France). He then came to The Pennsylvania State University where he began the Ph. D. program in the Aerospace Engineering department. He is a member of the American Institute of Aeronautics and Astronautics.